Type Ia Supernovae: Explosions and Progenitors

Wolfgang Eitel Kerzendorf

A thesis submitted for the degree of

Doctor of Philosophy

of The Australian National University

Research School of Astronomy & Astrophysics

August 2011

Disclaimer

I hereby declare that the work in this thesis is that of the candidate alone, except where indicated below or in the text of the thesis.

Chapter 2:
The candidate was not involved in the acquisition of Subaru data for Tycho-G. The theoretical calculations for the expected rotation were carried out by Philipp Podsiadlowski The surface gravity was measured by Anna Frebel.

Chapter 3:
The candidate was not involved in the acquisition of Keck data for the donor star candidates. The effective temperature, surface gravity and metallicity measurements were conducted by David Yong (except Tycho-B). The analysis of the Tycho-B HIRES spectrum was partly performed by Simon Jeffery. All other parameters and the LRIS spectrum were analyzed by the candidate.

Chapter 4:
All work (including data acquisition) was performed by the candidate, except rotation which was measured by John Laird (but confirmed by the candidate).

Chapter 5:
The spectrum synthesis code was written by Paolo Mazzali and his group. All other work was performed by the candidate.

W. Kerzendorf

Wolfgang E. Kerzendorf

15th November 2011

Acknowledgments

First and foremost I'd like to thank my supervisor Brian Schmidt. He struck a balance between academic independence and supervision that allowed me to explore a lot of different fields of astronomy, but also focused me on the thesis when necessary. Brian did not only guide me professionally but also personally making him a true 'Doktor Vater' (literally 'doctor father' german name for a PhD supervisor). Thank you for five exciting, interesting and wonderful years here at Mt. Stromlo and to many more years of fruitful collaboration and friendship in astronomy or otherwise.

I have to thank Rainer Wehrse (who unfortunatley passed away) without whom I would have never been able to start my PhD at Mt. Stromlo.

My supervisory panel consisted of Mike Bessell, Frank Briggs, Bruno Leibundgut and Reynald Payne. I thank Mike Bessell for many hours of chats about photometry and stellar spectroscopy. He has been a very patient teacher even in times when my questions were not posed all to well. I thank Frank Briggs for encouraging me to fearlessly ask questions about any subject in the many cosmlogy lunches that I was ignorant about. I thank both Bruno Leibundgut and Reynald Payne for being my external advisors.

At Mt. Stromlo there have been many people who made my stay fun, engaging and exciting. I will unfortunately only be able to name a few of them. In the academic ranks, Harvey Butcher has certainly contributed to my pleasant stay at Mt. Stromlo and I'd like to thank him for that. Not only through his financial support, but also through his advice on the Dalek project. He suggested that nonlinear optimisation is a very active field and that my problem is not unique (which I had assumed). I have to thank Ken Freeman for his help in particular with the use of Fourier transforms to analyse spectra. Peter Wood has always been very helpful when concerning questions of stellar evolution and I thank him for his patience. In the same spirit I thank Amanda Karakas who has taught me a lot stellar evolution and has tolerated the music and language next doors. Stuart Sim has been of invaluable help in the the recent months, educating me about supernova radiative transfer and supernova theory as well as many chats over tea or coffee - thank you. I have to thank Chris Onken for his unbreakable cheerful spirit throughout many projects that we have done together. David Yong has been very patiently teaching me stellar abundance analysis - thank you. I thank all the students at Mt. Stromlo for their friendship and support over the last few years. Especially I'd like to thank Brad Tucker for his catering services for many Mt. Stromlo events. Out of the Mt. Stromlo crowd I have to thank, last but not least, my office mate Simon Murphy for his four years of a fun-filled and enjoyable PhD experience as well as his zealous love for Python that we both share.

Finally I have to thank the Computer Section. All of them have been very helpful, but I have to thank especially Kim and Bill for their computer support as well as witty remarks.

I have to thank all of my collaborators for their help and comments and especially Philipp Podsiadlowski for his valuable insights in binary star evolution and his patience in teaching me. In addition I have to thank my collaborator James Montgomery for helping me with all things about Genetic algorithms. I have to thank the MPA Supernova group for their hospitality and companionship during my stays with them. Specifically I'd like to thank Stephan Hachinger my collaborator, who has helped me master the spectrum synthesis code and patient in teaching me about the theory underlying that code.

I'd like to thank Thomas Magill for designing such a wonderful cover. His artistic skill also made the film 'Starcatchers' a success.

Outside the astronomy community I have to thank all the people that contributed to the wonderful Numpy, Scipy and Matplotlib computing environment. I have to especially thank the support I have received from mailinglists of these products and the IRC Python chat room.

I have to thank all of my friends and family that have accompanied on this journey and helped when things seemed dire.

Last but not least I have to thank my parents Gertraud and Werner. Their unwaivering support, love and companionship have made it possible for me to reach this goal in life.

Abstract

Supernovae are the brightest explosions in the universe. Supernovae in our Galaxy, rare and happening only every few centuries, have probably been observed since the beginnings of mankind. At first they were interpreted as religious omens but in the last half millennium they have increasingly been used to study the cosmos and our place in it. Tycho Brahe deduced from his observations of the famous supernova in 1572, that the stars, in contrast to the widely believe Aristotelian doctrine, were not immutable. More than 400 years after Tycho made his paradigm changing discovery using SN 1572, and some 60 years after supernovae had been identified as distant dying stars, two teams changed the view of the world again using supernovae. The found that the Universe was accelerating in its expansion, a conclusion that could most easily be explained if more than 70% of the Universe was some previously un-identified form of matter now often referred to as 'Dark Energy'.

Beyond their prominent role as tools to gauge our place in the Universe, supernovae themselves have been studied well over the past 75 years. We now know that there are two main physical causes of these cataclysmic events. One of these channels is the collapse of the core of a massive star. The observationally motivated classes Type II, Type Ib and Type Ic have been attributed to these events. This thesis, however is dedicated to the second group of supernovae, the thermonuclear explosions of degenerate carbon and oxygen rich material and lacking hydrogen - called Type Ia supernovae (SNe Ia).

White dwarf stars are formed at the end of a typical star's life when nuclear burning ceases in the core, the outer envelope is ejected, with the degenerate core typically cooling for eternity. Theory predicts that such stars will self ignite when close to 1.38 $M_\odot$ (called the Chandrasekhar Mass). Most stars however leave white dwarfs with 0.6 $M_\odot$ and no star leaves a remnant as heavy as 1.38 $M_\odot$, which suggests that they somehow need to acquire mass if they are to explode as SN Ia. Currently there are two major scenarios for this mass acquisition. In the favoured single degenerate scenario the white dwarf accretes matter from a companion star which is much younger in its evolutionary state. The less favoured double degenerate scenario sees the merger of two white dwarfs (with a total combined mass of more than 1.38 $M_\odot$).

This thesis has tried to answer the question about the mass acquisition in two ways. First the single degenerate scenario predicts a surviving companion post-explosion. We undertook an observational campaign to find this companion in two ancient supernovae (SN 1572 and SN 1006). Secondly, we have extended an existing code to extract the elemental and energy yields of SNe Ia spectra by automating spectra fitting to specific SNe Ia. This type of analysis, in turn, help diagnose to which of the two major progenitor scenarios is right.

Understanding the progenitors of SN Ia has wide ranging applications. Not only would we better be able to calibrate SNe Ia for use as distance probes, but we could also dramatically improve our understanding of the chemical history of the universe, which SNe Ia play a seminal role in.

Contents

List of Figures

List of Tables

CHAPTER 1

Introduction

For millennia mankind has watched and studied the night sky. Apart from planets and comets it appeared as an immutable canvas on which the stars rested. It comes as no surprise that for ancient civilisations supernovae (which were very rare events, occurring only every few centuries) were interpreted as important omens as they broke the paradigm of the unchanging night skies. As these events are so rare their origin remained a mystery until in the first half of the last century. Baade & Zwicky (1934) suggested that *"the phenomenon of a super-nova represents the transition of an ordinary star into a body of considerably smaller mass"*. For the last 85 years the supernova-branch of astronomy has been developing. There have been many advances, but there are still many unknowns. This thesis addresses two sub fields of supernovae (supernovae is the plural of supernova): The unsolved progenitor problem for Type Ia supernovae as well as quantifying the nucleosynthetic yield and energies of Type Ia supernovae.

1.1. Ancient Supernovae

Although supernovae must have been observed since the beginning of humankind, reliable records only exist for the last thousand years. There are however transient star sightings mentioned in older text. For example, *Houhanshu* (Zhao et al., 2006), mentions a new star which was visible for 8 months (depending on the interpretation of the text it could also mean 20 months) in the year of AD185. This new star was reported to be in the *Nanmen* asterism which is close to Alpha Centauri. Observations in modern times have revealed a supernova remnant in a distance of roughly 1 kpc near Alpha Centauri (Zhao et al., 2006). Some believe this to be evidence that the star mentioned in the ancient text is the oldest written record of a supernova, others however interpret this text as reference to a comet (Chin & Huang, 1994).

The oldest undisputed record of a supernova is SN 1006, which also coincides with the brightest ever recorded supernova. It was observed worldwide by Asian, Arabic and European astronomers. Goldstein (1965) gives a good summary of the observations and interpretation given by these ancient observers. Ali Ibn Ridwan was an Egyptian astronomer who recorded the appearance of SN 1006. He wrote in a comment on Ptolemy's Tetrabiblos:

> *"I will now describe for you a spectacle that I saw at the beginning of my education. This spectacle appeared in the zodiacal sign Scorpio in opposition to the sun, at which time the sun was in the 15th degree of Taurus, and the spectacle in the 15th degree of Scorpio. It was a large spectacle, round in shape and its size 2.5 or 3 times the magnitude of Venus. Its light illuminated the horizon and twinkled very much. ... This apparition was also observed at the time by (other) scholars just as I have recorded it."*

Only 50 years after the bright supernova of 1006, Chinese and Japanese astronomers reported on another cataclysmic event which was at first even visible during the day. SN 1054 might have also been observed in North America where petroglyphs in the Chaco Canyon could be interpreted as a depiction of this event (see Figure 1.1). It is difficult to date these cave paintings precisely, but they were created around the time of the SN 1054 explosion. It is still debated if SN 1054 was the inspiration of the painting or the inspiration came from the passing of Halley's comet in 1066. More than 900 years later Staelin & Reifenstein (1968) detected a pulsar in the centre of SN 1054. This was the first time that the stellar remnant connected with a known supernova was found. SN 1181 ends the 180 year period with three confirmed supernovae that started with SN 1006. This Galactic supernovae first discovered in August of 1181 was visible for about half a year and was mentioned in eight different texts by Chinese and Japanese astronomers. 3C58, a pulsar found in SN 1181, is suggested to be the neutron star remnant of this stellar explosion.

Humanity had to wait for nearly 400 years before the next bright event occurred. Although the supernova was discovered by an abbot in Messina on 06 November 1572, Tycho Brahe is often attributed the discovery of this event. The attribution of SN 1572 to Tycho came from his angular distance and brightness measurements of unprecedented precision (location to a few arc minutes!; see Figure 1.2). These precise measurements proved that the star changed in brightness but stayed at a fixed position like stars. Therefore Tycho concluded that this transient event was far beyond the moon, where stars were suspected to be located. This broke the paradigm of the constancy of stars, which was believed by many. Having been studied for almost one and a half years the supernova finally faded from visibility in March 1574. The measurements of SN 1572, among other astronomy related subjects, were published by Brahe & Kepler (1602). Another 400 years elapsed before radio emissions identified the remains of SN 1572 (Hanbury Brown & Hazard, 1952).

Kepler, working with Tycho, discovered SN 1604 nearly 20 days before maximum light, which occurred on the 28th of October 1604. Serendipitously, around this time there was a conjunction of Jupiter and Mars, which was observed by many astronomers. This also led to an early upper limit, where astronomers described the conjunction but did not mention the supernova. As Tycho did before him, Kepler measured the location and the brightness of the supernova precisely (see Figure 1.3; Kepler, 1606) before it faded from visibility 18 months later. Kepler was not the only astronomer observing SN 1604 and there exist many texts from Korea and China mentioning this event. SN 1604 was the last confirmed observation of a supernova in our own Galaxy. A good review of these ancient supernovae can be found in Green & Stephenson (2003).

Figure 1.1 Chaco canyon petroglyphs show a hand, a moon and a bright celestial object. This could be SN1054 but it is ambiguous. (Source Wikipedia/ Photographer jamesdale10/ Creative Commons license)

Observations in modern times have revealed two additional supernovae that must have exploded after SN 1604 but are not mentioned in the historical literature. Cas A, a supernova remnant, is the brightest radio source in the sky. It has been estimated that this supernova should have been visible between 1660 and 1680, however there are no clear descriptions or references from astronomers in the seventeenth century. There has been much speculation to the reason (e.g. heavily obscured by interstellar dust and thus not visible), but it still remains unclear why it was not observed. Green & Gull (1984) detected another supernova remnant right in the heart of our Galaxy. Recent X-ray observations revealed the supernova to be less than 150 years old (Reynolds et al., 2008). This supernova happened very close to the galactic centre and is heavily obscured by dust. At the time of explosion it was not visible at optical wavelengths. In summary, the five ancient supernovae (SN 1006, SN 1054, SN 1181, SN 1572 and SN 1604) were all observed without the use of a telescope. Our ancient astronomy colleagues had only very primitive means to observe supernovae. However, the remarkably precise written records can be attributed to their ingenuity and assiduity. Even in an era of 10-meter telescopes the records of these explosions remain useful (see Figure 1.3).

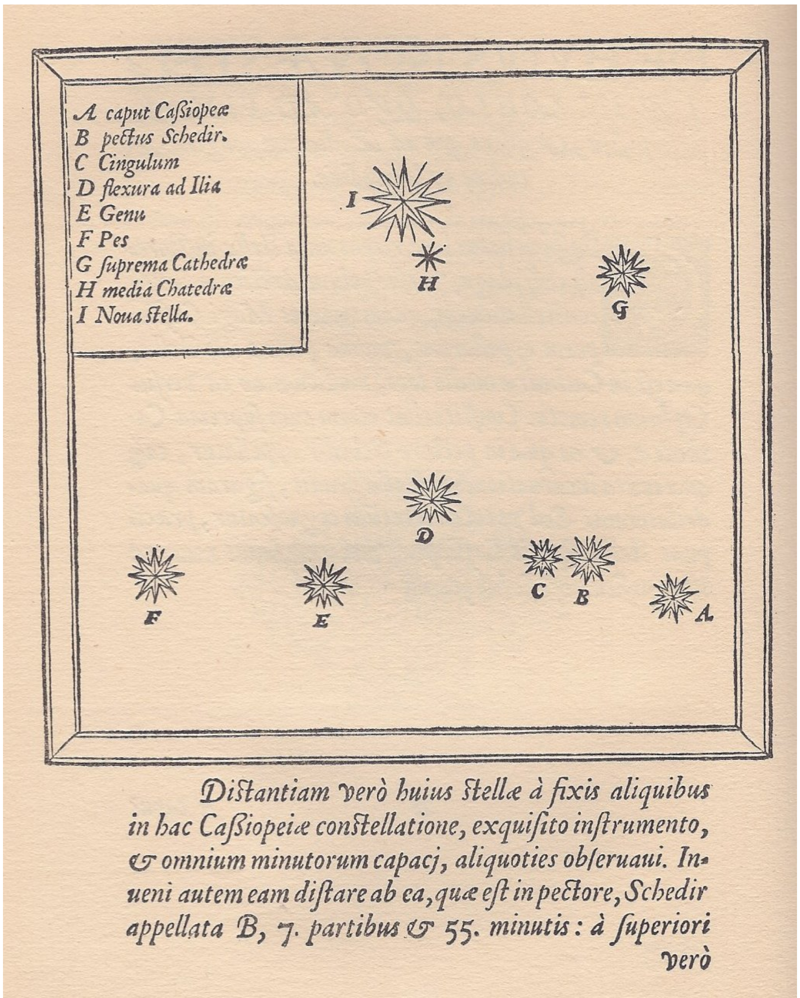

Figure 1.2 Brahe, Tychonis [A facsimile reprint of the original edition, 1573]. The supernova is marked with the letter I. The caption reads: *"I have indeed measured the distance of this star from some of the fixed stars in the constellation of Cassiopeia several times with an exquisite (optical) instrument, which is capable of all the fine details of measurement. I have further detected that it (the new star) is located 7 degrees and 55 minutes from the star at the breast of the Schedir designated by B."* translation kindly provided by Leonhard Kretzenbacher

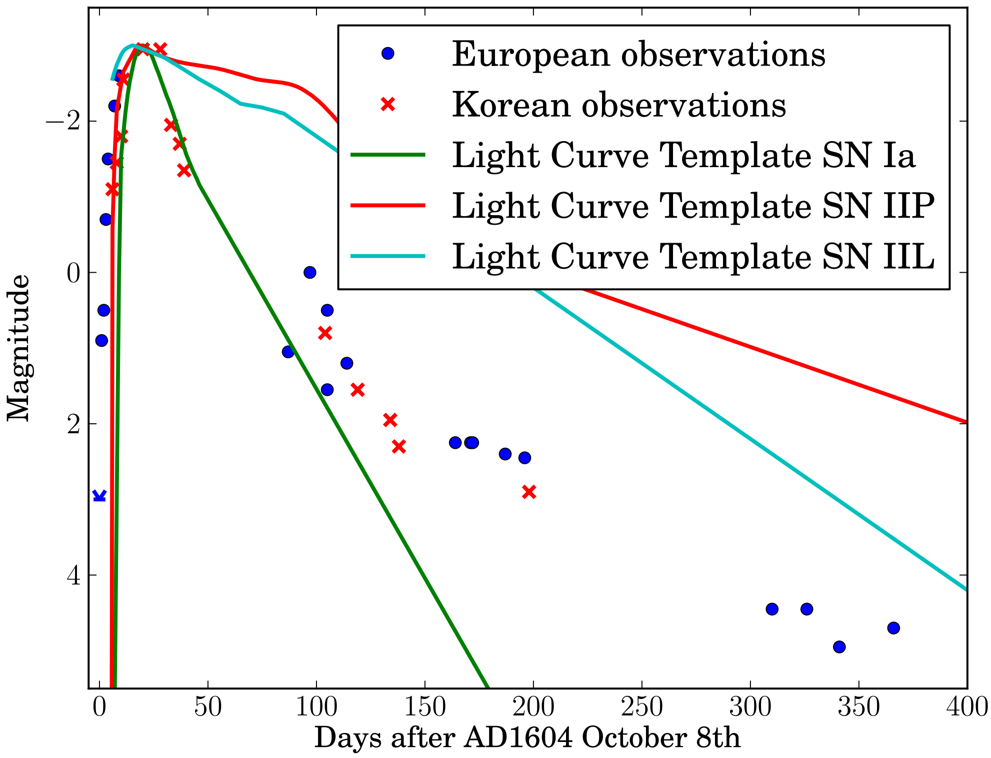

Figure 1.3 Light curve of SN 1604 obtained by ancient European and Korean astronomers. There is a European upper limit on the 8th of October 1604. Comparing these 400 year old measurements with modern day light curve templates by Li et al. (2011) show clearly that the supernova is a Type Ia supernova. Historical data graciously supplied by D.A. Green (Clark & Stephenson, 1977; Green & Stephenson, 2003)

1.2. Modern Supernova Observations and Surveys

The era of modern supernova observations started with the discovery of SN 1885. SN 1885 (also known as S Andromedae) was first spotted by Isaac Ward in Belfast in August of 1885 (Hartwig, 1885) and was visible until February 1886. More than 50 years later Baade & Zwicky (1934) coined the term supernova and established the difference between common novae and supernovae. Baade & Zwicky (1934) also suggested that these luminous events are caused by the deaths of stars.

In order to understand the phenomenon of supernovae better, Zwicky began a supernova search with the 18-inch Schmidt telescope. In those days the detectors were photographic plates, which were analysed with the help of a blink comparator. This device permitted rapid switching between viewing two different photographic plates which were observed on different nights and one could easily detect *new stars*. Using this method Zwicky found several supernovae which in turn inspired Minkowski to classify these supernovae by their spectra (Minkowski, 1941). Minkowski categorised the 14 known objects into two categories. Those without hydrogen he called *Type I*, those with hydrogen he called *Type II* (see Section 1.3.1 for a more detailed description of supernova classification).

With the advent of computing in the 1960s the first computer-controlled telescopes were built. A 24-inch telescope was constructed by the Northwestern University and deployed at the Corralitos Observatory in New Mexico with the express purpose of undertaking a Digitized Astronomy Supernova Survey (DASS; Colgate et al., 1975). While ultimately unsuccessful in finding supernovae, this search lead the way in computer controlled discovery and many later surveys would employ a similar design.

The advancements of detector technologies in 1980s, such as photoelectric photometers and later charged coupled devices (CCDs), together with increasing power and connectivity of computers, enabled the construction of automated telescopes with minimal human interaction (e.g. Genet et al., 1986). These first automated telescopes were used mainly for variable star surveys.

The Berkley Automatic Imaging Telescope (BAIT; Richmond et al., 1993) was one of the first automated telescopes designed specifically to find supernovae. This search produced 15 supernova discoveries by 1994 (van Dyk et al., 1994), including the famous SN 1994D, pictured here (Figure 1.4). Due to increasing light pollution in Berkley this project moved to the Lick Observatories and was named the Lick Observatory Supernova Search (LOSS; Li et al., 2000). With the switch to the new observatory the BAIT was replaced with the Katzman Automatic Imaging Telescope (KAIT; Filippenko et al., 2001). LOSS has been one of the most successful supernova surveys to date. By the year 2000 it had found 96 supernovae (Filippenko et al., 2001).

In the mid to late 1990s, as high quality data on supernovae became available (mainly contributed by the Calán/Tololo supernova survey (CTSS; Hamuy et al., 1993)), the long dream (e.g. Baade, 1938; van den Bergh, 1960; Kowal, 1968) of using these objects as reliable distance indicators finally became viable. Two main teams drove the advancement in the cosmological distance measurements (the Supernova Cosmology Project (SCP) and the High Z Supernova Search (HZSNS)) and independently arrived at the same conclusion: the expansion of the universe is accelerating (Riess et al., 1998; Perlmutter et al., 1999). For a more detailed overview of supernova cosmology see Section 1.3.6.

Figure 1.4 SN 1994D in NGC 4526 taken with the same HST. This image shows very clearly how the light from the explosion of only one star can outshine an entire galaxy (Pete Challis/NASA). This picture is also widely used in popular astronomy.

By the turn of the millennium and following the discovery of the accelerated expansion of the universe, a variety of groups started large surveys specifically for supernovae. Among them were the 'The Equation of State: SupErNovae trace Cosmic Expansion' (ESSENCE; Garnavich et al., 2002) project and Supernova Legacy Survey (SNLS; Pain & SNLS Collaboration, 2003). Both these programs have finished taking data, but have yet to publish all of their observations. Specialised surveys like the Nearby Supernova Factory (Aldering et al., 2002) used an Integral Field Unit (IFU) to capture light curves and spectra at the same time. The Higher-z survey (Strolger et al., 2004) focused on a high redshift range, available only through the HST.

This effort is continued by a multitude of large sky surveys that have started in recent years (or are just about to). Some of these focus exclusively on transients and supernovae, like the Palomar Transient Factory (PTF; Rau et al., 2009), whereas others, like the Panoramic Survey Telescope & Rapid Response System (PanSTARRS; Kaiser, 2004) and SkyMapper (Keller et al., 2007), have transient/supernova components. Upcoming surveys, like the Large Synoptic Survey Telescope (LSST; Pinto et al., 2006) and the space-based Global Astrometric Interferometer for Astrophysics (GAIA; Perryman et al., 2001) mission, will provide unprecedented detail about current supernova types as well finding several new classes of transients (e.g. GAIA will find $\approx 14,000$ Type Ia supernovae (SNe Ia) during its mission lifetime; Belokurov & Evans, 2003).

In addition to supernova searches in the optical, searches have commenced at other wavelengths and other physical messengers. Gamma Ray Bursts (GRBs) were first detected, as the name suggests, in gamma-rays and are thought to be the bolometrically brightest transients. The first detection of a GRB was on July 2 of 1967 by a Vela satellite. Vela satellites where designed to monitor gamma-ray signatures of banned nuclear weapons testing. It became quickly clear, due to the unusual form and direction of the signal, that these new GRBs where not of terrestrial origin. Six years later, the results from the Vela satellites were declassified and the existence of these GRBs made known to the world (Klebesadel et al., 1973).

At the beginning of the 1990s, new high-energy instruments like the Burst and Transient Source Experiment (BATSE) surveyed the sky in gamma-rays and detected thousands of GRBs. Meegan et al. (1992) showed that GRBs, due to their isotropic distribution, are events at cosmological distances rather than coming from our own Galaxy. The BeppoSAX satellite, launched in 1996, was able to provide accurate positions for GRBs. This advancement led to the discovery that GRBs occur in distant galaxies, establishing them as one of the most luminous events in the universe ($> 10^{52}$ erg). The co-location of SN 1998bw and GRB 980425 established the connection between supernovae and some GRBs (Galama et al., 1998). A class of short GRBs has remained supernovaless (Xu et al., 2009, e.g.). The subsequent High Energy Transient Explorer (HETE) mission established a new class of transients called X-ray-flashes. These new objects are thought to be similar to GRBs in physical nature but much less energetic (Zhang et al., 2004). Such work continues with the Swift mission.

Astronomy has been largely based on electromagnetic waves, but there are other messengers of astrophysical information. Gravitational waves, predicted by the theory of general relativity (Einstein, 1918), might provide us with another insight into supernovae. The most advanced detector today, the Laser Interferometer Gravitational Wave Observatory (LIGO; Abramovici et al., 1992) has not yet detected gravitational waves, although modelling indicates that it would have been highly unlikely, to have an event close enough to have been detected by LIGO. Advanced LIGO will likely detect gravitational waves from in-spiralling neutron stars, and possibly core collapse supernovae. The Laser Interferometer Space Antenna (LISA; Jafry et al., 1994), an ambitious mission planned for the coming decade, is definitely sensitive enough to detect the predicted gravitational waves (a non-detection would show problems with the theory of general relativity). In the supernova field LISA might give us an estimate on the number of in-spiralling white dwarfs, which are suggested as progenitors of SNe Ia.

SN 1987A was the first and only occasion on which neutrino emission from a supernova has been measured (Bionta et al., 1987; Hirata et al., 1987; Alekseev et al., 1988). New, more sensitive detectors, like IceCube (Karle, 2008), will hopefully enable accurate neutrino observations of future Galactic supernovae.

For now, the optical observations of supernovae provide the bulk of observations of these transients. Hopefully, future instruments and capabilities will enable us to combine measurements across the electromagnetic spectrum with gravitational wave and particle flux observations. Such an approach will unlock many of the secrets still held by these mysterious objects.

1.3. Observational Properties of Supernovae

1.3.1. Supernova classification

The classification of supernovae started in 1941 when Minkowski realised that there seem to be two main types (Minkowski, 1941). Those containing a Hα line he called Type II supernovae and those showing no hydrogen he called Type I supernovae. This basic classification has remained to this day, however the two main classes branched into several subclasses. During the 1980s, the community discovered that most SNe Ia showed a broad Si II line at 6150 Å. There was, however, a distinct subclass of objects that lacked this feature. These silicon-less objects were then subclassed further into objects that showed helium – now known as Type Ib supernova (SN Ib) – and those that did not, called Type Ic supernova (SN Ic) (see spectra in Figure 1.5; Harkness et al., 1987; Gaskell et al., 1986). The classical Type I supernova was renamed to SN Ia. Today we know that SNe Ia originate from the explosion of white dwarfs. Type II supernovae (SNe II) and Type Ib/c supernovae (SNe Ib/c) are believed to stem from the collapsing core of a massive star.

Only in the past two decades have we been able to explore the finer details of the SNe Ia class. Most objects have a small brightness scatter and are referred to as *Branch-normal* SNe

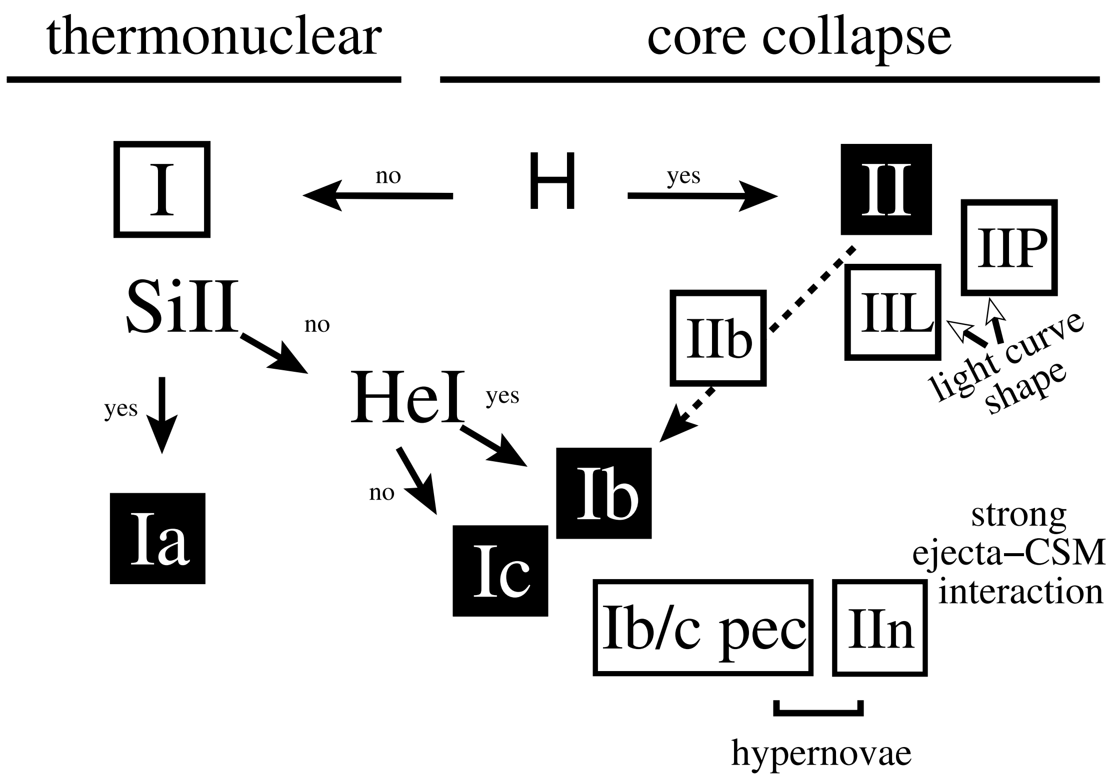

Figure 1.5 Classification scheme by Turatto (2003)

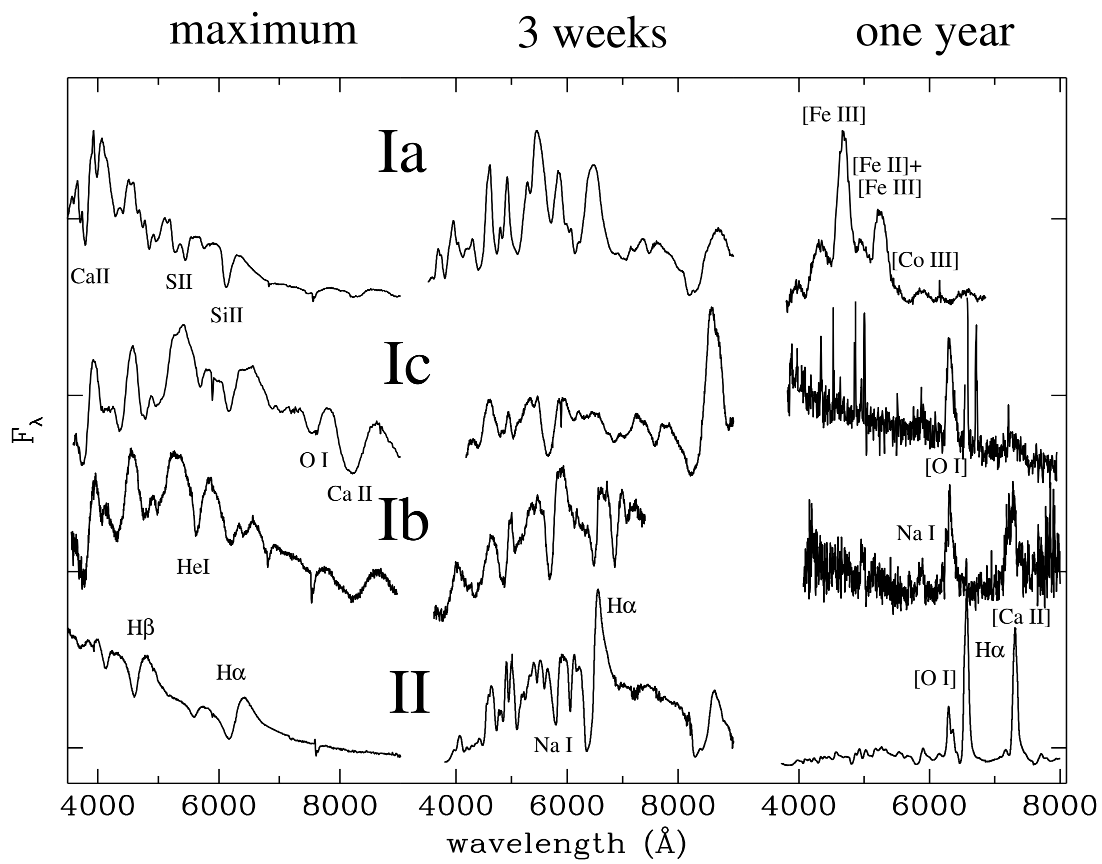

Figure 1.6 Spectral comparison from Turatto (2003)

Ia (Branch et al., 1993). In this class of *Branch-normal* SNe Ia, the community has found additional features that vary with brightness. For example, Benetti et al. (2005) found that the evolution of the photospheric velocity measured from the Doppler shift of the Si II line at 6355 Å is faster in more luminous SNe Ia (high velocity gradient - HVG) and slower in fainter SNe Ia (low velocity gradient - LVG) . Additionally, the luminosity of SNe Ia manifests itself in the spectra through the ratio of the Si II absorption features at 5800 Å and the feature at 6150Å (Nugent et al., 1995). Whereas faint supernovae have a pronounced trough at 5800 Å the luminous ones completely lack this feature but show a strong absorption line at 6150 Å instead.

In addition to the group of *Branch-normal* SNe Ia, there are more distinct subclasses with extreme luminosities and peculiar spectra. The overluminous class we call 91T-like after the bright supernova SN 1991T (Phillips et al., 1992). In their spectra, 91T-like SNe Ia at early times show weak silicon and calcium lines, leading to a nearly featureless continuum. At late times this class shows a spectrum similar to *Branch-normal* SNe Ia. The faint supernova SN 1991bg (Filippenko et al., 1992) is the namesake for the underluminous class (91bg-like). 91bg-like SNe Ia are characterised spectroscopically by their distinct lack of strong iron group element (IGE) features. A third prominent subclass (see Figure 1.7) is the 02cx-like SNe Ia (Li et al., 2003) SNe Ia named after SN 2002cx. Observationally, they can be seen as a chimera between 91bg-like SNe Ia and 91T-like SNe Ia, inheriting the low luminosity from the former and the pre-maximum featureless continuum from the latter. In addition,

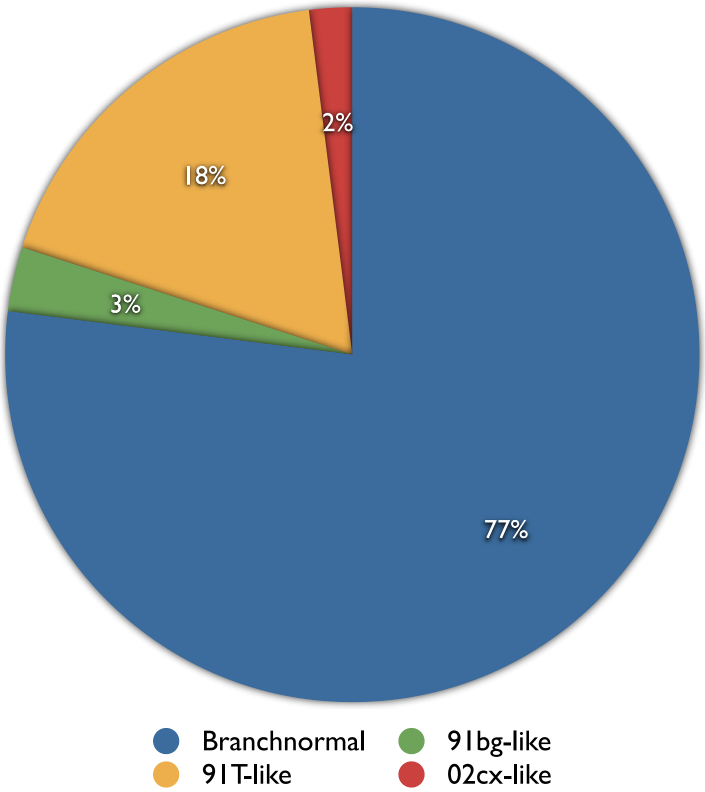

Figure 1.7 Estimated fractions for different Type Ia (SN Ia) classes for a purely magnitude limited search. Adapted from Li et al. (2011)

02cx-like spectra are dominated by IGE features. Li et al. (2011) have measured the fraction of different subclasses from the LOSS dataset. Figure 1.7 shows the fraction of the different subclasses that would be expected from a purely magnitude limited search. Although there are several different subclasses, the class of SNe Ia is relatively homogeneous as it is dominated by the *Branch-normal* SNe Ia- in stark contrast to the different SNe II.

SNe II span large ranges in observables. We can divide the main class into four subclasses. Type II Plateau supernovae (SNe IIP; Barbon et al., 1979) have a relatively flat light curve after an initial maximum (see Figure 1.9). In contrast the Type II Linear supernovae (SNe IIL; Schlegel, 1990) have a rapid linear decline after the maximum. The third subclass is the Type II narrow-lined supernova (SN IIn) which is characterised by narrow emission lines, which are thought to come from interaction with the circumstellar medium (CSM). Finally the Type IIb supernovae (SNe IIb) show strong hydrogen lines in their early spectrum, but evolve to become spectroscopically more like SNe Ib with no hydrogen lines but strong silicon and helium lines. SNe Ib and SNe Ic (often referred to as SNe Ib/c) are believed to originate from the same physical process as all SN II-classes - the collapse of stellar cores (often grouped as SN II/Ib/c). In contrast to the SNe Ia, which are dominated by one subclass (*Branch-normal* SNe Ia), the different subclasses of SNe II are much more uniformly distributed (see Figure 1.8). But the classes are also much less strict with numerous intermediate and some peculiar objects. For a more comprehensive review of the classification of supernovae the reader should consult Turatto (2003) and Turatto et al.

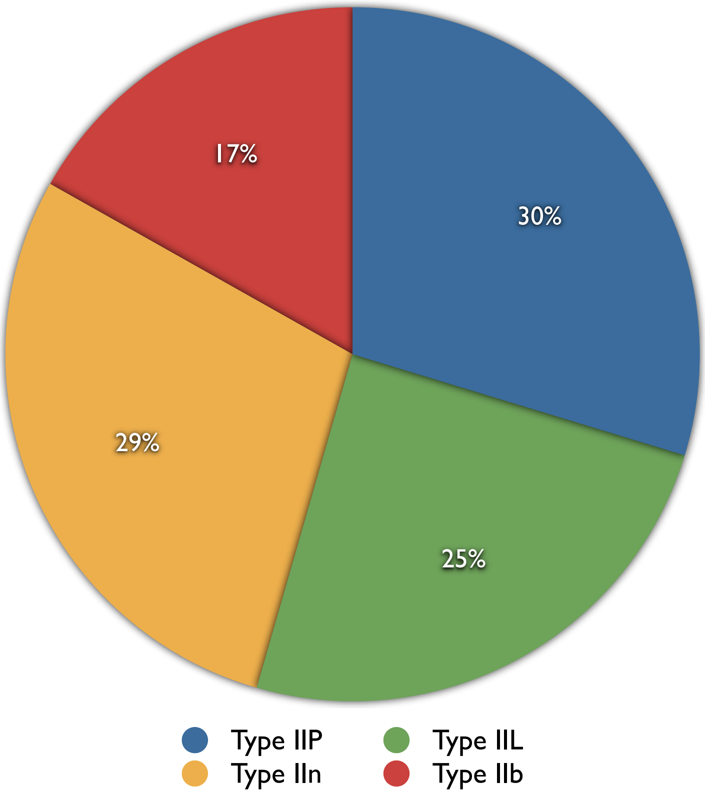

Figure 1.8 Estimated fractions for different Type II classes for a purely magnitude limited search. Adapted from Li et al. (2011)

(2007).

1.3.2. Supernova rates

The observed supernova frequency carries important information about the underlying progenitor population. In this section we will concentrate more on SNe Ia-rates but will mention SNe II and SNe Ib/c where applicable.

Zwicky (1938) was the first work that tried to measure the supernova rate. By monitoring a large number of fields monthly, he arrived at a supernova rate by merely dividing the number of supernova detections by the amount of monitoring time and number of galaxies. This crude method resulted in a rate of one supernova per six centuries per galaxy.

Over time many improvements were made to this first method. Individual rates were calculated for different galaxy morphologies and different supernova types. To combine measurements from different galaxies the rate was normalised by dividing the supernova rate (measured by number of events per century) by galaxy luminosity (e.g. van den Bergh & Tammann, 1991; Tammann et al., 1994).

In recent years, however, rate measurements have been made in reference to mass and/or star formation, rather than just galaxy luminosity (SNe per century per $10^{10}\ M_{\odot}$). The community (e.g. Mannucci et al., 2005) subsequently switched from B-Band photometry

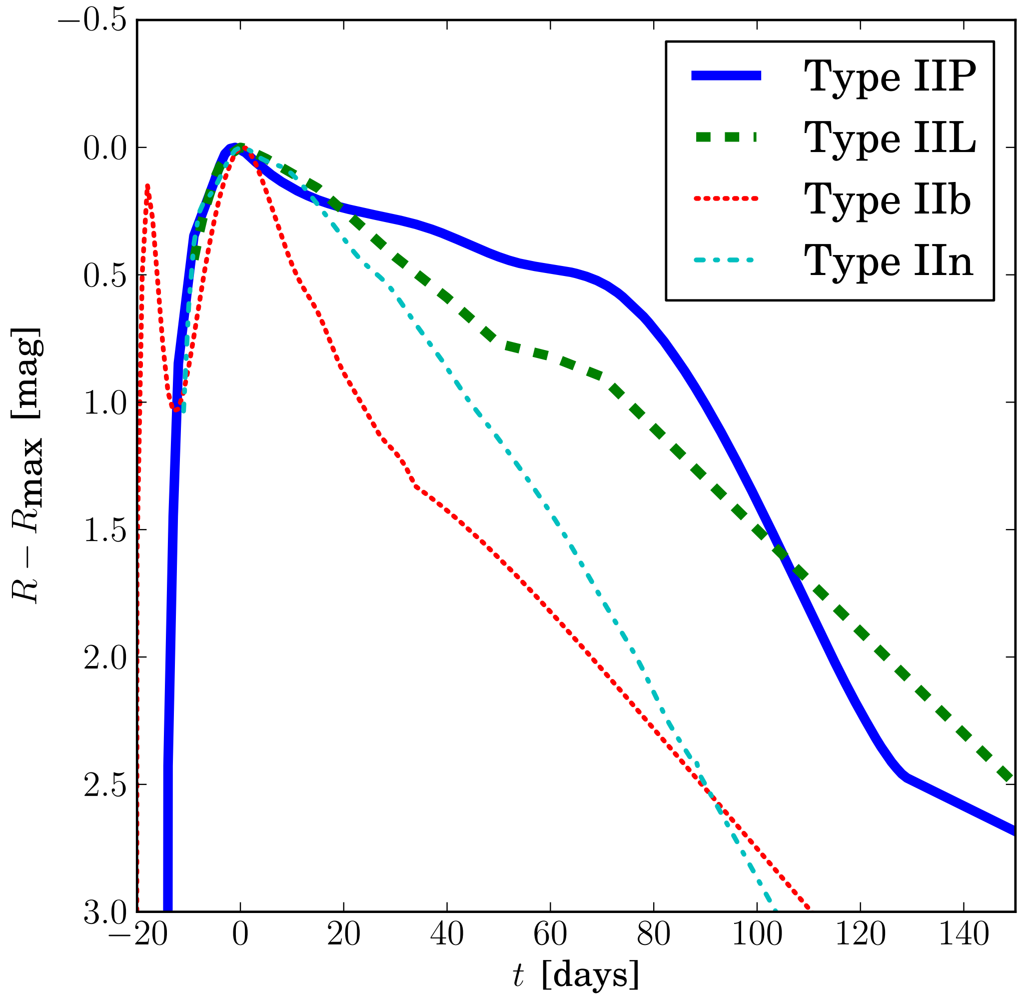

Figure 1.9 Light curve data taken from Li et al. (2011) templates. The time is relative to maximum light and the magnitude is the difference between maximum

to the use of infrared photometry as the near infrared (NIR) is thought to better represent star-formation. B-Band photometry does not separate between the stellar mass and star formation rate(Hirashita et al., 2003).

Figure 1.10 plots the rate of supernovae per solar mass of material versus the galaxy morphology. The data clearly shows that there is a strong connection between morphology and supernova rates. For a long time it has been realised that SNe II and SNe Ib/c occurred preferentially in galaxies with active star formation, whereas SNe Ia occurred in all galaxy types. This indicates that SNe Ia and SNe II/Ib/c have different progenitors - with SNe II/Ib/c being related to young and presumably massive stars, and SNe Ia coming from a population of older stars. Theoretical calculations confirmed the view that stars larger than 8 $M_{\odot}$ should explode in a process known as core collapse (leading to SNe II/Ib/c), whereas white dwarf stars approaching the Chandrasekhar mass ($M_{\mathrm{Chan}} = 1.38\,M_{\odot}$; Chandrasekhar, 1931) might explode as a SN Ia. The connection to

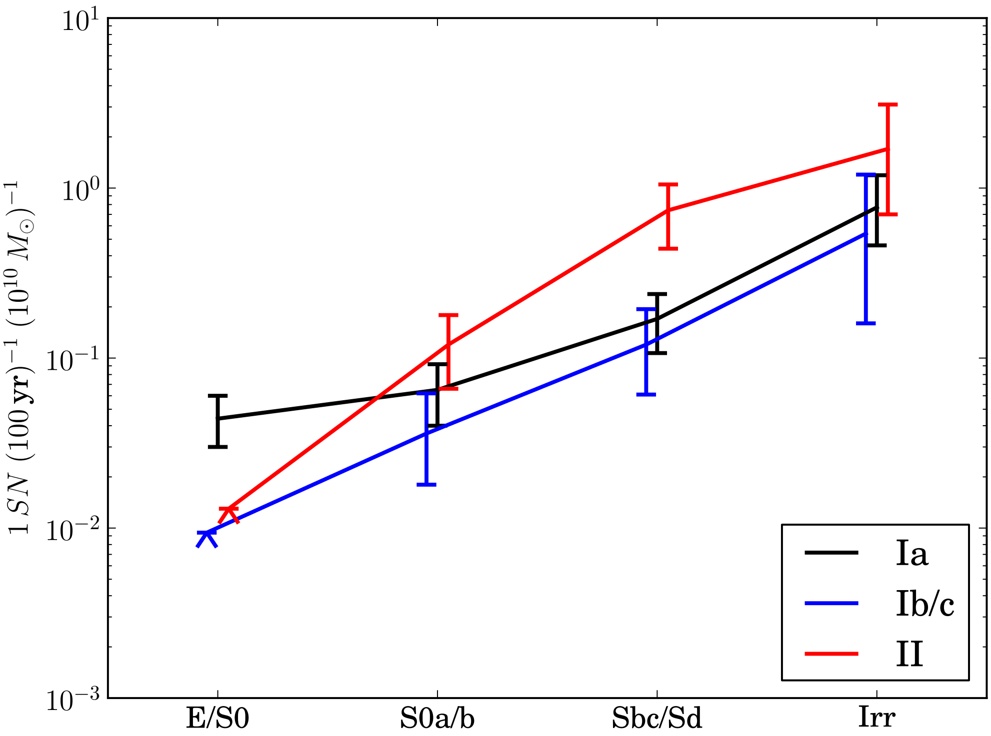

Figure 1.10 The plot shows the estimated supernova rate per unit mass in different galaxy morphologies (Mannucci et al., 2005). From left to right we plot old elliptical galaxies, lenticular galaxies, spiral galaxies and irregular galaxies. There have been no detections of SNe Ib/c and SNe II in old elliptical galaxies which suggests that these types only occur in galaxies with recent star-formation.

massive stars was confirmed when the progenitor of SN 1987A was asserted as a massive star, along with the detection of neutrinos in line with theoretical predictions. The progenitors of SN Ia remains an open question, and a central topic of this thesis. Additionally, it seems the progenitors of SNe Ia occur in both young and old populations. This could hint that there are two main progenitor types, one which occur soon after star-formation, and another that takes a long time between formation and explosion.

To address this issue several groups have tried to measure a SNe Ia-rate that is completely independent of galaxy morphology (e.g. Mannucci et al., 2006; Maoz et al., 2010). This so-called, delay time distribution (DTD), measures the supernova rate over time following a brief outburst of star formation. This technique requires a detailed knowledge of the star-formation history of these systems. Several new techniques are emerging that try to circumvent the intrinsically difficult task of determining star-formation for individual SNe Ia host galaxies (Maoz & Badenes, 2010; Barbary et al., 2010; Totani et al., 2008; Maoz et al., 2010).

Supernova rates and DTDs are an emerging tool to constrain progenitors. New upcoming surveys will provide an abundance of supernovae and measurements of their environments. However, fundamental uncertainties still exist on the theoretical front to predict DTDs for a given progenitor model.

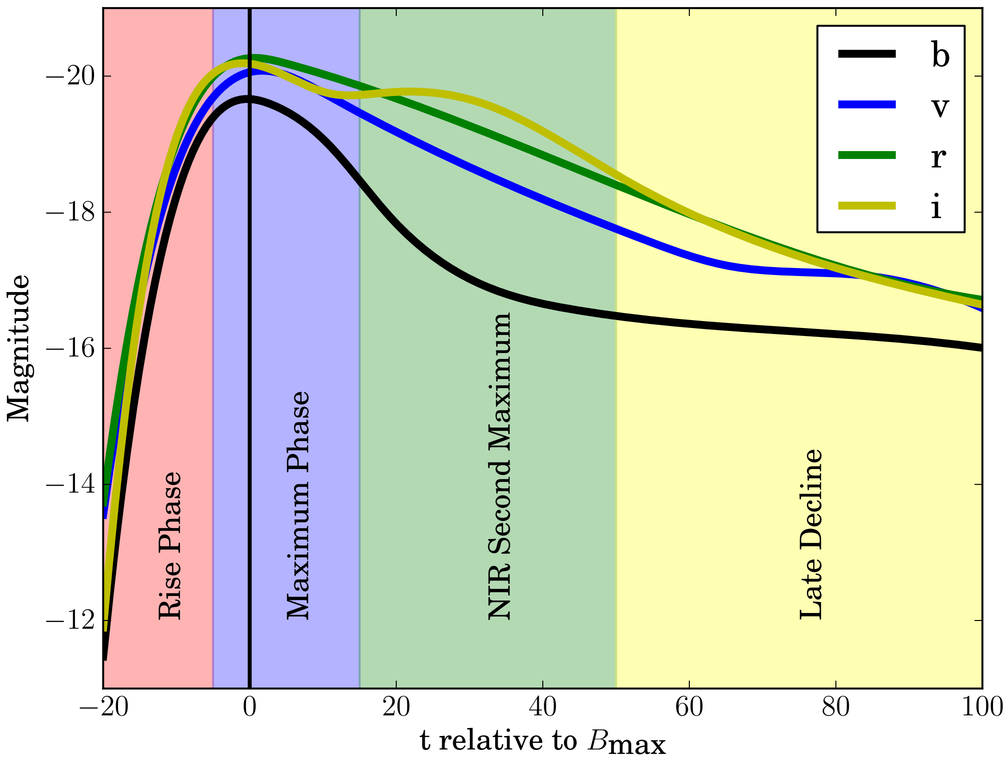

Figure 1.11 Light curves of SN 2002bo (data from Benetti et al., 2004)

1.3.3. Light Curves

Light curves give important insights into the physical processes occurring during the evolution of the supernova. Arnett (1982) for example deduced from the light-curve shape that Type I supernovae are eventually powered by the decaying ^{56}Co. For a brief overview of SN II light-curves we refer the reader back to Section 1.3.1.

For SNe Ia the light curve can be divided into four different phases (see Figure 1.11). In the first phase the SN Ia rises to the maximum brightness. Although only a small fraction of SNe Ia have been observed in the earliest parts of this phase, one can determine the time of the explosion by approximating the very early phase of a SN Ia with an expanding blackbody. The luminosity of this blackbody (in the Rayleigh-Jeans regime) is

$$L \propto v^2 (t + t_r)^2 T_{\mathrm{eff}}^4,$$

where v is the photospheric velocity, T_{eff} is the temperature of the fireball, t is the time relative to the maximum and t_r is the rise time. The canonical rise time of SNe Ia is 19.5 days (Riess et al., 1999). New measurements using light curves of nearly four hundred SNe Ia, many these from the LOSS dataset, have however shown a shorter rise time (in B-Band) of 18 days (Ganeshalingam et al., 2011). The rise is very steep and the brightness increases by a factor of ≈ 1.5 per day until 10 days before maximum. In the second phase the SN Ia reaches the maximum first in the NIR roughly 5 days before the maximum in the B-Band (see Figure 1.11; Meikle, 2000). During the pre-maximum phase the colour stays fairly constant at $B - V \approx 0.1$, but changes non-monotonically to $B - V = 1.1$ thirty days after maximum. In the third phase SN Ia starts to fade but a second maximum is observed in the NIR (Wood-Vasey et al., 2008). Pinto & Eastman (2000) and later Kasen (2006) have successfully explained this by fluorescence of iron-peak elements in the NIR. Finally, in the last phase, light curves at late times can be used to probe the amount of ^{44}Ti and other radioactive elements, but are complicated by light echoes (e.g. Schmidt et al., 1994b) and time dependent radiative transfer (Kozma et al., 2005). Leloudas et al. (2009) hold the record for the longest observed SNe Ia with SN 2003hv, which has been observed to nearly 800 days past maximum light.

1.3.4. Spectra

Spectra provide much more detailed information about supernovae than light curves. They are however, observationally much more expensive and difficult to precisely calibrate.

For all classes, supernova spectra can be divided into two phases: the photospheric phase and the nebular phase. In the photospheric phase, the spectrum can be very well approximated by a dense optically-thick core which has a black-body radiating surface with an optically thin expanding ejecta above. Photon creation is often negligible in the outer, optically-thin ejecta. The ejecta rather reprocesses the radiation field coming from the photosphere. In the case of SNe Ia this photosphere consists of layers of first intermediate mass elements (IMEs), and then IGEs, heated by the decay of ^{56}Ni. For SNe II the central region of the photosphere is hydrogen rich, which is kept hot by the energy deposited by the initial shock, diffusing outwards.

As the supernova expands the photosphere recedes inward in mass and the optically thin layer grows larger and larger. Once sufficiently expanded, the entire SN ejecta becomes optically thin, which is known as the nebular phase. This phase is dominated by strong emission peaks and little continuum.

Type Ia supernova spectra

The time evolution of SNe Ia spectra is characterised by the photosphere shining through the ashes of the explosion. The inner core has nearly completely burned to IGEs, the shell above consists mostly of IMEs like sulphur and silicon. With the photosphere moving inward we first see IMEs before the photosphere goes deeper and deeper and shines through some of the core material. This onion-like structure can be probed by a method called supernova tomography. By modelling subsequent spectra one is able to reconstruct the individual shells of the supernova (Stehle et al., 2005; Hachinger et al., 2009). Modelling of SNe Ia spectra is an important part in understanding the explosion process of SNe Ia. Chapter 5 discusses this topic, which was explored in this thesis.

Similar to light-curves, the spectra have different phases. We will use the *Branch-normal* Type Ia, SN 2003du, to demonstrate the spectral evolution (Tanaka et al., 2011):

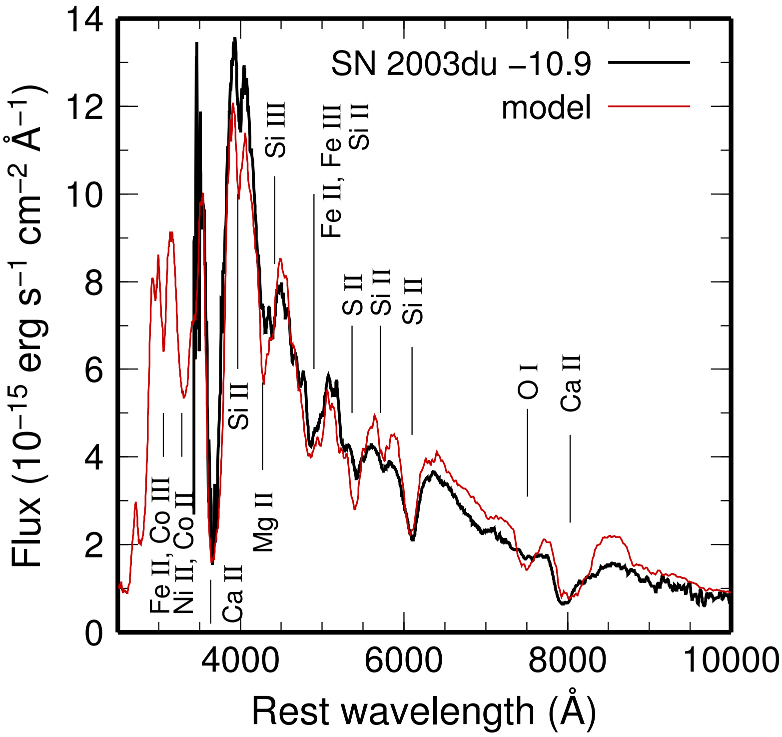

Figure 1.12 SN 2003du ten days before maximum light. The P Cygni-profiles of Silicon are clearly visible (Figure kindly provided by M. Tanaka; Tanaka et al., 2011)

Pre-Maximum Phase

In the pre-maximum phase the spectrum shows very high line velocities (up to $18,000\,\mathrm{km\,s^{-1}}$) which measure the location of the photosphere in the ejecta. There is a relatively well defined pseudo-continuum with strong P Cygni-profiles[1] of IMEs and IGEs (see Figure 1.12). The IGEs seen at this early phase are mostly primordial as the burning in the outer layers is incomplete and does not produce these elements.

The Ca II line is prominent in the blue and often shows extremely high velocities at early times (in SN 2003du $v_{\mathrm{ph}} \approx 25,000\,\mathrm{km\,s^{-1}}$). There have been multiple suggestions for the cause of this unusual velocity, including interaction with calcium in the CSM or high-velocity ejecta blobs (Hatano et al., 1999; Gerardy et al., 2004; Thomas et al., 2004; Mazzali et al., 2005; Quimby et al., 2006; Tanaka et al., 2006; Garavini et al., 2007). There is a strong Mg II feature at 4200 Å which is contaminated by several iron lines. Silicon and sulphur both have strong features at 5640 Å (S II) and at 6355 Å (Si II). While the strong silicon line at 6355 Å is the trademark of SNe Ia, the 'w' sulphur feature at 5640 Å cleanly separates SNe Ia from their SNe Ib/c cousins. It is believed that in these early phases one should be able to see carbon and oxygen from the unburned outer layers. There is the C II-feature at 6578 Å but it is normally very weak (if visible at all). The only strong oxygen feature is the O I triplet at 7774 Å. High temperatures that ionise a large amount of the oxygen as well as

[1] A profile which shows a emission peak at the rest wavelength of the line and a blue-shifted absorption trough

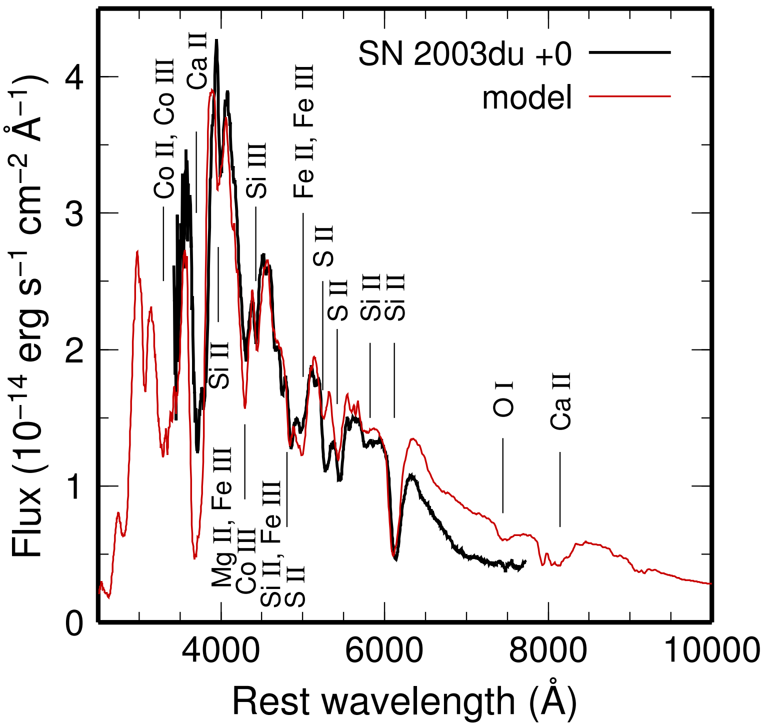

Figure 1.13 SN 2003du spectrum at maximum light. The light in the UV is being suppressed and fluoresced into the red part of the spectrum (Figure kindly provided by M. Tanaka; Tanaka et al., 2011).

contamination by magnesium and silicon near the only oxygen line, often make it hard to constrain the abundance of oxygen well. Thus, large fractions of oxygen in the ejecta might not be a visible in SNe Ia spectra.

Maximum Phase

As the supernova rises to the peak luminosity, opacity from the large fraction of IGEs (especially ^{56}Ni) is suppressing flux in the UV causing it to be reemitted in the optical/IR (see Figure 1.12). The photospheric velocity has now dropped to less than 10000 km s^{-1}. Nugent et al. (1995) suggested that at these epochs the ratio of Si II 5972 Å and Si II 6355 Å is a good indicator for luminosity and can be an additional calibration tool for the absolute magnitude of individual SNe Ia.

Post-Maximum phase

In the post maximum phase, the spectrum is increasingly being dominated by IGEs, as the photosphere has receded further into the ejecta. The photospheric velocity drops to less than 8000 km s^{-1}(see Figure 1.14). The spectrum continues to contain feature of IMEs, which are slowly overwhelmed by the IGEs.

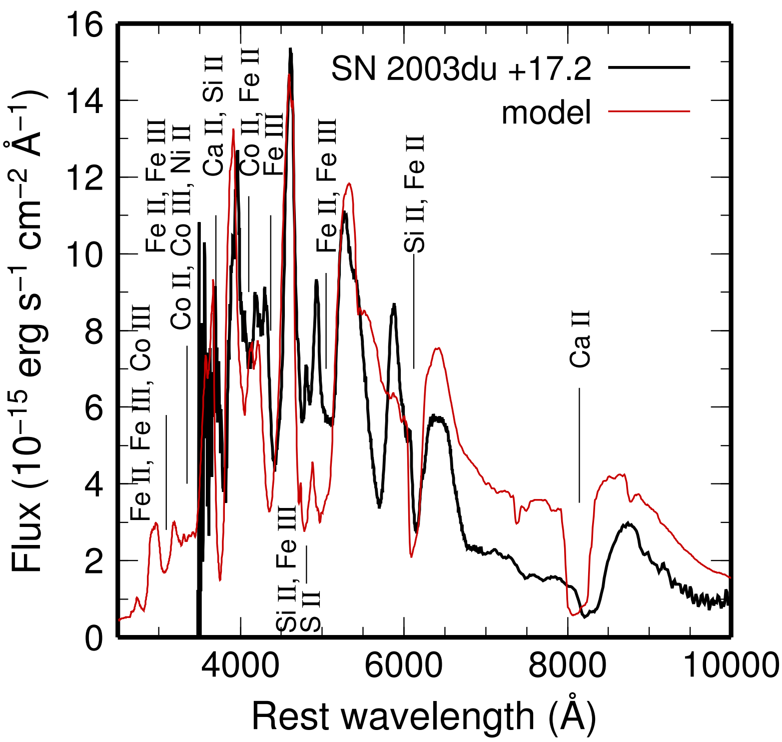

Figure 1.14 SN 2003du 17 days past maximum light. The contribution of IGE is still rising (Figure kindly provided by M. Tanaka; Tanaka et al., 2011).

Nebular Phase

As the supernova fades, the photosphere recedes into oblivion. At this stage the spectrum is characterised by strong emission lines which are produced by the IGEs from the very core of the explosion (see Figure 1.15). These are kept hot by the thermalisation of gamma rays and positrons from the radioactive decay of ^{56}Co, the daughter of ^{56}Ni. We are seeing into the slow moving ejecta with velocities under 5000 km s^{-1}.

Type II Supernova Spectra

SNe II show much more variation in spectra across their class than SNe Ia . In this section we will only give a very general and brief overview over SNe II spectra and spectral evolution. Compared to SNe Ia the initial spectrum is a relatively undisturbed continuum (see Figure 1.6). The only strong lines visible are those of hydrogen and helium which are the elements present in the envelopes of the progenitors. As the photosphere cools, the spectrum is broken up into P Cygni profiles of strong resonance lines of Ca II, Fe II, Na I, and elements like scandium in the envelope, which typically has near-solar composition. The nebular spectra of SNe II are characterised by hydrogen, oxygen and calcium emission lines powered by the radioactive decay of ^{56}Ni in the core of the supernova, which energises the large amounts of hydrogen as well as the intermediate mass elements synthesised in the star before explosion.

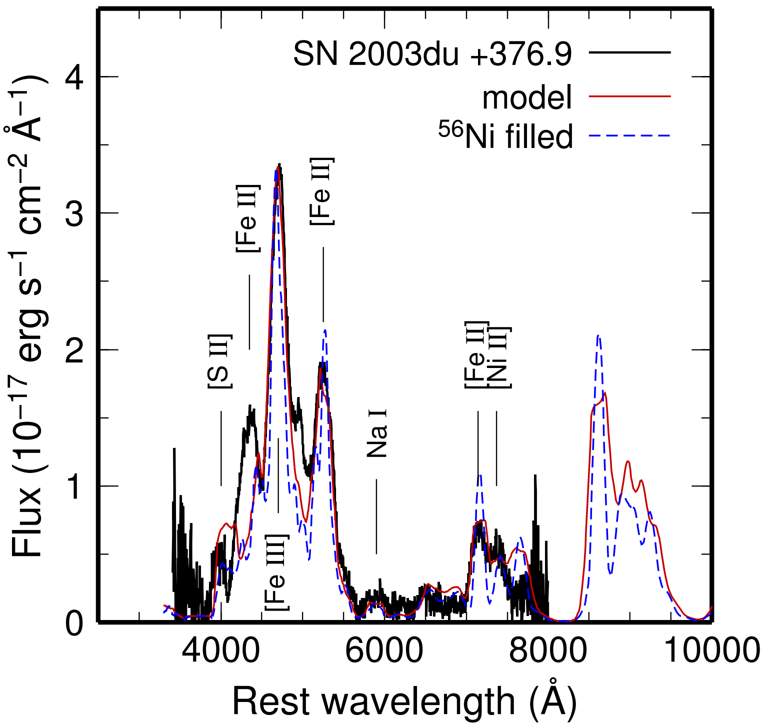

Figure 1.15 In the nebular phase strong emission lines are visible. This phase is not observed very often, but contains crucial information about the explosion physics (Figure kindly provided by M. Tanaka; Tanaka et al., 2011).

1.3.5. X-Ray & Radio observations

Compared to preponderance of optical observations, X-ray and radio observations of supernovae are relatively rare. The information, however, carried in the very high and low frequency photons is invaluable to understanding various transient events.

One mechanism to produce X-ray and radio radiation is in shocks. When the expanding ejecta of supernovae hits the CSM, it produces synchrotron radiation in both wavebands. There have been extensive radio and X-ray observations of SNe II and SNe Ib/c that detail the mass-loss history of these massive stars. It is interesting to note that SNe Ia have never been detected in either X-ray or radio which suggests that the CSM around these objects is not very dense (for more detail see Section 1.5.3). Jets, and their interaction with the CSM, are another phenomenon commonly associated with radio emission. The GRB-phenomenon has been suggested to be the relativistic jet launched from certain SN Ib/c (e.g. Umeda & Yoshida, 2010). It is believed that GRBs are visible when this jet points towards the observer (also known as on-axis) within the opening angle of the jet thought to be about 5 degrees in the case of bright GRBs. As they evolve, a GRB's jet spreads and is thought, after many months, to emit isotropically at radio frequencies. This radio glow should be visible to both on-axis and off-axis observers. Soderberg et al. (2006) have started a campaign to find this isotropic radio emission and were rewarded when SN 2009bb showed radio emissions at late times (Soderberg et al., 2010). This signal was interpreted as relativistic outflow powered by a central engine and suggests an off-axis GRB.

SNe II/Ib/c have long been theorized to emit X-rays when the shocks from the collapsing core breaks out of the surface of the massive stars (Klein & Chevalier, 1978; Colgate, 1974). To observe these so-called shock breakouts is technically very challenging as the supernova needs to be detected very early. SN 2008D was serendipitously discovered during an observation with the Swift satellite's X-ray telescope. Swift was in the process of observing another supernova SN 2007uy in the same galaxy when it picked up an extremely luminous X-ray source (Soderberg et al., 2008). Subsequent ground based follow-up revealed a brightening optical counterpart which turned out to be a SN Ib/c. The X-ray-flash is attributed to the theorized shock breakout.

Finally late time X-ray observations also probe weak high energy emission lines of the decaying radioactive ash. These weak emission lines are only visible in late time spectra of very nearby supernovae so it comes as no surprise that they have only been observed in SN 1987A (Sunyaev et al., 1987; Dotani et al., 1987). Radio and X-ray observation of both kinds of supernovae are still in their infancy and will provide great help when solving the current mysteries surrounding all types of supernovae.

1.3.6. Supernova Cosmology

Early in the last century astronomers were trying to gauge our place in the universe. Hubble (1926) was the first to definitively demonstrate that many nebulae were objects like our own Milky Way. He used, among other methods, the known intrinsic luminosity (L_0) of Cepheid variables and determined the distance using the observed luminosity ($L/L_0 \propto 1/r^2$). In addition, Hubble found that galaxies that were further away had a higher velocity away from the Milky Way than close galaxies (Hubble, 1929). He suggested that the universe was in a state of constant expansion. Since Cepheid distance measurements are only possible for very close-by galaxies, astronomers were feverishly searching for brighter more precise distance probes (also known as standard candles). The discovery that supernovae are distant objects Baade & Zwicky (1934) motivated many astronomers to try to use them as standard candles (Baade, 1938; van den Bergh, 1960; Kowal, 1968; Leibundgut & Tammann, 1990; Miller & Branch, 1990).

This work culminated, nearly 70 years after its first inception, in another paradigm changing discovery. The accelerating expansion of the universe was discovered by two teams (Riess et al., 1998; Perlmutter et al., 1999), using the same principal as Hubble used to discover the expansion of the universe. Over the past 13 years, the discovery of acceleration has been augmented by measurements of the CMB (e.g. WMAP7; Komatsu et al., 2011), large scale structure (e.g. Blake et al., 2011), and more supernovae (Astier et al., 2011, e.g.) to come up with the consensus flat,Λ - CDM model of the universe (e.g. Sullivan et al., 2011)

SN II Cosmology SNe IIP have been first suggested as cosmological probes by Kirshner & Kwan (1974) who showed that the Expanding Photosphere Method (EPM) could provide absolute distances to SNe II. Schmidt et al. (1994a) were able to measure SN II distances in the Hubble flow, and found H_0 = 73 km s^{-1}/Mpc^{-1}. They used sophisticated models to predict the emerging flux, and the absorption velocity of weak lines in the spectrum to estimate the photospheric velocity. SN IIP have also been used as relative distance indicators (Hamuy & Pinto, 2002), but are observationally expensive and not as accurate as SN Ia (15% error for SN II vs 7% error for SN Ia (Nugent et al., 2006)).

SN Ia Cosmology The story begins with Kowal (1968) plotting redshift of Type I supernova host galaxies against the luminosity distance implied by their peak magnitude (assuming a peak luminosity of $M_{\text{peak}} = -18.59$). Although crude (scatter of 0.6 mag), Kowal's measurement clearly showed that more distant supernovae were at a higher redshift. Roughly fifteen years later, the broad class of Type I supernovae was divided into three distinct subclasses (Ia, Ib and Ic). In the late 1980's many authors started to realise that the class of SNe Ia was very homogeneous (Branch & Tammann, 1992, and references therein) making them remarkable distance probes. Around the same time a Danish team discovered the first very distant supernova at $z = 0.3$ (Norgaard-Nielsen et al., 1989), but gave up their search when it became clear that technology was not yet in place to efficiently make cosmological measurements with SN Ia. The SCP started to target high redshift ($z > 0.3$) fields to use distant supernovae to study the deceleration of the universe (little did they know). The smart and successful strategy of comparing observations taken shortly before and shortly after dark time meant that they could discover a 'batch' of supernovae at once and do follow-up observations (Perlmutter et al., 1995). This 'batch' mode was required to convince time allocation committees on large telescopes (only very large telescopes could study distant supernovae) to award time to this seemingly high risk project. The Calán/Tololo supernova survey (CTSS; Hamuy et al., 1993) started in the early 1990's and targeted only supernovae at low redshift ($0.01 < z < 0.1$). By 1995 they had produced 30 new light curves for SNe Ia measured with only CCD technology to unprecedented detail (Hamuy et al., 1995). Advances in standardising the SN Ia candle were made by Phillips (1993). Phillips found that there was a tight correlation between the decline in luminosity and the peak magnitude of a SN Ia which made these objects unrivalled distance indicators. Convinced by the ability to calibrate SNe Ia (Phillips, 1993) and the ability to discover them at high redshift (Perlmutter et al., 1995) a group of astronomers founded the HZSNS. Then the developments started happening in rapid succession. Inspired by the method of calibrating peak luminosity with the decline of the supernova both SCP and HZSNS developed more precise ways to determine the intrinsic peak brightness. The HZSNS parametrised the shape of the light curve in different bands as a function of their peak magnitude. This Multicolor Light-Curve Shape method (MLCS; Riess et al., 1996) using many different bands was able to include measurements of dust extinction. The SCP team used a different method of stretching light curve templates in time to match the observations. Both methods were able to measure the distance of SNe Ia to a precision of $\approx 6\%$. Using these new tools both teams independently made the baffling discovery that the expanding universe was not decelerating but accelerating (Riess et al., 1998; Perlmutter et al., 1999). This revelation required a revision to the standard cosmological model where more than 70% of the Universe is made up of a form of matter called Dark Energy.

Over the past ten years the measurement of the universe's equation of state has become a prime driver of SNe Ia science. New light curve fitting tools try to implement more complex treatments of dust extinction and are still under active development (e.g. Jha et al., 2007; Guy et al., 2007). Recent work on NIR light curves (Kasen, 2006) suggests that the peak absolute luminosity is not influenced as much as optical light curves by the production of ^{56}Ni which depends on the unknown progenitor. In addition, it is beneficial that the effect of dust extinction at these wavelengths is also much less compared to optical bands. This has motivated some members of the community (e.g. Mandel et al., 2011) to use NIR to calibrate SNe Ia to standard candles.

1.3.7. Post-explosion observations of Supernovae

In most cases, for SNe Ia, SNe Ib/c and SNe II, the distance to the supernova is too large to make detailed studies of the remnants of these events in years post-explosion.

However, when supernovae happen in the nearest galaxies (or our own), we have the chance of detailed post-explosion follow-up. SN 1987A, which exploded in the nearby Large Magellanic Cloud (LMC), provided an ideal candidate for follow-up post-explosion. Observations confirmed that a previously observed blue super giant was not visible post-explosion (Walborn et al., 1989) confirming that this massive star was the progenitor of SN 1987A. It was the first time a progenitor was identified with this 'direct detection' method and since then many more progenitors have been unearthed post-mortem (for a review see Smartt, 2009).

Modern X-Ray space telescopes provide data of exquisite detail to study the remnants of supernovae. Hydrodynamic and non-equilibrium ionisation simulations of shocks from the supernova ejecta interacting with the interstellar medium (ISM) can be used to measure temperature, elemental abundances and other parameters related to the state of the ejecta (Badenes et al., 2003; Sorokina et al., 2004; Badenes et al., 2005). This technique of modelling has been used to scrutinise ancient remnants. Kepler and Tycho remnants have been unambiguously identified using X-ray spectroscopy to be remnants of SNe Ia with the models even able to distinguish between different types of SN Ia models (Badenes et al., 2006; Reynolds et al., 2007). This field is still at its infancy and future coupling of three dimensional models with X-ray observations will help understand the explosions mechanisms for both physical types of supernovae: thermonuclear explosions and core-collapse of massive stars.

Light-echoes are features that appear when light from a supernova scatters on dust in the ISM. This has been suggested by Zwicky (1940), but only advancements in imaging techniques as well as digital processing made it possible to detect these echoes. Rest et al. (2005) pioneered this technique and found several of these echoes in the LMC. Follow-up observations by Rest et al. (2008b) showed that it is possible to obtain a spectrum and identify the type of supernova with it. Krause et al. (2008) and Rest et al. (2008a) subsequently observed the light-echo of Tycho's supernova (SN 1572) and identified it as a *Branch-normal* SN Ia, confirming the previous X-ray modelling results. Future wide-field surveys will hopefully reveal many more of these light-echoes. Beyond classification, light-echoes can also be used for a three dimensional spectroscopic view of supernovae (demonstrated on the example of the Cas A remnant; see Rest et al., 2011).

Post-mortem observations of supernovae and their light-echoes, although only available for nearby events, provide us with unique insights into these events. Light echoes give us direct information about the explosion, but are only available for a few thousand years post-explosion. Radio and X-ray studies are possible for much older remnants. Maoz & Badenes (2010) have scrutinised remnants in the LMC and can reconstruct the supernova history for the last 20,000 years. Coupled with star formation history estimates they can infer a DTD.

1.4. Core-Collapse Supernova Theory

All SNe II and SNe Ib/c are believed to be powered by the collapse of the electron-degenerate iron cores of massive stars, as demonstrated by the direct detection of their progenitors on archival images in a number of cases (for a review see Smartt, 2009). For the iron core to form there had to be several prior stages of evolution.

1.4.1. Evolution of Massive Stars

To understand the state of the star shortly before the supernova explosion it is imperative to follow its evolution. For the topic of core-collapse we will concentrate on the nuclear physics of single massive star evolution. There is ample evidence that some SNe II and SNe Ib/c progenitors are influenced by binary evolution (Podsiadlowski et al., 1992), but this evolution is much more complex and is outside the scope of this work. In this context massive stars are stars more massive than 8 $M_{\odot}$, the minimum mass for a star that is believed to explode as a SN II. Like all stars, massive stars spend most of their lives on the main-sequence burning hydrogen. This happens via the carbon-nitrogen-oxygen cycle and its various side-channels (e.g $^{12}\mathrm{C}(p,\gamma) \rightarrow^{13} N(e^{+}\nu) \rightarrow^{13} C(p,\gamma) \rightarrow^{14} N(p,\gamma) \rightarrow^{15} O(e^{+}\nu) \rightarrow^{15} N(p,\alpha) \rightarrow^{12}$ C). For a 20 $M_{\odot}$ star this phase lasts for 8.13 Myr (see Woosley et al., 2002).

As the star evolves it begins to ignite Helium which burns via the triple-α process to Carbon ($3\alpha \rightarrow^{12}$ C) and then to Oxygen ($^{12}\mathrm{C}(\alpha,\gamma) \rightarrow^{16}$ O). Table 1 in Woosley et al. (2002) lists 1.17 Myr for this phase.

Due to neutrino losses the stellar evolution is qualitatively different after helium burning. A neutrino-mediated Kelvin-Helmholtz contraction of the carbon-oxygen core describes the advanced stages of nuclear burning in massive stars (Woosley et al., 2002). This contraction is occasionally delayed when the burning of new fuel sources counter-acts the neutrino losses. The star in the end is composited of a series of shells that burn the above fuel and deposit the ashes on the shell below (see Figure 1.16). There are four distinct burning stages. Their principal fuels are carbon, neon, oxygen, magnesium and silicon.

In the carbon burning stage, two ^{12}C nuclei are fused to a highly excited state of ^{24}Mg magnesium which then decays slowly to via three possible channels (see Equation 1.1) .

$$\begin{aligned} ^{12}\mathrm{C} +^{12} \mathrm{C} \rightarrow^{24} \mathrm{Mg}^{*} &\rightarrow {}^{23}\mathrm{Mg} + \mathrm{n} \\ &\rightarrow {}^{20}\mathrm{Ne} + \alpha \\ &\rightarrow {}^{23}\mathrm{Na} + \mathrm{p} \end{aligned} \tag{1.1}$$

Although oxygen has a lower coulomb barrier, the next nucleus to burn after carbon is neon. This layer is composed of ^{16}O, ^{20}Ne and ^{24}Mg and burns neon with high-energy photons from the tail of the Planck distribution ($^{20}\mathrm{Ne}(\gamma,\alpha)^{16}\mathrm{O}$).

In the next shell there is a composition of mainly ^{23}O, ^{24}Mg and ^{28}Si. The bulk nucleosynthetic reaction is shown in Equation 1.2.

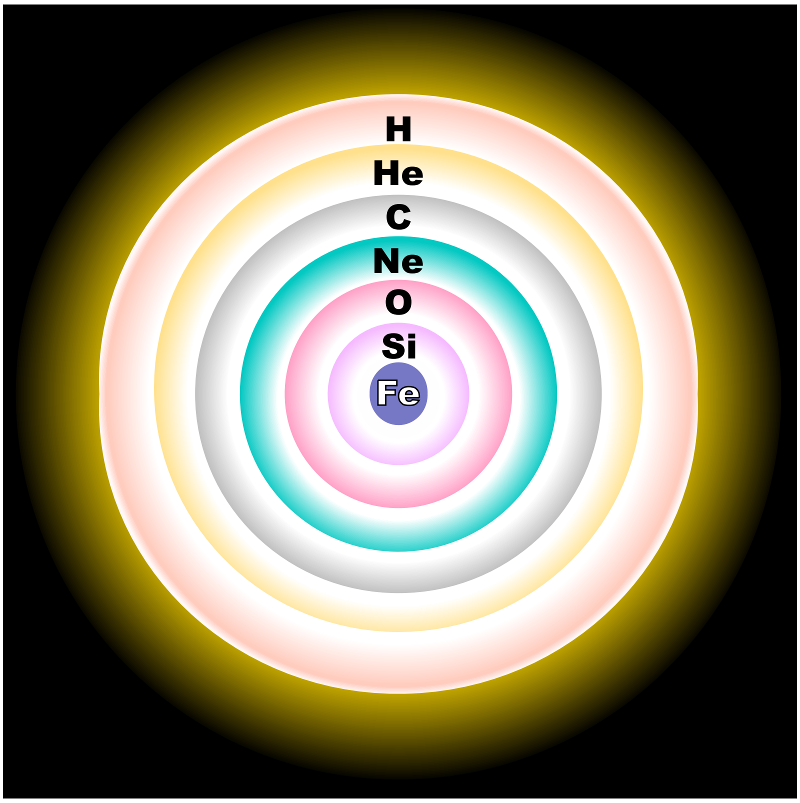

Figure 1.16 Shell Burning of a massive star before Type II. (Source Wikipedia)

$$\begin{aligned} {}^{16}O + {}^{16}O \rightarrow {}^{28}Si &\rightarrow {}^{31}S + n \\ &\rightarrow {}^{31}\mathrm{P} + \mathrm{p} \\ &\rightarrow {}^{30}\mathrm{P} + \mathrm{d} \\ &\rightarrow {}^{28}\mathrm{Si} + \alpha \end{aligned} \tag{1.2}$$

The last shell converts ^{28}Si to IGE. The obvious reaction $^{28}\mathrm{Si} + ^{28}\mathrm{Si} \rightarrow ^{56}\mathrm{Ni}$ does not take place, but is replaced by a very complex network of isotopes that results in IGE being synthesised.

1.4.2. Core collapse

Before the collapse, the core consists of iron peak elements (see Figure 1.16). Neutrino losses during carbon and oxygen burning decreased the central entropy sufficiently so that the core becomes electron degenerate. Such a degenerate core, which is more massive than the Chandrasekhar mass (adjusted for Y_e, entropy, boundary pressure and other parameters) and with no material capable of being burned, will collapse.

There are two main instabilities that facilitate the collapse. As the density rises the Fermi-Energy becomes high enough for electrons to capture onto iron-group nuclei. This capture process removes electrons that were providing degeneracy pressure and reduces the structural adiabatic index. In addition, the temperature rises to values where the nuclear statistical equilibrium favours many free α-particles. The nuclear binding energy of this α-particle rich state is less and the core does not gain sufficient thermal energy to hinder gravity from advancing the collapse.

The collapse eventually leads to nuclear densities, the hard nuclear potential acts as a stiff spring during the compressive phase. It stores up energy and eventually releases this energy resulting in a *core bounce*. Recent simulations, however show that the ensuing bounce shock is not sufficient for a SN II explosion with the shock loosing energy by photo disintegrating the nuclei it encounters (loosing roughly 10^{51} erg per 0.1 $M_{\odot}$).

The energy for a successful explosion is now thought to come from neutrino energy deposition. This reinvigorates the shock and leads eventually to an explosion which ejects the envelope of the massive star (Herant et al., 1994). Several variants of neutrino driven explosion now exist, with the neutrino driven convention leading to a Standing Accretion Shock Instability (SASI; Blondin & Mezzacappa, 2006), or acoustic g-mode oscillations (Burrows et al., 2007) . There is not yet a consensus on how stars more massive than 12 $M_{\odot}$actually explode. Regardless, in most cases for stars < 15 $M_{\odot}$, it is believed that a newly born neutron star is left behind in these explosions.

Woosley et al. (2002) provide a very comprehensive review of the theory of evolution and core collapse. In particular they go into more detail describing the scenarios after core-bounce.

1.4.3. Pair Instability Supernova

One alternate explosion scenario is the pair-instability supernova. This scenario is believed to only happen in stars with a helium core of more than 40 $M_{\odot}$. After core helium burning the star starts to contract at an accelerated rate, and enters a regime of temperature and density where the energy goes into electron-positron pair production rather than raising the temperature. This leads to a structural instability in the star (where the adiabatic index drops below $4/3$), leading to collapse. This collapse, if significant densities are reached, will result in oxygen fusion, which eventually halts the implosion and the collapse turns into an explosion. For very high stellar masses, it is believed that oxygen fusion does not provide enough energy to halt the contraction and the star collapses to a black hole.

Gal-Yam et al. (2009) measure that the extremely bright Type Ic SN 2007bi had a core mass of $\approx 100\ M_{\odot}$ which unambiguously points to a Pair Instability Supernova. This is the first time such an event has been observed.

1.4.4. Type II Supernovae

After the collapse of the core, the supernova goes through three distinct phases. The observables of these stellar cataclysms are the light curve, spectra and for one case (SN 1987A), even the neutrino wind.

The shock-waves generated by the collapsing core reaching the surface, is the first visible signal from the supernova. Ensman & Burrows (1992) calculated a duration for the so-called shock breakout of SN 1987A to 180 s, its luminosity of 5×10^{44}erg s^{-1}. Such a breakout thus far has been observed only once - in the case of the lucky observations of SN 2008D - a SN Ib/c (Soderberg et al., 2008). This star, more compact than SN 1987A, had a shock breakout of 400 s with a luminosity of 6.1×10^{43}erg s^{-1}.

Secondly Shocks in the ejecta and the decay of ^{56}Ni irradiate the expanding hydrogen envelope and the energy slowly diffuses out causing a plateau, for the SNe IIP. SN IIL have lost most of their extensive hydrogen envelopes and radiate their energy much more quickly - resulting in the observation of a linear decline, rather than a plateau. The last phase begins after the photosphere moves through the entirety of the H envelope, the ejecta transform to become optically thin, the supernova suddenly drops in brightness, and then fades exponentially, following the 77 day half life of ^{56}Co, the daughter nucleus of ^{56}Ni. Some light might also be produced by shock interaction with the CSM.

1.4.5. Type Ib/c Supernovae

In the case of a SN Ib/c, the progenitor has lost at least all of its hydrogen envelope prior to core-collapse. This loss of envelope is presumed to be caused by stellar winds and/or binary interactions (Podsiadlowski et al., 1992). Thus the hydrogen can not provide a energy buffer and no plateau is visible, similar to a SN IIL. Instead the light-curve is powered by radioactive decay after shock breakout, with the energy diffusing out from the core. The missing envelope also causes the lack of hydrogen lines in the spectrum leading to the supernova being classified as Type Ib. If both hydrogen and helium envelopes are lost then the supernova is classified as Type Ic.

1.5. Thermonuclear Supernova Theory

In this section we will discuss the theory of SNe Ia which are thought to be thermonuclear explosions of degenerate carbon/oxygen matter. The different progenitor scenarios leading to an explosion of a massive white dwarfs are discussed in Section 1.5.1.

1.5.1. Progenitors of Type Ia Supernovae

There are two basic scenarios for SNe Ia progenitors. The single degenerate scenario (SD-scenario) has a white dwarf accreting from a non-degenerate companion until the white dwarf ignites leaving behind the companion star (first introduced by Whelan & Iben, 1973). In the second scenario, the double degenerate scenario (DD-scenario), two white dwarfs merge and ignite, leaving no stellar remnant behind (first suggested by Webbink, 1984; Iben & Tutukov, 1984).

Single Degenerate Scenario

The SD-Scenario assumes a binary system with one evolved white dwarf and one non-degenerate companion. In most cases this non-degenerate companion is thought to be a main sequence to red giant star. There are also scenarios that involve 'exotic' companions such as helium stars. In most cases, the companion (or donor) star is believed to have filled its Roche-Lobe and lose mass via Roche Lobe Overflow (RLOF).

An outstanding problem of the SD-Scenario is the accretion process. As most white dwarfs are born with masses significantly less than the Chandrasekhar mass, they need to accrete mass to reach the critical 1.38 $M_{\odot}$. The accretion process needs to efficiently burn any accreted hydrogen into helium and subsequently to carbon/oxygen to explain its absence in SNe Ia spectra, and to prevent recurrent novae from removing material from the system. Theoretically, there is only a very narrow range of accretion rates that allows the white dwarf to accrete hydrogen, stably burn it and efficiently grow to the Chandrasekhar mass. Yoon & Langer (2004) have suggest that rotation of the accreting white dwarfs might increase this very narrow parameter range.

If the mass-accretion rate is too low, it causes nova explosions which are thought to eject more mass than the accretion prior has gained (Nomoto, 1982). However, there are some systems (e.g. RS Ophiuchi, U Scorpii) that have white dwarf masses close to 1.38 $M_{\odot}$ which undergo recurrent nova outbursts. It is very likely that these systems were not born with a white dwarf this massive, but that these white dwarfs have successfully grown in mass through the accretion of material. This suggest that in some cases, despite nova outbursts, efficient accretion is possible. Too high accretion rates would cause the binary to be engulfed in an extended red giant envelope. The debris of such an envelope are not seen in most SN Ia explosions - an exception might beSN 2002ic.

There are several possible identified progenitor systems. A class of binaries called supersoft X-ray sources has a white dwarf accreting hydrogen from a non-degenerate companion at an appropriate rate such that hydrogen and helium burn hydrostatically. In cases where the white dwarf (WD) is a carbon/oxygen White Dwarf (CO-WD), rather than a oxygen/neon White Dwarf (ONe-WD; whose ultimate fate is described in Section 1.5.2) these objects are strong contenders for SN Ia progenitors (Di Stefano et al., 2006, and references therein). Another subclass of possible SD-Scenario progenitors are AM CVn stars (Nelemans, 2005). In this type of cataclysmic variable, material is accreted onto the WD from a helium star or helium WD (van den Heuvel et al., 1992). This scenario would conveniently explain the lack of hydrogen in SN Ia explosions. A SN Ia explosion in such systems is discussed in Section 1.5.2.

Donor Stars

The SD-Scenario requires a secondary companion star (also known as donor star). If this companion survives the explosion it would be a calling card for the SD-Scenario. One consequence of this explosion is an unusual spatial velocity of the companion post-explosion. The main fraction of this velocity stems from the gravitational unbinding whereas only a small amount would originate in the kick from the supernova ejecta (see Figure 1.17; Canal et al., 2001; Han, 2008). Marietta et al. (2000) have simulated the impact of SN Ia ejecta on a main-sequence, sub-giant and red-giant companion. In the case of the main-sequence companion, the supernova ejecta heats a small fraction (1-2%) of the envelope which is lost post-explosion. Pakmor et al. (2008) have repeated the simulations for the main-sequence companion and find similar results, but suggest that even less mass is lost. Post-explosion the main-sequence star should be very luminous (500 – 5000 $L_{\odot}$) and is expected to cool down over next 1000 – 10,000 years and follow the main-sequence track (Marietta et al., 2000).

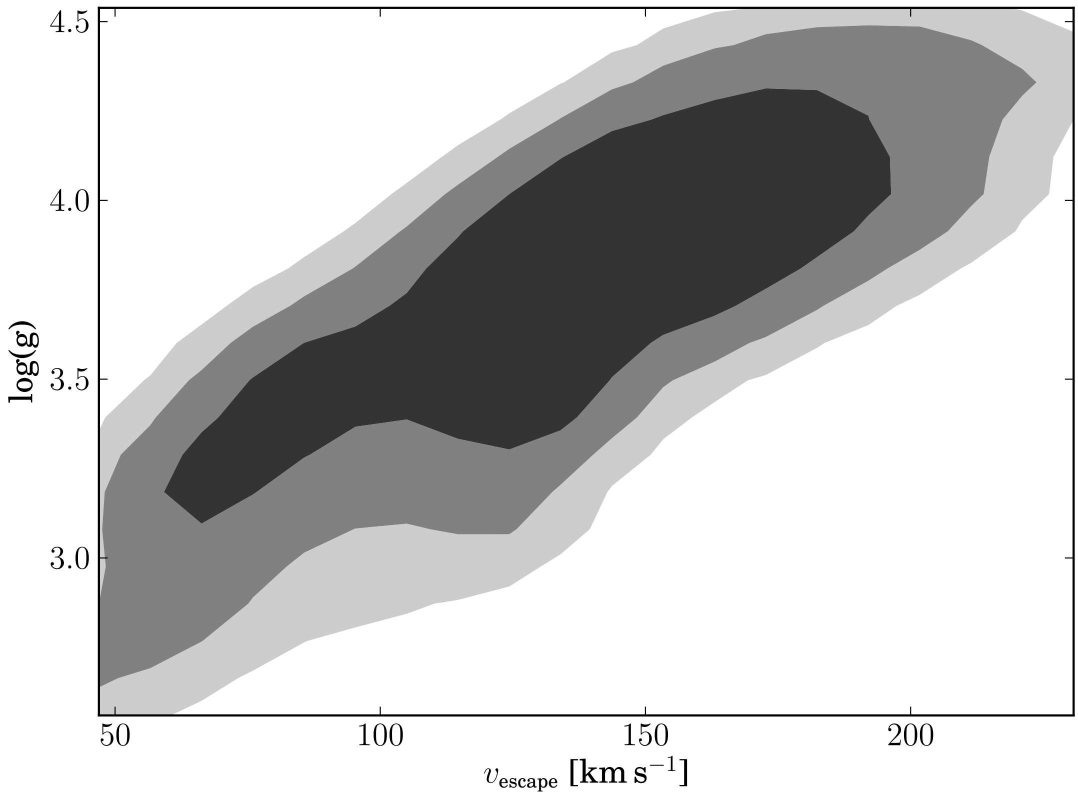

Figure 1.17 Confidence limits ($1-\sigma$, $2-\sigma$ and $3-\sigma$) of the expected escape velocity for different evolutionary states of the donor star based on binary population synthesis (Han, 2008, data kindly provided by Z. Han)

For the sub-giant companion the simulations show very similar results to the main-sequence companion. The sub giant looses only a small fraction of the envelope (10 – 15%) and like the main-sequence star, it will be very luminous shortly after the explosion. After thermal equilibrium is established, the companion will return to a post-main-sequence track.

The case of the red-giant, however, is different. Marietta et al. (2000) suggest that it will lose most of its loosely bound envelope. Post-explosion core contracts and the temperature rises to more than 3×10^4 K. The object may appear as an under luminous main-sequence O or B star. Justham et al. (2009) have suggested the population of low-mass single white dwarfs to be the remaining cores of such red-giant donor stars. This would result in a convenient explanation for the existence of these objects.

One feature of surviving companions may be an unusually large rotational velocity post-explosion (Kerzendorf et al., 2009, Chapter 2 of this work). Due to tidal coupling during the RLOF phase, the rotational velocity of the donor star, post explosion, is directly tied to the binary rotational velocity (see Figure 1.18). Since stars of F spectral-type and later do not display such high rotational velocities, this feature is a very useful discriminant when looking for donor stars.

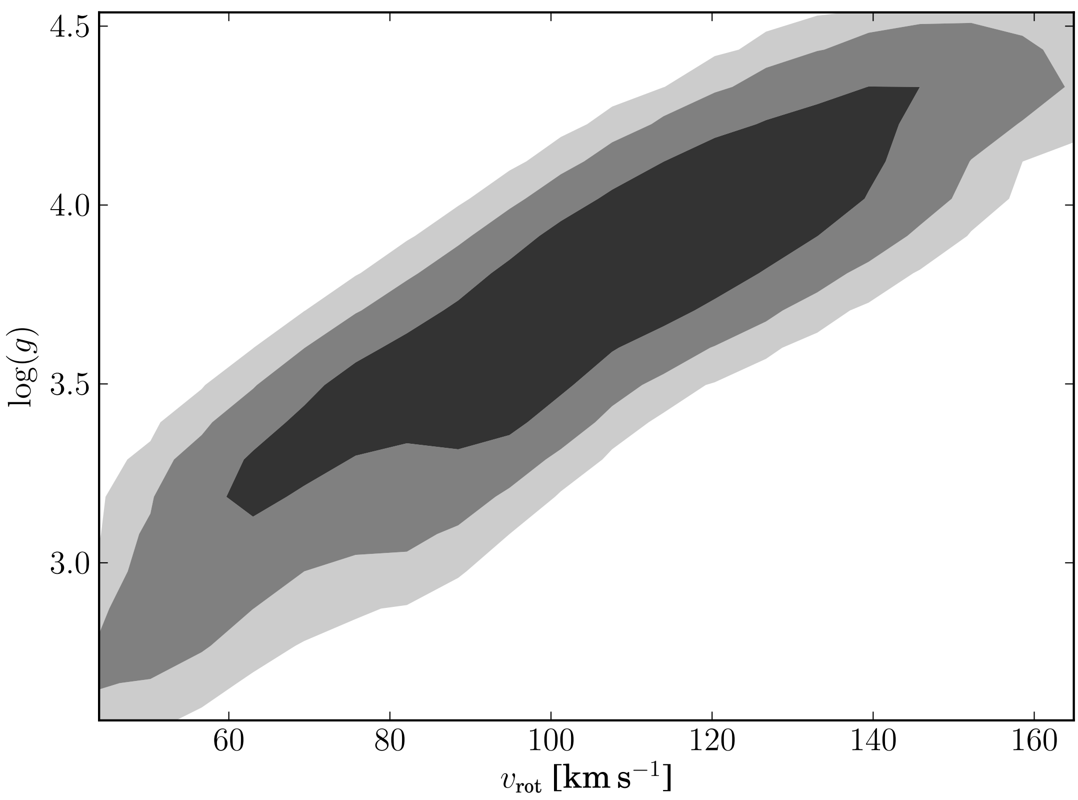

Figure 1.18 Confidence limits ($1-\sigma$, $2-\sigma$ and $3-\sigma$) of the expected rotational velocity for different evolutionary states of the donor star post-explosion based on binary population synthesis (Han, 2008, data kindly provided by Z. Han)

There have been several attempts to find these objects in ancient supernova remnants. Schweizer & Middleditch (1980) found a OB subdwarf star located 2.5′ from the centre of the remnant of SN 1006 and suggested this as the donor star. Subsequent analysis by Wu et al. (1997, 1983) however, have revealed strong Fe II features with a profile broadened by a few thousand km s^{-1}and ionised redshifted silicon features. In the very likely case that these features are caused by the remnant this indicates the star to be located behind the remnant rather than being involved in the SN Ia explosion as a donor star.

The search for donor stars in ancient remnants is one of the main parts of this thesis and we direct the reader to Chapter 2 through Chapter 4.

Double Degenerate Scenario

Webbink (1984) and Iben & Tutukov (1984) were the first to suggest merging white dwarfs as progenitors for SN Ia. There are several advantages to the DD-Scenario. For example, it naturally explains the lack of hydrogen in SN Ia spectra. The accretion problem encountered in the SD-Scenario is dispensed with in the DD-Scenario, as long as the sum of masses of both CO-WD's is above Chandrasekhar mass - although new ideas might make this an upper limit rather than a requirement (van Kerkwijk et al., 2010).

One problem with this scenario, however, is that most SN Ia form a relatively homogeneous class. It is hard to reconcile this fact with the merger of two white dwarfs with different initial masses, composition, angular momenta and different impact parameters. There are however supernovae with estimated nickel masses of more than the Chandrasekhar mass, which strongly suggests that they are the result of merging white dwarfs (see Section 1.5.2). A potentially even larger problem, however, is that the accretion of the disrupted lighter white dwarf onto the more massive white dwarf is thought to lead to accretion induced collapse (AIC) rather than a thermonuclear explosion (see Section 1.5.2).

Pakmor et al. (2010) have simulated the merger of two equal-mass white dwarfs (0.9 $M_\odot$) and conclude that the outcomes of these mergers might be subluminous SNe Ia.

In summary, mergers of white dwarfs might be able to explain some of the SN Ia class. It is however still debated if these events are responsible for the abundance of*Branch-normal* SNe Ia.

1.5.2. Evolution and Explosion of Type Ia Supernovae

White Dwarfs

CO-WDs are thought to be the progenitor stars of SNe Ia. White dwarfs are among the most common stellar objects that are not composed primarily of hydrogen, which is consistent with the lack of hydrogen in SN Ia spectra. Furthermore, there is a clear theoretical avenue to exploding white dwarf stars, through accretion of material to near the Chandrasekhar mass. It is general believed that these objects accrete matter (for the possible scenarios see section 1.5.1) until they get close to the Chandrasekhar mass. It is a delicate balance between conditions for ignition that results in a thermonuclear run-away and reaching the Chandrasekhar mass threshold, which would lead the collapse of the star to a neutron star.

There are three main classes of white dwarfs: helium WDs, CO-WDs and oxygen/neon White Dwarfs (ONe-WDs). Originally ONe-WDs were called ONeMg WDs but the mass fraction of magnesium had been overestimated and thus now only oxygen and neon are mentioned (Ritossa et al., 1996).

The accretion onto a helium WD would lead to helium burning well before the Chandrasekhar mass and thus these objects are not considered as potential progenitors. Although not considered as the SN Ia progenitor itself helium, WDs as companions to CO-WDs are an interesting suggestion as SN Ia progenitor systems (see Section 1.5.2). The ultimate fate of an accreting ONe-WD is thought to be the collapse into a neutron star. Theoretical models predict that before oxygen can be ignited, electron capture begins in the core ($^{20}\mathrm{Ne}(e^-, \nu)^{20}\mathrm{F}(e^-, \nu)^{20}\mathrm{O}$). Heating by the resulting γ-rays starts explosive oxygen burning. However, the electron-capture is much faster than the oxygen burning and promotes the collapse to a neutron star (Nomoto & Kondo, 1991; Gutiérrez et al., 2005). It should be noted that the AIC of the ONe-WD of an 8 – 12 $M_\odot$ star, although not a Type Ia event, gives rise to the so-called electron capture supernova (Miyaji et al., 1980).

The favoured progenitor for a SN Ia are CO-WDs. Theoretical calculations predict that these objects ignite when very close to the Chandrasekhar mass (1.38 $M_\odot$). The vast majority of white dwarfs are born with masses around 0.6 $M_\odot$ (Kepler et al., 2007) due to the large abundance of $\approx 1\ M_\odot$ stars compared to stars with a mass $> 5\ M_\odot$ which would turn into more massive WDs. It is, however, quite frequent to have WD stars built up to more than 1 $M_\odot$ through mass transfer in binary systems with an intermediate mass companion ($2\ M_\odot < M < 8\ M_\odot$). Such systems are thought to be the eventual progenitors of SN Ia.

Pre-Supernova Evolution

The white dwarf gradually accretes more and more material. Close to Chandrasekhar mass mild carbon burning ensues

$$\begin{aligned} ^{12}\mathrm{C}(^{12}\mathrm{C},p) &\rightarrow ^{23}\mathrm{Na} \\ ^{12}\mathrm{C}(^{12}\mathrm{C},\alpha) &\rightarrow ^{20}\mathrm{Ne} \\ ^{12}\mathrm{C}(^{12}\mathrm{C},n) &\rightarrow ^{23}\mathrm{Mg}, \end{aligned} \tag{1.3}$$

but is mediated by photon and neutrino losses (Lesaffre et al., 2005; Iliadis, 2007). As these cooling processes become less effective convection starts in the core and the energy output in the core increases. At this stage the thermal structure is largely controlled by what is termed *Urca* pairs. These reaction pairs consist of alternating electron captures and β^- decays involving the same pair of parent and daughter nuclei. Two prominent examples which are important in pre-supernova evolution are $^{21}\mathrm{Ne}/^{21}\mathrm{F}$:

$$\begin{aligned} ^{21}\mathrm{Ne}(e^-,\nu) &\rightarrow ^{21}\mathrm{F} \\ ^{21}\mathrm{F}(\beta^-\nu) &\rightarrow ^{21}\mathrm{Ne} \end{aligned} \tag{1.4}$$

These processes can lead to either cooling or heating (Lesaffre et al., 2005).

At present, the pre-supernova evolution has proven difficult to model theoretically as it is likely to be non-local, time-dependent, three-dimensional and stretches over hundreds of years. The exact conditions at the time of explosion are therefore poorly constrained, and all explosion models have to assume simple initial conditions. The main steps leading to the explosion follow.

Explosion mechanisms

Ignition The *Urca* processes will dominate core evolution for the last thousand years until explosion. As the temperature rises to $T \approx 7 \times 10^8$ K (Hillebrandt & Niemeyer, 2000) the convection time (τ_c) increases and becomes comparable to the burning time (τ_b). Consequently the convective plumes burn as they circulate. Once the temperature reaches $T \approx 10^9$ K, τ_b becomes very small compared to τ_c and carbon and oxygen largely burn in place. This is the moment of ignition. As the convective plumes burn while they rise it is likely that the initial flame seed does not start in the centre of the core. Röpke & Hillebrandt (2005) have used multiple flame seeds in their three dimensional full star models.

Thermonuclear Explosion After ignition, there has historically been two main options. The first option was the complete detonation (supersonic flame front) of the CO-WD (Arnett, 1969). It was quickly, discovered, however that this method burns the entire star to nuclear statistical equilibrium (NSE) (^{56}Ni dominant), and thus leaves none of the IMEs observed in SNe Ia.

To counteract this problem, it was suspected that the star instead of detonating would deflagrate (subsonic flame wave, mediated by thermal conduction). The fuel in front of the deflagration becomes rarefied by the energy from the flame, with hot light burning bubbles rising into the cold dense fuel creating Rayleigh-Taylor instabilities (see Figure 1.19 at t=0.72 s). Detailed calculations show that once the deflagration wave has run through the star, the resulting production of ^{56}Ni is lower than that observed in SNe Ia. More critically IMEs are left throughout the expanding debris, leading to an un-observed distribution of IMEs at low velocities (Mazzali et al., 2007).

The currently favoured scenario is the one of delayed detonation. Here, the star initially burns like in the deflagration scenario with the inhomogeneities in the deflagration front producing hot spots. We refer the reader to Schmidt et al. (2010) and references therein, for a detailed explanation of the transition from a deflagration to a detonation wave. Once the detonation wave has formed it travels through the unburned star - not penetrating the already deflagrated nuclear ashes. This produces an event which observationally is a good match to the spectral evolution of SNe Ia (e.g. Kasen et al., 2009). Figure 1.19 shows clearly how the detonation wave wraps around the cold ashes over the course of the detonation. An open question is if and how these transitions from deflagration to detonation occur in SNe Ia.

Sub Chandrasekhar Mass detonations Livne (1990), Shigeyama et al. (1992), Livne & Arnett (1995) and Sim et al. (2010) have explored the detonation of CO-WDs at sub Chandrasekhar Masses. Sim et al. (2010) show that the detonation of a sub Chandrasekhar mass CO-WD reproduce observed light-curves and early-time spectra of SNe Ia fairly well.

A significant issue in this scenario is the ignition. Fink et al. (2010) have studied an explosion mechanism in which a surface detonation of a helium shell drives a shock-wave into the core. In the core this shock wave triggers an ignition by compression. As an initial model they use a CO-WD accreting from a helium rich companion building a thin helium shell around its CO interior (described in Bildsten et al., 2007). This helium shell is ignited and sends out a shock wave. As the helium flame spreads in the shell around the star it sends a shock wave into the core. Once the shock waves converge off-centre they create an environment hot and dense enough that the ignition of a detonation wave may be possible (see Figure 1.20.)

This scenario reproduces the intrinsic luminosity variability in the class of SN Ia as each exploding white dwarf can have a different mass, but might predict too much variation.

Super Chandrasekhar Mass Detonations As well as sub Chandrasekhar mass explosions, the community has also studied the explosion of white dwarfs with $M > M_{\mathrm{Chan}}$. There have been a small number of SNe Ia which were extremely luminous (e.g. SN 2003fg, SN 2006gz, SN 2007if and SN 2009dc) suggesting ejecta masses of more than 1.38 $M_{\odot}$

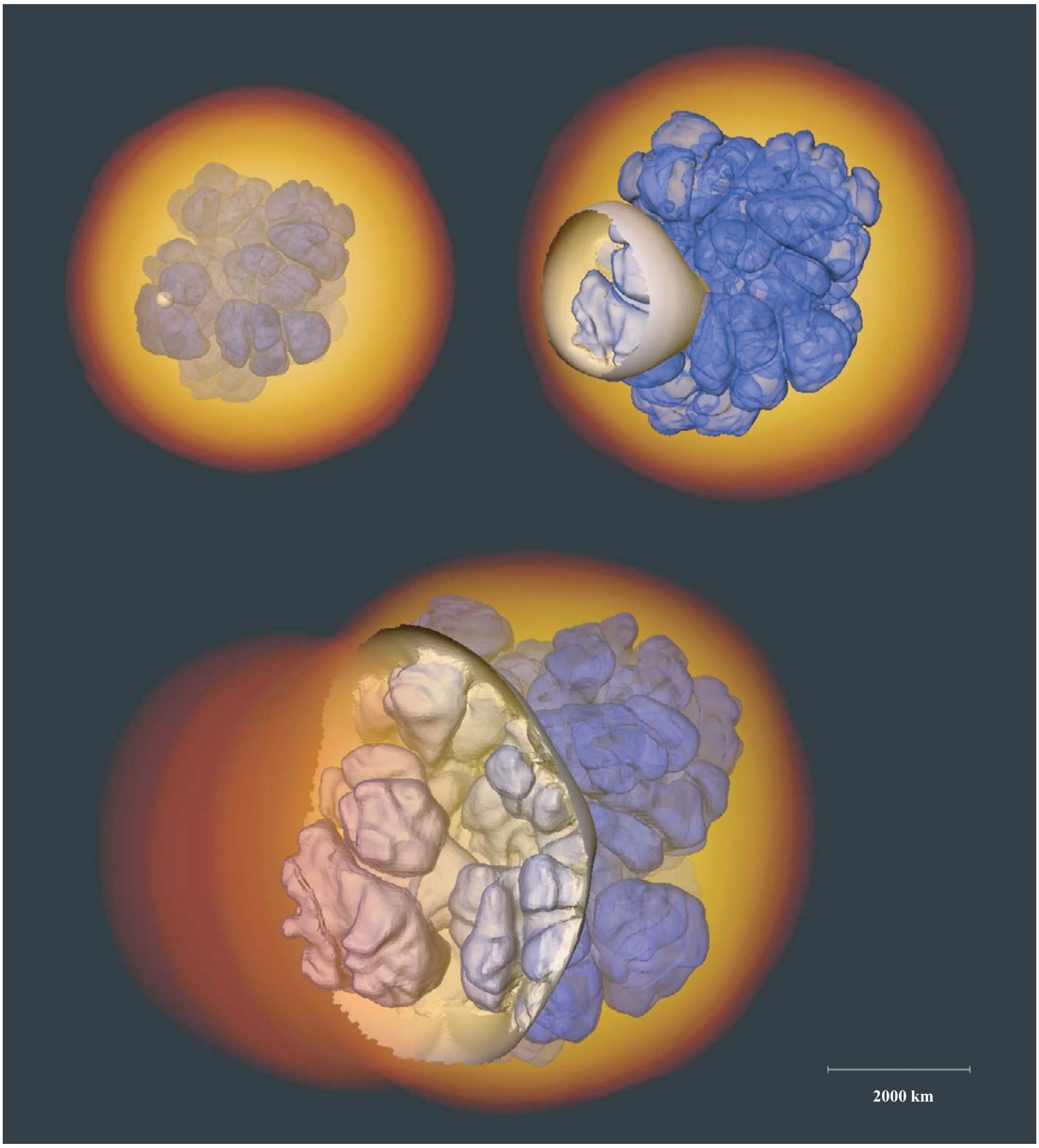

Figure 1.19 Delayed detonation simulation from Röpke & Bruckschen (2008). The upper panels show the deflagrated interior (marked in blue) and the detonation ignition point (small white sphere). The detonation wave wraps around the deflagration ash and consumes the cold fuel. (Image reproduced with kind permission of Fritz Röpke)

(estimates ranging from slightly above the Chandrasekhar mass to roughly 3 $M_{\odot}$; Howell et al., 2006; Hicken et al., 2007; Yamanaka et al., 2009; Scalzo et al., 2010; Tanaka et al., 2010; Silverman et al., 2011; Taubenberger et al., 2011). This raises the question why these objects do not undergo AIC. Yoon & Langer (2005) suggest that through rapid rotation these objects will increase the effective Chandrasekhar mass. Another possibility is the merger of two massive white dwarfs. Pakmor et al. (2010) however suggested, for the merging of equal-mass 0.9 $M_{\odot}$ CO-WDs (a total mass of 1.8 $M_{\odot}$), the resulting supernova would resemble the class of 91bg-like objects. A core collapse scenario for some of these

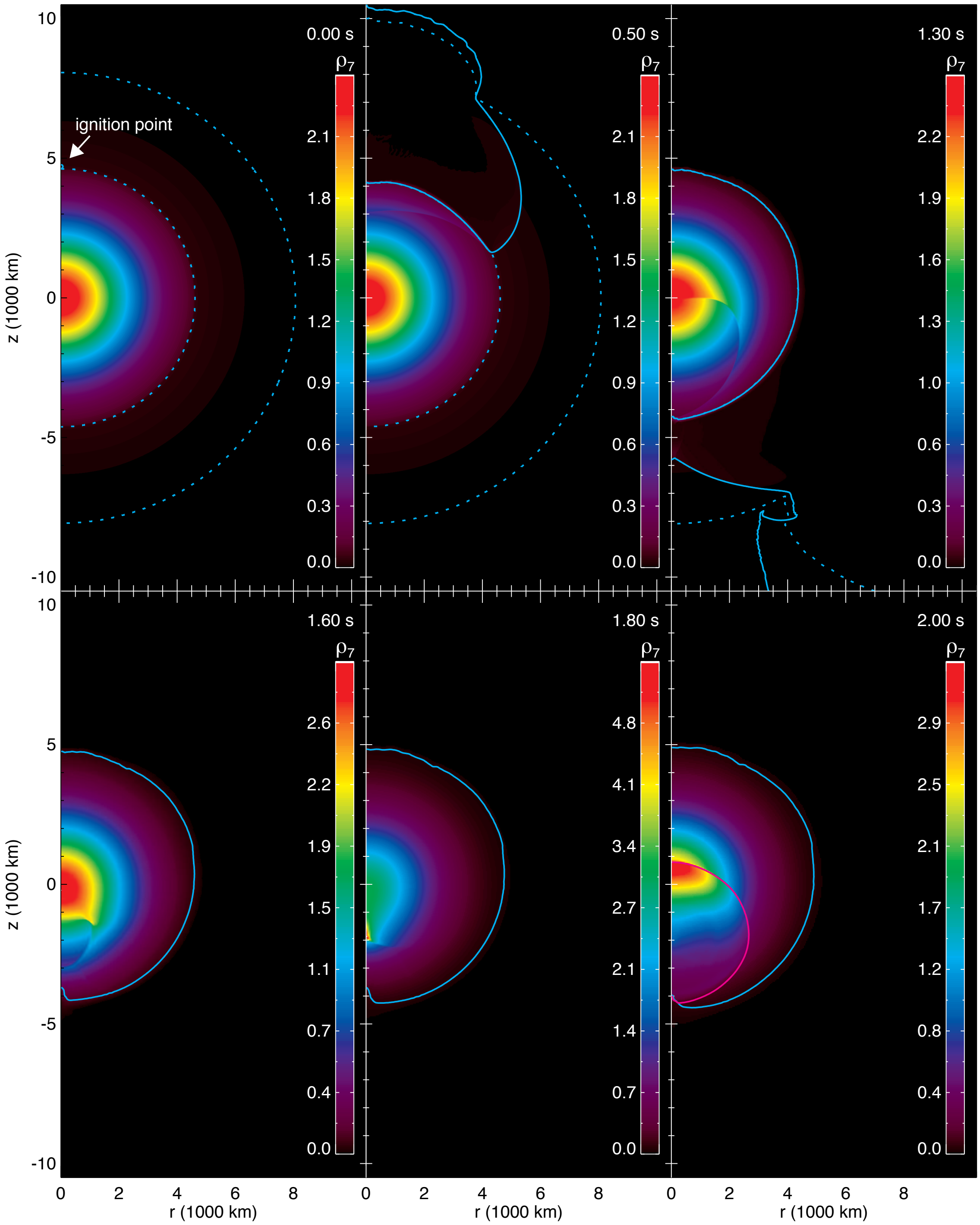

Figure 1.20 The ignition point of the helium shell is marked in the upper left image. We can follow the helium shell sending shock waves into the core of the white dwarf. They converge in the lower left image at the opposite site of the Carbon/Oxygen core (data from Fink et al., 2010, Figure kindly provided by Michael Fink).

events has also been constructed. The number of observed super Chandrasekhar mass supernovae is as of yet too low to define common characteristics or a class.

1.5.3. Constrains for different progenitor scenarios

The question of the progenitors of SNe Ia is a main part of this thesis and one of the most highly debated subjected in current SNe Ia research. There are various arguments for and against the SD-Scenario and the DD-Scenario, with some suggesting that both scenarios contribute to the class of *Branch-normal* SNe Ia.

Patat et al. (2007) have found a variable blue-shifted sodium absorption feature using high-resolution spectra of SN 2006X This suggests that there is sodium rich material in the line-of-sight. The variability suggests that this material is close to the supernova explosion. One explanation of this variability is the change in the ionisation state of the sodium atoms in a nearby CSM caused by the variable SN Ia radiation field. Very recently a study by Sternberg et al. (2011) observed sodium features in 30 SNe Ia. They found that many of these SNe Ia show blue-shifted sodium features relative to the host galaxies rest frame, which can be explained by expanding winds from the progenitor system. Finally, Patat et al. (2011) have seen similar features in the recurrent nova RS Ophiuchi. This could hint that recurrent novae with red giant donor stars might be responsible for some SNe Ia.

Di Stefano (2010) have not found enough supersoft X-ray source to account for the rate of SNe Ia. In addition, Gilfanov & Bogdán (2010) have not found enough accumulated X-ray flux from elliptical galaxies if all SN Ia progenitors were supersoft X-ray source (assuming the X-Ray flux calculated for these objects is correct). The main caveats here are that the SN Ia-progenitors might only be in the supersoft X-ray source phase for a short amount of time and at other times, these objects could be engulfed in a envelope, which would reprocess the produced X-rays to optical or infrared wavelengths. In stark contrast to the negative X-ray studies described above, Voss & Nelemans (2008) have suggested that they found the progenitor of the Type Ia SN 2007on in X-rays. Further analysis has put this claim in doubt (Roelofs et al., 2008). Although the detection might have been spurious, their technique remains promising: Following up SNe Ia in X-ray-archives could detect potential SNe Ia progenitors in a pre-explosion X-ray phase and could confirm the supersoft X-ray source scenario for some SNe Ia.

It remains a mystery that SNe Ia do not show lines of hydrogen which might be expected from the wind or stripped envelope in the SD-Scenario. Leonard (2007) has searched in the nebular spectra of two SNe Ia for hydrogen and place an upper limit of 0.1 $M_\odot$ for both these explosions. On the other hand, Justham (2011) suggest that a red giant donor could significantly shrink during the RLOF and the material stripped by the ejecta might be negligible. This would place the stripped hydrogen below the current detection limit.

Kasen (2010) predicts excess in ultra violet (UV) flux in the SN Ia light curve at early times for SN Ia from single degenerate systems. This effect depends on orientation of the system to the line of sight and the state of the donor. The effect would be biggest for a red giant donor star. Hayden et al. (2010) do not see this excess in the SDSS supernova set indicating that the red giant channel is not common for SNe Ia. A study by Bianco et al. (2011) using the SNLS data set comes to the same conclusion. To conclusively state a lack of this predicted excess a big sample of very early light curves is needed, which does not exist yet.

Radio observations in the case of SNe Ia can, for example, reveal the shock interaction of the ejecta with the CSM. The SD-Scenario predicts a more dense CSM than the double degenerate scenario. Hancock et al. (2011) have stacked radio observations of SNe Ia in the visibility plane and have not detected any source. At present, it is not clear that this limit is in conflict with the SD-Scenario. Future stacked Extended Very Large Array (EVLA) measurements will push the limits substantially down and will hopefully provide constraints that will allow us to rule out one or the other scenario, at least for some SNe Ia.

Finding a donor star of the SD-Scenario in a supernova remnant (SNR) post-explosion would resolve the question for the progenitor system, at least in the searched remnants. The main work of this thesis investigates this technique and we refer the reader to Chapter 2 through 4.

Population synthesis together with observations of DTDs are an important step in exploring the different progenitor scenarios. Hachisu et al. (2008); Han & Podsiadlowski (2004) have explored the SD-Scenario parameter space and suggest, when compared to observations, that the SD-Scenario can almost explain the observed DTD (for references on DTD see section 1.3.2). Ruiter et al. (2009) and Mennekens et al. (2010), however, have explored the SN Ia-rate using several progenitor scenarios (SD-Scenario, DD-Scenario and AM CVn). Both suggest that the SD-Scenario on its own can not explain the observed SNe Ia rate. The rate of the DD-Scenario seems to be much closer to the observed frequency. Possibly a mix of all channels is required to explain the observed rate.

In addition to the standard SD and DD channels, alternative scenarios are continually being explored. For example, a *core-degenerate* scenario in which a white dwarf merges with the hot core of a massive AGB star (Ilkov & Soker, 2011). Another alternative is given by Di Stefano et al. (2011) and Justham (2011), who suggest that the accreting white dwarf would be spun-up during accretion. The ignition of these highly spinning white dwarfs would be delayed and the companion might have time to evolve substantially from its RLOF phase.

van Kerkwijk et al. (2010) explores the merger of two equal mass white dwarfs with a total mass less than the Chandrasekhar mass. When coupled with the work on sub-Chandrasekhar mass detonations by Sim et al. (2010), this might actually provide a viable progenitor scenario. Its main advantage is the predicted rate of these low-mass white dwarf mergers might be high enough to reproduce the observations, but it is yet unclear if the conditions for an ignition can be reached in such a merger.

In summary, the question of the progenitors of SNe Ia remains one of the most highly debated topics in SNe Ia research. We have not yet found a scenario that elegantly explains all aspects of the SN Ia phenomenon. In addition, different measurements seem to provide conflicting evidence for either scenario. More extensive and novel observations of SNe Ia and SNR will hopefully identify the nature of SN Ia progenitors scenario.

1.6. Thesis motivation

One of the pivotal moments in astronomy in recent years was the discovery of the accelerating expansion of the universe by Riess et al. (1998) and Perlmutter et al. (1999). This discovery made SNe Ia the cynosure of the astronomical community. There have been many advances in recent years in the understanding of these cataclysmic events (explosion models, rates, etc.). One critical piece of the puzzle, however, has so far eluded discovery: the progenitors of SNe Ia. This work's main aim is to look for evidence for one SN Ia progenitor scenario. The SD-Scenario proposes a white dwarf accreting from a non-degenerate donor star. All calculations suggest that this donor star will survive the explosion and would be visible thereafter. We have tried to find this companion in two of the three easily accessible ancient supernova remnants (SN 1572 and SN 1006). In Chapter 2 we have obtained spectra of Tycho-G, which had been suggested as the donor star of SN1572 (Ruiz-Lapuente et al., 2004). Although we confirmed some of the suggested parameters, we could not reproduce the unusually high radial velocity, which led to the claim. We also showed that the star exhibited no rotation, at odds with the star being the donor star.

We revisited SN 1572 in Chapter 3 with new observations of Tycho-G and five other stars in the neighbourhood of SN 1572. This work indicates Tycho-G is consistent with a background interloper, and is likely not to be the donor star (although it is hard to completely rule any star out). We discovered a curious A-star located right in the centre of SN1572. Despite its a priori unusual parameters, we are unable to reconcile this star (Tycho-B) with any feasible progenitor model.

SN 1006 provides an additional opportunity to search for progenitor stars. It is the closest known remnant of a SN Ia (2 kpc) and is largely unreddened. We have obtained 80 spectra of stars close to the centre of the remnant and present them in Chapter 4. Again we do not find any obvious donor stars. We have obtained spectra of stars around SN 1604 but these are not presented in this thesis. They will be analysed as part of future work.

Progenitor hunts provide us with information of the scenarios pre-explosion. Spectra, on the other hand, help to unravel the physics during and post-explosion. Mazzali et al. (2008) have developed a code that can produce synthetic SN Ia spectra from fundamental input parameters. Fitting an observed SN Ia is, for the moment, a manual task. This requires many days, if not weeks, of tweaking. The deluge of spectroscopically well-sampled SNe Ia from surveys is already upon us. Manual analysis of all of these spectra is impossible. The information about the explosion hidden in the spectra is, however, crucial to our understanding of these events. In Chapter 5 we present our work towards automating this fitting process. We have tried a variety of algorithms to explore the vast and extremely complex search space. Working together with members of the computer science community, we are exploring the use of genetic algorithms to solve this problem. This thesis does not attempt to completely solve this problem, but we present preliminary methods in SN Ia-fitting in Chapter 5. When completed, we can apply this method not only to fitting SN Ia, but fitting different supernovae and to other areas of astronomy.

In summary, this work explores two areas of supernova physics: progenitors and explosion physics. The hunt for progenitors has not yielded obvious candidates, but may suggest a rethinking of the 'normal' SD-Scenario. The automated fitting of supernova spectra is in a preliminary stage. We have, however, shown that it is possible to explore the parameter space in an automated fashion. This will hopefully yield elemental abundances and energies for many thousands of supernovae. The close collaboration with computer science community was very helpful and shows how important cross-disciplinary research is in the modern era of science.

CHAPTER 2

Subaru High-Resolution Spectroscopy of Tycho-G in the Tycho Supernova Remnant

This Chapter was published as Subaru High-Resolution Spectroscopy of Star G in the Tycho Supernova Remnant - Kerzendorf, W. E., Schmidt, B. P., Asplund, M., Nomoto, K., Podsiadlowski, P., Frebel, A., Fesen, R. A., & Yong, D. 2009, ApJ, 701, 1665

2.1. Introduction

SNe Ia are of broad interest. They serve as physically interesting end points of stellar evolution, are major contributors to galactic chemical evolution, and serve as one of astronomy's most powerful cosmological tools.

It is therefore unfortunate that the identity of the progenitors of SNe Ia is still uncertain. For example, without knowing the progenitors, the time scales of SNe Ia enriching the ISM with iron remains highly uncertain. But it is the crippling impact on the cosmological application of these objects which is especially profound; it is impossible to predict the consequences of any cosmological evolution of these objects or even gauge the likelihood of such evolution occurring.

There is broad agreement that the stars which explode as SNe Ia are white dwarfs which have accreted material in a binary system until they are near the Chandrasekhar mass, then start to ignite carbon explosively, which leads to a thermonuclear detonation/deflagration of the star. It is the identity of the binary companion that is currently completely undetermined. Suggestions fall into two general categories (Iben, 1997):

- Single degenerate systems in which a white dwarf accretes mass from a non-degenerate companion, where the companion could be a main sequence star, a subgiant, a red giant, or possibly even a subdwarf.

- Double degenerate systems where two CO-WDs merge, resulting in a single object with a mass above the Chandrasekhar limit.

The detection of circumstellar material around SN 2006X (Patat et al., 2007) has provided support for the single degenerate model in this case, although the lack of substantial hydrogen in several other SNe Ia (Leonard, 2007) poses more of a challenge to this scenario.

These models also make different predictions for the nature of the system following the explosion. In the double degenerate case, no stellar object remains, but for a single white dwarf, the binary companion remains largely intact.

In the single degenerate case, the expected effect of the SN on the donor star has been investigated by Marietta et al. (2000), who have calculated the impact of a SN Ia explosion on a variety of binary companions. Canal et al. (2001) have explored many of the observational consequences of the possible scenarios, and Podsiadlowski (2003) has presented models that follow both the pre-supernova accretion phase and the post-explosion non-equilibrium evolution of the companion star that has been strongly perturbed by the impact of the supernova shell. To summarize these results, main sequence and subgiant companions lose 10–20 % of their envelopes and have a resulting space velocity of 180–320 km s^{-1}. Red-giant companions lose most of its hydrogen envelope, leaving a helium core with a small amount of hydrogen-rich envelope material behind, and acquire a space velocity of about 10–100 km s^{-1}. Pakmor et al. (2008) have used a binary stellar evolution code on a main sequence star and exposed the evolved star to a SN Ia. Their simulations show that even less material is stripped due to the compact nature of a star that evolved in a binary. We will use their results where applicable.

Ruiz-Lapuente et al. (2004) (RP04) have identified what might be the donor star to Tycho's SN, a SN Ia which exploded in the Milky Way in 1572. These authors presented evidence that this star, Tycho-G by their naming convention, is at a distance consistent with the Tycho supernova remnant (henceforth SNR), has a significant peculiar radial velocity and proper motion, roughly solar abundance, and a surface gravity lower than a main sequence star. However, Tycho-G is located at a significant distance from the inferred center of the remnant, and any process that has displaced the star must preserve the remnant's nearly perfectly circular projected shape. During the final stages of refereeing of this paper we were made aware of the article by Hernandez et al. (2009, henceforth González Hernández et al. (2009) (GH09)), who used Keck High Resolution Echelle Spectrometer (HIRES; Vogt et al., 1994) data to better constrain Tycho-G's stellar parameters, and in addition, found an enhancement in nickel abundance, relative to normal metal rich stars.

Ihara et al. (2007) have looked for iron absorption lines from the remnant, using nearby stars as continuum sources, with the hope to better constrain the distance of these stars to the SNR. With their technique, stars in the remnant's center should show strong blue-shifted Fe absorption lines, formed by material in the expanding shell of Fe-rich material from the SN, moving towards the observer. Stars in the foreground would show no Fe absorption, and background stars both red- and blue-shifted absorption. Their study shows that Tycho-G does not contain any significant blue-shifted Fe absorption lines, suggesting that Tycho-G is in the remnant's foreground. However, these observations and their analysis, while suggestive, cannot be considered a conclusive rebuttal of Tycho-G's association with the remnant; this technique requires a significant column depth of iron which is not guaranteed. A lack of iron column depth may be indicated by the fact that no stars were found in the vicinity of the remnant that showed both blue- and red-shifted absorption lines.

To further examine the RP04 suggested association of Tycho-G with the SN Ia progenitor, we have obtained a high-resolution spectrum of the star using Subaru and its High Dispersion Spectrograph (Noguchi et al., 1998).

We summarize, in Section 2.2, the observational circumstances of the Tycho remnant and any donor star, and argue in Section 2.3 that rapid rotation is an important, previously unrealised signature in a SN Ia donor star. In Section 4 we describe our Subaru observations. Section 5 covers the analysis of data and the results of this analysis. Section 6 compares the relative merit for Tycho-G being the donor star to the Tycho SN or being an unrelated background star, and in Section 7 we summarize our findings and motivate future observations.

2.2. Observational Characteristics of the Tycho Remnant and Star-G

RP04 have done a thorough job summarizing the relevant details of the Tycho remnant. The remnant shows the characteristics expected of a SN Ia based on its light curve (measured by Tycho Brahe himself), chemical abundances, and current X-ray and radio emission (Ruiz-Lapuente, 2004). In figure 2.1 we have overlaid radio contours[1] on an optical image and have marked the position of the stars mentioned in this and RP04's work.

Although it is not easy to measure the remnant's distance precisely, RP04 estimated Tycho's SNR distance to be 2.8 ± 0.8 kpc, using the ratio of the SN 1006 and Tycho SNR's angular sizes and their relative ages, and the direct distance measure of SN 1006 by Winkler, Gupta, & Long (2003). As this method is relatively crude - both remnants are expanding into media of very different densities - the derived distance estimate for Tycho's SNR carries a much large error bar (by a factor of 10). However, the large error of 0.8 kpc Krause et al. (2008) have recently shown, from a spectrum of a light echo associated with the SN1572, that this SN was a normal SN Ia. Using Tycho's observed light curve, the properties of SN Ia as standard candles, and an extinction value they find a distance to the SN of $3.8^{+1.5}_{-1.1}$ kpc. Updating their values for the extinction values determined in this paper (section 2.6.1), as well as using an absolute magnitude for SN Ia of -19.5 ± 0.25 (Altavilla et al., 2004), we find a distance of $3.4^{+1.3}_{-1.0}$ kpc. In summary, we believe the remnant's distance is poorly constrained, but probably between 2 and 4.5 kpc. RP04 also report the spectroscopic and photometric properties for the bright stars near the center of the Tycho remnant and find a uniform value of approximately $E(B-V) = 0.6$ for stars more distant than 2 kpc. GH09 have revised the $E(B-V)$ value for Tycho-G to 0.76.

In addition, for a select list of stars, RP04 provide radial velocities and proper motions. For Tycho-G, RP04 report a value of $v_{\rm rad} = -99 \pm 6$ km s^{-1} for the radial velocity in the *local standard of rest* (LSR), a proper motion of $\mu_b = -6.1 \pm 1.3$ mas yr^{-1}, $\mu_l = -2.6 \pm 1.3$ mas yr^{-1}, $\log g = 3.5 \pm 0.5$, and $T = 5750$ K. Using HIRES data GH09 have improved the measurements of Tycho-G's stellar parameters, finding $v_{\rm rad} \approx -80$ km s^{-1}, $\log g = 3.85 \pm 0.3$,

[1]The National Radio Astronomy Observatory is a facility of the National Science Foundation operated under cooperative agreement by Associated Universities, Inc.

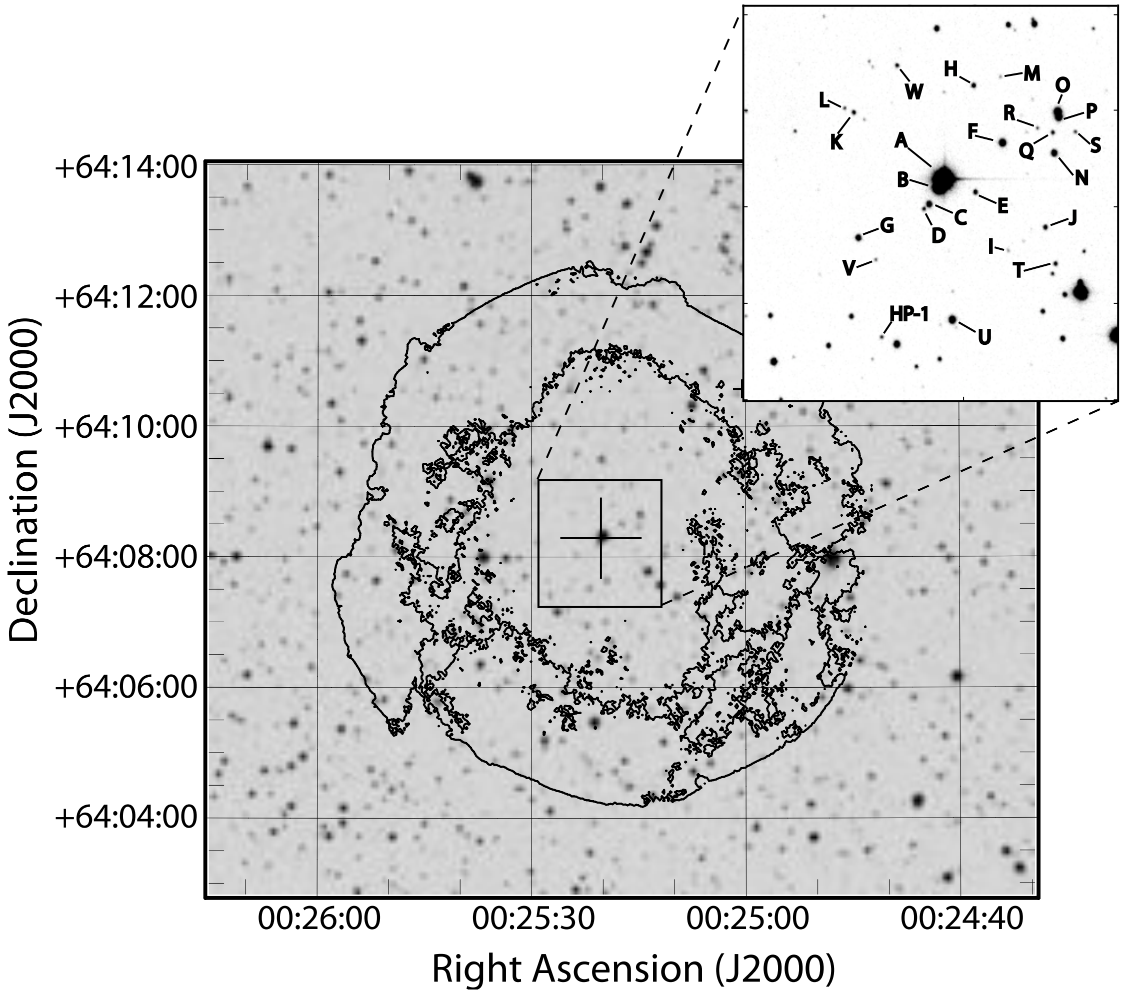

Figure 2.1 Radio Contours (VLA Project AM0347) have been overlaid (Gooch, 1996) on an R-Band Image (NGS-POSS). The cutout is an INT image (see text). The stars marked in the figure are mentioned in this work and in RP04's work.

$T_{\rm eff}$ = 5900 ± 100 K, and [Fe/H] = −0.05 ± 0.09 dex. We note that Ihara et al. (2007) have classified Tycho-G as an F8V star ($T \approx 6250$ K, $\log g \approx 4.3$, Aller et al. 1982), in significant disagreement with the RP04 temperature and gravity. We believe the GH09 values are based on by far the best data, and for the purpose of this paper, we will adopt their values.

Based on the observations, RP04 asserted that Tycho-G was located at approximately 3 ± 0.5 kpc – consistent with the remnant's distance. They note that this star has solar metallicity, and therefore its kinematic signature was not attributable to being a member of the Galactic halo. They further argued that Tycho-G's radial velocity and proper motion were both inconsistent with the distance, a simple Galactic rotation model, and the star being part of the disk population of the Milky Way. The derived physical characteristics of the system were nearly identical to what was proposed by Podsiadlowski (2003) for a typical SN Ia donor star emerging from a single degenerate system (e.g., U Sco; also see Hachisu et al., 1996; Li & van den Heuvel, 1997; Hachisu et al., 1999a; Han & Podsiadlowski, 2004; Han, 2008). The revision in the stellar parameters by GH09 leads to different distance with a larger uncertainty, but by and large, has not altered the conclusions above. Taken in total, the data provide a rather convincing case for the association of Tycho-G with the Tycho SN.

2.3. Rapid Rotation: A Key Signature in Type Ia (SN Ia) Donor Stars

In the single degenerate SN Ia progenitor channel, mass is transferred at a high rate from a secondary star onto a white dwarf (Nomoto, 1982; Nomoto et al., 2007). These high mass-transfer rates require that the secondary star overflows its Roche lobe. Due to the strong tidal coupling of a Roche-lobe filling donor, the secondary is expected to be tidally locked to the orbit (i.e., have the same rotation period as the orbital period). At the time of the SN explosion, the donor star is released from its orbit, but will continue with the same space velocity as its former orbital velocity and continue to rotate at its tidally induced rate.

There is a simple relationship between the secondary's rotation velocity ($v_{\mathrm{orb},2}$) and its orbital velocity:

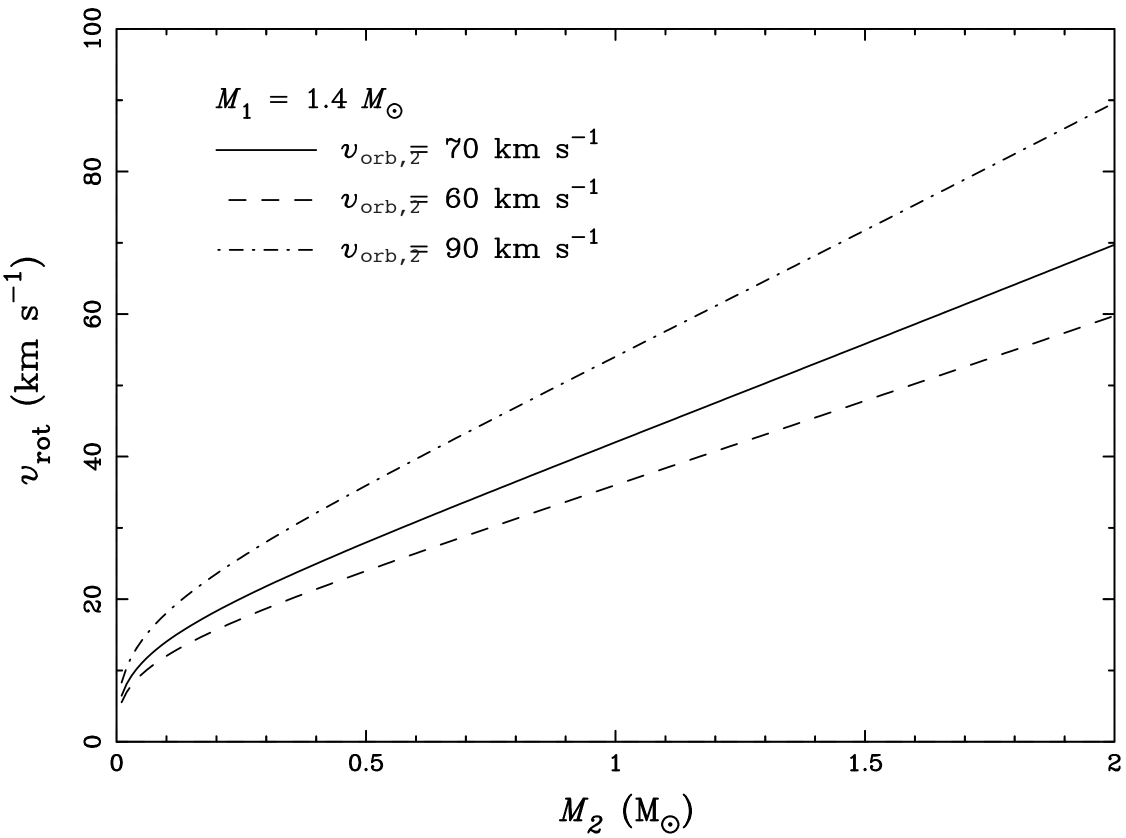

Figure 2.2 The expected rotation rate for a donor star as a function of its mass at the time of the explosion. The three curves show the results for 3 final space velocities of the donor star (similar to those suggested by RP04 for Tycho-G). It is assumed that the white dwarf has a mass of 1.4 $M_\odot$.

$$v_{\rm rot} = \frac{M_1 + M_2}{M_1} f(q)\, v_{\rm orb,2},$$

where $f(q)$ is the ratio of the secondary's Roche-lobe radius to the orbital separation (e.g., given by Eggleton, 1983) and $q = M_1/M_2$ is the mass ratio of the components at the time of the explosion. Figure 2.2 shows the rotational velocity as a function of secondary mass for several values of $v_{\rm orb,2}$ (consistent with RP04s measurement, and at the low end of values expected for a subgiant star), where we assumed that the exploding white dwarf had a mass of 1.4 $M_\odot$.

This estimate is strictly speaking an upper limit, as it does not take into account the angular-momentum loss associated with the stripping of envelope material by the supernova and any bloating due to the supernova heating. The latter would reduce the rotational velocity to first order by a factor equal to the bloating factor (i.e. the ratio of the new to the old radius), but the star would likely find itself in a state where its radius and temperature was atypical of a normal star.

The mass stripping effect is not likely to be significant if the companion is a main sequence star or a sub giant (Marietta et al., 2000). Furthermore, following binary evolution of a main sequence star, Pakmor et al. (2008) have shown that even less material is stripped. However, if the companion is a giant, it would be stripped of most of its envelope. Such a star would not show any signs of rapid rotation since the initial giant would have been relatively slowly rotating; e.g., if one assumes solid-body rotation in the envelope, the rotation velocity at $\sim 1\ R_\odot$ will only be ~ 0.5 km s^{-1} for a pre-SN orbital period of 100 d. Moreover, the material at the surface may have expanded from its original radius inside the giant, further reducing the rotational velocity. However, if the stripping is less than estimated by Marietta et al. (2000), then it is possible for the signature of rotation to persist for a giant, albeit at a much lower velocity.

Marietta et al. (2000) also showed that due to the interaction of the SN blast wave with the companion, the secondary may receive a moderate kick of up to a few 10 km s^{-1}, but this kick is generally much lower than $v_{\rm orb,2}$ and therefore does not significantly affect the resulting space velocity.

Finally, we note that the observed rotation velocities are reduced by a factor $\sin i$, where i is the inclination angle. However, because the donor star's rotational axis can be assumed to be parallel to its orbital axis, a minimum observed rotation speed can be computed from the observed peculiar radial velocity (observed radial velocity minus the expected radial velocity of an object at that distance and direction). It is only if the orbital motion (and hence final systemic velocity) is solely in the plane of the sky, that $\sin i$, and therefore, the observed rotation, approaches zero.

2.4. Subaru Observations

To investigate the rotational properties of Tycho-G, we were granted time with the Subaru telescope. Our observations of Tycho-G were taken in service mode on the nights of 2005 10 17 and 2005 10 18. 9 spectra were taken with the High Dispersion Spectrograph (HDS, Noguchi et al., 1998) with a resolution of R $\simeq$ 40000 (measured using the instrumental broadening of the Thorium-Argon arc lines), an exposure time of 2000 seconds each (totalling to 5 hours) and a signal to noise ratio of about 10 per pixel (measured at 8300 Å with 0.1 Å pixel^{-1}) . The HDS features two arms, with each arm feeding a 2-chip CCD mosaic. The blue arm covers 6170 Å to 7402 Å and the red arm 7594 Å to 8818 Å. An OG530 filter was used to block contamination from light blueward of our observing window, and data were binned by 4 in both the spatial and spectral directions, resulting in a pixel size of 0.1 Å (at 8000 Å) by 0.55″.

Data were pre-processed using tools provided by the HDS team and then bias-subtracted. We created a mask from bias and flatfielded frames, where we isolated the echelle orders and flagged bad pixel regions. The data were flatfielded using internal quartz flats, and the 2-D images cleaned of cosmic rays (and checked carefully by eye to ensure there were no unintended consequences) using an algorithm supplied by M. Ashley (private communication). The spectrum of each echelle order was extracted using IRAF[2] echelle routines, with wavelength calibrations based around low-order fits of a Thorium-Argon arc. Wavelength calibration of each extracted spectrum was checked against atmospheric O_2, and our solutions were found to be accurate in all cases to within 1 km s^{-1} (Caccin et al., 1985). Unfortunately, we lacked a smooth spectrum standard star for setting the continuum, and we resorted to calculating a median of the spectra (6 Å window) and dividing the spectra through this smoothed median. This unusual method was chosen over the common approach of fitting the spectrum with a polynomial, due to the special characteristics of this observation (low signal to noise ratio, and a complex instrumental response). While this does not affect the narrow lines our program was targetting, it does affect broad lines such as the Hα and the CaII IR triplet. The final step was to combine all spectra and remove any remaining cosmic rays (in the 1D spectra) by hand.

2.5. Analysis and Results

2.5.1. Rotational measurement

To attain the rotational velocity of the candidate star, we measured several unblended and strong (but not saturated) Fe I lines in the spectrum (Wehrse, 1974). Since our spectrum only had a combined signal to noise ratio of approximately 10, we added the spectra of the lines after normalizing them to the same equivalent width. As a reference we created three synthetic spectra (one broadened only with the instrumental profile, the others with the instrumental profile and $v_{\rm rot} \sin i$ of 10 and 15 km s^{-1} respectively) with the 2007 version of MOOG (Sneden, 1973), using GH09's temperature, gravity and metallicity. We use a standard value of $\beta = 3/2$ for the limb darkening although the choice of this value is not critical, which we confirmed by checking our results using significantly different values of β. Figure 2.3 shows the comparison between the synthetic spectra of different rotational velocity and the spectrum of Tycho-G. We have scaled the synthetic spectrum using the equivalent width. This comparison indicates that the stellar broadening (rotational, macro turbulence, etc.) is less than broadening due to the instrumental profile of 7.5 km s^{-1}, and

[2]IRAF: the Image Reduction and Analysis Facility is distributed by the National Optical Astronomy Observatory, which is operated by the Association of Universities for Research in Astronomy (AURA) under cooperative agreement with the National Science Foundation (NSF).

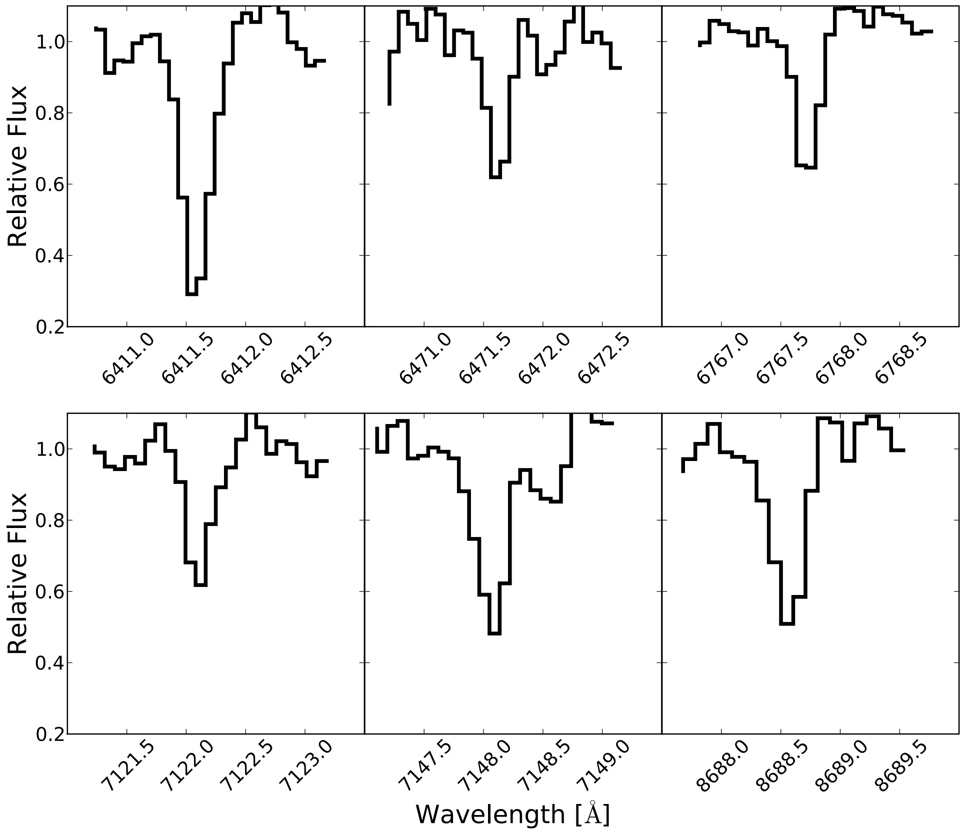

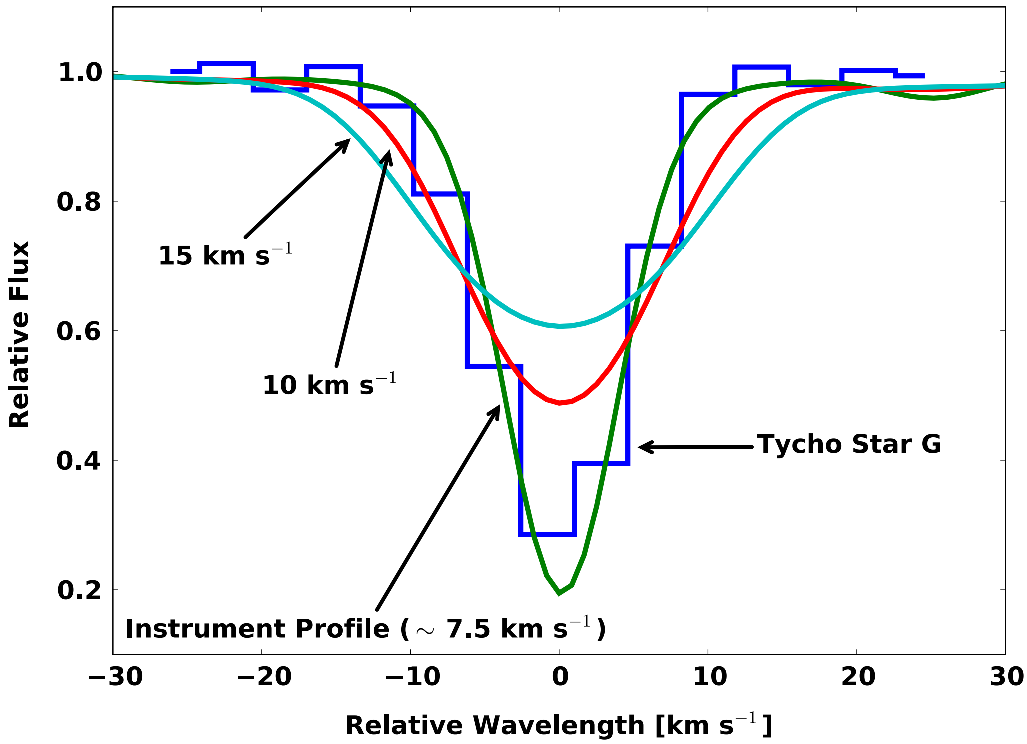

Figure 2.3 Six observed Fe I line profiles of Tycho-G are shown on the left panel. The right panel shows the combination of these line profiles after normalization to the same equivalent width and compares them to the spectrum of the Sun, which is convolved with 3 different values for the rotational broadening kernel. Tycho-G does not show significant rotation, indicating $v_{\rm rot} \sin i \lesssim 7.5$ km s^{-1}.

therefore we adopt 7.5 km s^{-1} as our upper limit to the rotation of the star. If one were to adopt RP04's measurements of the peculiar spatial motion, it could be concluded that $\sin i$ is much closer to 1 than 0 (see the end of section 2.3 for further explanation) and thus that the rotational speed is $v_{\mathrm{rot}} \lesssim 7.5$ km s^{-1}.

2.5.2. Radial velocity

To determine the radial velocity, we used 63 lines to measure the shift in wavelength. We find a radial velocity in the topocentric (Mauna Kea) frame of reference of $v_{\mathrm{top}} = -92.7 \pm 0.2$ km s^{-1}(the error being the standard deviation of 63 measurements) . The conversion from the topocentric to the Galactic LSR for our observations was calculated to be 13.6 km s^{-1} (IRAF task RVCORRECT) using the IAU standard of motion. Including the uncertainty in the LSR definition, we find a radial velocity in the LSR for Tycho-G of $v_{\mathrm{LSR}} = -79 \pm 2$ km s^{-1}. This is in significant disagreement with that reported by RP04, but agrees with the revised value published by GH09.

2.5.3. Astrometry

RP04 have measured a significant proper motion for Tycho-G of $\mu_b = -6.1 \pm 1.3$ mas yr^{-1}, $\mu_l = -2.6 \pm 1.3$ mas yr^{-1}. Because Tycho-G is metal rich, and at a distance of $D > 2$kpc, this measurement provides one of the strongest arguments for Tycho-G being the donor star to Tycho SN. It is almost impossible to account for this proper motion, equivalent to a $v_b = 58\left(\frac{D}{2\ \mathrm{kpc}}\right)$km s^{-1} or 3 times the disk's velocity dispersion of $\sigma_z = 19$km s^{-1}, except through some sort of strong binary star interaction.

However, the HST data present an especially difficult set of issues in obtaining astrometry free of systematic errors. For Tycho-G these issues include the PSF on the first epoch Wide-Field Planetary Camera 2 (WFPC2) image being grossly undersampled, both the ACS and WFPC2 focal planes being highly distorted, poor and different charge transfer efficiency across the two HST images, and that Tycho-G was, unfortunately, located at the edge of one of the WFPC2 chips, making it especially difficult to understand the errors associated with it. Smaller issues include the small field of overlap between the two images, making the measurement subject to issues of the correlated motions of stars, especially in the μ_l direction.

To cross-check RP04's proper motion of Star-G , we have scanned a photographic plate taken in September 1970 on the Palomar 5 meter, and compared this to an INT CCD archive image (INT200408090414934) of the remnant taken in August 2004. The Palomar plate has an image FWHM of 1.7″, and the INT image 0.88″. While our images have a much larger PSF than the HST images, the images have significantly less distortion, are matched over a larger field of view with more stars, have fully sampled PSFs, and were taken across nearly an 8 times longer time baseline. The photographic nature of the first epoch does add complications not present in the HST data. The non-linear response of photographic plates causes their astrometry to have systematic effects as a function of brightness (Cannon et al., 2001), especially affecting objects near the plate limit, where single grains are largely responsible for the detection of an object.

Table 2.1 Proper motions of stars within 45″ of the Tycho SNR center.

α [hh:mm:ss.ss]	δ [dd:mm:ss.ss]	μ_l [mas yr^{-1}]	μ_b [mas yr^{-1}]	m_R [mag]	θ [arcsec]	Name
00:25:20.40	+64:08:12.32	-0.90	-0.56	17.05	08.9	c
00:25:18.29	+64:08:16.12	-4.25	-0.81	18.80	10.0	e
00:25:17.10	+64:08:30.99	-1.82	1.78	16.87	20.3	f
00:25:23.58	+64:08:02.02	-1.58	-2.71	17.83	31.1	g
00:25:15.52	+64:08:35.44	1.94	0.83	20.28	31.4	r
00:25:15.08	+64:08:05.95	-0.67	1.49	18.86	33.3	j
00:25:23.89	+64:08:39.33	-0.31	1.08	19.20	33.5	k
00:25:14.74	+64:08:28.16	2.60	1.46	17.45	33.5	n
00:25:14.81	+64:08:34.22	4.05	-2.05	19.35	35.0	q
00:25:13.79	+64:08:34.50	2.32	1.01	19.90	41.3	s
00:25:14.59	+64:07:55.10	-3.94	2.35	19.23	41.7	t
00:25:19.25	+64:07:38.00	1.75	-3.43	16.86	42.1	u
00:25:22.45	+64:07:32.49	81.29	-2.68	19.81	48.7	HP-1

The position of stars on the INT image were matched to the 2MASS point source catalog (Skrutskie et al., 2006) to get a coordinate transformation (pixel coordinates to celestial coordinates) using a 3rd-order polynomial fit with an RMS precision of 40 mas with 180 stars. This fit is limited by precision of the 2MASS catalog and shows no systematic residuals as a function of magnitude, or position. Using this world coordinate system (WCS) transformation, we then derived the positions of all stars on the INT image. The coordinates of 60 uncrowded stars on the Palomar plate were matched to the INT-based catalog, and a 3rd-order polynomial was used to transform the Palomar positions to the INT-based positions. The fit has an RMS of 65 mas in the direction of galactic longitude, and 45mas in the direction of galactic latitude. We believe the larger scatter in the direction of Galactic longitude is due to the shape of the PSF being slightly non-symmetric in the direction of tracking on the Palomar plate. This tracking (in RA, which is close to the direction of galactic longitude), causes the position of stars to depend slightly on their brightness. This explanation is supported by a small systematic trend in our astrometric data in μ_l, not seen in μ_b, as a function of m_R. An alternative explanation is that the trend in μ_l is caused by the average motion of stars changing due to galactic rotation as a function of distance, which is proxied by m_R. We have used the Besançon Galactic model [3](Robin et al., 2003) to estimate the size of any such effect, and find the observed effect is an order of magnitude larger than what is expected. The systemic difference between assuming either source of the observed effect is less than 1 mas yr^{-1} in μ_l, and has no effect in our μ_b measurement. In our final proper motions, presented in table 2.1, we remove the systematic trend as a function of m_R with a linear function.

To measure the proper motion of each star, we exclude each star from the astrometric transformation fit so as not to bias its proper motion measurement. Comparing the stellar

[3]The Besançon model is a population synthesis model, which treats the Disc, Thick Disc, Stellar halo and Bulge separately with different input parameters (e.g. age, metallicity, star formation rate, etc.). When data is requested Monte-Carlo drawings on the different distributions of quantities (e.g. luminosities, ages, kinematics) for the different components are performed and presented as a list of sample stars.

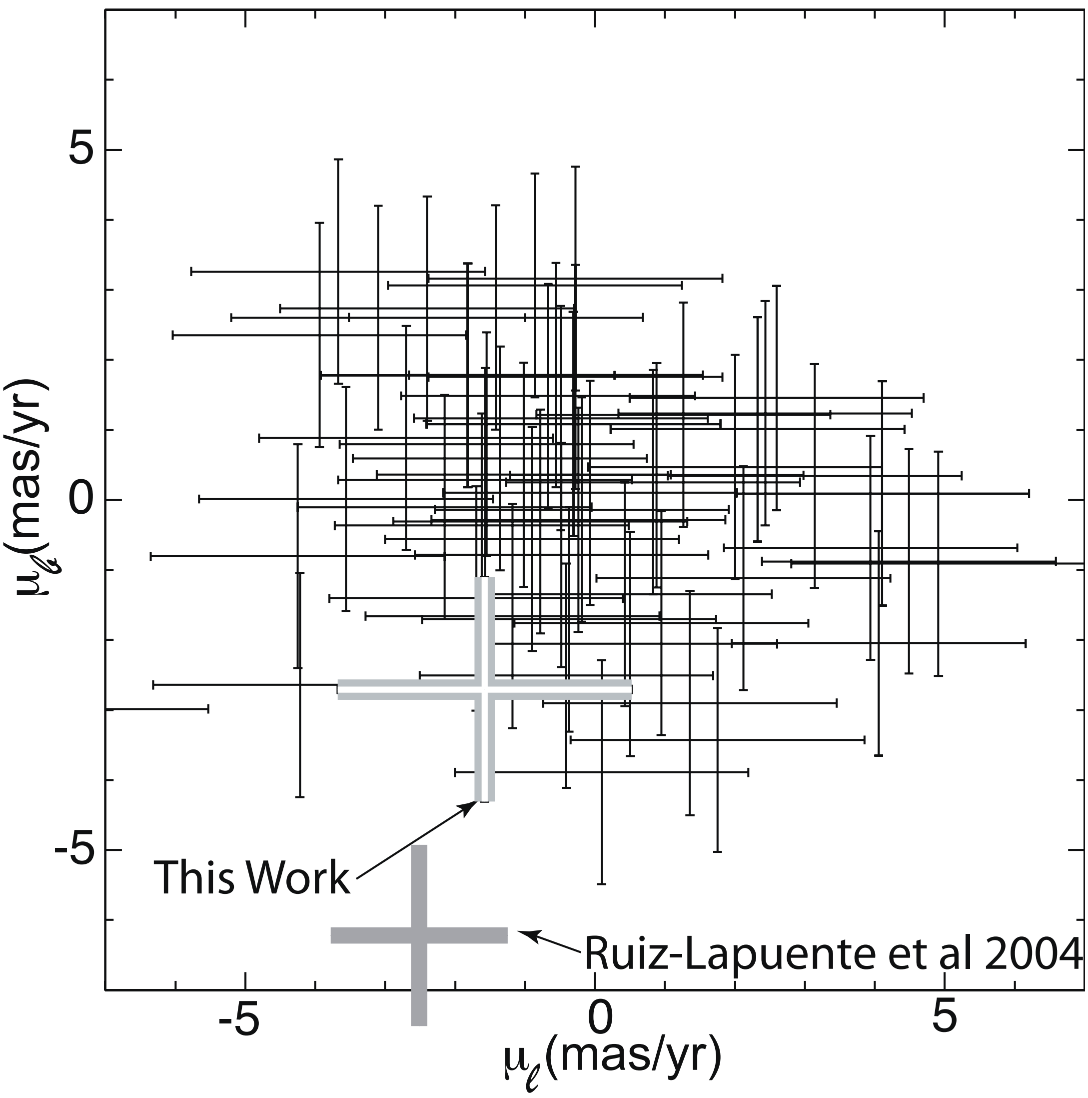

Figure 2.4 The astrometric motions of 60 stars measured in the Tycho SNR center. The measurements have a RMS dispersion of 1.6 mas yr^{-1}. Shown in grey is the proper motion of Tycho-G measured here and by RP04, showing a moderate discrepancy in the two measurements. Our measurement is consistent with no proper motion.

positions in the 34 year interval we find that these 60 stars show an RMS dispersion $\sigma_{\mu_l} = 2.1$mas yr^{-1}, $\sigma_{\mu_b} = 1.6$ mas yr^{-1}. For Tycho-G we measure $\mu_l = -1.6 \pm 2.1$ mas yr^{-1}, $\mu_b = -2.7 \pm 1.6$ mas yr^{-1}; this implies that no significant proper motion is detected. We do note that this measurement has a similar precision to that of RP04, is consistent with no observed motion, and is in moderate disagreement with the RP04 measurement.

In table 2.1 we present our astrometric measurements of all stars listed by RP04 for which we were able to measure proper motions. We also give the apparent magnitudes in R (partly measured by this work and partly by RP04) and the distance from center θ. Due to crowding caused by the relatively poor resolution of the first epoch photographic plate, several stars are not included that could be measured using HST. We include an additional star, not cataloged by RP04, which exhibits high proper motion. This high proper motion star, which was off the WFPC2 images of RP04, we designate HP-1, and has a proper motion of $\mu_l = 81.3$, $\mu_b = -2.7\,\mathrm{mas\,yr^{-1}}$. Due to the distance from the remnant's center, (we estimate HP-1 would have been located 51″ from the remnant's center in 1572), we doubt this star is connected to the Tycho SN, but we include it for the sake of completeness.

2.6. Discussion

2.6.1. A Background interloper?

A previously unrecognized property for many progenitor scenarios is the rapid post-explosion rotation of the donor (as described in Section 2.3). The expected rotation as calculated in Figure 2.2 is large compared to that expected of stars with a spectral type later than F and should be easily observable. We have shown Tycho-G's rotation to be less ($v_{\mathrm{rot}} \sin i \lesssim 7.5$ km s^{-1}) than what is expected of an associated star if the companion was a main sequence star or subgiant. A red giant scenario where the envelope's bloating has significantly decreased rotation could be consistent with our observation of Tycho-G, and this will be discussed in section 2.6.2.

The primary basis for which RP04 selected Tycho-G as a candidate for the donor star to the Tycho SN was the combination of its large peculiar radial velocity and its observed proper motion. In Figure 2.5 we use the Besançon Galactic model (Robin et al., 2003) to construct an expected set of radial velocities for metal-rich stars in the direction of SN1572.

Measuring the distance to Tycho-G is a key discriminant in associating the star to the SN explosion. To improve the uncertainty of the distance to the star, due both to temperature and extinction uncertainty, we base our distance on the observed m_K (Skrutskie et al., 2006) and $(V-K)$ color (RP04). We interpolate ATLAS9 (Castelli & Kurucz, 2004) models without overshoot (Bessell et al., 1998) to find a theoretical $V-K$ and absolute magnitude for the GH09's values of temperature and gravity. Using a standard extinction law (Cardelli, Clayton, & Mathis, 1989) ($A_V = 3.12E(B-V)$ and $A_K/A_V = 0.109$) to match the theoretical and observed colors, we find $A_V = 2.58 \pm 0.08$mag, $A_K = 0.28 \pm 0.01$ mag, and $E(B-V) = 0.84 \pm 0.05$. To better show the uncertainties, we present our distance moduli scaled to the observed and derived values of extinction, temperature and gravity. The temperature coefficients were determined by integrating blackbodies of the appropriate temperature with a filter bandpass and fitting a powerlaw to the resulting flux.

$$\begin{aligned}(m_V - M_V) = {} & 12.93 - 3.12(E(B-V) - 0.84) - 2.5(\log g - 3.85) + \\ & +2.5\log\left(\frac{M}{1\,M_\odot}\right) + 2.5\log\left(\frac{T_{\mathrm{eff}}}{5900}\right)^{4.688}\end{aligned} \tag{2.1}$$

$$\begin{aligned}(m_K - M_K) = {} & 12.93 - 0.275(E(B-V) - 0.84) - 2.5(\log g - 3.85) + \\ & +2.5\log\left(\frac{M}{1\,M_\odot}\right) + 2.5\log\left(\frac{T_{\mathrm{eff}}}{5900}\right)^{1.937}\end{aligned} \tag{2.2}$$

Assuming a companion mass of $1\,M_\odot$ we find a $(m-M) = 12.93 \pm 0.75$ mag. This uncertainty is dominated by the precision of $\log g$, and equates to a distance of $D = 3.9 \pm 1.6$kpc. Tycho-G, within the errors, is at a distance consistent with the remnant. As seen in Figure 2.5,

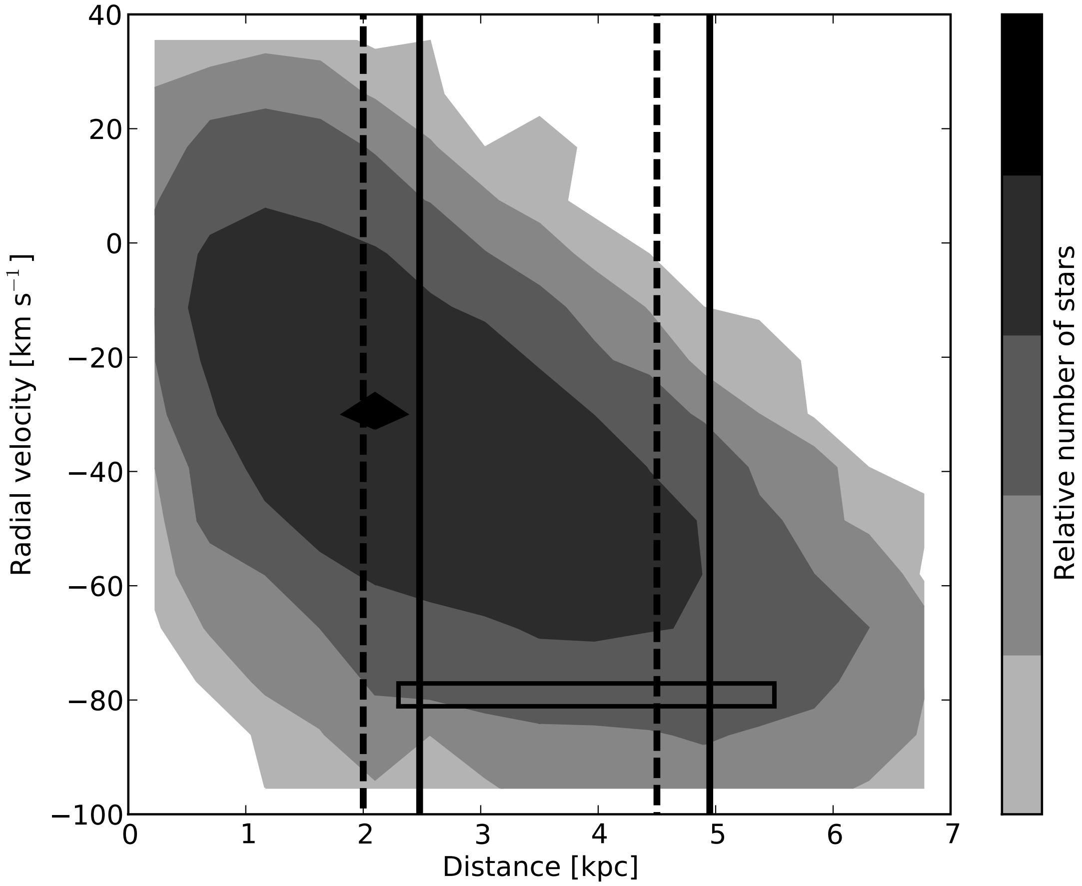

Figure 2.5 Besançon model for a metal rich ([Fe/H] > -0.2) Galactic population between 0 and 7 kpc in the direction of Tycho SNR (l = 120.1, b=1.4) with a solid angle of 1 square degree. The remnant's distance is represented by the black dashed lines (as calculated in section 2.2). The contours show the radial velocity distribution of 21470 stars (the contour levels from light gray to black are 10, 30, 100, 300, 1000). Our measured radial velocity corrected to LSR and our distance are shown, with their respective error ranges, as the black rectangle. The distance range calculated by GH09 are indicated by the two solid lines. The observed LSR $v_{\rm rad}$ for Tycho-G is mildly unusual for stars at the remnant's distance, and is consistent with the bulk of stars behind the remnant.

the observed radial velocity of Tycho-G is consistent with a significant fraction of stars in its allowed distance range. We also note that if Tycho-G is indeed associated with the SN, that it is likely that Tycho-G could have a mass considerably less than 1 $M_{\odot}$, due to mass transfer and subsequent interaction with the SN, although in this case, the distance to the star would still be consistent with SNR distance.

Ihara et al. (2007) looked for absorption due to Fe I in the remnant's expanding ejecta for 17 stars within the Tycho remnant. No such absorption was seen in the spectrum of Tycho-G, potentially placing it in front of the remnant. However, the amount of Fe I currently within the remnant is uncertain with predicted column densities spanning several orders of magnitude ($0.02 - 8.9 \times 10^{15}$ cm^{-2}; Hamilton & Fesen, 1988; Ozaki & Shigeyama, 2006). Therefore, we do not believe the lack of significant Fe I 3720 Åabsorption in Tycho-G to be significant.

In summary, we find that Tycho-G's radial velocity, distance, and stellar parameters are all consistent with an unrelated star, but also with it being the donor star. There is disagreement in Tycho-G's measured proper motion. The measurements of RP04 are inconsistent with normal disk stars at the known distance and strongly point to Tycho-G being associated with the SN, whereas the measurements presented here are consistent with a normal disk star, unrelated to the SN. In addition, we have shown the rotation of Tycho-G is low (confirmed by GH09; $v_{\rm rot} \leq 6.6$ km s^{-1}), arguing against association with the SN, as does its off center placement in the remnant. Finally, GH09 have presented evidence that Tycho-G is strongly enhanced in Nickel, an observation that, if confirmed, would strongly point to an association of the star with the SN. If either the high proper motion, or significant Nickel enhancement can be confirmed, then it is likely that Tycho-G is the SN donor star. Otherwise, we believe it is much more likely that Tycho-G is simply an interloper.

2.6.2. Tycho-G as the Donor Star to the Tycho SN

While the case for Tycho-G's association with the SN is not conclusive, it is intriguing, and we believe it is worthwhile to look for a consistent solution assuming the association is true. While not apriori probable, a self-consistent model can be constructed in which Tycho-G was the companion, as we shall discuss now.

To make such a model work, Tycho-G has to be a stripped giant that presently mimics a G2IV star. At the time of the explosion, the star would have been a moderately evolved giant (in a binary with an orbital period ~ 100 d). The SN ejecta will strip such a giant of almost all of its envelope (Marietta et al., 2000) due to its low binding energy; only the most tightly bound envelope material outside the core will remain bound. Due to the heating by the SN, even this small amount of material (perhaps a few $\times 0.01\ M_{\odot}$) will expand to giant dimensions, and the immediate-post-SN companion will have the appearance of a luminous red giant. However, because of the low envelope mass, the thermal timescale of the envelope is sufficiently short that it can loose most of its excess thermal energy in 400 years and now have the appearance of a G2IV star (Podsiadlowski, 2003).

A lower mass for Tycho-G ($0.3 - 0.5\ M_{\odot}$) also reduces the distance estimate, and makes the observed radial velocity more unusual for stars at this distance. The expected spatial velocity depends on the pre-SN orbital period and should be in the range of $30 - 70$ km s^{-1} for a period range of $20 - 200$ d (Justham et al., 2008). These velocities are consistent with the inferred spatial velocity of the object relative to the LSR if Tycho-G is at the distance of the remnant, even if no significant proper motion has been measured (see Figure 2.5).

A stripped-giant companion would link the progenitor to the symbiotic single-degenerate channel (Hachisu et al., 1999b) for which the symbiotic binaries TCrB and RS Ophiuchi are well studied candidates. Indeed, (Justham et al., 2008) argued that the ultracool low-mass helium white dwarfs (with masses $> 0.3\ M_{\odot}$) that have been identified in recent years are most likely the stripped-giant companions that survived SN Ia explosions, which could provide some further possible support for such a scenario for Tycho-G.

If the association is real, Tycho-G's displacement to the SE of the geometric center of the remnant as defined by radio and X-ray observations might be interpreted as being due to the remnant's interaction with an inhomogeneous ISM. Deep optical images of the remnant do show extended diffuse emission along the eastern and northeastern limbs interpreted as shock precursor emission (Ghavamian et al., 2000). This along with an absence of detected Balmer-dominated optical emission along the whole of the western and southern limbs suggests a density gradient of the local ISM with increasing density towards the NE. An east-west density gradient has also been inferred from detailed radio expansion rate measurements (Reynoso et al., 1997). Such an E–W density gradient could have led to a more rapid expansion toward the west giving rise to a small shift in the apparent geometric center away from the SE without creating a highly distorted remnant. However, there are problems with this explanation. Deviations from spherical symmetry in both radio and X-ray images of the remnant are relatively small (Reynoso et al., 1997; Cassam-Chenaï et al., 2007), and the remnant is most extended along the eastern and northeastern limbs, just where one finds the greatest amount of extended diffuse optical emission. Moreover, the remnant's expansion rate appears lowest toward the northeast (PA = 70 degrees), not the southeast (Reynoso et al., 1997). Although the argument that Tycho-G's SE displacement from the remnant's current geometric center is a result of an asymmetrical expansion is not strong, it remains a possibility.

The most conclusive way of confirming a stripped-giant scenario for Tycho-G would be an independent, precise measurement of the distance to Tycho-G which in combination with measurements of the gravity and effective temperature would help to constrain Tycho-G's mass. Unfortunately, such a measurement will most likely have to wait for the advent of the GAIA satellite. Alternatively, one may be able to single out a stripped giant from a normal G2IV star through nucleosynthesis signatures, specifically evidence for CNO-processed material (or other nucleosynthetic anomalies). While a normal G2IV star is unlikely to show CNO-processed material at the surface, a stripped giant is likely to do so. Unfortunately, the data presented here are not of adequate quality to explore the detailed properties of Tycho-G's atmosphere.

2.7. Outlook and Future Observations

Presently, we believe the evidence for Tycho-G's association with the Tycho SN is interesting, but not conclusive. A possible scenario if Tycho-G is the donor star, would be that of a stripped giant scenario discussed in section 6. However, there are still other stars that have not been adequately scrutinized. Ihara et al. (2007) have found a star (RP04 Star-E) which may contain blueshifted Fe I lines, indicating their association with the remnant. Unfortunately, the star has neither a significant peculiar radial velocity (Ihara et al. 2007; RP04) nor a significant peculiar proper motion (RP04 and confirmed by our work; see Table 2.1).

High-resolution spectroscopy of each candidate in the remnant's center is necessary to precisely determine each star's physical parameters. However, the small observed velocities of the remaining stars suggest that the donor star would have needed to be a giant at the time of explosion. Using RP04's observed values, none of the stars in the remnant's center appear consistent with what is expected of a giant star as the donor star except possibly for Star-A. We also note that there is an additional star present in archived HST images, not cataloged in RP04, offset from RP04's star A by 0.5″ E and 0.2″ N at $m_V = 16.8$, $(B-V) = 1.0$.

This star, near the remnant's centre, has a color consistent with an F-star (assuming that it is behind the bulk of the line of sight reddening), but it will require adaptive optics to obtain its spectrum given its proximity to the 13th magnitude Star-A. This star could potentially be a non-giant progenitor.

If future observations are unable to pinpoint a viable donor star, other progenitor scenarios will have to be considered. These include the double degenerate scenario, or a scenario where there is a long time delay between the accretion phase of a donor star onto the white dwarf, and the ultimate supernova explosion.

We would like to thank the Subaru HDS team for taking these observations in service mode. This paper makes use of data obtained from the Isaac Newton Group Archive which is maintained as part of the CASU Astronomical Data Centre at the Institute of Astronomy, Cambridge. This publication makes use of data products from the Two Micron All Sky Survey, which is a joint project of the University of Massachusetts and the Infrared Processing and Analysis Center/California Institute of Technology, funded by the National Aeronautics and Space Administration and the National Science Foundation. This work also makes use of POSS-I data. The National Geographic Society - Palomar Observatory Sky Atlas (POSS-I) was made by the California Institute of Technology with grants from the National Geographic Society. WEK, BPS and MA are supported by the Australian Research Council (grant numbers DP0559024, FF0561481). This paper was conceived as part of the Tokyo Think Tank collaboration, and was supported in part by the National Science Foundation under Grant No. PHY05-51164. This work was supported in part by World Premier International Research Center Initiative (WPI Program), MEXT, Japan, and by the Grant-in-Aid for Scientific Research of the Japan Society for the Promotion of Science (18104003, 18540231, 20540226) and MEXT (19047004, 20040004). Additionaly we would like to thank Pilar Ruiz Lapuente and her team for the valuable discussions we had in regards to the manuscript. We would also like to thank our referee, who provided us with a very detailed and thorough analysis of the first manuscript and subsequent revisions.

CHAPTER 3

Tycho's Six: High Resolution spectroscopy search for the donor of the Tycho supernova

This Chapter is being prepared for publication as 'Tycho's Six: High-Resolution spectroscopy search for the donor of the Tycho supernova' - Kerzendorf, W. E., Schmidt, B. P., Yong, D., Jeffery, C.S. , Anderson, J.P., Nomoto, K., Podsiadlowski, Ph., Simon, J.D., Gal-Yam, A., Silverman, J.M., Filipenko, A.V., Murphy, S.J., Bessell, M.S.

3.1. Introduction

SNe Ia are of great interest for astronomy. They represent some of the most extreme physical situations in stellar astronomy, produce substantial amounts of IGE which impacts the chemical evolution of galaxies and the Universe, and are uniquely powerful cosmic distance probes. Despite their wide ranging significance, fundamental uncertainties remain around the progenitor of these cataclysmic events.

There is general consensus that SNe Ia are caused by the deflagration/detonation of a CO-WD which is accreting material from a binary companion. Scenarios exists where the explosion can be initiated from a detonation on the surface of the star (Livne & Arnett, 1995; Fink et al., 2010), through runaway carbon burning in the white dwarf's interior, or through a cataclysmic merger of objects.

Observationally, two main scenarios for this accretion process can be identified. The SD-Scenario sees the accretion process occurring through RLOF of a close non-degenerate companion (also known as donor star). This companion, which has undergone common envelope evolution with the white dwarf, can be a helium, main-sequence, sub-giant, or red giant star. In all cases the donor star should survive the explosion (except for possibly in the case of the helium star donor; priv. comm. Rüdiger Pakmor) and remains visible post-explosion.

The second scenario is the dynamical merger of two white dwarfs (DD-Scenario). In this scenario, the co-evolution of two stars eventually leads to a close binary of two white dwarfs, which are able, through the emission of gravitational radiation, to merge over a wide range of times after the initial formation of the system. In most cases this would leave no remaining star (e.g. Pakmor et al., 2010).

Both scenarios have support in observation and theory. The detection of circumstellar material around certain SN Ia such as SN 2006X (Patat et al., 2007), provides support for the SD-Scenario. On the other hand the lack of substantial hydrogen in the majority of other SNe Ia (Leonard, 2007) poses a challenge to the SD-Scenario.

Kasen (2010) suggests that the interaction with the non-degenerate companion should imprint an observable signature on a SN Ia light curve, depending on viewing angle, and radius of the companion. Such an excess has not yet been observed (Hayden et al., 2010; Tucker, 2011; Bianco et al., 2011) which is at odds with red giant companions forming the majority of SNe Ia.

Population synthesis calculations are challenging, with various authors getting different results for the same inputs (e.g. Nelemans, 2010). However there is a general trend from these calculations that neither single-degenerate nor double degenerate stars can provide enough systems to explain the SN Ia rate (Ruiter et al., 2009; Mennekens et al., 2010; Yu & Jeffery, 2010; Han, 2008). Several authors suggest the population might comprise both single and double degenerate systems.

The physics of white dwarf mergers is challenging to simulate numerically, but in the simplest calculations, these mergers will lead to the formation of a neutron star via an electron capture, rather than a thermonuclear explosion (Saio & Nomoto, 1985). Recently Pakmor et al. (2010) have shown that for certain parameters (white dwarf binaries with a mass ratio very close to one) the merger may explain sub-luminous supernovae (e.g. 91bg-like SNe Ia), although Dan et al. (2011) note that the initial conditions of the system may change these conclusions.

To investigate the nature of progenitors observationally RP04 have tried to directly detect donor stars in SN Ia remnants within the Milky Way. They have identified two historical Galactic SNe well suited to this task - SN 1006 and SN 1572 (Tycho's SN). Both remnants are young (440 and 1000 years old, respectively), almost certainly SN Ia from both their observational signatures (Badenes et al., 2006; Ruiz-Lapuente, 2004) and not overwhelmed by Galactic extinction. In this paper, we will focus on SN 1572.

SNR 1572 is relatively close (2.8 ± 0.8 kpc), very young and has been confirmed as a normal SN Ia remnant both from the remnant (Badenes et al., 2006) and from a light echo (Krause et al., 2008; Rest et al., 2008a).

RP04 investigated most bright stars in the central regions of SN 1572 and found a star with an unusual spatial motion (Tycho-G by their nomenclature) and suggested this as a possible donor star for SN 1572. While the star has an unusual spatial motion compared to other stars in the field, its current location and proper motion place it a significant distance from the remnant's center - a feature difficult to explain in connecting Tycho-G to SNR 1572. One consequence of RLOF is a rotational velocity induced on the donor star by tidal locking in the system. This results in an unusually large rotationally velocity, related to the orbital velocity of the binary system and can be used to single out donor stars against nearby unrelated stars. Kerzendorf et al. (2009) (WEK09) investigated rotation for Tycho-G but found no excess rotation velocity compared to a normal star. WEK09's measurements of Tycho-G, including a revised radial velocity, compared to Galactic kinematic models showed it is statistically consistent with an interloping star. However, WEK09 were able to provide an a priori unlikely scenario, where the star was able to lose its rotational signature.

GH09 analysed a spectrum of Tycho-G observed with the HIRES instrument on the Keck telescope. In addition to confirming WEK09's radial velocity for Tycho-G, GH09 measured its stellar parameters and metallicity. GH09 concluded that Tycho-G has an unusually large amount of nickel. GH09 claim that this enhancement in nickel can be attributed to the accretion of ejecta material on the donor star during the explosion.

In this paper we analyse HIRES spectra of the six bright stars in SNR 1572 center. These spectra were taken by the same program that obtained the data used by GH09 and we independently reanalyze this spectrum as part of our program. We describe the observational data and our data reduction procedures in Section 3.2. Section 3.3 is divided into five subsections detailing the measurements of proper motion, radial velocity, rotation, stellar parameters and abundances. In Section 3.4 we analyse the measurements of each star to investigate its potential association with SNR 1572, and present our conclusion in Section 3.5.

3.2. Observations and Data Reduction

We obtained spectra with the HIRES on the Keck 10m telescope on Mauna Kea. The observations were made on two nights on 2006 September 10 and 2006 October 11. The slits B5 and C1 (with the same width of 0.86″ but different lengths, B5 length 3.5″, C1 length 7.0″) were used resulting in a wavelength coverage of 3930–5330 Å, 5380–6920 Å and 6980–8560 Å with $R \approx 50,000$, providing us with the necessary spectral resolution and wavelength coverage to determine stellar parameters. The spectra were reduced using the MAKEE package. All spectra were corrected to heliocentric velocities, using the MAKEE skyline method. The spectra were not corrected for telluric lines as they will not influence our analysis of the stellar parameters. The final exposure times of the combined spectra for each candidate and signal to noise ratio at 4000-4100 Å are shown in Table 3.1. Finally we normalized the spectrum using the IRAF task CONTINUUM. We note that Tycho-C and Tycho-D were observed on the same slit (C1) with a separation of 2.1″.

Table 3.1 Observations of Stars

Tycho	RA (J2000) (hh:mm:ss.ss)	Dec (J2000) (dd:mm:ss.ss)	Date (dd/mm/yy)	Slit	t_{exp} (s)	S/N
A	00:25:19.73	+64:08:19.60	10/09/06	B5	900	≈ 65
B	00:25:19.95	+64:08:17.11	10/09/06	B5	1200	≈ 50
C	00:25:20.40	+64:08:12.32	11/10/06	C1	10800	≈ 10
D	00:25:20.60	+64:08:10.82	11/10/06	C1	10800	≈ 5
E	00:25:18.29	+64:08:16.12	11/10/06	C1	9000	≈ 15
G	00:25:23.58	+64:08:02.06	10/09/06 & 11/10/06	B5&C1	24000	≈ 30

In addition, we obtained low-resolution spectroscopy ($R \approx 1200$) of Tycho-B with the dual-arm Low-Resolution Imaging Spectrometer (LRIS; Oke et al., 1995) mounted on the 10-m Keck I telescope. The observations were taken on one run on 2010 November 07, using only the blue arm with the 600/4000 grism and the 1″ wide slit. This resulted in a wavelength coverage of 3200 – 5600 Å. These observations were taken to obtain a precise measurement of the surface gravity for Tycho-B using the size of the Balmer decrement (Bessell, 2007). The spectrum of Tycho-B was reduced using standard techniques (e.g. Foley et al., 2003). Routine CCD processing and spectrum extraction were completed with IRAF, and the data were extracted with the optimal algorithm of Horne (1986). We obtained the wavelength scale from low-order polynomial fits to calibration-lamp spectra. Small wavelength shifts were then applied to the data after measuring the offset by cross-correlating a template sky to the night-sky lines that were extracted with the star. Using our own IDL routines, we fit a spectrophotometric standard-star spectrum to the data in order to flux calibrate Tycho-B and remove telluric lines (Horne, 1986; Matheson et al., 2000).

3.3. Analysis

3.3.1. Astrometry

Proper motions can be used to identify potential donor stars because donor stars freely travel with their orbital velocity after the SN explosion disrupts the system. RP04 suggested Tycho-G as a possible donor due to its unusually high proper motion and unusually high radial velocity. For this work we measured proper motions for 201 stars within one arcminute of the remnant's centre. We used archival HST images for three different epochs (HST Program ID 9729 & 10098; November 2003, August 2004, May 2005) each consisting of three exposures (1 s, 30 s and 1440 s) in the F555W using the Advanced Camera for Surveys (ACS). The pixel size in each exposure is 50 mas pixel^{-1}. This dataset results in a maximum baseline of 30 months.

We used an image from the middle epoch (2004) to establish a reference frame and oriented the pixel coordinate system with the equatorial system. We then applied a distortion correction for the F555W filter (Anderson & King, 2006) to each images and then calculated transformations between all other images and the reference image. We then used these transformations to calculate the position of all stars in the reference coordinate system with the overall uncertainty of each position estimated. Some faint stars where not detected in the shorter exposures and were thus excluded from proper motion measurements (with 114 stars remaining).

For each star, we fit a linear regression for the stellar positions over time in the pixel coordinates (which were aligned with the equatorial system). The x and y data were treated as independent measurements, with separate regressions solved for each axis directions. Errors were estimate using standard least squares analysis and the individual error estimates each object's positions.

There are three measurements of the geometric center of SN 1572 using different datasets. Reynoso et al. (1997) using Very Large Array (VLA) data measured the center to $\alpha = 00^h25^m14\overset{s}{.}95$ $\delta = +64°08'05.7''$ J2000, Hughes (2000) using ROSAT data measured $\alpha =$

Table 3.2 Proper motion of Candidates

Tycho	RA (J2000) (hh:mm:ss.ss)	Dec (J2000) (dd:mm:ss.s)	μ_α mas yr^{-1}	μ_δ	$\Delta\mu_\alpha$ mas yr^{-1}	$\Delta\mu_\delta$	r $''$
B	0:25:19.97	64:08:17.1	-1.24	0.56	0.62	0.64	4.86
A	0:25:19.73	64:08:19.8	-0.09	-0.89	1.17	0.90	6.21
A2	0:25:19.81	64:08:20.0	-0.71	-3.60	0.69	0.64	6.58
C	0:25:20.38	64:08:12.2	-0.21	-2.52	0.65	0.65	6.66
E	0:25:18.28	64:08:16.1	2.04	0.54	0.66	0.69	7.60
D	0:25:20.62	64:08:10.8	-1.12	-1.99	1.01	0.86	8.60
1	0:25:16.66	64:08:12.5	-2.27	-1.37	1.60	1.15	18.00
F	0:25:17.09	64:08:30.9	-4.41	0.20	0.70	0.71	22.69
J	0:25:15.08	64:08:05.9	-2.40	-0.25	0.62	0.62	29.44
G	0:25:23.58	64:08:01.9	-2.50	-4.22	0.60	0.60	29.87
R	0:25:15.51	64:08:35.4	0.28	0.24	0.89	0.80	33.23
N	0:25:14.73	64:08:28.1	1.18	0.89	0.86	0.98	33.66
U	0:25:19.24	64:07:37.9	0.01	-3.04	0.73	0.75	36.06
Q	0:25:14.81	64:08:34.2	1.45	3.07	0.64	0.72	36.19
T	0:25:14.58	64:07:55.0	-3.85	0.52	0.72	0.62	36.78
K	0:25:23.89	64:08:39.3	0.18	0.17	0.73	0.69	38.73
L	0:25:24.30	64:08:40.5	0.16	-0.44	0.75	0.82	41.59
S	0:25:13.78	64:08:34.4	4.16	0.58	0.83	0.84	42.09
2	0:25:22.44	64:07:32.4	74.85	-4.43	0.82	0.83	46.09

$00^h25^m19\overset{s}{.}0$ $\delta = +64°08'10''$ J2000 and Warren et al. (2005) with Chandra data measured the center to $\alpha = 00^h25^m19\overset{s}{.}40$ $\delta = 64°08'13.98''$ J2000.

Table 3.2 lists the proper motions and errors of all stars mentioned in RP04 (19 stars) which were analyzed in this work as well as the distance to the geometric X-ray center measured by Chandra.

We compared the distribution of proper motions of all measured stars to ours candidates in Figure 3.1.

3.3.2. Radial Velocity

The radial velocity of each star was measured using the IRAF task FXCOR (Tonry & Davis, 1979). MAKEE was used to calculate an intrinsic velocity shift by comparing offsets of the nightsky-lines. The radial velocity standards were reduced in the same fashion.

Each order of each star was then cross-correlated with at least two other radial velocity standards (HR6349, HR6970 & HR1283) which had been observed on the same night.

The radial velocity for Tycho-B was measured in the course of determining the stellar parameters for Tycho-B with the stellar parameter fitting package SFIT. The SFIT result consistently gives $v_{\mathrm{helio}} = -55$ km s^{-1} for different stellar parameters with an error of ≈ 2 km s^{-1}.

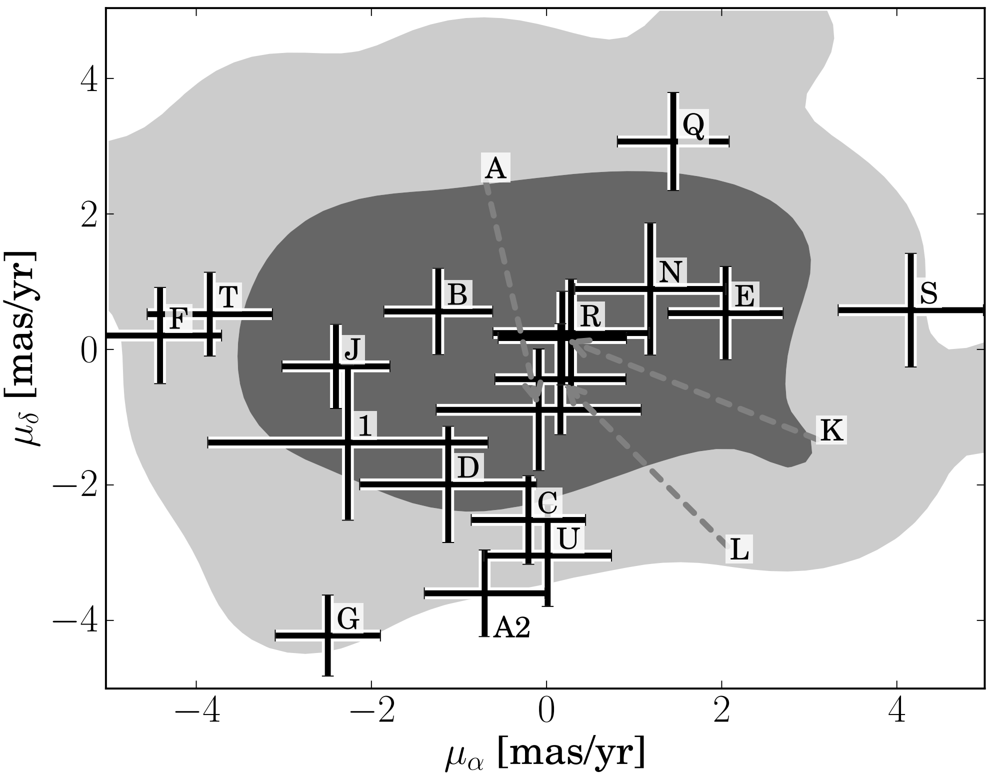

Figure 3.1 The contours show the distribution of proper motions (68% and 95% probability) for all stars measured towards the Tycho SNR - excluding the named stars. We show the location of the candidate stars and their errors on top of this distribution. Tycho-2 was not shown in this figure as it is an extreme outlier with μ_α = 75 mas yr^{-1} and μ_δ = −4.4 mas yr^{-1} but also at a large distance to the center of the remnant's geometric center (46″).

In Table 3.3 we have listed all the radial velocities both in a heliocentric frame and a LSR frame. We will be referring to the heliocentric measurements from here on. The listed error is the standard deviation of the radial velocity measurement of all orders added in quadrature to the error of the radial velocity standards.

In Figure 3.2 we have compared the radial velocity of our sample stars to radial velocities of stars in the direction of Tycho's SNR using the Besançon Model (Robin et al., 2003). The distance as well as the error in distance are taken from Section 3.3.5. The candidates radial velocities are all typical for their distance. Finally, we note the measurement of Tycho-G is consistent with WEK09 and GH09.

3.3.3. Rotational Velocity

We have measured rotational velocities of all stars except Tycho-B in the same fashion as described in WEK09. We selected several unblended and strong (but not saturated) Fe I lines in the stellar spectra . We added these lines after shifting them to the same wavelength and scaling them to the same equivalent width (EW). This was done to improve the S/N ratio for the faint stars as well as providing consistency throughout all stars.

Table 3.3 Radial velocities

Name designation	Date (dd/mm/yy)	v_{helio} (km s^{-1})	v_{LSR} (km s^{-1})	Δv (km s^{-1})
Tycho-A	09/09/06	-36.79	-28.5	0.23
Tycho-B	09/09/06	-55.0	-57.0	≈ 2
Tycho-C	11/10/06	-58.78	-50.49	0.75
Tycho-D	11/10/06	-58.93	-50.64	0.78
Tycho-E	11/10/06	-64.2	-55.91	0.27
Tycho-G	09/09/06	-87.12	-78.83	0.25
Tycho-G	11/10/06	-87.51	-79.22	0.78

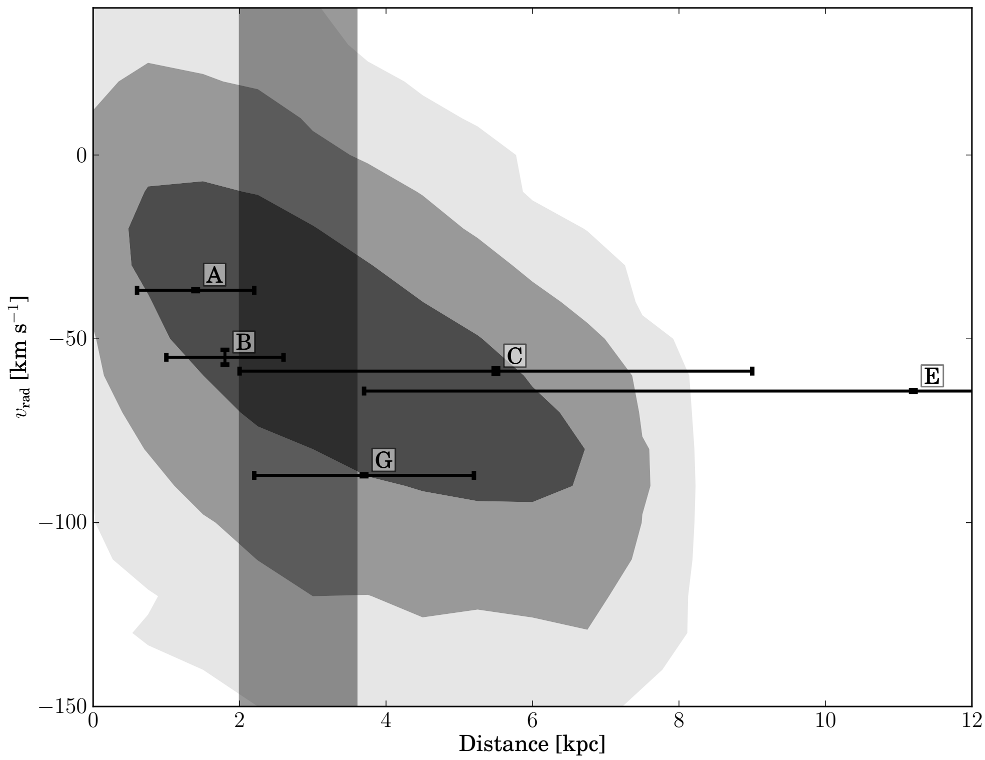

Figure 3.2 The contours indicate 1, 2 and $3-\sigma$ levels of the distance and radial velocity using the Besançon Model (Robin et al., 2003) with $\approx 60,000$ stars in the direction of SN 1572 (only including stars with $10 < V < 20$ and stars with a metallicity of [Fe/H] > -1). We have over plotted our candidate stars with error bars. One should note that the errors in distance are a marginalised approximate of the error, the proper error surfaces can be seen in Figure 3.6. The vertical gray shade shows the error range for the distance of SNR1572.

As a reference we created three synthetic spectra for each star (one broadened only with the instrumental profile, the others with the instrumental profile and $v_{\mathrm{rot}} \sin i$ of 10 and 13 km s^{-1} respectively) with the 2010 version of MOOG, using our derived temperature, gravity and metallicity. As input data to MOOG we used the Castelli & Kurucz (2004) atmospheric models and a line list from Kurucz & Bell (1995). We then applied the same

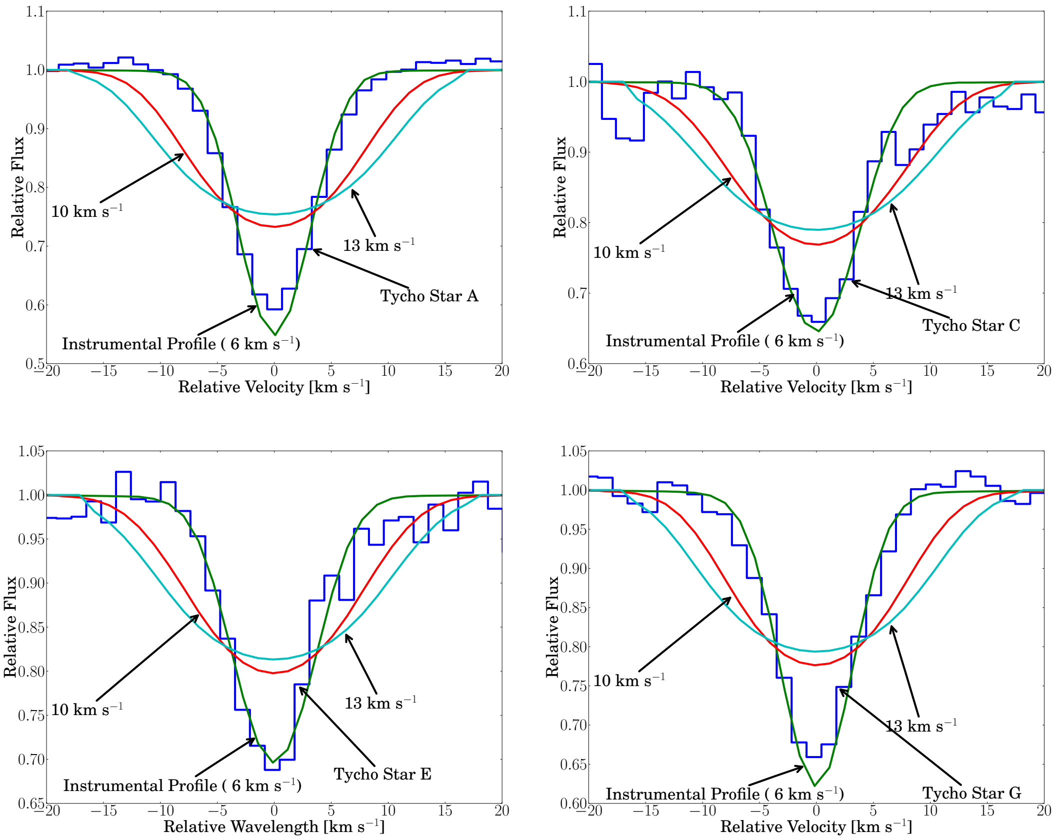

Figure 3.3 The figures show the combination of iron line profiles after normalization to the same Equivalent Width and compare them to synthetic line profiles created by MOOG. We convolved the synthetic lines first with a rotational kernel with three different values for rotation and then with the instrumental profile. All stars show rotation less than 6 km s^{-1} which is equal to the instrumental profile at this resolution.

process of line selection and adding as for the lines in the observed spectra.

Figure 3.3 shows the comparison between the synthetic spectra of different rotational velocity and the observed spectra. This comparison indicates that the stellar broadening (rotational, macro turbulence, etc.) is less than broadening due to the instrumental profile of 6 km s^{-1} for each star. We adopt 6 km s^{-1} as an upper limit to the rotation for all stars.

Due to its high temperature and rotation, we fit the rotational velocity for Tycho-B with the program SFIT (Jeffery et al., 2001, described in section 3.3.4) as part of the overall fit for this star's stellar parameters. We find $v_{\rm rot} = 171^{+16}_{-33}$ km s^{-1}. While Tycho-B's rotation is very high compared to the other candidate stars, for stars of this temperature and gravity a high rotation is not unusual. In summary, other than Tycho-B, none of the stars show rotation which is measurable at this resolution.

3.3.4. Stellar parameters

The stellar parameters are presented in Table 3.5 and were determined using a traditional spectroscopic approach based on the EWs of lines of different excitation and ionisation levels. These measurements exclude Tycho-B, due to its hot temperature, and we measure its stellar parameters by direct comparison to models, in a separate procedure.

EWs for a set of iron lines were measured using routines in IRAF (compiled from Reddy et al. (2003, henceforth Reddy03) and Ramírez & Cohen (2002, henceforth RC02) Table 3.4 shows the EWs measured for each of the stars. Missing values indicate that the line was not detected.

We used the local thermodynamic equilibrium (LTE) stellar line analysis program MOOG and LTE model atmospheres from the Castelli & Kurucz (2003) grid to derive an abundance for a given line. The effective temperature was adjusted until the abundances from Fe I lines displayed no trend as a function of excitation potential. The surface gravity was adjusted until the abundances from Fe I and Fe II lines were in agreement. The microturbulent velocity, ξ_t , was adjusted until there was no trend between the abundances from the Fe I lines and EW. This process was iterated until self consistent stellar parameters were obtained for each star. In our analysis, we explored stellar parameters at discrete values. For effective temperature, we considered values at every 25 K (e.g. 4000, 4025 K, etc.), for surface gravity , we considered values at every 0.05 dex (e.g., 1.00, 1.05 dex, etc.), and for ξ_t , we considered values at every 0.05 km s^{-1} (e.g. 1.70, 1.75 km s^{-1}, etc.). We assumed that excitation equilibrium was satisfied when the slope between $\log\epsilon$(Fe I) and lower excitation potential (χ) was ≤ 0.004. We assumed that ionization equilibrium was achieved when $|\log\epsilon(\text{Fe I}) - \log\epsilon(\text{Fe II})| \leq 0.02$ dex. The microturbulent velocity was set when the slope between $\log\epsilon$(Fe I) and reduced EW ($\log W/\lambda$) was ≤ 0.004. In all cases we found appropriate solutions in which the trends between Fe I, Fe II, EWs and excitation potentials were small. We estimate that the internal errors are typically $T_{\text{eff}} \pm 100$ K, $\log g \pm 0.3$ dex, and $\xi_t \pm 0.3$ km s^{-1}. For further details regarding the derivation of stellar parameters, see Yong et al. (2008).

The final iron measurements are the average of Fe I and Fe II assuming the solar abundances of Asplund et al. (2009) In addition, we measured abundance for the Elements nickel and lithium via EW analysis. We could not see any unusual abundance pattern for any of the sample stars (see Figure 3.4; Tycho-B's abundances are not presented on the plot as they were measured in a different fashion).

In summary, the inferred metallicities for all candidates show that the candidates are of roughly solar metallicities with the exception of the metal-poor Tycho-C. The range of metallicities spanned by the program stars is compatible with membership of the thin disk. Based on metallicity alone, we do not regard any of the program stars to be unusually metal-poor or metal-rich. Additionally, we find the [Ni/Fe] abundance to be consistent with stars of similar metallicity (see Figure 3.4). The stellar paramaters and elemental abundances are listed in Table 3.5.

Because Tycho-B has a temperature greater than 9000 K and is quickly rotating, the process described above cannot be used to measure stellar parameters. Instead we used the program SFIT to match the HIRES spectrum to a grid of model spectra. To determine the stellar parameters for Tycho-B we have used a model grid with [Fe/H] = −1.0, $8000 < T_{\text{eff}} < 16000$, $7 < \log g < 2$. This low metallicity is suggested by a very weak Calcium K line and Mg II lines, but is hard to measure. We can not measure Helium directly in this spectrum and thus adopt N(He) = 0.1 as this is empirically a very common Helium abundance in stars.

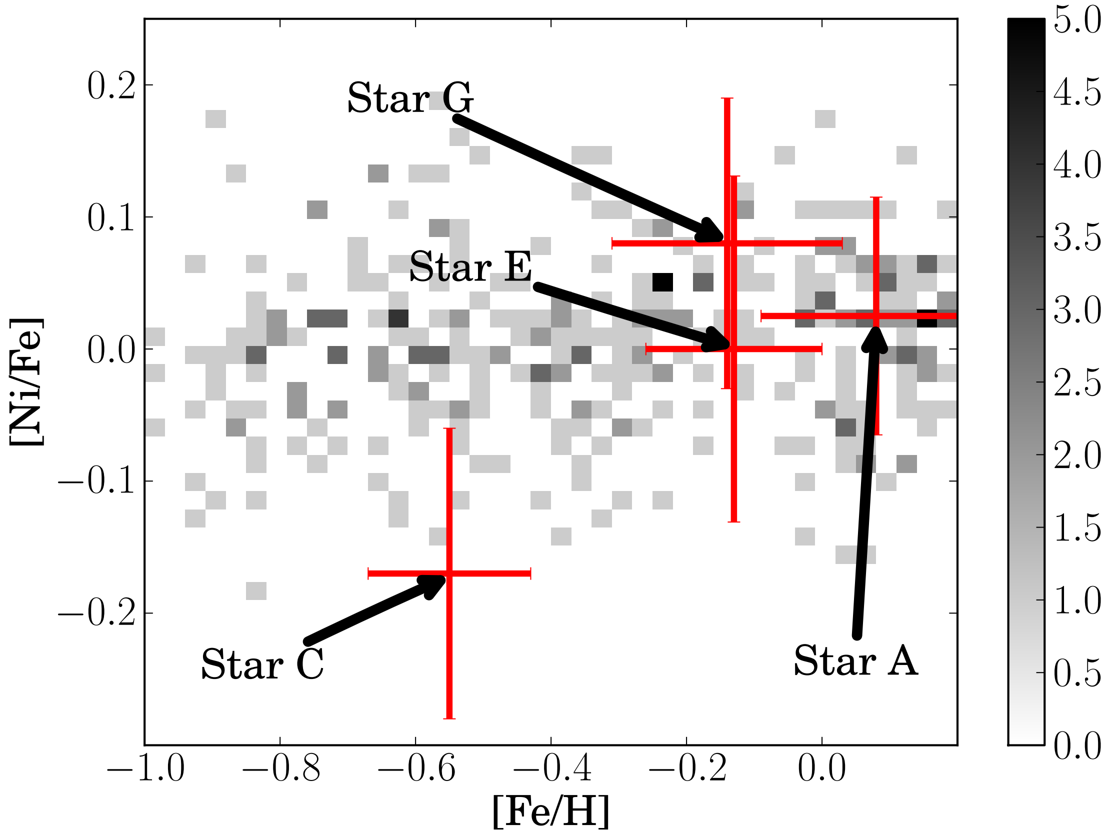

Figure 3.4 Kobayashi et al. (2006) has compared nucleosynthetic models of the Galaxy with a compilation of observed abundances (including Bensby et al., 2003). We use this compilation of observed abundances as a comparison to our candidate stars and show the distribution as the underlying gray shades. We have plotted the candidate abundances with error bars in red. All of the measured candidates are consistent within the errors with stars of the same metallicity.

This analysis resulted in $T_{\rm eff} = 10000^{+400}_{-200}$ K, $\log g = 3.67$ with slope $\partial \log g/\partial T_{\rm eff} = 0.27/500\,{\rm K}^{-1}$, rotational velocity $v_{\rm rot} \sin i = 171\,{\rm km\,s}^{-1}$ with slope $\partial v_{\rm rot} \sin i/\partial T_{\rm eff} = -41/500\,{\rm km\,s}^{-1}\,{\rm K}^{-1}$. From qualitative analysis this object seems metal poor (e.g. in comparison to stars of similar stellar parameters but solar metallicity), but its high rotation and temperature make it hard to determine this parameter precisely. For the present, we assume [Fe/H] = -1.0 unless otherwise noted.

In addition, using the high-resolution spectrum, we measured the EWs of several lines predicted to be strong in the Vienna Atomic Line Database (VALD; Kupka et al., 2000). The abundances were deduced from the EWs using a model atmosphere having T_{eff} = 10000 K, $\log g$ = 3.67 and [Fe/H] = -1.0 (see Table 3.6).

One caveat regarding these abundances is the use of EWs from single lines with large rotational broadening, since the effect of blending with nearby weak lines cannot be taken into account. A second is that these abundances invariably rely on the strongest lines, which are precisely those most susceptible to departures from LTE. Nevertheless, they do confirm the earlier impression that the star is metal-poor, and justify the adoption of [Fe/H]=-1.0 ± 0.4.

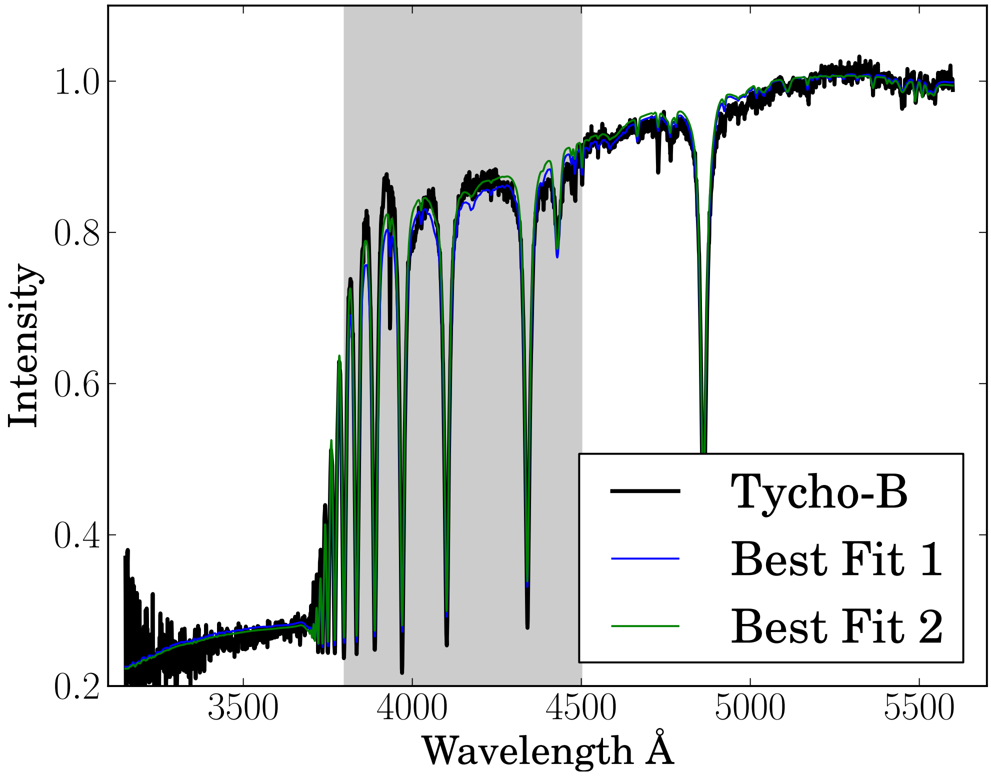

Figure 3.5 The plot shows the normalised spectrum of Tycho-B with the fit which excluded the spectral region between 3800–4500 Å(Best Fit 1) and the fit with the problematic region (Best Fit 2). The region is marked with a grey shade.

As a second approach to determine the stellar parameters of Tycho-B we used the low resolution spectra observed with LRIS. The observation range of LRIS was chosen to be centred around the Balmer jump as this feature is sensitive to the surface gravity (Bessell, 2007). We fitted the spectra to a grid of model spectra (Munari et al., 2005) using a spectrum fitting tool described below. The final grid we used covered $\log g$ from 3.5 to 4.5 in steps of 0.5 and effective temperature from 9000 to 12000 K in steps of 500 K. In addition we expanded the grid by reddening the spectra with the PYSYNPHOT[1] package. We also added diffuse interstellar bands (Beals & Blanchet, 1937; Herbig, 1966, 1967, 1975, 1995; Hibbins et al., 1994; Jenniskens & Desert, 1994; Wilson, 1958) to the synthetic spectra which were scaled with reddening. The included E(B-V) ranged from 0.5 to 1.3 in steps of 0.2. We assumed a rotation of 171 km s^{-1} in the grid (see section 3.3.3).

We used χ^2 as a figure of merit in our fitting procedure. To find the best fit for Tycho-B we used the MIGRAD algorithm provided by MINUIT and linearly interpolated between the grid points using LINEARNDINTERPOLATOR provided by the SCIPY package (see Appendix A for a more detailed description of the interpolation process). The fit of Tycho-B results in $T_{\rm eff}$=10570 K, $\log g$=4.05, [Fe/H]=-1.1 and E(B-V)=0.85. The model fits the synthetic spectrum poorly in the wavelength region between 3800 – 4280 Å in (see Figure 3.5). The adopted mixing length parameter used in 1D model atmospheres, used to construct the

[1]pysynphot is a product of the Space Telescope Science Institute, which is operated by AURA for NASA.

spectral grid, influences the fluxes in that region as well as affecting the hydrogen line profiles. Heiter et al. (2002) and others show that a mixing length of 0.5, rather than 1.25 as used in the Kurucz/Munari grid, better fits the violet fluxes and the hydrogen line profiles. Spectra using a mixing length parameter of 0.5 are brighter in the UV and the H_γ, H_δ and H_β profiles give the same effective temperature as the Hα profiles. We have chosen, however, to fit the spectrum and ignore the problematic spectral region (3800 – 4280 Å) to avoid a systematic error. This yields $T_{\rm eff}$ = 10722 K, log g = 4.13,[Fe/H] = −1.1 and E(B-V)=0.86. The differences are indicative of the size of systematic errors in the model fits. We adopt the fit excluding the problematic wavelength region in the further analysis. Exploring the complex search space we estimate the error to be $\Delta T_{\rm eff}$ = 200 K, Δlog g=0.3 and Δ[Fe/H]=0.5, and note that the parameters are correlated.

3.3.5. Distances

To measure the distance to the candidate stars we used colours and absolute magnitude from isochrones by Pietrinferni et al. (2004). We used the MIGRAD algorithm (James & Roos, 1975) to find close matches of the measured values to $T_{\rm eff}$-log g isochrones by varying the age of the isochrone. Subsequently we calculate E(B-V) using the isochrone's colour and we extract a mass from the isochrone. The results can be seen in Table 3.7. To estimate the errors in all distance, reddening and mass we employed the *Monte Carlo* (MC) method with 10,000 samples of effective temperature , surface gravity, metallicity, B- and V-magnitude (see Figure 3.6). Errors included in Table 3.7 are the standard deviations of the Monte-Carlo sample. The data shows that all stars are compatible with the distance of the remnant. This is not unexpected as the uncertainties of the measurements in stellar parameters are relatively large.

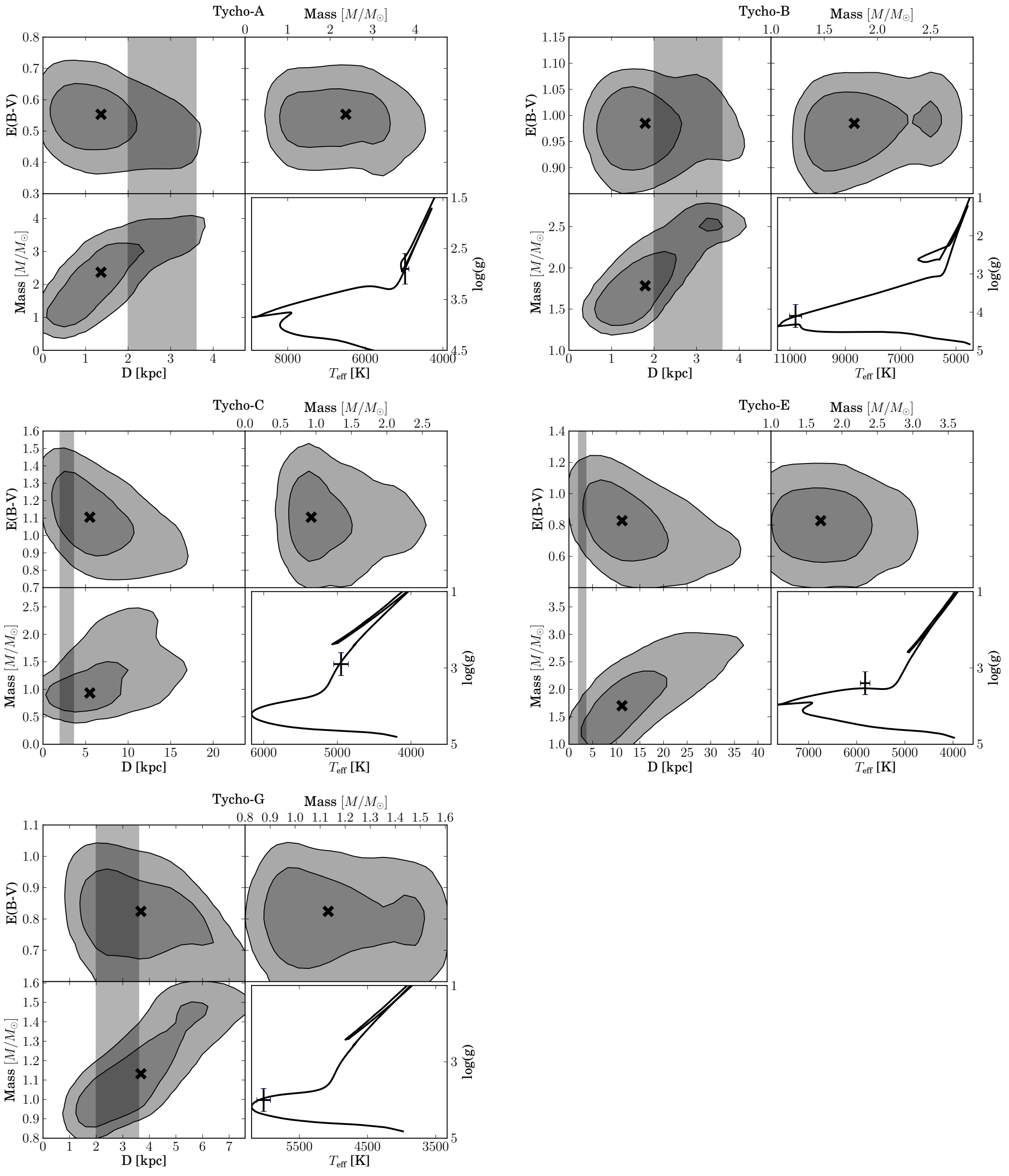

Figure 3.6 The figures show error contours for distance, extinction and mass of the candidates ($1-\sigma$ and $2-\sigma$). The gray shade in the distance plots indicates the distance range to SNR 1572. The lower right shows the optimal isochrone (Pietrinferni et al., 2004) for the measured values of effective temperature and surface gravity .

Table 3.4 Measured EWs from the Keck HIRES spectra

λ (Å)	χ (eV)	$\log gf$ (dex)	Source[a]	Tycho-A (dex)	Tycho-G (dex)	Tycho-C (dex)	Tycho-E (dex)
5082.35	3.658	-0.59	Reddy03	6.31	6.44		6.2
5088.54	3.85	-1.04	Reddy03	6.19	6.33		
5088.96	3.68	-1.24	Reddy03	6.21			
5094.42	3.83	-1.07	Reddy03	6.1			
5115.4	3.834	-0.28	Reddy03	6.22			
5682.20	4.10	-0.47	RC02	6.34			
5748.351	1.68	-3.26	RC02	6.33		5.74	
5749.297	3.94	-1.99	RC02	6.38			
5847.01	1.676	-3.41	Reddy03	6.26		5.55	
6007.31	1.68	-3.34	RC02	6.2		5.45	
6053.685	4.23	-1.07	RC02	6.33			
6086.28	4.26	-0.52	RC02	6.25	6.22		
6108.116	1.68	-2.44	RC02	6.26	6.11	5.33	
6111.08	4.088	-0.81	Reddy03	6.33		5.38	
6130.14	4.266	-0.94	Reddy03	6.31			
6175.37	4.089	-0.55	Reddy03	6.25	6.35	5.7	
6176.82	4.09	-0.26	Reddy03	6.3	6.27	5.43	6.01
6177.25	1.83	-3.51	Reddy03	6.23			
6186.71	4.10	-0.97	RC02	6.33	6.23		
6204.61	4.09	-1.11	Reddy03	6.32			
6322.17	4.15	-1.17	RC02	6.31			
6370.346	3.54	-1.94	RC02	6.37			
6378.26	4.154	-0.83	Reddy03	6.3		5.81	
6482.80	1.93	-2.63	RC02	6.2		5.38	
6598.60	4.23	-0.98	RC02	6.3		5.74	
6635.12	4.42	-0.83	RC02	6.37			
6643.64	1.68	-2.03	Reddy03	6.48	6.02	5.34	5.97
6767.772	1.83	-2.17	RC02	6.35	6.19	5.67	
6772.32	3.658	-0.97	Reddy03	6.31			
6842.037	3.66	-1.47	RC02	6.4	6.36		
7030.011	3.54	-1.73	RC02	6.42			
7122.197	3.54	0.048	RC02	6.33		5.34	
7261.918	1.95	-2.7	RC02		6.26		
7327.648	3.8	-1.77	RC02	6.38	6.44		
7409.35	3.8	-0.1	RC02			5.24	
7414.502	1.99	-2.57	RC02		6.2	5.57	6.03
7422.275	3.63	-0.129	RC02	6.47		5.32	5.84
7574.048	3.83	-0.58	RC02	6.3	5.97	5.12	
7748.89	3.7	-0.38	Reddy03	6.42	6.17	5.41	6.27
7788.93	1.95	-2.42	RC02			5.87	6.33
7797.59	3.9	-0.35	Reddy03	6.41	6.16	5.59	6.2
7917.44	3.74	-1.5	RC02		6.14		

[a] Reddy et al. (2003) abbrv. as Reddy03; Ramírez & Cohen (2002) abbrv. as RC02

Table 3.5 Stellar Parameters

Name designation	$T_{\mathrm{eff}}{}^{a}$ (K)	$\log g^{b}$ (dex)	[Fe/H] (dex)	Δ[Fe/H] (dex)	[Ni/H] (dex)	Δ[Ni/H] (dex)	[Li/H] (dex)
Tycho-A	4975	2.9	0.02	0.16	0.025	0.1	0.09
Tycho-C	4950	2.9	-0.57	0.23	-0.17	0.14	0.11
Tycho-E	5825	3.4	-0.16	0.21	0.0	0.2	0.131
Tycho-G	6025	4	-0.15	0.18	0.08	0.14	0.11

[a] $\sigma_{T_{\mathrm{eff}}} \approx 100$ K
[b] $\sigma_{\log g} \approx 0.3$ dex

Table 3.6 Tycho-B abundances

Ion designation	λ Å	W_λ Å	ϵ dex	$[X/H]$ dex	$\frac{\partial \epsilon}{\partial \log g}$	$\frac{\partial \epsilon}{\partial T_{\mathrm{eff}}}$ K⁻1
Mg II	4481.13+4481.33	220 ± 15	6.18 ± .08	-1.40	0.08	8×10^{-5}
Si II	6347.1	140 ± 5	6.96 ± .18	-0.59	-0.02	1×10^{-4}
O I	7771.9+7774.2+7775.4	460 ± 30	8.43 ± .10	-0.58	0.24	-4×10^{-5}

Table 3.7 Distances, Ages and Masses of candidate stars

Name designation	Mass $M/M_\odot$	σ_{Mass} $M/M_\odot$	Age Gyr	σ_{Age} Gyr	Distance kpc	$\sigma_{\mathrm{Distance}}$ kpc
Tycho-A	2.4	0.8	0.7	2.3	1.4	0.8
Tycho-B	1.8	0.4	0.8	0.3	1.8	0.8
Tycho-C	0.9	0.4	10.0	3.4	5.5	3.5
Tycho-E	1.7	0.4	1.4	1.1	11.2	7.5
Tycho-G	1.1	0.2	5.7	2.1	3.7	1.5

3.4. Discussion

In our sample of six stars we find no star that shows characteristics which strongly indicate that it might be the donor star of SN 1572. On the other hand, it is difficult to absolutely rule out any star, if one is able to invoke improbable post-explosion evolutionary scenarios.

Tycho-A is a metal rich giant. It seems to be likely that Tycho-A is a foreground star. Its principal redeeming feature as a donor star candidate is that it is located in the geometric centre of the remnant, and that it has a relatively low gravity. Tycho-A shows a very low spatial motion which is consistent with a giant donor star scenario, although its lack of rotation is in conflict with a donor star scenario. Taking all measurements into account we regard Tycho-A to be a very weak candidate.

Tycho-B's high temperature, position at the centre of the remnant, high rotational velocity and unusual chemical abundance made it the most unusual candidate in the remnant's centre. Despite the a posteriori unlikely discovery of such a star in the remnant's centre, Tycho-B's high rotational velocity coupled with its low spatial velocity, seem to be in conflict with any viable donor star scenario. These scenarios predict that the donor star will tidally couple to the white dwarf star before explosion, causing the rotation and spatial motion to be correlated post explosion (as discussed in WEK09). The large rotation seen in Tycho-B should accompanied by a large spatial motion, which is ruled out by the observations presented here, a problem we are unable to reconcile with Tycho-B being the donor star.

Tycho-C consists of two stars which are only resolved in HST images. It consists of a brighter bluer component and a dimmer redder component (RP04). In our analysis we find a consistent solution for the spectrum and infer that this is from the bluer brighter component. We find that Tycho-C is a metal-poor giant, probably located beyond the remnant. Tycho-C, similar to Tycho-A might be compatible with a giant donor star scenario. It's lack of rotation and kinematics, however, make it an uncompelling candidate.

Tycho-D is roughly ten times dimmer than the close star Tycho-C ($\approx 0.6''$). Our tools to measure stellar abundances are not effective for spectra with a S/N less than 10. A visual inspection of the star's spectral features shows it to be consistent with a cool star with low rotation. It's brightness precludes it being a relatively slowly rotating giant, and its lack of a fast rotation precludes it being a sub giant or main sequence donor star. All of this suggest Tycho-D is an uncompelling donor candidate star.

Tycho-E is the most distant star in this set (11.2 kpc), although large uncertainties in the distance remain. It seems to be similar to Tycho-G in temperature, but appears to have a lower gravity. It is located $7''$ from the geometric centre, but has no unusual stellar parameters or kinematics. Ihara et al. (2007) have looked at iron absorption lines in stellar spectra made by the remnant and found Tycho-E to be unusual. They suggest that a star in the background would show blue and redshifted iron lines, whereas a star inside the remnant would only show blueshifted iron lines, and a foreground star will not show any iron features from the remnant. Ihara et al. (2007) suggest that Tycho-E only shows blue-shifted lines and thus is suggested as being in the remnant. We believe however that Tycho-E is located far behind the remnant and suggest that a low column density on the receding side of the remnant could cause a lack of red-shifted iron features. In summary, a lack of rotation, kinematic signatures, and an inconsistent distance make Tycho-E a very weak candidate.

Tycho-G is located 30″ from the X-ray centre which makes it the most remote object to the centre in this work. This work confirms the radial velocity measured by GH09 and WEK09. Figure 3.2 shows the expected distribution of radial velocities from the Bescançon model of Galactic dynamics. Tycho-G lies well within the expect range of radial velocity for stars with its stellar parameters and distance. In addition, this work has analysed the proper motion of stars around the centre of SN 1572. Figure 3.1 shows Tycho-G to have a marginally significant proper-motion measurement. However, these proper motion measurements show other outliers at a rate higher than expect by Galactic models (Besançon), to study this difference we have selected candidates within a 1° radius around SN 1572 from the proper motion catalogue PPMXL (Roeser et al., 2010). To exclude the many foreground stars we have introduced the additional selection criteria $R > 16$ and $V - R < 1$ (the sun has a colour of $V - R = 1.3$). Using these same selection criteria on the Besançon Model resulted in 95% of stars more distant than 2 kpc. This set shows stars with similarly high proper motions like Tycho-G are relatively common - it is not unexpected to have a star with Tycho-G's motion inside the remnant's centre (see Figure 3.7). We conclude that the Besançon Model, although a good rough estimate, does not provide a detailed overview of proper motion space, and it is more appropriate to compare to the PPMXL catalog. Finally, the HST proper motion measurements are challenging, and there might be systematic errors in our proper motion measurements which are larger than our reported statistical errors. The errors tend to increase the chance of larger than actual proper motion measurements. Taken in total, while Tycho-G may have an unusual proper motion, the significance of this motion, even if current measurements are exactly correct, is not exceptional. As described, the kinematic features of a donor star might easily be lost in the kinematic noise of the Galaxy. WEK09, however, suggested using post-explosion stellar rotation as a possible feature for a donor star. This work suggests that Tycho-G has a rotation below the instrumental profile of 6 km s^{-1}.

We find Tycho-G to be a subgiant/main sequence star with roughly solar temperature and metallicity. GH09 measure a slight nickel enhancement, which they believe to originate in the contamination from the ejecta. Figure 3.4 compares our measurement of Tycho-G to the distribution of nickel (see Figure 3.4) and we find it to be consistent. In addition, we could not measure a significantly enhanced lithium-abundance as suggested in GH09. Finally, we have measured the distance to Tycho-G and find that most likely Tycho-G lies behind the remnant, although the range of uncertainties includes the remnant distance.

In summary, Tycho-G may have unusual kinematics as indicated by its proper motion, the significance of this motion is not large when compared to a large sample of similar stars in the direction of the Tycho remnant. Furthermore, such a kinematic signature, if it were related to the binary orbital velocity, predicts rotation for Tycho-G which we do not observe (modulo the weak caveats from WEK09). Furthermore, we have not found a reasonable explanation for Tycho-G's large distance to the geometric centre, and suggest that Tycho-G is unlikely to be related to the Tycho SNR.

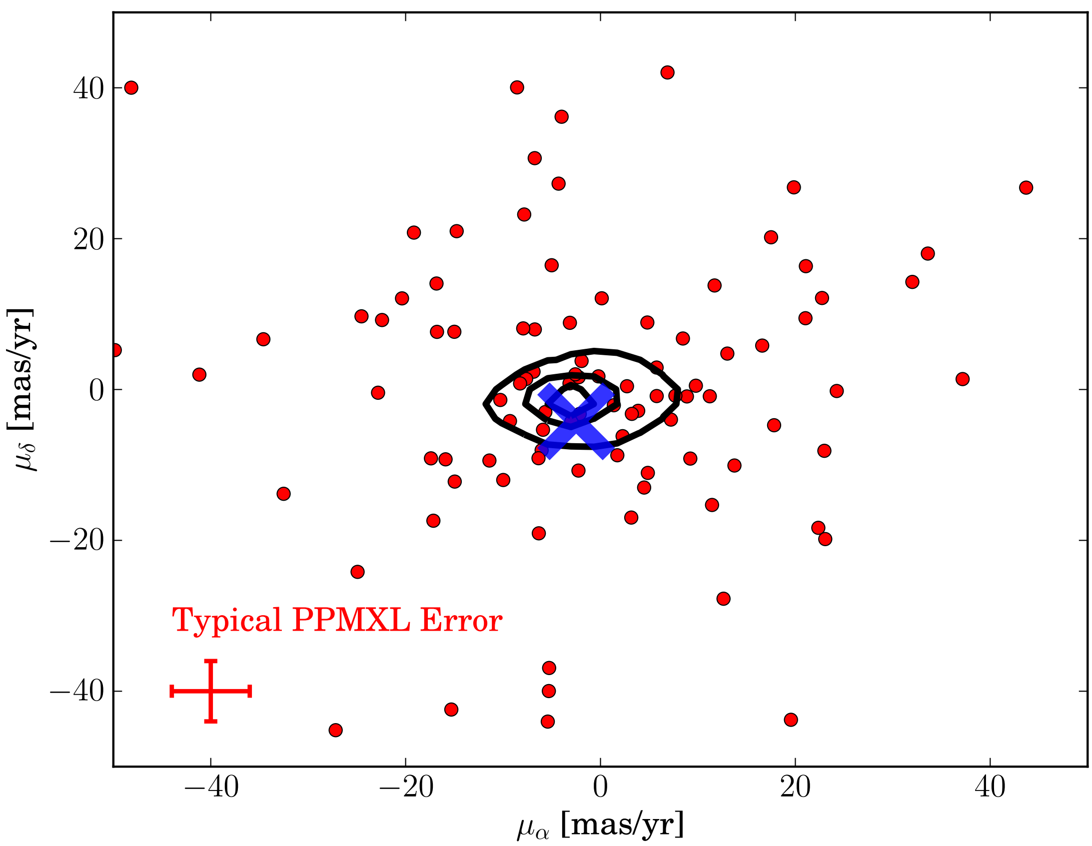

Figure 3.7 The red points are PPMXL stars within 1°of SN 1572. Tycho-G has been marked with a blue cross. In addition, we show the distribution for the Besançon Model with an area of 1 square degree (a third of the search area of the PPMXL sample) around the remnant and a distance between 2.2 kpc and 5.2 kpc as the black contours ($1-\sigma$, $2-\sigma$ and $3-\sigma$) The Besançon Model shows, as expected, a much smaller scatter.

3.5. Conclusion

This work did not detect an unambiguously identifiable donor star candidate. Although stars Tycho-B and Tycho-G have unusual features, there remains no convincing explanation for all of their parameters which can be attributed to the donor star scenario. Further theoretical predictions are needed to make a more precise distinction between donors and unrelated stars.

Our observations provide a case that the Tycho SNR does not have a main sequence, sub giant, or red giant donor star, but other possibilities remain. These include a helium donor, such as the so-called sub Chandrasekhar Mass explosions discussed by Livne & Arnett (1995); Sim et al. (2010). These progenitor systems might leave behind a very faint and fast moving helium star, or no remnant at all (priv. comm. Rüdiger Pakmor) . Such a progenitor would probably evade detection, and would likely not leave behind traces, such as circumstellar interaction (CSI) with the remnant, or early light curve anomalies (Kasen, 2010). However, deep multi-epoch wide field optical images should catch any such star speeding away from the remnant centre - these are observation not yet taken. Finally, a double degenerate progenitor, in most cases, does not leave behind a remnant , and is consistent with finding no donor star in SNR 1572.

SN 1006 and SN 1604 (Kepler's SN) are two other SN Ia remnants in the Milky Way. SN 1006 is far from the plane and shows no signs of CSI. SNR 1604 while far from the galaxy plane, shows CSI with its remnant, and has all the indications of what might be expected from a SD-Scenario with an AGB donor (Chiotellis et al., 2011). Observations of these remnant will better establish if there is a continued pattern to the unusual stars in SN Ia remnant centres, or whether the lack of viable donor stars persists in multiple systems.

CHAPTER 4

Progenitor search in SN 1006

4.1. Introduction

The search for a donor star in SN 1572 has not turned up an obvious candidate. However, we have detected two objects (Tycho-B and Tycho-G) exhibiting some unusual properties, which while interesting, ultimately seem inconsistent with the expectations of any viable donor star scenario. Donor star scenarios are theoretical in their nature and any actual donor star is likely to not exhibit all features predicted by the model. Therefore, we have reached an impasse with SN 1572 and more detailed observations will likely not provide a definitive answer if either of these two stars were involved in the progenitor system. An obvious way forward is to scrutinise stars in other SN Ia remnants and see if any of those have similar properties to Tycho-B or Tycho-G. The remnant of SN 1006 is the ideal object for this kind of follow-up search.

The lack of a central neutron star, observation of several tenths of a solar mass of iron inside the remnant (Hamilton et al., 1997) and the high peak luminosity and basic light curve shape (visible for several years Goldstein & Peng Yoke, 1965) all indicate that SN 1006 was a SN Ia. The remnant has a secure distance, measured by Winkler et al. (2003), who combined the proper motion and the radial velocity of the expanding shell to measure the distance to 2.2 kpc, making SN 1006 the closest of the ancient SN Ia remnants (consistent SN 1006 being the brightest). The geometric centre of the remnant is well determined from both X-ray and radio observations (Winkler et al., 2003). In addition, the interior of the remnant has been probed with UV background sources (Winkler et al., 2005).

This revealed the aforementioned iron core as well as a silicon-rich shell. The remnant has been searched for possible objects associated with the supernova explosion previously, and an unusual O-star had been identified as a possible donor star to SN 1006. This unusual O-Star was identified near the centre of SN 1006 by Schweizer & Middleditch (1980) and is now called Schweizer-Middleditch Star (SM-Star). After successful identifications of neutron stars in both the Vela Remnant and the Crab Remnant this was thought to be the third identification of a stellar remnant in a historical supernova. Subsequent UV spectroscopic follow-up of the SM-Star by Wu et al. (1983), showed strong Fe II lines with a profile broadened by a few thousand km s^{-1}. In addition, Wu et al. (1983) identified redshifted Si ii, Si iii and Si iv lines. Their conclusion was that these absorption lines stem from the remnant and place the SM-Star behind the remnant, making it unrelated to SN 1006. Although unrelated, the SM-Star is an ideal object to probe the remnant and measure upper limits for interstellar extinction (E(B-V) = 0.1 Wu et al., 1993; Winkler et al., 2003).

SN 1006 has several properties which make it well suited to undertake a progenitor search. Although the remnant is the oldest among the known SN Ia remnants, its age is still young enough that the remnant's centre is well determined, and the motion of any potential donor star low enough that only a small area of stars need to be searched. Furthermore, this elapse of 1005 years is a short length of time relative to the timescales of stellar evolution for donor stars (see Marietta et al., 2000) - we still expect a potential donor star to be close to the same state as directly after the supernova explosion. In addition, SN 1006 has a low interstellar extinction, which eases the determination of stellar parameters. These serendipitous conditions for the SN 1006 remnant led us to launch a photometric and spectroscopic campaign to search for the donor star. Our photometric observations were taken at Siding Spring Observatory with the 2.3m Telescope imager. The spectroscopic observations were undertaken with the high resolution multi-object spectrograph FLAMES attached to the Very Large Telescope (VLT).

In Section 4.2 we outline the observations as well as data reduction of the photometric and spectroscopic data. Section 4.3 is split into four subsections, namely radial velocity, stellar rotation and stellar parameters. We conclude this chapter in Section 4.4 and discuss the possible implications of our initial find as well as outlining some future work.

4.2. Observations and Data Reduction

4.2.1. Photometric Observations

CCD images of SN 1006 were obtained using the imaging camera at the Nasmyth-B focus of the ANU 2.3 m Telescope at the Siding Spring Observatory, on 11 May 2004. We exposed for 1860 s in U-Band, 1490 s in B-Band, 788 s in V-Band and 1860 s in I-Band. For calibration purposes we took images of the PG1633 and PG1047 standard star regions in the same filters. The seeing ranged between 1″and 2″, and the conditions were photometric. The data were bias corrected and flatfielded (using skyflats) using PyRAF [1].

For our photometric data reduction we fitted an astrometric solution using astrometry from the 2MASS point source catalogue (Skrutskie et al., 2006) to our frames. We used SExtractor (Bertin & Arnouts, 1996) to measure the magnitudes of the objects in the frames and then calibrated our photometry to a standard Bessell Filter system using the Stetson magnitudes [2] of our standard fields PG1633 and PG1047 .

The measured magnitudes were supplemented with near infrared magnitudes from the 2MASS point source catalogue (see Table C.2 and C.1). Subsequently we checked the photometric measurements, by plotting the obtained $B-V$ colours against the $V-K$ colours (see Figure 4.1).

[1]PyRAF is a product of the Space Telescope Science Institute, which is operated by AURA for NASA.
[2]This research used the facilities of the Canadian Astronomy Data Centre operated by the National Research

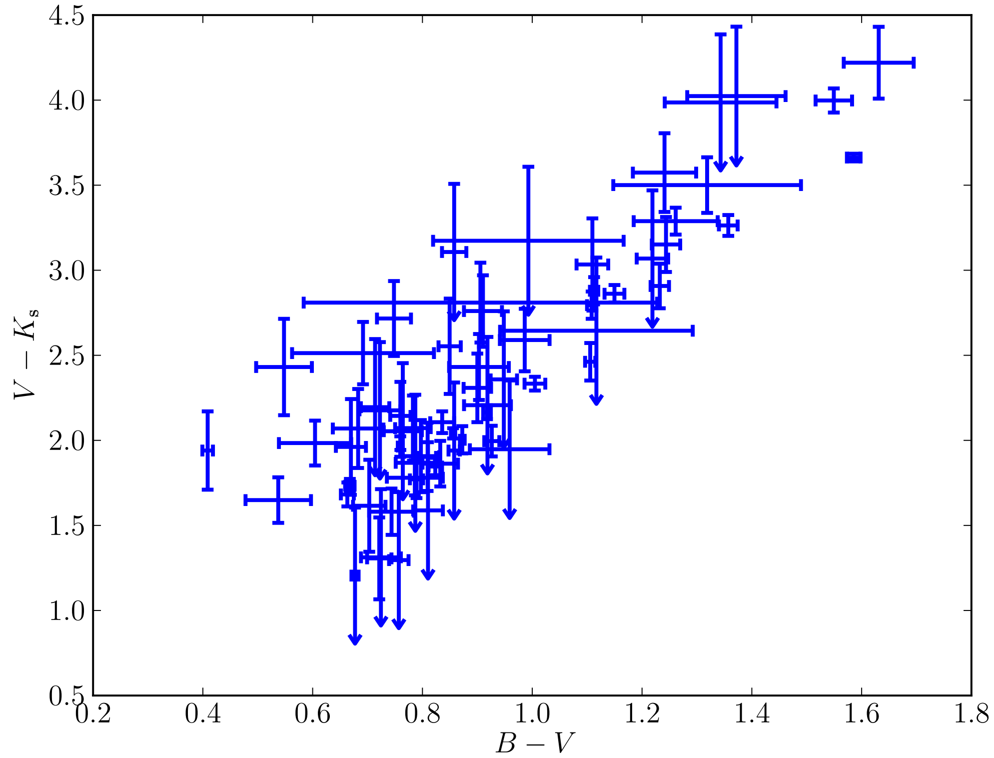

Figure 4.1 Colour-colour plot of all candidates in SN 1006 to check photometry. The correspondence is as expected given the uncertainties in the measurements.

We have also computed temperatures from photometric colours by using the polynomials given in Casagrande et al. (2010). In the first instance, we assumed a solar metallicity for all stars, but the choice of metallicity only has a minor influence on the temperature calculation (e.g. change of 300K between [Fe/H]=0 and [Fe/H]=-1) for the temperature. In addition, the temperature polynomial coefficients incorporating the metallicity are particularly small for the $V-K$ colour. All temperatures are listed in the optical photometry Table C.1 and infrared photometry Table C.2.

4.2.2. Spectroscopic Observations

For the spectroscopy survey we used the VLT instrument FLAMES, which can provide high resolution (R=25,000) optical spectra over a 25′ field of view for up to 130 objects. In this mode, the spectral coverage is limited to 200 Å, and we chose the wavelength region from 5139 Å to 5356 Å which contains the gravity sensitive Mg I b Triplet as well as many iron lines to accurately measure metallicity. For the centre of our spectroscopic survey we chose the mean of the X-ray and radio centre ($\alpha = 15^h02^m22\overset{s}{.}1$ $\delta = -42°05'49''$; Winkler et al., 2003). We chose a search radius of 120″ - corresponding to the motion of a star travelling 1250 km s^{-1}at 2.2 kpc over 1000 years. This generous choice, which is

Council of Canada with the support of the Canadian Space Agency

Table 4.1 Flames Observations of SN1006 program stars

ObsID -	MJD d	FWHM $''$	Airmass -	Setup name -	v_{helio} correction km s^{-1}
360737	54965.1	1.2	1.2	SN1006 1	1.5
360739	54965.1	1.2	1.1	SN1006 1	1.5
360740	54965.1	1.0	1.1	SN1006 1	1.4
360741	54985.0	0.7	1.4	SN1006 1	-7.4
360742	54964.2	1.5	1.1	SN1006 1	1.7
360743	54985.0	0.8	1.2	SN1006 2	-7.5
360745	54985.0	0.9	1.1	SN1006 2	-7.6
360746	54985.1	1.0	1.1	SN1006 2	-7.7
360747	54985.1	1.0	1.1	SN1006 2	-7.7
360748	54985.2	0.9	1.1	SN1006 2	-7.8
360749	54963.1	1.2	1.2	SN1006 3	2.4
360751	54963.1	1.1	1.1	SN1006 3	2.3
360752	54963.2	1.1	1.1	SN1006 3	2.3

more than four times our maximum expected escape velocity (see Figure 1.17 on page 30), was made to accommodate any errors in the choice of the centre. Although the models predict the surviving companion to be several hundred $L_{\odot}$ (Marietta et al., 2000), we chose a limiting magnitude of $V = 17.5$ ($0.5\ L_{\odot}(V)$ at 2.2 kpc including extinction of E(B-V)=0.1) to accommodate a wide range of potential donor stars. An exposure time of 3.8 hours was chosen to obtain spectra with high enough quality to measure rotation and basic stellar parameters (S/N ratio > 20). For completeness and to not waste fibres we chose additional stars down to a magnitude limit of $V = 19$, which are only used for radial velocity measurements. These constraints yielded 26 stars with $V < 17.5$ mag and 53 stars in the bin between $17.5 < V < 19$ mag (for a total of 79 stars) for our survey (see Figure 4.2). With fibre buttons not being able to be placed less than 11″ apart, we had to split our candidates over three different setups. The first two setups were observed five times with 2775 seconds each. We deliberately chose bright stars for the last setup so that it only had to be observed three times with 2775 s each. In addition, we placed spare fibres on three bright stars (R≈ 10; 2MASS J15032744-4204463, 2MASS J15031746-4204165, 2MASS J15033195-4202356) located close to the edge of the 25′ field of view for calibration purposes. Additional spare fibres were placed on sky positions, which were chosen to be far from 2MASS sources and manually inspected on DSS images to be in star free regions. In addition, to our night time calibration, which included simultaneous arc exposures with four fibres for each observation block, we received standard daytime calibrations. In total, 13 observation blocks with an exposure time of 2775 seconds each were obtained. Table 4.1 provides the Observing ID, modified julian date, mean seeing, mean airmass, setup name and heliocentric correction for all observations (all data is available under ESO Program ID: 083.D-0805(A)). Due to broken fibres, not all stars where observed for the expected length of time. Broken fibres caused SN1006-31 not to be observed at all in this project (see Figure 4.3) - although a $V = 17.87$ mag is not part of our primary sample.

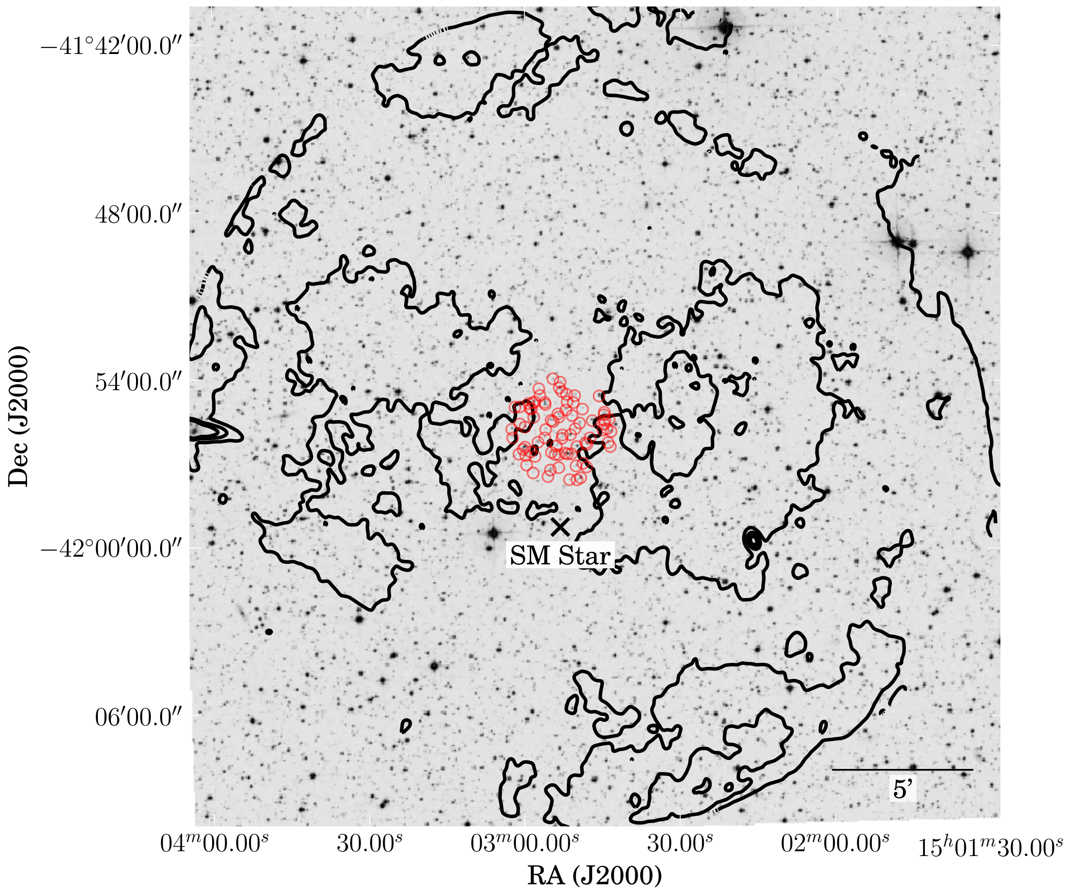

Figure 4.2 Optical DSS image with radio contour overlay (VLA). The black circles in the centre show the 79 program stars. Additionally we have marked the ‘spurious‘ donor the SM-Star.

We first applied a cosmic ray removal tool on the raw 2D frames (van Dokkum, 2001). The data was then reduced with the ESO-CPL pipeline (version 5.2.0), using the GIRAFFE instrument recipes (version 2.8.9). The only variation that was made to the default parameters was the usage of the Horne extraction algorithm instead of the "Optimal"-extraction algorithm. This yielded 366 individual spectra of the candidate stars and an additional 39 calibration star spectra.

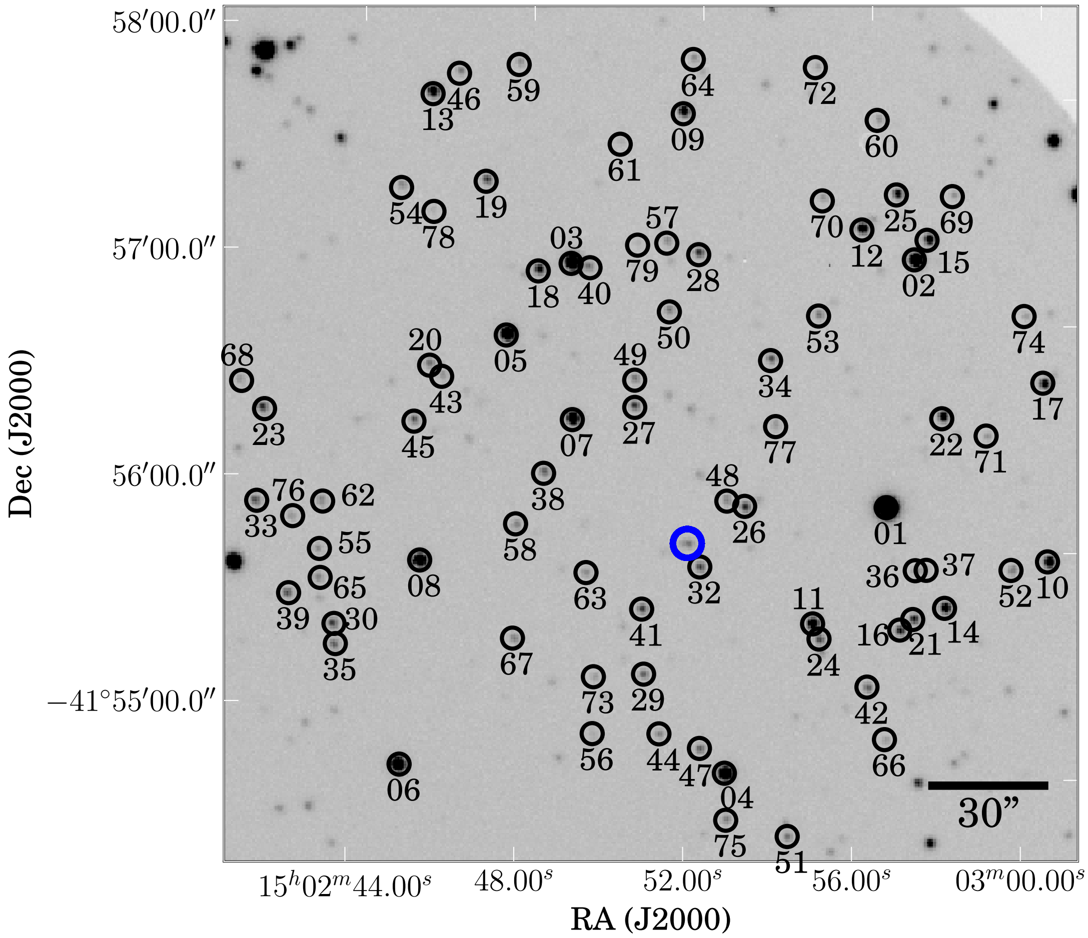

Figure 4.3 V-Band image taken by the 2.3 m Telescope. We have marked SN1006-31, which was not observed due to broken fibres, with a blue circle. With the a brightness of V = 17.87 SN1006-31 is fainter than our primary catalog (V < 17.5 mag), and is the only star which lacks a spectrum to V = 19 mag in the remnant's centre.

4.3. Analysis

4.3.1. Radial Velocity

To obtain radial velocities we employ a two step process. We used a solar spectrum from Kurucz et al. (1984) with the standard cross-correlation technique described in Tonry & Davis (1979) and implemented in the PyRAF task fxcor. The cross-correlation was performed on each individual spectrum. The results were then heliocentrically corrected, and then averaged for each star with a sigma clipping algorithm (see Table C.3). We note that especially for faint objects we observe a second cross-correlation peak at 0 km s^{-1}and believe that this is reflected sun light from the moon. We believe that this has a negligible effect on our radial velocity measurement. In Figure 4.4 we have compared our radial velocity measurements with the Besançon kinematic model of the Milky way (Robin et al.,

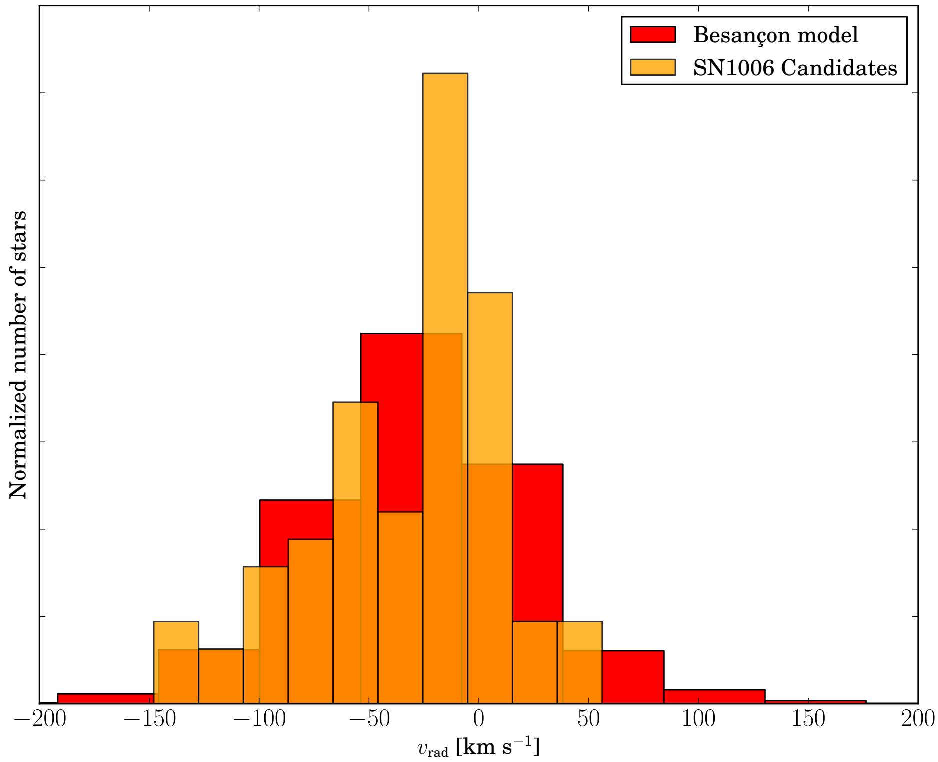

Figure 4.4 Comparison of all candidate stars with the distribution of stars taken from the the Besançon kinematic model. The model input parameters were a search area of 1 square degree around the centre of SN 1006 and a magnitude limit of 10 < V < 17.5

2003). Our selection criteria for creating the Besançon kinematic model was all stars within 1 square degree of SN 1006 and a magnitude cut of $10 < V < 17.5$. We compared the resulting 10000 stars to our 78 stars in the sample in Figure 4.4.

4.3.2. Rotational Velocity

Due to the direction looked through the Galaxy, there is a large velocity spread in the direction of SN 1006 (see Figure 4.4) making it hard to isolate a donor star based just on kinematic features. A distinguishing feature for a donor star should be rotation (discussed in Chapter 2), especially if the donor star isn't a giant. The rotational velocities in Chapters 2 & 3 were all measured manually. In these previous measurements we selected weak iron lines and stacked them to obtain a line profile, which was compared to synthetically rotationally broadened lines. This was a feasible way for six spectra, it is however not feasible for more than 200 spectra.

Measuring repetitive structures like line profiles is much more straight forward in Fourier space. The intrinsic spectrum ($f_{\rm spectrum}$) of a star is broadened by a convolution of the intrinsic spectrum with a rotational broadening kernel ($g_{\rm rotation}$). The next broadening is introduced by the instrument (instrumental kernel $h_{\rm instrument}$) before being recorded on the detector. Assuming an unbroadened synthetic spectrum ($f_{\mathrm{synthetic}}$), matching the intrinsic stellar spectrum, we can describe a convolution in Fourier space as,

$$
\begin{aligned}
f_{\mathrm{observed}} =& f_{\mathrm{spectrum}} \otimes \underbrace{g_{\mathrm{rotation}} \otimes h_{\mathrm{instrument}}}_{f_{\mathrm{profile}}} \\
F(f_{\mathrm{spectrum}} \otimes g_{\mathrm{rotation}} \otimes h_{\mathrm{instrument}}) =& F(f_{\mathrm{spectrum}}) \times F(g_{\mathrm{rotation}}) \times F(h_{\mathrm{instrument}}) \\
\Rightarrow \frac{F(f_{\mathrm{observed}})}{F(f_{\mathrm{synthetic}})} \approx& F(f_{\mathrm{profile}}),
\end{aligned}
$$

where F denotes the Fourier transform. This yields the line profile which we can separate, knowing the resolution of the instrument, into an instrumental profile and a rotational kernel . This technique has been described by a selection of authors (e.g. Gray, 1977). FXCOR uses this technique to measure radial velocities from shift of the profile peak relative to rest. We have applied this technique successfully to extract the rotation for some of the stars were the quality of the spectra was adequate (see Table C.3).

4.3.3. Stellar Parameters

We obtained detailed stellar parameters for the donor candidates with $V < 17.5$ by employing a grid based technique (three dimensional grid in T_{eff}, $\log g$ and [Fe/H]). MOOG was used to synthesise the spectral grid using the model stellar atmospheres by Castelli & Kurucz (2003). Line wings were taken into account up to 8 Å away from line centre, which seemed to be a reasonable compromise between grid creation time and accuracy. For the atomic lines we merged values from the VALD with adjusted values (to reproduce the Arcturus and the Sun) from Gustafsson et al. (2008). In addition, we used the measured molecular lines described in Kurucz & Bell (1995). The final grid extends from 3500 K to 7500 K in effective temperature with a step size of 250 K, in surface gravity it ranges from 0 to 5 with a stepsize of 0.5 and in [Fe/H] it ranges from -2.5 to 0.5 with a stepsize of 0.5 (with an extra set of points at 0.2).

We used the appropriate sections from the Solar spectrum (Kurucz et al., 1984) and the Arcturus spectrum (Hinkle et al., 2000) to calibrate our spectral grid. We measured stellar parameters by first finding the best fitting grid point and then using the minimizer MINUIT to find a minimum by interpolating between the gridpoints (described in Appendix A of this thesis; Barber et al., 1996). For the Sun we obtain stellar parameters of T_{eff}=5825 K, $\log g$=4.4 and [Fe/H]=-0.12 and for Arcturus we obtain stellar parameters of T_{eff}=4336 K, $\log g$=1.9, [Fe/H]=-0.67. We acknowledge the discrepancy between our measured values and the canonical values for the sun and arcturus, but believe our spectral grid to be accurate enough for distinguishing a potential donor candidate against an unrelated star.

To measure our observed spectra we first fitted the continuum with Legendre polynomials with a maximum order of 3 and a sigma clipping algorithm discarding the lines. The order that gave the lowest RMS of the fit was used. We then combined the spectra using the previously measured radial velocity and the computed heliocentric correction. In addition, we broadened the synthetic spectral grid with a rotational kernel for each star where applicable. These spectra were then fitted using the previously described algorithm, except that we added the $B-V$ photometric temperature as a prior. As the photometric

Table 4.2 SN 1006 candidates (V < 17.5) stellar parameters

Name	T_{eff} K	$\log g$ dex	[Fe/H] dex	V mag	v_{rot} km s^{-1}
01	4285	2.0	−1.0	13.50	< 10
02	4001	0.8	−1.4	15.37	< 10
03	5446	4.0	−0.6	15.04	< 10
04	5347	4.0	−0.6	15.47	< 10
05	5191	3.7	−0.6	15.50	< 10
06	5874	4.5	−0.7	15.50	< 10
07	4884	4.2	−0.8	15.90	< 10
08	5954	4.2	−0.5	15.86	< 10
09	4217	3.9	−2.5	16.58	< 10
10	5662	4.3	−0.8	16.30	10
11	5489	4.1	−0.8	16.33	< 10
12	5313	4.4	−0.9	16.39	16
13	5114	4.0	−0.7	16.49	< 10
14	5245	4.3	−0.7	16.56	< 10
15	5503	4.2	−0.7	16.63	< 10
16	4448	4.0	−1.8	17.26	14
17	5515	4.4	−1.2	16.66	< 10
18	5341	4.1	−0.9	16.77	12
19	3846	4.1	−2.4	17.39	17
21	4510	3.1	−1.3	17.36	13
22	6448	4.2	−0.4	16.71	13
23	4429	4.0	−1.8	17.39	14
25	6119	4.9	−0.7	17.03	< 10
26	5619	4.0	−1.1	17.23	< 10
27	5336	4.0	−1.3	17.47	< 10
28	5379	4.3	−1.1	17.43	< 10

temperature uses the metallicity as an input parameter we recalculated the photometric temperature prior using the metallicity determined by the fit. This procedure was repeated until the gravity estimate converged to less than 0.1 dex. We believe our temperatures to be good to a few hundred K, our surface gravities as well as metallicities have a systematic uncertainty of roughly 0.5 dex.

The stellar parameters can be seen, as fits to the spectra, in Figure C.1 and in tabulated form in Table 4.2. The final set of stellar parameters shows a typical distribution of many dwarfs and a few giants. None of the stars seem to be unusual in any way. Giant stars, which are expected to have relatively low v_{rot} post explosion (but still > 20 km s^{-1}), are absent from the remnant's centre.

4.4. Conclusions

In this work we have scrutinised all stars to a limit of 0.5 $L_{\odot}(V)$ at the distance of the SN 1006 remnant. None of the stars scrutinised in our sample show features consistent with those expected for donor star models.

Giant star progenitors are easily ruled out because there is no star bright enough to be at the distance of the remnant. Marietta et al. (2000) suggests that giant donors have a luminosity of $\approx 1000\, L_{\odot}$ ($V \approx 9$ at the distance of the remnant) for at least 100,000 years. Furthermore, these models suggest that the giant donor is likely to have a high temperature of more than $10^4\, K$. In addition, the star should have some rotation in excess of what has been measured for any of the stars in this sample. In summary, there is no viable giant star donor star scenario for the stars located in SN 1006.

Sub giant donors should also be very luminous (Marietta et al., 2000) with a minimum expected luminosity of $L \approx 500\, L_{\odot}$ ($V \approx 9.7$ at the distance of the remnant) lasting for 1400–11,000 years, although theoretical models allow much more larger scope for variation of this class of stars (Podsiadlowski, 2003). While they might have a radial velocity which could be masked by the large expected dispersion in the direction of SN 1006, the expected $v_{\mathrm{rot}} \approx 80\,\mathrm{km\ s^{-1}}$ (see Figure 1.17 on page 30 and Figure 4.5), far exceeds any star in our sample. Therefore, we believe we can confidently rule out sub giant donor stars in this case as well.

Finally, main sequence stars, according to Marietta et al. (2000) are expected to have a similar brightness to sub giant stars, although this enhanced luminosity depends on the details of how energy is deposited from the explosion (see Podsiadlowski, 2003). However, main sequence donors should have both substantial spatial motion coupled with very high rotation (see Figure 1.17 on page 30 and Figure 4.5). No star shows any of these features in our sample, and our sample's depth should cover all conceivable post-evolutionary scenarios, even for a main sequence donor star.

There are two additional issues worthy of further discussion. Firstly, rotation can be lost due to expansion (see Section 2.3). This, however is a priori unlikely (priv. comm. Chris Tout), and should result in a star with a low gravity, relatively high luminosity (unless it were to become extremely cool). No such star is present in SNR 1006. Secondly, measurements by Winkler et al. (2005, see Figure 4.6) cast doubt on a precise determination of the centre. Their research suggests that the centre of the iron core is offset from the geometric centre determined by the shocked ISM. However, we argue that this does not mean that the centre of mass (where a donor star would reside) is necessarily off centre. In fact, Maeda et al. (2010) suggest that the iron ejecta is offset from the centre of mass, which suggests that the centre of the iron core will be different than the centre of mass. In general, explosion models are consistent with the center of mass being given by the outer shock, not the iron core. In addition, other groups are also currently surveying SN 1006 with a spatially larger but photometrically shallower field (priv. comm. Pilar Ruiz-Lapuente) and have not yet found a viable companion. In summary our research shows a consistent result to SN 1572 - no identifiable donor star.

The observations presented here for SN 1006 are in conflict with the standard SN Ia donor star scenarios, which include accretion onto a white dwarf from a main sequence, sub giant, or giant companion. A few non-standard scenarios survive our observational tests.

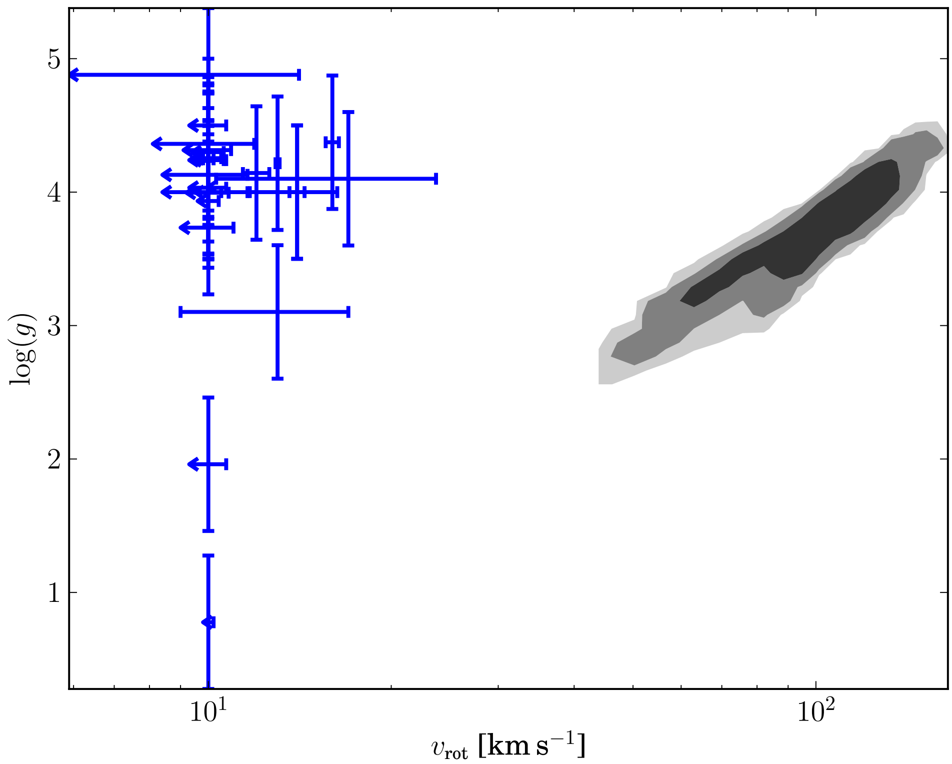

Figure 4.5 Comparison of the evolutionary state and rotational velocity of 55000 binary synthesis SD-Scenario progenitors (gray shades show $1-\sigma$, $2-\sigma$ and $3-\sigma$ contours; data from Han, 2008) with the measured rotation from this work. Due to the resolution of the spectrograph most of these stars only have an upper limit of the rotation speed of $v_{\rm rot} = 10$ km s^{-1}

These include a helium white dwarf as a donor star (see Section 1.5.2), which would not be detectable with our observations, although it is unlikely that a helium white dwarf would survive the explosion (priv. comm. Rüdiger Pakmor). The other possibility is that SNe Ia (or at least SN 1006 and SN 1572) do not have donor stars, consistent with a DD-Scenario.

Another remnant that can be subjected to such an intensive search is Kepler (SN 1604). Kepler seems to be different from either SN 1572 and SN 1006 due to detection of interaction with the CSM. Observational facts of the Kepler remnant as well as the description of the donor star search will be discussed in the conclusion of this thesis (Chapter 6).

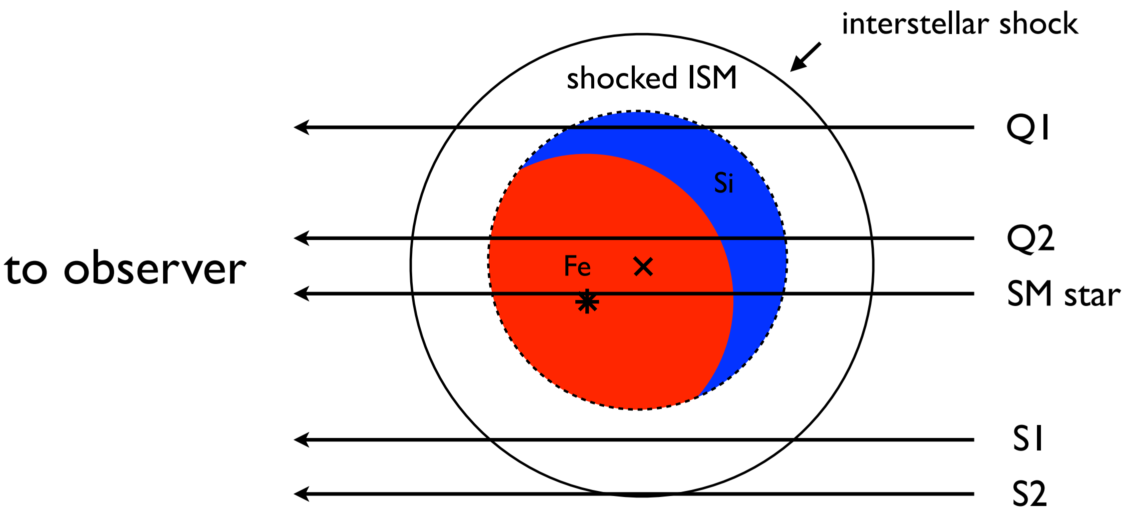

Figure 4.6 Background UV sources probing the remnant. Figure adapted from Winkler et al. (2005)

CHAPTER 5

Automatic fitting of Type Ia Supernova spectra

5.1. Introduction

Chapter 2 through 4) were dedicated to the hunt for the posited donor stars in SN Ia single degenerate explosions and did not use the measurements from the SNe Ia themselves. In this chapter we will describe the deduction of the abundance distributions and energies from optical spectra as well as the automation of this process.

Encoded in a SN Ia spectrum is the distribution of the elements synthesised in a SN Ia explosion, which can tell us about the explosion process of a SN Ia. Not only do the different scenarios predict different explosion physics, but uncertainties within, for example the single degenerate channel, of number of detonation points, transition from deflagration to detonation all predict different abundance structures.

The main sources of information in spectra are the shape/strength of the spectral features and their evolution with time. There have been a few attempts to extract the details of the stellar explosions from one or both of these sources. All of them employ the technique of fitting the observations using synthetic spectra. A critical part of this process is the radiative transfer algorithm used to generate the synthetic spectra, which has been implemented in several different codes.

Fisher (2000) wrote a very simple radiative transfer code called SYNOW. SYNOW is a highly parametrized code and thus is mainly used for line identification rather than actual fitting of SN Ia spectra. The main code used in this work is a further development of the code described in Mazzali & Lucy (1993) and Mazzali (2000), henceforth named the 'Mazzali and Lucy Monte Carlo' code (MLMC). Compared to the SYNOW code, the MLMC code calculates a radiative equilibrium temperature and uses this to compute internally consistent ionization ratios. In addition, MLMC takes electron scattering into account as well as allowing for non-resonance line scattering.

Codes such as PHOENIX Hauschildt & Baron (1999), SEDONA Kasen et al. (2006) and ARTIS (Kromer & Sim, 2009) are powerful 3D radiative transfer codes. They are the most 'physical' codes available but take hours to days on supercomputers to produce spectra. As they take a considerable amount of time and computational power, these codes, however, are not practical for fitting many observed spectra.

Mazzali et al. (2007) showed that the brightness of a supernova relies mainly on the production of ^{56}Ni. Faint SNe Ia (91bg-like) produce roughly $0.2\,M_{\odot}$ of ^{56}Ni. Most SNe Ia produce roughly $0.6\,M_{\odot}$, with some luminous SNe Ia (91T-like) producing up to $0.9\,M_{\odot}$. All luminosity types enclose approximately $1\,M_{\odot}$ of ash. This remarkable find was made by manually fitting 23 SNe Ia using the MLMC. There are however many more spectroscopically well sampled SNe Ia and soon there will be even more observed expected from the next generation supernova searches. Such large datasets cannot be effectively studied with manual fitting techniques. An automated procedure can not only fit many supernovae, but will also explore the parameter space to calculate error estimates. Strict quality measures necessary for an automatic fitter can also help when interpreting physical quantities generated by the code. We present an automated way of fitting supernovae using the MLMC (in collaboration with Stephan Hachinger and Paolo Mazzali).

In section 5.2, we will introduce the inner workings of the MLMC-code. We will discuss the properties of the parameter space on one example fit in Section 5.3. Section 5.4 provides an introduction to GA, which are the optimisation strategies of choice in the automation of the MLMC. We will present the current implementation of the autofitting code in Section 5.5 (Dalek code). Finally, we will conclude and give an outlook over future work of this project in Section 5.6.

5.2. The MLMC Code

The MLMC code, used in this work, is described in detail in Mazzali (2000) and we will give only a very short introduction to the key concepts here. We refer the reader to Mazzali (2000) for a more detailed description of the code. A more advanced version, using abundance stratification, but not used in this work is described in Mazzali (2000).

Based on spectra, the phase of the evolution of a supernova can be divided into the photospheric phase and the nebular phase. The MLMC only creates synthetic spectra for SN Ia in the photospheric phase. In the photospheric phase the supernova can be approximated by a sharp photosphere emitting a black-body spectrum with a fast moving ejecta-layer on top.

5.2.1. Radiative Transfer

Radiative transfer calculations attempt to provide the wavelength-dependent flux emerging from the atmosphere, for a given input boundary condition at the base of the atmosphere. Computing the attenuation for the given input flux (F_0) is a critical part of this process. This wavelength-dependent attenuation factor is called the opacity, τ:

$$F(\lambda) = F_0(\lambda)\, e^{-\tau(\lambda)}, \tag{5.1}$$

where F is the observed flux and F_0 is an assumed distribution of input flux before being absorbed by the plasma, which imposes the attenuation factor $e^{-\tau}$. There are many physical processes relevant to supernova radiative transfer. The line opacity (bound-bound transitions) has the biggest impact on the final spectrum. The lines in SN Ia spectra are the prime indicators for elemental abundance. In contrast to lines, which occur at one specific frequency, Thomson scattering ($\tau_e = \sigma_t n_e s$, where σ_t is the Thomson cross section, n_e is the electron density and s is the path travelled) is independent of frequency and only depends on the state of the atmosphere. Thomson scattering is an important way to redistribute photons in angular space (i.e. making the radiation field more isotropic) and thus also has a strong influence on radiative heating/ionization of the plasma. Other sources of opacity like free-free absorption and bound-free absorption are thought of as second order effects (see Figure 1 in Pinto & Eastman, 2000) and are not implemented in the MLMC. As the MLMC is required to be fast only bound-bound opacity and Thomson scattering is implemented in the code.

Unlike stellar atmospheres, in supernova ejecta one needs to consider the photon's Doppler shift in relation to the surrounding medium. One major assumption that the code makes is the so-called Sobolev approximation. The Sobolev approximation assumes that lines have only a single frequency at which they can be excited (no natural, thermal or other line broadening). This assumptions is a good approximation where photons are moving through a medium where the velocity gradient is so high that they are only in resonance with one line (no blending) in a very small region. This Sobolev approximation is one important factor of making the code fast yet still reproducing the observed spectra rather well.

In addition, the MLMC assumes the ejecta to be in homologous expansion. This means that the ejecta are freely expanding, such that the velocity and radius are simply related by:

$$v = r/t.$$

Combining both the Sobolev approximation with the assumption of homologous expansion yields this relatively simple formula for line opacities:

$$\tau_{lu} = \frac{\pi e^2}{m_e c} f \lambda t_{\exp} n_l \left(1 - \frac{g_l n_u}{g_u n_l}\right), \tag{5.2}$$

where τ_{lu} denotes the opacity going from the lower state to the upper state of an atom, e is the electron charge, m_e is the electron mass, f is the absorption oscillator strength of the line, λ denotes the wavelength, $t_{\exp}$ the time since explosion, n_x the number of atoms in the state x and g_x is the statistical weight of the state x.

Although producing relatively good synthetic spectra, the assumptions of homologous expansion and Sobolev approximation have their caveats. In the case of homologous expansion it is thought to be a very good approximations after the first few minutes of the explosion, but maybe effected when, for example, the ejecta interacts with surrounding material - a case we are not exploring in this work. In addition, the energy deposited by the decay of ^{56}Ni also causes a deviation from the homologous expansion. Compared to other uncertainties, however, this effect is negligible (see Figure 2 in Woosley et al., 2007). The main caveat for Sobolev approximation is that a line is not a delta-function, as assumed in the Sobolev approximation. If two strong lines are close in frequency space it can lead to the first line shielding the second line. Despite these caveats, however, the Sobolev approximation and homologous expansion are widely used and have been demonstrated to provide an adequate compromise between accuracy and computational practicality for fitting the spectra of supernova ejecta.

We have discussed the propagation of the photons in the plasma but have not discussed the state of the plasma yet. The simplest assumption for the state one can make is LTE. In this case, the Boltzmann formula describes the level populations in a single ion:

$$\frac{n_j}{n_{\text{ground}}} = \frac{g_j}{g_{\text{ground}}} e^{-(\epsilon_j - \epsilon_{\text{ground}})/kT},$$

where n_j is the population of the j-th state of the atom, g_j is the statistical weight of the j-th state, ϵ_j is the energy of the j-th state, and T is the temperature of the plasma. Similarly, we can calculate the ionisation state using the Saha-equation:

$$\frac{N_j}{N_{j+1}} = n_e \frac{U_j(T)}{U_{j+1}(T)} C_I T^{-3/2} e^{\chi/kT},$$

where N_x are the total ion population with ionisation state x, U_x is the partition function for the ionisation state x, n_e is the number density of electrons, C_I is a universal constant and all other symbols have their usual meaning.

In the nebular approximation, we approximate the radiation field by a diluted black body:

$$J = WB(T_R),$$

where J is the mean intensity, T_R is the radiation temperature and W is the dilution factor. In the standard nebular approximation W differs from 1.0 due to purely geometrical reasons: the photon count falls with distance to the source ($1/r^2$ for a point source). For an extended source the geometric part of the dilution factor takes the following form (Mihalas, 1978):

$$W(r) = \frac{1}{2}\left[1 - \sqrt{1 - \left(\frac{r_{\text{ph}}}{r}\right)^2}\right] \tag{5.3}$$

This concept can be generalised to a modified nebular approximation, where the effects of attenuation and scattering (e.g. line and Thomson scattering) on W can also be included. Using W and J and assuming LTE one can easily calculate the electronic and ionization states of the plasma:

$$\frac{n_j}{n_{\text{ground}}} = W\left(\frac{n_j}{n_{\text{ground}}}\right)^{\text{LTE}}_{T_R}$$

and

$$\frac{N_j}{N_{j+1}n_e} = W\left(\frac{N_j}{N_{j+1}n_e}\right)^{\text{LTE}}_{T_R}.$$

This simple form of the nebular approximation only considers radiative excitation/de-excitation and ionisation/recombination from and to the ground state, but has the advantage of solving the state of the plasma computationally inexpensively. The MLMC uses a variant of the modified nebular approximation which includes radiative excitation/de-excitation from excited states and a different treatment of the UV radiation field (which contains most ionisation edges). For a detailed description of the modifications please refer to Mazzali & Lucy (1993) and references therein.

In the MLMC code the two fundamental properties of the radiation field - temperature and the dilution factor - are determined from a MC simulation. We first measure the mean frequency of the photons and bolometric intensity. We then infer the temperature by requiring the black body to have the same mean frequency (Wien approximation). The dilution factor can then be fitted to match the bolometric intensity. We note that close to the photosphere the dilution factor is influenced mainly by the geometry and should be close to 0.5 (see Equation 5.3 for $r = r_{\mathrm{ph}}$). As the MC process is statistical and the dilution factor an approximation this might vary, but we assume this to be still an important factor to determine if the model is realistic.

In summary, the approximations described in this section make the MLMC fast, yet still providing an acceptable representation of reality. This makes the MLMC code suitable to use for modelling data.

5.2.2. Monte Carlo Radiative Transfer

We have so far only described the approximations made by the code, but not how these are implemented and work together. In this section we will give an overview of the process and design of the MLMC code.

First the ejecta in the MLMC code is divided into 20 concentric shells with an equal thickness in $1/r$, where r is the radius from the centre of the explosion. Each shell has a uniform density which is drawn from the well known empirical W7 model (Nomoto et al., 1984). The MLMC also allows the change of this density structure, but for all this work we have kept the W7 model density structure. In addition, we assume a homogeneous abundance distribution throughout the whole model. There is, however a *stratified* version of the code that allows for different abundances in each shell. We have opted to use the simple homogeneous version as the parameter space is very complex even for this homogeneous version. We plan to extend the automatic fitting procedure to use the stratified version at a later date. In addition, we calculate the time since explosion t_{exp} using the time of the photometric maximum and adopting a rise time estimate of 19.5 days. The photospheric velocity, the L_{bol} and abundances for the chosen elements are the input parameters to the MLMC code.

To conserve radiative equilibrium the MLMC uses photon packets instead of individual photons. Each photon packet, described by frequency and number of photons, contains the same energy (more photons per packet in the red than in the blue). For pure elastic scattering events - the absorption frequency is the same as the reemission frequency - the number of photons is conserved in each packet. For line absorptions this is generally not the case. The MLMC allows for photon branching, which means that the photon can be emitted in a different transition than it was absorbed in. Once absorbed the new emission transition is chosen by a weighted random process (for a more details see Mazzali, 2000). The number of photons in the packet is adjusted to conserve the co-moving energy of the packet, thus preserving the energy between matter and radiation field (radiative equilibrium).

The MC simulation begins by calculating the plasma condition using an initial guess of temperature and dilution factor for each shell. A photon packet is emitted with a random frequency and a random angle drawn from a blackbody distribution. An event optical depth is calculated from a uniform random distribution so that $\tau_{\mathrm{event}} = -ln(z),\ z \in (0,1]$ (follows from sampling the Equation 5.1). There are three possible outcomes for the photon in each Monte Carlo step. First we calculate the length of the path (s_e) that the packet can travel freely before τ_{event} is equal to the Thompson scattering opacity $\tau_{\mathrm{event}} = \sigma_{\mathrm{T}} n_e s_e$. Secondly we calculate the same path length for the lines s_l using as a target opacity $\tau_e + \tau_{\mathrm{line}}$ for line scattering (where $\tau_e = \sigma_{\mathrm{T}} n_e s_l$ and τ_{line} is the line opacity calculated with Equation 5.2). If s_e is the shortest then Thomson scattering occurs and the photon is assigned a new direction and a new τ_{event} is drawn and we start anew. If $s_e < s_l < s_{\mathrm{exit}}$, where s_{exit} is the length to exit the shell, line scattering occurs and the photon is absorbed by an atom. This excited atom can then de-excite through many lines. MLMC randomly chooses a downward transition for the whole packet (taking the appropriate weights into account) and adjusts the photon number in the packet to ensure radiative equilibrium. Finally, if both paths are longer than the path to exit the current shell, then the photon exits the current zone and a new MC step begins.This process is iterated until either the photon packet escapes the outermost shell - in which case the photon number and frequency is recorded - or penetrates the photosphere in which case the photon is discarded and a new one drawn.

This iterative process is first used in the MLMC code to prepare the plasma state. In this initial simulation each packet status is recorded at the mid-point of each shell. This information is used to calculate a new temperature and dilution factor which then leads to updated plasma conditions (level populations and ionisation). This procedure is repeated until the plasma temperature converges. Once convergence is reached the actual Monte-Carlo simulation begins.

The final spectrum is not calculated using the number and frequency of the escaping photon packets. Instead we use the photon packets to estimate the source function as a function of wavelength and then calculate the emerging spectrum using a formal integral solution of the radiative transfer equation (a more detailed description of this method in Mazzali, 2000). This has the advantage of reducing noise in the spectrum due to MC noise.

In summary, the MLMC produces realistic spectra in a competitive calculation time (one spectrum per minute on a modern computer). A more detailed description of the code can be found in Mazzali & Lucy (1993) and Mazzali (2000). There is a abundance stratified version of the MLMC code, which has not been described in this work but can be reviewed in Stehle et al. (2005).

5.3. Manually fitting a Type Ia supernova

We extract physical quantities from the SN Ia spectra by adjusting the parameters of the MLMC until the code produces a similar synthetic spectrum to the observed one. For now this fitting process for SNe Ia is an arduous manual task, which requires detailed knowledge about the inner workings of the MLMC and its approximations. Known problems, like the excess in the NIR (described in more detail later) and the high velocity calcium, necessitate one to prioritise between different quality measures. This also leads to a subjective 'best-fit', although experts in MLMC fitting seem to come to the same conclusion despite their different approaches. We will first illustrate this fitting process on one example - SN 2002bo 10 days before maximum (Benetti et al., 2004) - which has been fitted manually by Hachinger (2007), before moving to our automatic optimisation attempts in Section 5.5.

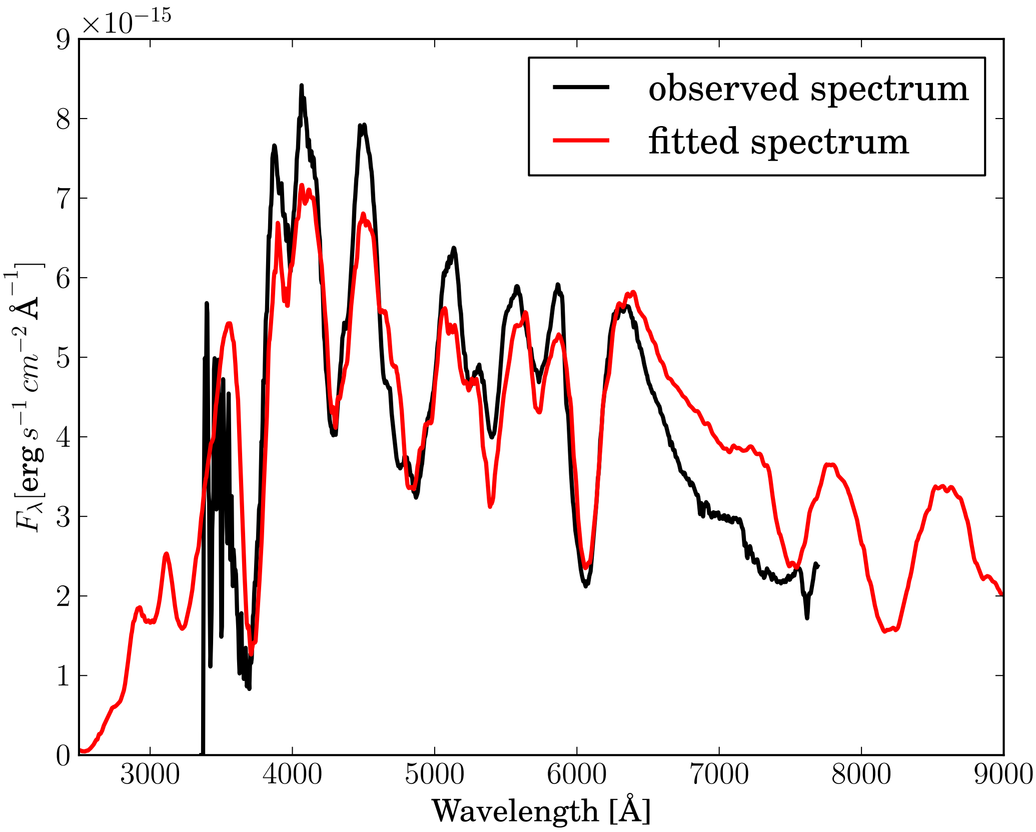

Figure 5.1 Spectrum of SN 2002bo (Benetti et al., 2004) with MLMC fit by Hachinger (2007). The excess in redwards of 6500 Å is a common problematic features of these fits.

The first step in any fitting procedure is to initialise the parameters. The luminosity distance, redshift and time since explosion (t_{exp}) are initialised from data available on the supernova and are not fitted with the MLMC code. The initial choice of luminosity and photospheric velocity is based empirically on photometry and time since explosion. When manually fitting the spectrum we only consider contributions from the elements listed in Table 5.1. When initialising these for a manually fitting procedure we use empirical data (this procedure is described in detail in Section 5.5). In the fitting process several elements are treated specially. The abundance of ^{56}Ni for example, is given as the abundance of initial nickel synthesised in the explosion. Since ^{56}Ni is unstable this unified mass of ^{56}Ni will decay first to ^{56}Co which then decays to ^{56}Fe. This decay is accounted for (i.e. the abundances of ^{56}Ni, ^{56}Co and ^{56}Fe are calculated from the initial ^{56}Ni mass and time since explosion). In all further discussions, cobalt will always refer to radioactive ^{56}Co, the daughter of ^{56}Ni (we do not consider any stable isotopes of cobalt that may have been synthesised in the explosion). The ^{56}Fe abundance is determined by adding the ^{56}Fe obtained from the ^{56}Ni decay to the iron and pre-existing ^{56}Fe (Fe_0). In addition, we lock the ratio of titanium and chromium as this ratio is degenerate in the spectral fitting.

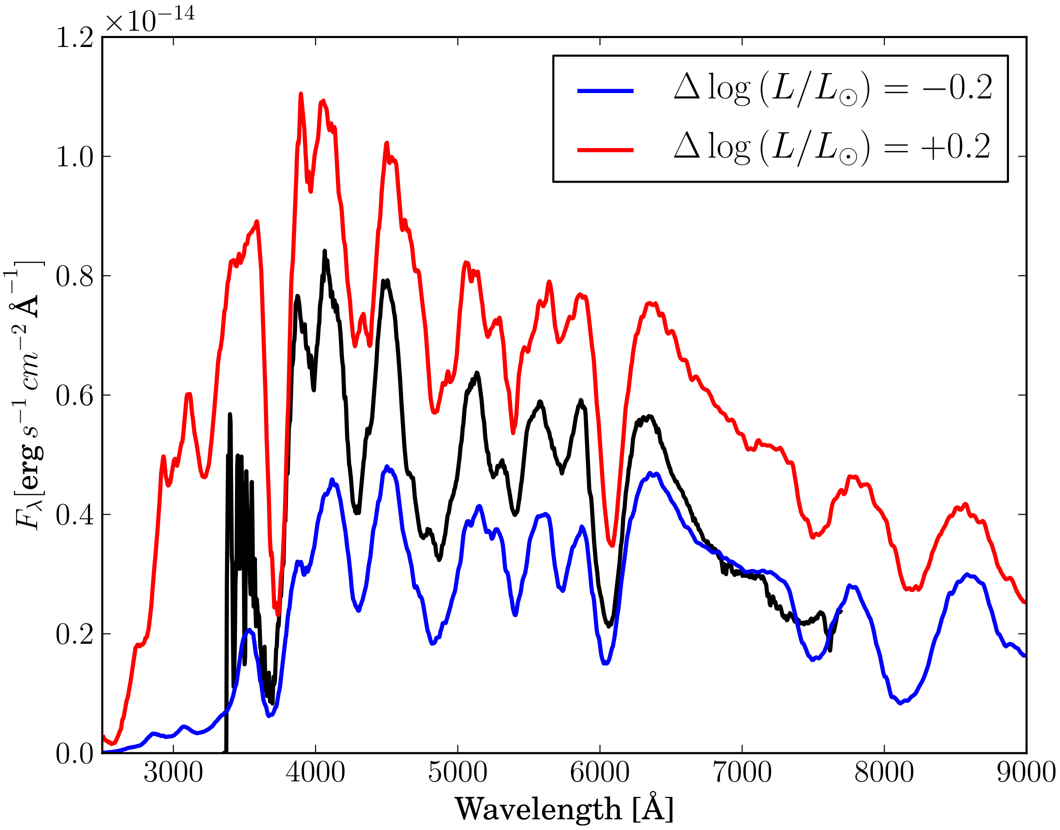

Figure 5.2 We have perturbed the luminosity around the best fit value. The most noticeable effect is the continuum offset. There is also a slight change in the overall slope of the spectrum.

Next we will describe the unique impact each parameter has on the spectrum and how that is used to arrive at a best fit. There are three main parameters that have the most influence on the overall spectrum fit: Luminosity, photospheric velocity and abundance in IGE. A large offset in L, relative to the best fit parameter, is easily visible as a large offset of the continuum (see Figure 5.2). Thus it is easy to constrain the parameter space in L. L also has influence on the temperature of the model through:

$$L_{\mathrm{bol}} = 4\pi\sigma R^2 T_{\mathrm{eff}}^4 = 4\pi\sigma(v_{\mathrm{ph}} t_{\mathrm{exp}})^2 T_{\mathrm{eff}}^4,$$

where T_{eff} can be calculated by the model parameters L and v_{ph}.

Velocity in astronomy is often measured using the Doppler shift of atomic lines. In this case however it is hard to measure the photospheric velocity from atomic lines. Lines are created at different depths and thus at different velocities. This smears out the line profiles which makes fitting velocities nearly impossible using this technique. The main impact of photospheric velocity is establishing the temperature structure with the given luminosity. A model with a too high photospheric velocity will have expanded more than the observed spectrum and thus will be cooler. This results in a spectrum that is too luminous in the red and not luminous enough in the blue (see Figure 5.3). A secondary effect is that the ionisation state will be wrong (blue radiation field will lead to more photoionization and vice versa), which can be seen in various lines.

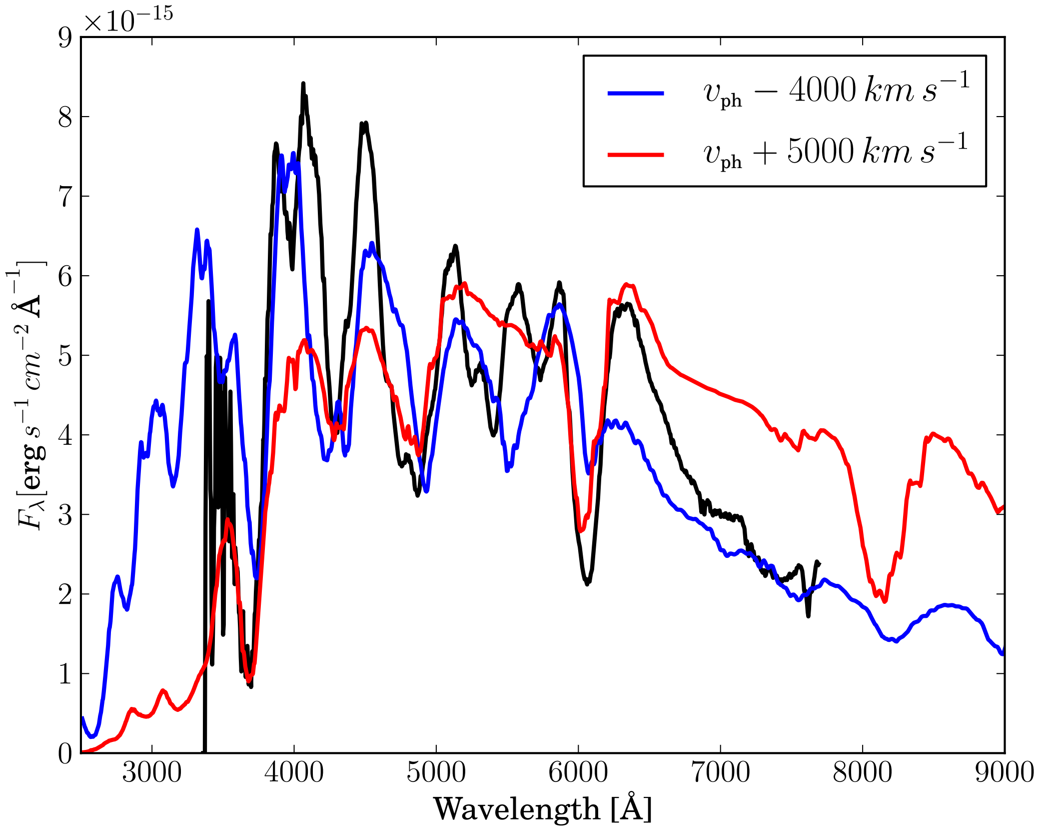

Figure 5.3 The photospheric velocity has been perturbed around the bestfit. If the velocity is too small, the spectrum is too blue and vice versa.

The IGE have a similar influence on the overall flux distribution as the photospheric velocity. We assume, as discussed previously, no stable cobalt. All IGE elements reprocess the flux heavily by absorbing bluewards of $\approx$ 3800 Å and fluoresce in the red part of the spectrum. For example, a too high abundance will suppress the flux in the blue too much and will cause the spectrum to be over-luminous in the red (see Figure 5.4). Although physically different from the photospheric velocity, phenomenologically these are similar. The degeneracy is broken by identifiable iron lines in the spectrum as well as the ionization balance determined by the temperature (mainly influenced by photospheric velocity and luminosity). This near degeneracy causes a very complex parameter space. The titanium/chromium abundance ratio is fixed and only one of these elements is fit. Like Ni_0 and Fe_0, titanium and chromium provide strong flux suppression in the blue and fluoresce in the red. Chromium can be partly constrained due to a blended line just blueward of the UV calcium feature, but other than that we believe them to be slightly degenerate with the other IGE. We disregard the elements scandium, vanadium and manganese as they seem to have little influence on the spectrum at their predicted abundances.

There are six other abundances that are taken into account when fitting: carbon, oxygen, magnesium, silicon, sulphur and calcium (see Figure 5.5). Judging the fit of the Ca II line at 3700 Å is relatively easy and thus the calcium abundance is usually changed first. An additional constrain on the calcium abundance is the NIR triplet near 8500 Å, which

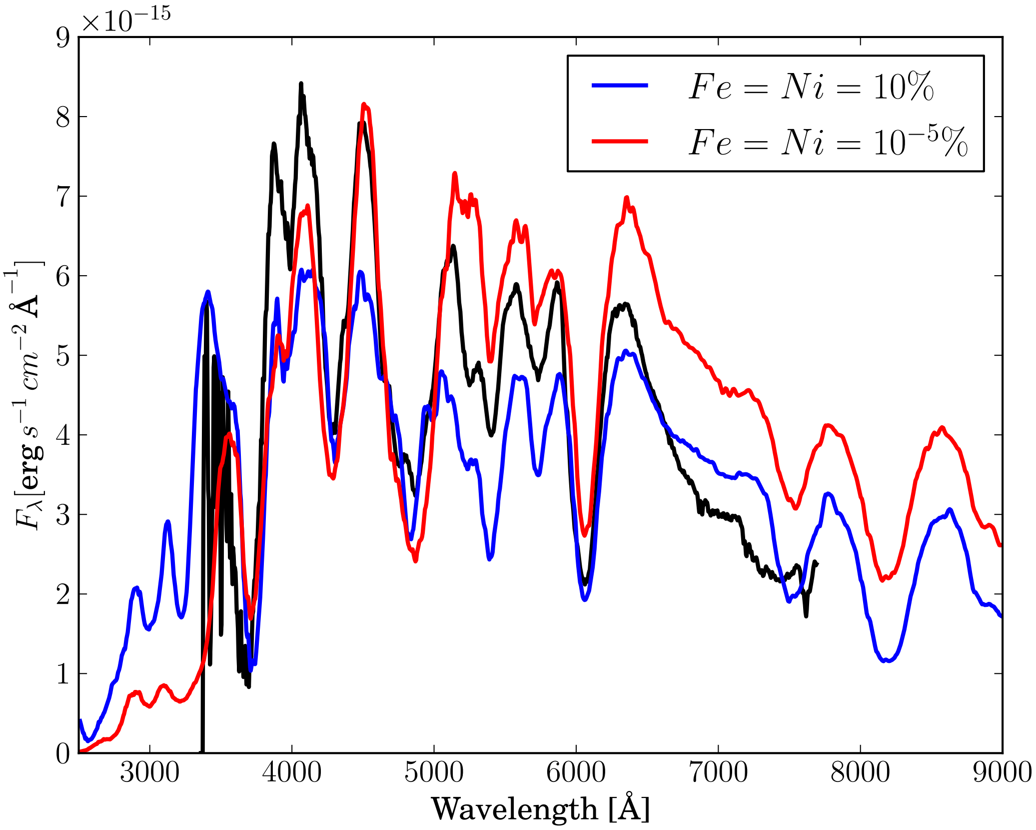

Figure 5.4 When changing the IGE (in this case we have only changed Fe_0 and Ni_0) the flux is altered in the blue and red part. Too much IGEs and there's not enough flux in the blue and too much flux in the red and vice versa.

is however often missing in spectral coverage. The choice of temperature imposed by photospheric velocity and luminosity does not have an immense influence on this line. One caveat however is that the Ca II line saturates at a certain abundance. If the observed Ca II line is close to that limit one can only extract a lower limit for the calcium abundance.

Silicon and sulphur are usually the next elements to be fine-tuned. Both of these elements are linked through nuclear synthesis and we do not expect there to be more sulphur than silicon (e.g. Iwamoto et al., 1999). We also expect no less sulphur than a third of silicon. Silicon also provides an important measure for temperature through the ionisation balance, which is seen as the ratio between Si II at 6150 Å versus the fit of Si II at 5700 Å (see Figure 5.3). This effect was first mentioned in Nugent et al. (1995) and is explained in detail in Hachinger et al. (2008). The strong Mg II feature near 4300 Å helps constrains the magnesium abundance. The weak C II feature at $\approx$ 6300 Å is the only line to provide constraints for the carbon abundance. In most SNe Ia spectra this line is weak or not visible and mainly provides an upper limit for the amount of carbon.

The last element to be described is oxygen, which takes the rest of the mass fraction when all other elements have been assigned abundance fractions. We will sometimes refer to this as a buffer element, but we caution the reader to not think of this as a physical description but rather a description of implementation. Such a buffer is needed as we have chosen

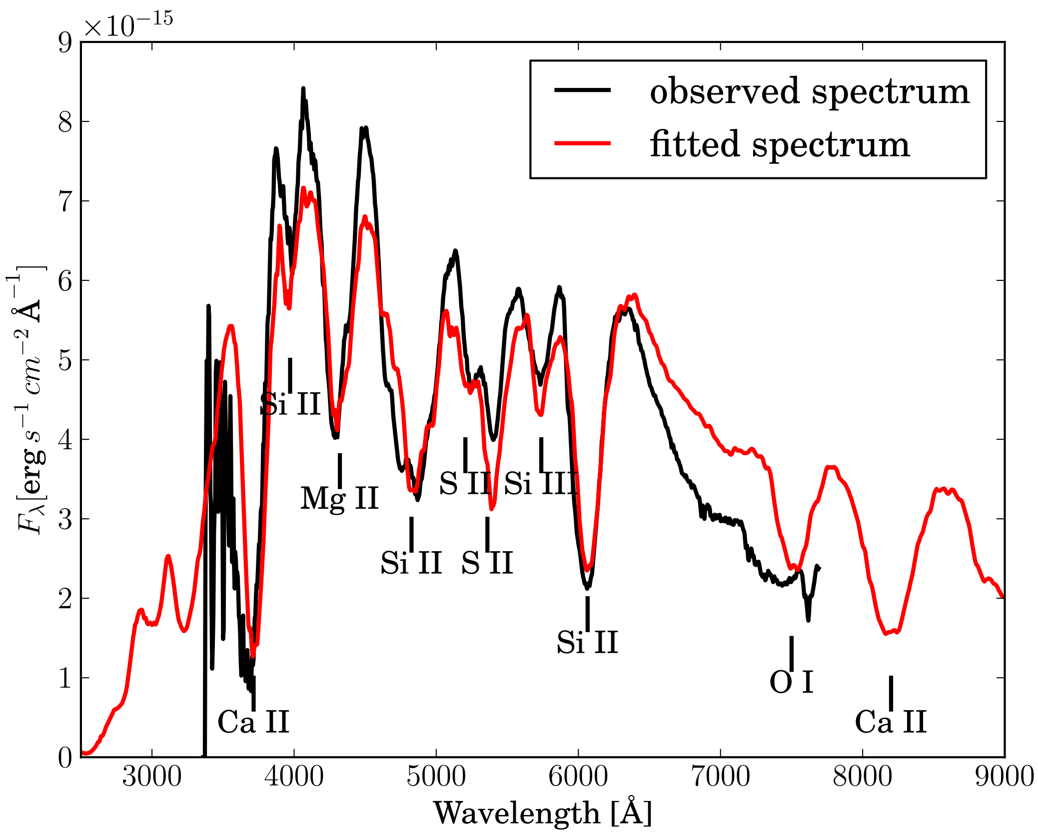

Figure 5.5 The best-fit model for SN 2002bo We have identified some of the strongest lines that are scrutinised when fitting a Type Ia (SN Ia) spectrum.

a density distribution (W7 model) and the elemental abundances are fractions by mass. Oxygen is chosen for that role as it does not have strong influence over the overall spectrum. Oxygen in general is not a major contributor to lines, the only strong lines are the O I triplet at 7774 Å. This line is often very weak as a large fraction of oxygen is ionised and significant contamination from silicon and magnesium to the triplet. Both of these arguments mean that large fractions of oxygen might not be visible in the spectrum making it a perfect buffer element.

The fitting process usually involves first adjusting luminosity, then IGEs and finally photospheric velocity. This is followed by adjusting the other elemental abundances from the initial values. After the elemental abundances are adjusted we re-adjust the luminosity, photospheric velocity and IGE. This iterative process continues until a satisfactory fit has been obtained. When closing in on the optimal fit we consider the dilution factor. Purely theoretical we would expect this to be close to 0.5 for a 'physical' fit. We do, however, accept values between 0.4 and 0.7 as physical. This large range is accepted due to numerical fluctuation and approximations made by the MLMC. The parameters are often improved further by checking their time evolution through fits of photospheric spectra at different times.

Finally, during and after the fitting process the elemental abundances and ratios (listed in

Table 5.1 Parameters for best fit

Parameter	Value	Realistic Constrains
$\log L/L_{\odot}$	9.05	
v_{ph}	11700	
Carbon	0.08 %	C < 12.5 %
Oxygen	54.9 %	C < O
Magnesium	10 %	-
Silicon	25 %	Si > 1 %
Sulphur	4.5 %	1 < Si/S-ratio < 3
Calcium	1 %	Ca < 5 %
Titanium	0.01 %	Ti + Cr < 1 %
Chromium	0.07 %	$\mathrm{Cr/Ni_0}$-ratio < 10
pre-existing Iron	0.07 %	$\mathrm{Fe_0/Ni_0}$-ratio < 10
undecayed Nickel	1.5 %	$\mathrm{Ni_0}$ < 80 %

Table 5.1) are also checked against theoretical nucleosynthetic yields (e.g. Iwamoto et al., 1999). If the abundances and abundance ratios are outside of these generous bounds one normally tries to find another reasonable fit within the bounds. We have also implemented this checking into our automatic optimisation routines (see Section 5.5).

In summary, the fit is relatively good as seen in Figure 5.5. There are however some problems that are intrinsic to the MLMC and can not be rectified by adjusting parameters. The calcium line at 3900 Å can be seen to be to blueshifted in relation to the model. This property is not unusual and is thought to come from high velocity calcium components at the outer edge of the ejecta. This can often be rectified in the stratified version of the MLMC which is not discussed in this work. The next major known discrepancy is the excess of flux redwards of $\approx$ 6200 Å. This is a common problem, due to the assumption of an underlying black body spectrum, which overestimates the flux in this region. Although the continuum is offset we still believe the line depth to be representative, thus when fitting manually often one tries to fit the depth of the lines instead of the continuum. This excess makes it difficult to use traditional fitness measures and we will discuss the path we took in Section 5.5.

In the end, the fitting of a supernova is a complex procedure and requires a lot of practice. For automating this process we initially tested simple gradient methods. These failed abysmally. We quickly discovered the search space is too complex and evaluation time takes too long (each synthetic spectrum roughly one minute on a modern computer) to use these simple methods. Research in numerical optimisation techniques has made significant process in the last decades. These areas of mathematics have yielded impressive algorithms. Genetic algorithms are easy to implement and are intrinsically parallel. A perfect match for our problem.

5.4. Brief Introduction to Genetic Algorithms

Before advancing to the description of the automation of the MLMC we will give a brief introduction to GAs which are used in the automation endeavour. We urge the reader to review GAs in Appendix B before proceeding.

The complexity of an optimisation problem rises with the number of dimensions, but more so with the correlation of the input parameters. Iterative algorithms, often using gradients to find extrema by solving a Hessian matrix, are very good at problems with a low number of dimensions and small correlation between input parameters. They can exactly solve the problem in a very small amount of computational time. However as the search space gets more complex and multiple extrema start to appear. The iterative algorithm often converge on those and are only useful when starting close to the global optimum. For these complex multi-dimensional parameter spaces stochastic optimisation techniques that rely heavily on random numbers are often the best choice. Unlike the iterative methods, however, stochastic optimisation algorithms are not guaranteed to find any optimum.

Automatically fitting SN Ia spectra is a very complex multi-dimensional parameter space with many highly correlated parameters. We have chosen GAs - a stochastic optimisation algorithm - to conquer this problem. GAs use terminology which borrows from its roots in evolutionary science. At the core of each GA is the individual. The individual represents one solution in search space. The genotype of the individual is the vector representation of all of its parameters, sometimes referred to as genome. Evaluating the genotype leads to the phenotype which is the individual's representation in solution space (e.g. a spectrum obtained from parameters). For optimisation one needs to have a quality measure which in terms of GAs is the fitness. The fitness is calculated using a fitness function from the phenotype of the individual (e.g. the χ^2 value calculated for a synthetic spectrum against the observed spectrum).

GA have a number (called population size; as a rule of thumb ten times the number of parameters) of these individuals in a collection known as a population or generation. This enables them to probe multiple areas in search space simultaneously, which makes these algorithms intrinsically parallel. During the optimisation process GAs go through several stages first of which is the initialisation of the first generation. The easiest is to draw random parameters from the parameter space (there are more advanced techniques which are described in Appendix B). Once this first generation is populated with the required number of individuals we evaluate their phenotypes and then their fitness. Once this step is complete we want to form the second generation out of the old generation. Appendix B gives a very detailed overview over the different processes building a new population, we will here only describe one path. First we use a method of randomly choosing individuals that still favours more fit individuals over less fit individuals. Using this process we select two individuals of the old population for mating. For the mating process we employ a technique called single-point crossover to create a new individual. This means that we select a random point in the genome of both parents. Parameters before this point are taken from the first parent, parameters after that point are taken from the second parent. This newly created individual (or child) is then subjected to possible mutation, where each parameter has a small chance of being multiplied by a random number. We repeat this process of choosing two parents and creating children until the new generation has the same number of individuals as the old population. One should note that in this process it is possible, unlike in nature, that the parents are the same individual twice. This case normally only happens when the parent is very fit and chosen twice consecutively in a random process. The crossover in this case does not change the child but creates a copy of the parent, which is then however subjected to mutation.

To visualize this process we have created a flowchart in Figure 5.6. This process of the creation of a new generation and subsequent evaluation is repeated until either a whole generation or an individual has reached a certain threshold in fitness. GAs are relatively resistent to converging on local optima, but are not entirely immune to it. The convergence to a local optimum in GA terms is called premature convergence.

In summary, we have chosen GAs because they are known to be able to navigate in complex search spaces. In addition, they are inherently parallelisable which makes it easy to speed up the optimisation routine. For a more detailed overview we urge the reader again to consult Chapter B.

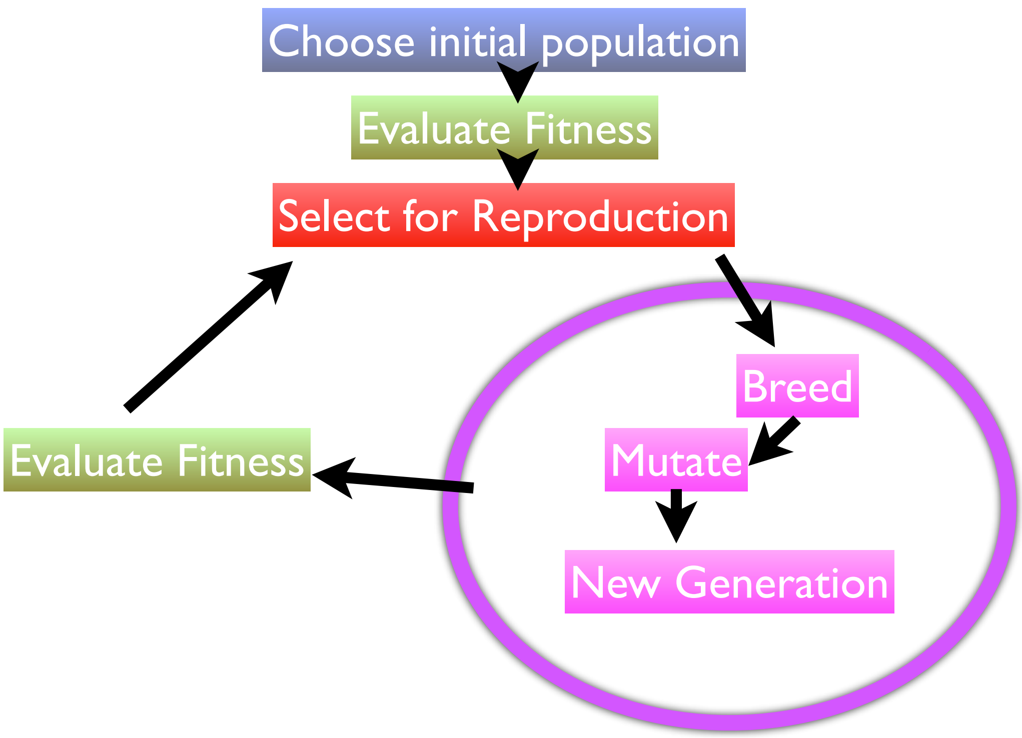

Figure 5.6 Flow chart overview over the process of a GA

5.5. Genetic Algorithms fit Type Ia Supernovae: The Dalek Code

In the following section I will outline the current progress of the automation of fitting the SNe Ia spectra with the MLMC. The torrent of new spectra observed by a multitude of surveys requires the swift and self consistent analysis of many SNe Ia spectra in a short time. As described in Section 5.3 the search-space for fitting SNe Ia spectra is very complex and vast. It thus requires a smart and quick algorithm for analysis.

The parameters that need to be fit are luminosity, photospheric velocity, carbon, magnesium, silicon, sulphur, calcium, chromium and nickel prior to decay (Ni_0) as well as stable iron (Fe_0). As in the manual fitting example the time since explosion as well as the luminosity distance (for scaling purposes) are given. We initially tried a Newton-Raphson approach with multiple phases. In the first phase the algorithm would adjust luminosity and normally came close to the optimum. In a second phase we tried to let the algorithm re-adjust luminosity, then photospheric velocity and last IGE s. This was modelled after the manual approach that is taken by Hachinger (2007) and Hachinger (2011). The process was time consuming and did not readily converge. We realized quickly the search space is far to complicated for such simple methods. In addition, we were limited to one processor with the Newton-Raphson-like method and could not utilize the large number of multi-processor machines that are currently available. GAs seem the perfect choice for this problem, as they are intrinsically parallel, are easy to implement and are relatively immune to local optima.

The first task was to wrap the MLMC code so that it is able to easily interface with any optimisation routine and run in parallel in multiple instances. The initial version of this *launcher* code was able to run on multiple processors on one machine. Next we extended the *launcher* code to be able to distribute jobs on the network. As the institute has a heterogeneous computer structure (different processor types, different operating systems) we were forced to write a custom software to distribute it among the many nodes. An additional advantage to this cloud-like process structure is that we could use unused resources as well as avoid servers that are heavily demanded by other users. For the scheduling we used a simple first in, first out queue. Finally, the *launcher* code has a simple application program interface (API) that accepts arrays with parameter sets and returns the results in a simple array format. Invisibly to the user, it writes the parameter sets to the relevant disks in a format that the MLMC understands. Upon completion it reads the data files and cleans up any temporary files created by the MLMC. This abstraction of the MLMC allowed us to quickly explore the intricacies of the GAs (and in the future possibly other optimisation algorithms).

As described in Section 5.4 the first step for any GA is to create an initial population (first generation). One can easily draw uniform randomly for luminosity and photospheric velocity (within some bounds). However, this method does not work for the elemental abundances as the sum of the abundances needs to add up to one. As explained previously these abundances are abundances by mass with a pre-chosen W7 model density structure. A population that is distributed around the optimum value converges much quicker than a uniformly sampled one. Thus we have chosen to use the W7 model abundances as an input parameter as it seems to be a good starting point for many SN Ia. To calculate these abundances we need to know the photospheric velocity. Using data from Benetti et al. (2005) we have estimated an empirical relationship between the time since explosion and the photospheric velocity (see Figure 5.7). This will serve as a rough first guess.

Once we know a photospheric velocity estimate we can determine at what depth the photosphere is located in the W7 model. We use this point and integrate outwards to find our initial abundance fractions.

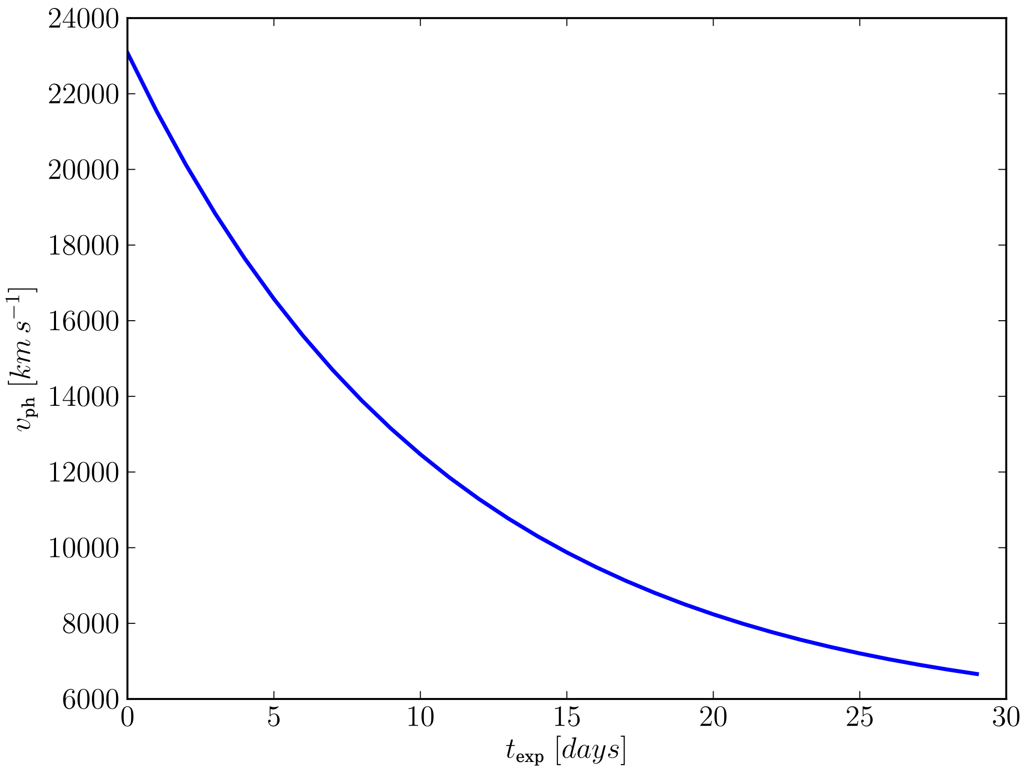

Figure 5.7 Estimated initial guess for photospheric velocity against days after explosion (Benetti et al., 2005).

When creating our initial population, we draw randomly from a uniform distribution for a preselected luminosity range (for the moment determined manually) and a photospheric velocity range 4000 km s^{-1}above and below the photospheric velocity estimate. The random sampling of the elements poses some problems.There are a lower and an upper bound when it comes to the initial abundance ratios. We have a lower bound for each abundance (established as the smallest abundance an element can have by MLMC) at 10^{-7} and a upper bound which is determined by the requirement that all abundances need to add up to one. Knowing the minimum and maximum bound we then use a log-normal asymmetric random distribution around the actual W7 model value with the lower and upper bound being at three sigma. If we would draw the abundances every time in the same order it would mean that the last element to be drawn would always have a very low chance of obtaining a high abundance value. Thus we randomise the order of drawing the elemental abundances. This ensures that the initial population is sufficiently dispersed to avoid the GA's premature convergence on a local optimum, but close enough to the region of interesting parameter space, which avoids unnecessary delay in the convergence.

After creating an individual through the random drawing process, we also check abundance ratios allowed by explosive nucleosynthesis of a CO-WD outlined in Table 5.1. If the newly created individual does not conform with the abundance limits laid out in Table 5.1 it is discarded and a new one is drawn. Once the initial population (we chose 150 for our population size) is created it is distributed among the compute nodes by the *launcher* module of the Dalek code.

The resulting spectra are then subjected to a fitness function. The selection of the fitness function is one of the most crucial choices for any GA. The correct fitness function is still a field of active research in the Dalek code. As an initial approach we calculated the mean-square of the residuals remaining from subtracting the observed spectrum and the spectrum of the current individual.

This approach has two main issues. First for almost all observed spectra in the early phase the fitted spectrum has a large continuum excess beyond 6500 Å (see Figure 5.1). However, we still regard the line depth and line shape to be correct. As described previously this is a known issue of the MLMC code. This large difference in the infrared means that the Dalek code will try to optimise this large offset and pay less regard to a good fit in the rest of the spectrum. To alleviate this we have tried multiple approaches. At first we tried to de-weight the fit in the problematic region. This artificially introduced weighting factor introduces another parameter which might have to change it for the GA to succeed on different spectra. This would defeat the point of an automatic fit. As a second approach we tried to fit and subtract the continuum in the problematic region before creating our fitness figure.

Secondly there are different parameters, including the dilution factor, that help guide the fit which are neglected when just using the traditional mean-square approach. For example, the dilution factor is expected to be close to 0.5 (see description in Section 5.2). Hachinger (2007) and Hachinger (2011) have found that in all cases a good fit will have a value of the dilution factor between 0.4 and 0.7. We have incorporated this into the fitness calculation and de-weight the fitness of spectra with a value outside this range to a great extent. Due to both these reasons, we now include a traditional goodness of fit measure in the blue, the more complex fitness calculation described above and an inclusion of the dilution factor W in the final fitness.

We should mention that we have tried, in addition to calculating the root-mean-square of the spectral fit, a number of completely different methods. Most notably we tried to use neural networks to perform a goodness of fit analysis. We however abandoned this effort as the training set to calibrate neural networks requires a large number of well fitted spectra which are not available. In recent years there have been a few successful alternative approaches to the classical root-mean-square fitness functions in supernovae (Blondin & Tonry, 2007; Jeffery et al., 2007). Both these approaches are not directly applicable to our problem as they address either a different supernova kind or address a classification problem. Although they are not directly applicable, we plan on testing fitness functions that incorporate some traits of these new methods.

Once the fitness is calculated for each individual we use the method of fitness scaling to preempt premature convergence in early generations (caused by the so called 'super-individuals') as well as creating a steeper fitness gradient in later generations. We have decided to use a linear fitness scaling as described in Goldberg (1989, see page 76 of):

$$f' = af + b,$$

where f' designates the scaled fitness and f the raw fitness. In all cases we want to make sure that the average of the scaled fitness f'_{avg} equals that of the average of the raw fitness f_{avg}. We will first try to find a linear relation so that the new maximum fitness f'_{max} is C_{mult} times the average fitness (f_{avg}). We choose $C_{\mathrm{mult}} = 2$ as suggested by Goldberg (1989).

This operation will scale early 'super-individuals' down and the rest of the population up and preempts premature convergence. In the later phases of the GA, when the fittest individuals and the bulk of the population have similar fitness values, this operation would lead to negative fitness values for some individuals. In that case we find a scaling parameters that maps the least fit individual to a fitness value of 0, while still maintaining $f'_{\mathrm{avg}} = f_{\mathrm{avg}}$. Once we have scaled the fitnesses we move to the selection process.

In the current version of the Dalek code we employ *elitism* (10% of fittest individuals advance immediately to next generation). We have also experimented with other modifications to the mating population, but found them to be subpar. The mating pool we have chosen has only two slots. For now we select the individuals for the mating pool using the standard roulette wheel selection.

We use a crossover probability of 90%, this means that in 10% of the cases we do not perform crossover. This means that the child is a copy of the first parent. If crossover occurs, we perform a uniform crossover as we felt that we do not want the ordering of the parameters to matter. We have also experimented with arithmetic crossovers by taking the mean of the parents. This meant that often useful traits would entirely disappear and we switched back to uniform crossovers. We will experiment in the near future with different crossover techniques like single-point crossovers.

The new individual, created by crossover, is subjected to possible mutations before being placed into the new population. The Dalek code employs different mutation strategies for the different parameters. The abundances are just multiplied by a uniform random number (we have tried Gaussian random numbers, but this led to premature convergence in many cases) with a relatively high chance of currently 7%. Luminosity and photospheric velocity are physically different from the element abundances and as such are treated differently in the mutation process. In both cases we add a uniform random number, in addition to having different mutation probabilities (this applies to all elements but oxygen). After the mutation step we see if the buffer element oxygen has a negative abundance. A negative abundance implies that the other elements add up to more than one. If oxygen has positive abundance the code goes on to check the abundance ratios. If the child passes both these tests it is placed in the new population, if not it is discarded. This process is repeated until the size of the new population (including the members of the old population that advanced through *elitism*) reaches 150.

This process of selection, recombination and mutation is repeated over many generations. We have experimented with up to a 1000 generations in one run. Our scheduler can achieve a throughput of one generation per minute (in optimal conditions where all CPUs are free). Our principal spectrum for testing the GA was SN 2002bo 10.4 days post explosion (see Figure 5.1). We have also tried different spectra with varying degree of success.

In the presented case we let the GA run for 188 generations. Figure 5.8 shows how the genetic algorithm over many generations improves the fitness of the individuals.

The step-pattern is very common in genetic algorithms: One individual has a favourable mutation and it takes several generations for the other individuals to catch up. During the last generations one can clearly see that there is a gap between the bulk of the population and the top 10%. This gap is caused by the contrast of relatively high mutation in the main individuals against the mutation free advancement of the top 10% (elitism).

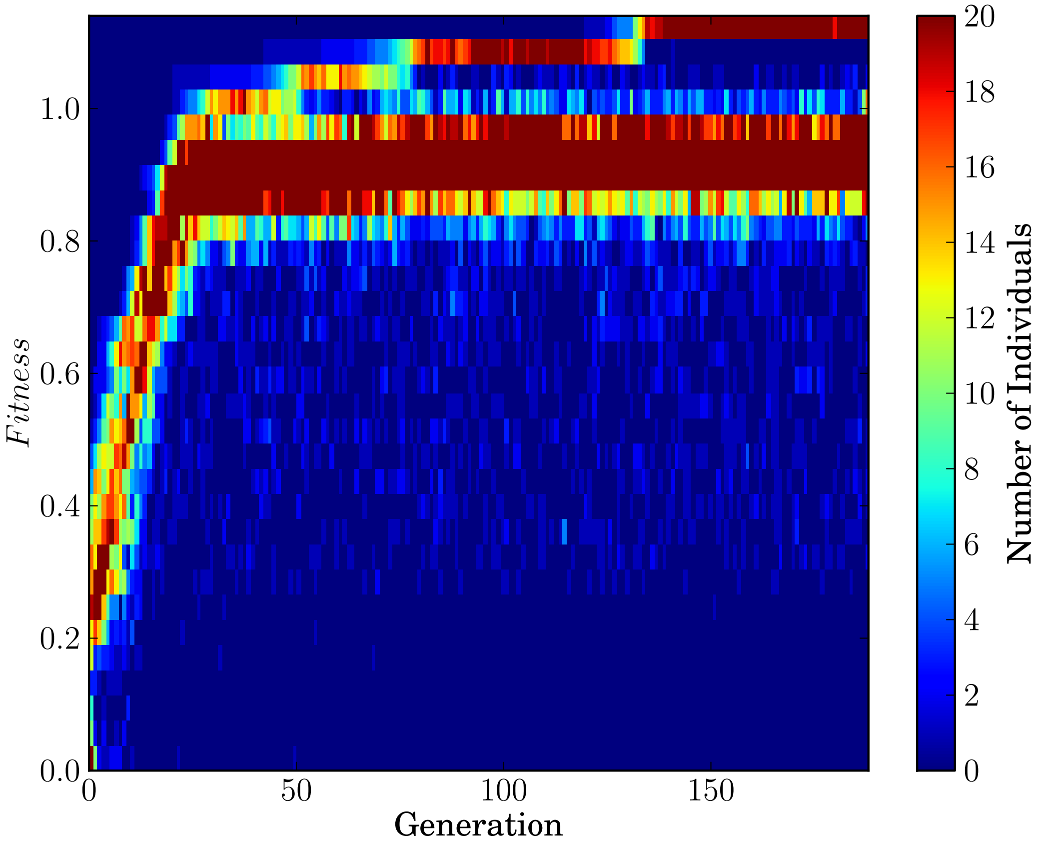

Figure 5.8 Evolution of fitness over the generations. In later generations there is a clear divide between the members that have advanced through elitism and the bulk of the population. This suggests a too high mutationrate or the convergence of the algorithm.

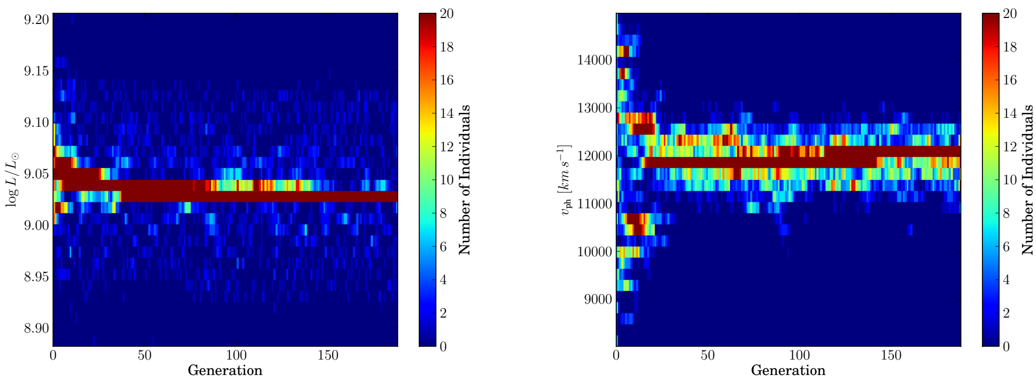

Figure 5.9 The evolution of both luminosity and photospheric velocity shows that even at late phases of the algorithm there are still new combination that are being trialled. The very quick convergence in both cases however is a bit worrisome and will be analysed in future experiments.

Figure 5.9 gives a good overview of how the genetic algorithm wanders through the parameter space. In our example the algorithm converges relatively fast (after roughly

30 generations). Even though there is a 'main'-population the algorithm still tries out different combinations. Currently we still have the problem that for certain initial random seeds the algorithm does not find the global optimum but converges prematurely on a local optimum. We believe the quick convergence seen in Figure 5.9 might be evidence for this. This again is an area of active research and two experts in evolutionary optimisation joined our team recently to address this problem.

Although there are still many outstanding problems we can show that the GAs are able to solve the SNe Ia fitting problem. In Figure 5.10 we show the best fit in the first generation as well as the best-fit in the last generation. As comparison we show the best fit obtained by Hachinger (2007). The GA has been successful in reproducing the main features of the SNe Ia-spectrum. The de-weighting in the infrared is working very well. Finally, we are currently trialing the Dalek code on different spectra with mixed results.

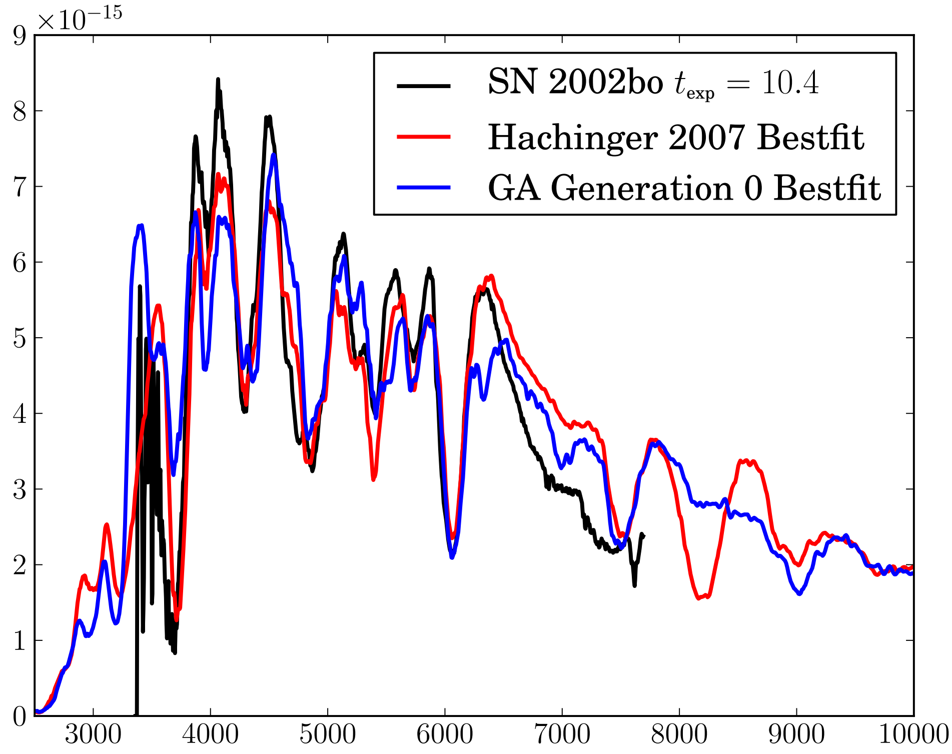

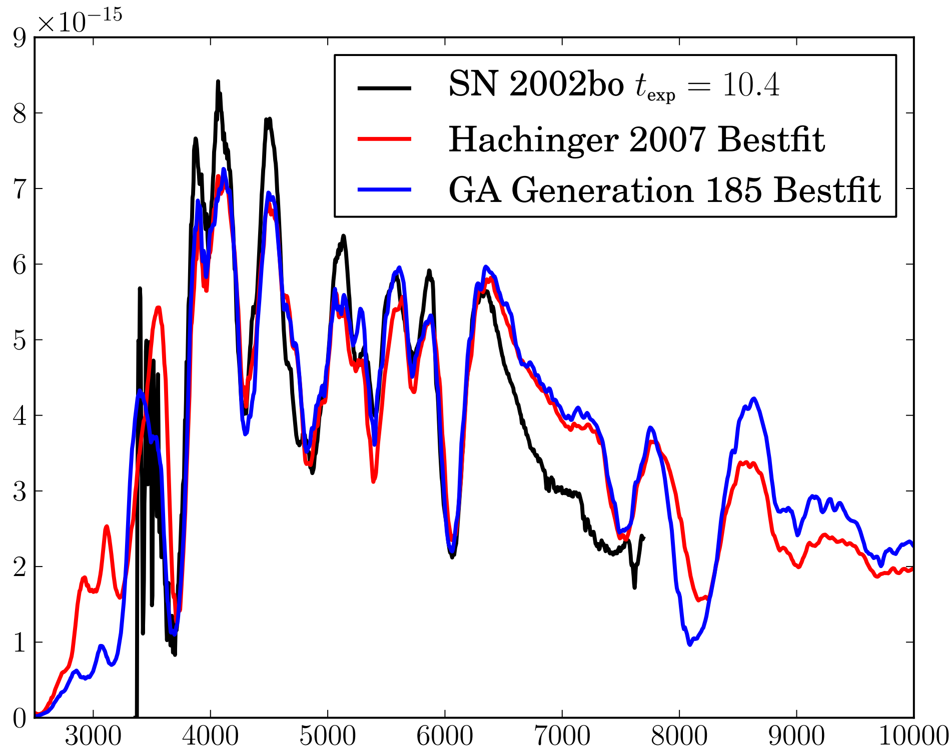

Figure 5.10 The best individual of the first generation (left) and the best individual after 185 generations (right). This initial result demonstrates that GAs are able to conquer this problem. A more stable convergence and thorough exploration of the parameter space is however necessary to use this technique on a set of supernova spectra.

5.6. Conclusion

We have completed two major steps for the automation of SNe Ia fitting. First we have written an easy API that allows many synthetic spectra to be created simultaneously on an array of machines. Secondly we have demonstrated that GA are powerful tools which can find solutions efficiently in the vast parameter space of SNe Ia spectra. We do acknowledge that our current implementation does not reliably work on all spectra and there remains lots of fine-tuning work to be done. This tweaking is very common in GA implementations, but often requires experts in numerical optimisation for speedy advancement. James Montgomery and Irene Moser are experts in evolutionary optimisation (their research focuses on differential evolutionary algorithms) and are currently exploring with our help the search space.

Once the Dalek code is able to fit spectra reliably with the current code we plan to first use this on a large set of SNe Ia spectra and explore general abundance trends. Similar to Mazzali et al. (2007) we plan to unravel the stratification and mass of the ejecta. Depending on the explosion mechanism (deflagration or detonation) we will find different elemental abundances. Either explosion mechanism will likely hint at the mass of the white dwarf just prior to explosion. This will be an important indicator for the still unsolved progenitor question addressed in the other chapters of this thesis. Finally, we will plan to extend the Dalek code to use the stratified version of the MLMC, while much more complicated, will help us to improve the models of the layered structure of SN Ia.

On a different front we are also exploring ways to optimise the parameter space exploration speed. Even on current high-end machines the MLMC takes one minute per synthetic spectrum per CPU. One of the ideas is creating a parameter grid around all or some of our search area. We could then use fast and efficient interpolation techniques (one of these is described in Chapter A) and explore different settings for our genetic algorithm much more quickly.

Over the course of this project we have realised that the field of numerical optimisation has made huge strides in the last decades. Most of the new algorithms are not well known in astronomy and are used even rarer. On the other hand experts in the field of numerical optimisation are often in desperate need for 'real world' applications. They are more than willing to apply their knowledge to problems in our field. We strongly believe that there is an important ground for collaboration that would benefit both sides immensely.

In summary, automatic analysis of SNe Ia is an important task to understand the nature of these explosions better. We have shown that through cloud-like computing and the use of GAs we can reach that goal.

CHAPTER 6

Conclusions and Future Work

On the one hand there remain many unknowns about the explosions and progenitors of SNe Ia. On the other hand, there are many question that have been answered. The community has the unified believe that the SN Ia phenomenon is caused by the explosive burning in degenerate carbon and oxygen material. This suggests with a high probability a CO-WD - a remnant of a $0.5\,M_{\odot}$ to $8\,M_{\odot}$star. Traditionally there have been two assumptions: first that a CO-WD will accrete from a main sequence to red giant companion - known as the SD-Scenario; second that this growth will end at the Chandrasekhar mass and the CO-WD will explode as a SN Ia.

Recent work by several authors (e.g. Bianco et al., 2011; Hayden et al., 2010; Maoz & Badenes, 2010) has started to suggest that at least one of these assumptions - the SD-Scenario - is unlikely to be entirely responsible for the bulk of SNe Ia. These authors often suggest the merger of two white dwarfs - known as the DD-Scenario - as the favoured scenario. Accreting mass to achieve $1.38\,M_{\odot}$ is one of the difficulties, especially in the SD-Scenario, which led some authors to speculate on a lower explosion mass of $1 - 1.2\,M_{\odot}$(e.g. Sim et al., 2010) where stars explode, rather than reaching the Chandrasekhar mass, via a detonation on the stars' surface which triggers a detonation in the stars' center.

This thesis is trying to address both the question of the progenitor as well as the explosion mass. The SD-Scenario predicts that post-explosion the companion star of a SN Ia is easily visible. In this thesis we have tried to find these companion stars, but to no avail in the two most favourable cases. Secondly to address, among other questions, the progenitor mass we have started to automate the fitting of SN Ia spectra. This technique has been applied successfully to a handful of supernovae (Mazzali et al., 2007), but is currently only possible manually. The automation is technically very challenging, but we have currently completed two milestones - the ability to calculate many solutions in a cloud-like environment and the implementation of GAs as the optimization algorithm of choice.

This thesis has contributed important pieces of the puzzle that is the SN Ia phenomenon, but the question remains: How and why do these objects explode?

6.1. Single or Double Degenerate?

The initial idea for this thesis was simple: High resolution spectroscopy and high precision astrometry of close and young SN Ia remnants should reveal the suggested donor star. At this time the only viable scenario was the SD-Scenario. The DD-Scenarios were almost unanimously believed to lead to accretion induced collapse (AIC) and not SNe Ia. The first project (Chapter 2) was to confirm Tycho-G as the progenitor of SN 1572 and then move on and find the progenitors in both SN 1006 and SN 1604.

The observations however started to show a completely different picture. The very unusual kinematics claimed for Tycho-G by Ruiz-Lapuente et al. (2004), were only slightly unusual. Comparison with the Besançon Galactic model suggested the unusual radial velocity to actually be typical if Tycho-G was placed at a distance that would make it compatible with a background interloper (see Section 2.6.1 on page 52). This problem plagues kinematic evidence, and it motivated us to find a more tangible feature. The SD-Scenario in almost any viable scenario has Roche Lobe Overflow (RLOF) as the means of mass transfer. A consequence of this mass transfer mode is tidal coupling of the donor star's rotation to the orbital rotation. This tidal coupling also implies that the rotation of the donor post-explosion is coupled to its escape velocity (see Section 2.3 on page 45 and Figure 2.2 on page 45). Most low-mass stars (spectral type later than F) rotate much less than the predicted rotational velocity of a donor post-explosion - leading to a powerful new diagnostic for donor stars. Our work in Chapter 2 indicated that Tycho-G does not have an unusually high rotation. Follow-up work with improved data (see Chapter 3) established this low rotation not only for Tycho-G but also for five other stars close the the centre of SN 1572. While this finding is not entirely without caveats, as the rotation might vanish post-explosion if the star sufficiently increases its radius. In addition, the observable is not the rotation but the projected rotation ($v_{\rm rot} \sin i$). However, if $\sin i$ would approach zero we would expect the star to have a high proper motion in the plane of the sky (because the rotation and orbit will be in the same plane). None of our candidates show such a trait (see Figure 3.1 on page 62). We have, however, found one star that exhibits very high rotation (consistent with the predictions for a donor star). However, this star (Tycho-B) is a hot A-star where high rotation is not unexpected. In addition, we found Tycho-B to have a very low spatial velocity. As the escape velocity and the rotational velocity are coupled we would expect a high spatial velocity for such a high rotation. Finally, we have calculated a distance from measurements of the surface gravity and temperature, which suggests Tycho-B to be a foreground star. We conclude that observations of the stars in the remnant of SN 1572 strongly suggest that SN 1572 has no surviving donor star.

Finally, for SN 1572 we have found one more central bright star that thus far has eluded spectroscopic scrutiny. This star (Tycho-A2 by our nomenclature) has an unusual proper motion (see Figure 3.1 on page 62) and is located very close to the X-ray center of SN 1572 making it a prime candidate. Unfortunately Tycho-A2 hides 0.4″away from the 4 magnitude brighter Tycho-A (see Figure 6.1), making it impossible to obtain ground-based optical spectroscopy, but offers the possibility for challenging infrared observations aided by adaptive-optics. We are currently running a GNIRS campaign to obtain the fundamental stellar parameters, radial velocity and rotation. Initial measurements indicate this star does not possess unusual characteristics, and may be very similar to Tycho-A.

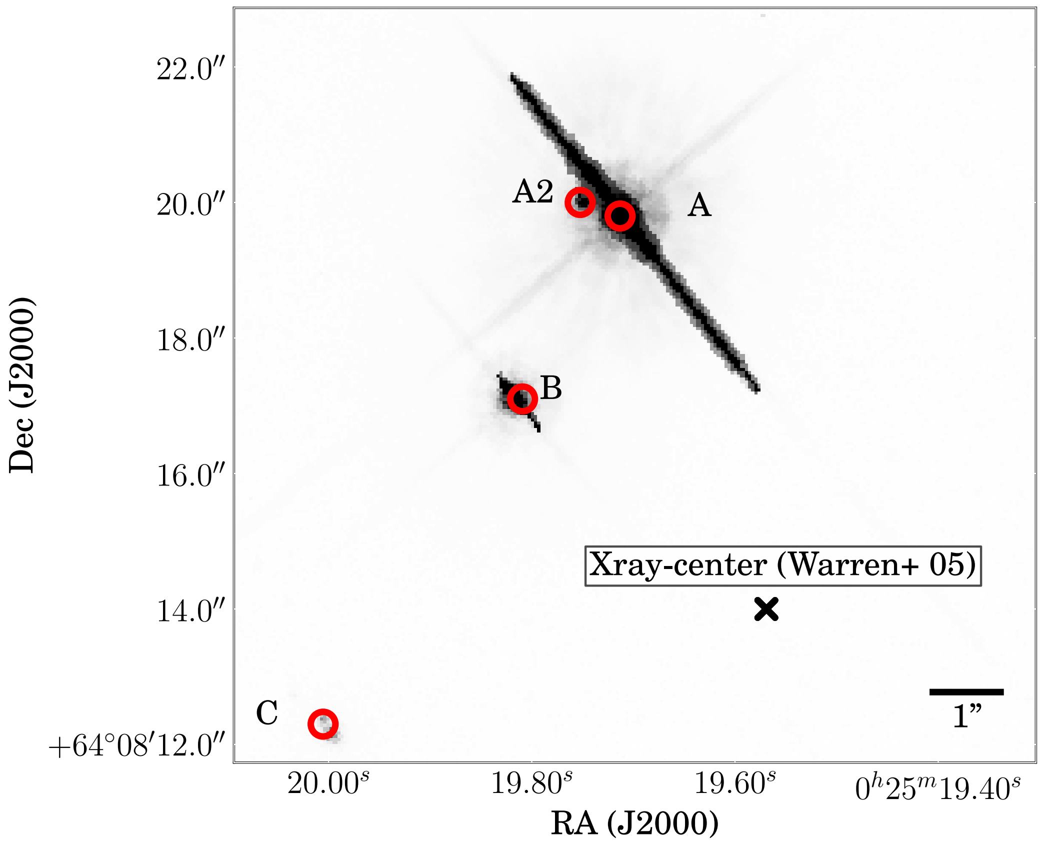

Figure 6.1 Overview of inner region of the remnant of SN1572. All labelled stars except Star-A2 have existing high-resolution spectra. Tycho-A2 is located very close to Tycho-A (0.6″). Spectroscopy can only be obtained with adaptive optics in the infrared.

The second remnant we scrutinised was SN 1006 (see Chapter 4). Using the FLAMES instrument on the VLT we obtained spectra of stars around the centre to a limiting magnitude of $V < 19$. Our primary set were stars with $V < 17.5$, resulting in complete coverage of all stars with $L(V) > 0.5L_{\odot}(V)$ at the distance of the remnant. Models predict any remaining donor star with much higher luminosity (10–100$L_{\odot}$ Marietta et al., 2000), although a range of luminosities are possible (Podsiadlowski, 2003). We have analysed our prime candidate list for $v_{\rm rot}$, effective temperature, metallicity and surface gravity and again find no stars to have unusual rotation or spatial velocity. Stars fainter than $L < 0.5\,L_{\odot}$ have not all had their parameters extracted due to their low S/N ratio, although we have identified a path to estimate these quantities from the data in hand. However, models of single degenerate progenitors do not predict donor stars of such low luminosity. These results are consistent with our finding for SN 1572 - no identifiable donor star.

The bottom line for both SN 1572 and SN 1006 seems to be that there are no remaining donor stars as predicted by the SD-Scenario's models. If SN Ia donor stars exists, they must be much different than predicted by models. Although there are always caveats, we do not think that with current theoretical knowledge and instrumentation it is worthwhile to scrutinise candidate stars in either remnant further. One exception might be the use of multi-epoch photometrically deep observations of these remnants to look for a hot white dwarf or helium star, not detectable by our current data, suggested by some new models (e.g. Fink et al., 2010).

6.2. The curious case of Kepler

The last of the young, moderately extinguished Galactic remnants, and the most distant one (Vink, 2008, estimates a distance of $\geq$ 6 kpc), is SN 1604 - also known as Kepler's supernova. The morphology of this remnant is not as clean and spherical as SN 1006 and SN 1572 (see Figure 6.2). For a long time SN 1604 was believed to be a SN Ib, but prominent iron emission in X-ray spectra (Reynolds et al., 2007) suggests this event to be a SN Ia (Hughes et al., 1995). SN 1604 shows an abundance in nitrogen which is unusual for a SN Ia, and shows evidence for circumstellar interaction (CSI). In addition, Blair et al. (1991) and Sollerman et al. (2003) find that the remnant itself possesses a very high systemic velocity of $\approx$ 250 km s^{-1}. A recent study by Chiotellis et al. (2011) suggests that a SD-Scenario with an AGB star as a donor would explain all of the observed peculiarities. In addition, Chiotellis et al. (2011) make the prediction that this star should be visible and very bright post-explosion.

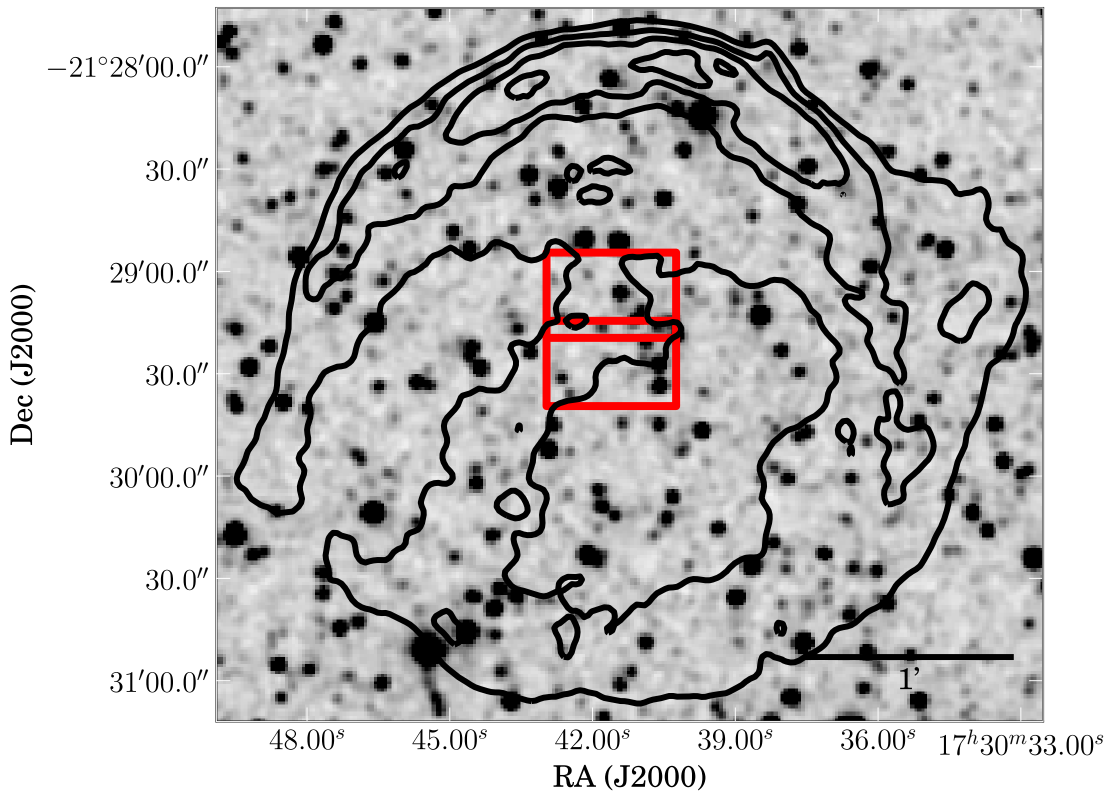

Figure 6.2 VLA contours of Kepler's remnant (SN1604) overlayed on a 2MASS image. The red rectangle show the overlapping north and south field of our WiFeS observing campaign.

We have obtained data with the WiFeS integral field spectrograph of SN 1604. The field of view for this instrument is rectangular with dimensions of $25'' \times 38''$, sampled at $1.1''$. We have two overlapping fields that cover all stars at a projected velocity of $1300\,\mathrm{km\ s^{-1}}$(assuming a distance of 6 kpc) (see Figure 6.2). Extracting stellar spectra from our poor seeing data ($> 1.5''$) is technically challenging and we have not yet attempted this work.

A very recent study (Williams et al., 2011) has suggested that a fourth SN Ia remnant has features that suggest a SD-Scenario. This remnant - RCW 86 - shows large amounts of iron in the X-ray spectrum and no central neutron star has been found potentially indicating a SN Ia event. A distance of 2.5 kpc places it between SN 1006 and SN 1572 a territory that we are very familiar with. We plan to observe this remnant, like SN 1006 with FLAMES in the coming semester.

6.3. Divide et impera

Maybe finding the progenitors of SNe Ia is too difficult using our current techniques. It might be much easier to employ the successful "Divide et Impera" - "Divide and Conquer" strategy. We believe it might be sensible to divide the question of the progenitor into accretion method and the mass of the CO-WD at the time of explosion. For the accretion method in the SD-Scenario tests seem to frequently fail (e.g. no donor in remnants, not enough supersoft X-ray sources) and for the DD-Scenario there are no strong testable predictions yet. We believe a different path - namely understanding the explosion mechanism (delayed detonation or pure detonation) and CO-WD mass at explosion might be the best way forward. In terms of explosion mass there are currently two favoured scenarios. First the explosion of a CO-WD close to Chandrasekhar mass ($1.38\,M_{\odot}$). As shown in Chapter 1 the burning of a $1.38\,M_{\odot}$ CO-WD only produces the right abundance pattern when introducing a (slightly contrived) delayed detonation. When exploding a $1\,M_{\odot}$ CO-WD this problem does not exist, a detonation of such a star produces the right optical photospheric spectrum (Sim et al., 2010). The main problem with these sub Chandrasekhar mass explosions is that there exists no incontrovertable theory for the ignition yet - however some suggestions exist (e.g. Fink et al., 2010). We believe that fitting many SN Ia spectra in the photospheric phase might yield the answer to the explosion mechanism and might help differentiate between viable explosion mechanisms through abundance patterns and mass estimates. We are currently exploring this option with the Dalek code. Another key to find the explosion mass of any given SN Ia might be the abundance of stable iron in nebular spectra. Theory predicts more iron for the Chandrasekhar mass case and less for the sub Chandrasekhar mass scenario, and that the sub Chandrasekhar mass case should produce far less stable iron group elements.

6.4. The Dalek Code

We have presented two major milestone of the automatic fitting process of SNe Ia (see Chapter 5). For the actual synthesis of the spectra we have chosen the MLMC code as it strikes the right balance between speed and accurate representation of the spectra for this task. In a first step we have wrapped the MLMC and enabled it to access a cloud-like computing environment (heterogeneous computing environment). This makes it very easy to test different optimization algorithms in a speedy and efficient manner. As the parameter space for SN Ia fitting is extremely complex and large, the automation is a technically challenging and ambitious project. We have however shown that GAs are able to solve this problem. To continue our advancement of this problem, we have added two GA experts to our team, which initially consisted only of radiative transfer experts and observers. Currently we are fine-tuning our GAs with our newfound skill base and will soon try to fit many SN Ia spectra. Similar to Mazzali et al. (2007), we hope to explore the explosion parameter space but with many more datapoints. A trend in such a dataset might then again give insights into the unanswered progenitor question.

6.5. Trouble in Paradise

During the work of this thesis the field of SN Ia research has changed significantly. When we started the donor star search there seemed little doubt in the community about the SD-Scenario. Over the recent years the SD-Scenario, however has been seriously shaken and there has been some newfound support for the DD-Scenario. The renaissance of the DD-Scenario is often based on the fact that this scenario does not provide as strong predictions as the SD-Scenario. This contention has reinvigorated the field of SN Ia progenitors and makes it a challenging but exciting area to work in.

New transient and all sky surveys are starting to drown us in a deluge of data. Currently, the astronomical community is ill equipped to deal with such large amounts of data. This is not suprising as most astronomers are experts in physics and not data processing. This problem is not unique to astronomy, more and more fields are gathering much more data than is ever processable by individuals. We believe this is a great opportunity to start cross-disciplinary research. The fundamentals of science (e.g. pattern recognition) are definitley not unique to individual areas. New areas of science like eScience are trying to provide techniques and tools for scientists irregardless of the field. We have tried to conduct cross-disciplinary research in automatically fitting SNe Ia spectra. Stephan Hachinger (the expert in manual fitting and radiative transfer) and myself initially have tried using the methods that were taught to us during our undergraduate years in physics (e.g. Newton-Raphson). These methods are still useful for very simple problems, however do not scale to today's highly non-linear problems with many correlated variables. Sam Inverso, a computer scientist working in the area of neuro-science, joined us first and helped us do our first baby-steps in GAs. His help has advanced the Dalek code to its present state. In the last half year two new members have joined the team, whose research is in numerical optimization. They are very interested in applying their techniques to 'real world' problems, which are scarce in the optimization community.

This thesis demonstrates that multidisciplinary research is not only a buzzword, but can advance individual fields of science much faster than they could advance in isolation.

Glossary

2MASS Two Micron All Sky Survey (Skrutskie et al., 2006). 49, 78, 79, 114

ACS Advanced Camera for Surveys mounted on the HST. 60
AGB Asymptotic Giant Branch. 38, 75, 114
AIC Accretion Induced Collapse. 32, 34, 111
Alpha Centauri one of the brightest stars in the night sky and a close binary. 1
AM CVn AM Canum Venaticorum star (white dwarf accreting hydrogen poor matter from a companion star; see Nelemans (2005)). 29, 38
API application program interface. 103, 110
ATLAS9 grid of stellar atmospheres (Castelli & Kurucz, 2004). 52

BAIT Berkley Automatic Imaging Telescope (Richmond et al., 1993). 6
BATSE Burst and Transient Source Experiment mounted on the Compton Gamma Ray Observatory. 8
BeppoSAX X-ray satellite named in honor of Giuseppe "Beppo" Occhialini. 8
Besançon Model Model of stellar population synthesis of the Galaxy, including kinematics. `http://model.obs-besancon.fr/`.

Cas A Cassiopeia A supernova remnant - probably a SN Ib event. 2
CCD Charged Coupled Device. 6, 22, 78
CDM Cold Dark Matter. 21
Cepheid very luminous variable star with a strong luminosity period relationship. 21
Chandra Chandra X-ray Observatory (space-based). 60, 61
CMB Cosmic Microwave Background. 21
CSI Circumstellar Interaction. 74, 75, 114
CSM Circumstellar Medium. 11, 17, 20, 28, 37, 87
CTSS Calán/Tololo Supernova Survey (Hamuy et al., 1993). 6, 22

Dalek code Automatic SN Ia spectrum fitting code. 90, 104–106, 108, 110, 115, 116
DASS Digitized Astronomy Supernova Survey (Colgate et al., 1975). 6
DD-Scenario double degenerate scenario (merging of two white dwarfs). 28, 31, 36, 38, 57, 86, 111, 115, 116

donor non-degenerate companion in the SD-Scenario. 28, 43, 57–59, 74, 77, 79, 83, 112–114
DTD delay time distribution - expected supernova rate over time after a brief outburst of starformation. 14, 23, 38

EPM Expanding Photosphere Method (Kirshner & Kwan, 1974). 21
Equivalent Width width of a rectangle that has the same area as a spectral line when taken to zero flux. 62, 64–66
ESSENCE The 'Equation of State: SupErNovae trace Cosmic Expansion' project (ESSENCE; Garnavich et al., 2002). 6
EVLA Extended Very Large Array radio telescope located in North America. 37

metallicity [Fe/H] iron abundance relative to the sun. i, 43, 65–68, 78, 84, 85, 112, 144, 153
FLAMES Multi-object, intermediate and high resolution spectrograph mounted on the VLT. 78, 79, 112, 115
FWHM Full Width Half Maximum. 49

GA genetic algorithm.
- **child** member of the new generation created by parents (members of the old generation). 101, 150
- **crossover** binary operator to create new individual from two or more old individuals. 101, 106, 147, 148, 150, 151
- **elitism** certain percentage of the fittest individuals advance unaltered to the next generation. 106, 149, 150, 153
- **fitness** goodness of fit term in Genetic Algorithms. 101, 102, 146, 148, 149, 151
- **gene** Genetic Algorithm term for an individual parameter. 146, 148–150
- **genome** describes the parameter set of an indivdual. 101, 146, 148, 150
- **genotype** vectorized representation of the parameters. 101, 146
- **individual** single representation of a parameter set. 101, 102, 106, 118, 146–152
- **mutation** unary operator to alter a newly created individual. 147, 148, 150, 151
- **parent** member of the old generation creating a child (member of the next generation). 150
- **phenotype** solution to a set of parameters. 101, 146, 148
- **roulette wheel selection** special selection function in Genetic algorithms see Figure B.2 on page 150. 106, 149, 151, 153
- **superindividual** Individual with extremely high fitness, which has only one parameter close to optimal. 148, 149

GAIA Global Astrometric Interferometer for Astrophysics (Perryman et al., 2001). 7
GH09 short for González Hernández et al. (2009). 42–44, 47, 49, 52, 54, 59, 62, 72, 73
GNIRS Gemini Near InfraRed Spectrograph mounted on the Gemini North Telescope. 112
GRB Gamma Ray Burst. 8, 20

Hα First line of the Balmer series at 6563 Å. 9, 67
HETE2 High Energy Transient Explorer. 8
HIRES High Resolution Echelle Spectrometer mounted on the Keck Telescope. 42, 59, 65
HST Hubble Space Telescope. 6, 49, 51, 55, 60, 72, 117, 121
HZSNS High Z Supernova Search, led by Brian Schmidt. 6, 22

IAU International Astronomical Union. 49
IDL Interactive Data Language. 59
IFU Optical instrument combining spectrographic and imaging capabilities, used to obtain spatially resolved spectra. 6, 121
IGE Iron Group Element. 10, 16, 18, 19, 26, 57, 95, 96, 99, 103
IME Intermediate Mass Element. 16, 18, 33, 34
INT Isaac Newton 2.5 m Telescope. 43, 49
IRAF Image Reduction and Analysis Facility maintained by NOAO. 47, 49, 59, 61, 65, 120
ISM Interstellar Medium. 23, 41, 54, 86

KAIT Katzman Automatic Imaging Telescope (Filippenko et al., 2001). 6

$L_{\mathbf{bol}}$ bolometric luminosity. 93
LIGO Laser Interferometer Gravitational Wave Observatory. 8
Advanced LIGO Advanced LIGO. 8
LISA Laser Interferometer Space Antenna (Jafry et al., 1994). 8
LMC Large Magellanic Cloud. 23
surface gravity $\log g$ gravity at the surface of a star. i, 65–68, 84, 85, 112, 144, 153
LOSS Lick Observatory Supernova Search (Li et al., 2000). 6, 10, 15
LRIS Low Resolution Imaging Spectrometer mounted on the Keck Telescope. 59, 66
LSR Local Standard of Rest. 43, 49, 52, 54, 61
LSST Large Synoptic Survey Telescope. 7
LTE Local Thermodynamic Equilibrium. 65, 66, 92

main sequence main sequence star. 74, 111
MAKEE MAuna Kea Echelle Extraction by Tom Barlow available at `http://spider.ipac.caltech.edu/staff/tab/makee/index.html`. 59
MC Monte Carlo. 68, 92–94
Chandrasekhar Mass M_{Chan} Mass when the core of a star collapses due to insufficient degeneracy pressure - for a white dwarf $\approx 1.38\,M_{\odot}$ see Chandrasekhar (1931). 13, 26, 28, 31–34, 38, 41, 111, 115
Mg I b Triplet at 5167 Å, 5173 Åand 5184 Å. 79
MIGRAD numerical gradient optimization tools - part of MINUIT. 67, 68
MINUIT collection of numerical optimization tools (James & Roos, 1975). 67, 84, 119
MLCS Multicolor Light Curve Shape method (MLCS; Riess et al., 1996). 22
MLMC Mazzali and Lucy SN Ia spectrum synthesis code. 89–95, 99, 100, 102, 103, 105, 110, 115
MOOG spectral synthesis software (Sneden, 1973). 47, 62, 65, 84

nebular approximation Assumes that the plasma condition are controlled by a central radiation source. The radiation field decreases with the distance to the source by geometrical dilution. See Mihalas (1978) for details. 92, 119
modified nebular approximation In contrast to nebular approximation where only geometrical dilution is taken into account, the modified nebular approximation also takes dilution by other radiative processes into account. 92
NIR near infrared. 12, 15, 22, 94, 97
No Free Lunch Theorem 'No Free Lunch' theorem described in Wolpert & Macready (1997). 146, 148

NSE Nuclear Statistical Equilibrium. 33

P Cygni a hypergiant luminous blue variable with strong winds. Often referred to as a description for their line profiles showing a emission peak at the rest wavelength of the line and a blue-shifted absorption trough.. 16, 19

PanSTARRS Panoramic Survey Telescope & Rapid Response System (Kaiser, 2004). 7

PPMXL PPMXL Catalog of Positions and Proper Motions on the ICRS (Roeser et al., 2010). 72, 73

PSF Point Spread Function. 49

PTF Palomar Transient Factory (Rau et al., 2009). 7

PyRAF Python wrap of IRAF maintained by STSCI. 78, 82

radiative equilibrium The net flux of energy between matter and radiation field is zero. 89, 93

RCW 86 supernova remnant sometimes associated with SN 185. 115

red giant red giant star. 58, 111

RLOF Roche Lobe Overflow (see Paczyński (1971) for a more detailed description). 28, 30, 37, 38, 57, 58, 112

RMS Root Mean Square. 49–51, 84

ROSAT short for Röntgensatellit. 60

RP04 short for Ruiz-Lapuente et al. (2004). 42–44, 46, 47, 49–52, 54, 55, 58, 60, 61, 72

RS Ophiuci white dwarf accreting from a red giant - assumed progenitor of the SD-Scenario. 29, 37, 54

SciPy Scientific Python Jones et al. (2001). 67, 144

SCP Supernova Cosmology Project, led by Saul Perlmutter. 6, 22

SD-Scenario single degenerate scenario (single white dwarf accreting from non-degenerate companion). 28, 29, 31, 36–39, 57, 58, 75, 111–117, 120, 121

SDSS Sloan Digital Sky Survey. 37

SExtractor Source Extractor photometry program (Bertin & Arnouts, 1996). 78

SFIT spectral fitting program for hot stars (Jeffery et al., 2001). 61, 64, 65

SkyMapper SkyMapper telescope (Keller et al., 2007). 7

SNLS Supernova Legacy Survey (Pain & SNLS Collaboration, 2003). 6, 37

Sobolev approximation Lines are approximation with an infinitley thin interaction region (e.g. no broadening Sobolev, 1960). 91

SSS supersoft X-ray source - believed to be emitted by nuclear fusion on a white dwarf's surface. 29, 37, 115

Supernova exploding star (plural Supernovae).

- **Remnant (SNR)** Remnant left visible post-explosion. 38, 52
- **Type Ia (SN Ia)** Thermonuclear explosion of a white dwarf - spectra show no hydrogen but a strong silicon line.
  - **02cx-like** Peculiar class of Type Ia supernovae similar to SN 2002cx (Li et al., 2003). 10
  - **91bg-like** Faint class of Type Ia supernovae similar to SN 1991bg (Filippenko et al., 1992). 10, 34, 58, 90
  - **91T-like** Luminous class of Type Ia supernovae similar to SN 1991T (Phillips et al., 1992). 10, 90

branch-normal Large homogeneous class of Type Ia Supernovae, defined in Branch et al. (1993). 9–11, 16, 23, 32, 36

HVG high velocity gradient - Type Ia supernovae with a fast evolution of photospheric velocity. 9

LVG low velocity gradient - Type Ia supernovae with a slow evolution of photospheric velocity. 9

Type Ib/c Collapse of the core of a massive star - spectrum shows no hydrogen and no silicon line. 9, 11–13, 17, 20, 23, 25, 27, 28

Type Ib Spectrum shows no hydrogen and no silicon, but helium line. 9, 11, 114, 117

Type Ic Spectrum shows no hydrogen, no silicon and no helium line. 9, 11

Type II Collapse of the core of a massive star - spectrum shows strong hydrogen line. 9–14, 16, 19–21, 23, 25, 27

SN II Linear Lightcurve shows no plateau, but linear decline. 11, 28

Type II narrow-lined (Type IIn) Spectrum shows narrow lines. 11

Type II Plateau (Type IIP) Lightcurve shows plateau. 11, 21, 28

Type IIb Spectrum shows hydrogen and helium lines. 11

Swift Swift Gamma-Ray Burst Mission. 8, 20

effective temperature T_{eff} Temperature of a blackbody emitting the same total energy. i, 15, 43, 65–68, 84, 85, 96, 112, 144, 153

time since explosion t_{exp} time since explosion (measured in days). 95, 96

Thomson scattering Scattering of photons on low energy electrons. 90, 92, 93

Urca process predominatly contributing to cooling in stars. The *Urca* process consists of alternating electron-capture and β^{-} decay of two nuclei pairs.. 33

U Scorpii white dwarf accreting from a main sequence star - assumed progenitor of the SD-Scenario. 29

UV ultra violet. 37, 67, 92, 96

VALD Vienna Atomic Line Database (Kupka et al., 2000). 66, 84

VLA Very Large Array radio telescope located in North America. 60

VLT Very Large Telescope located on Cerro Paranal (Chile). 78, 79, 112, 118

photospheric velocity v_{ph} photospheric velocity of a supernova. 9, 17, 18, 93, 96, 99, 103

radial velocity v_{rad} radial velocity. 43, 52, 72, 84, 86, 153, 160

stellar rotationv_{rot} radial velocity. 54, 62, 64, 65, 85, 86, 112, 153, 160

W7 model W7 model (Nomoto et al., 1984). 93, 98, 103

WEK09 short for Kerzendorf et al. (2009). 58, 59, 62, 72, 73

WFPC2 Wide-Field Planetary Camera 2 mounted on the HST. 49, 51

White Dwarf (WD) White Dwarf - extremely dense stellar remnant. 29, 32

Carbon/Oxygen (CO) Carbon/Oxygen White Dwarf. 29, 31–34, 41, 57, 104, 111, 115

Oxygen/Neon (ONe) Oxygen/Neon White Dwarf. 32

WiFeS Wide Field Spectrograph - IFU mounted on the 2.3 m telescope at Siding Spring Observatory. 114

Bibliography

Abramovici, A., et al. 1992, Science, 256, 325 (ADS entry)

Aldering, G., et al. 2002, in Presented at the Society of Photo-Optical Instrumentation Engineers (SPIE) Conference, Vol. 4836, Society of Photo-Optical Instrumentation Engineers (SPIE) Conference Series, ed. J. A. Tyson & S. Wolff, 61–72 (ADS entry)

Alekseev, E. N., Alekseeva, L. N., Krivosheina, I. V., & Volchenko, V. I. 1988, Phys. Lett., B205, 209

Aller, L. H., et al. 1982, Landolt-Börnstein: Numerical Data and Functional Relationships in Science and Technology (Berlin: Springer) (ADS entry)

Altavilla, G., et al. 2004, MNRAS, 349, 1344 (ADS entry)

Anderson, J., & King, I. R. 2006, PSFs, Photometry, and Astronomy for the ACS/WFC, Tech. rep. (ADS entry)

Arnett, W. D. 1969, Ap&SS, 5, 180 (ADS entry)

—. 1982, ApJ, 253, 785 (ADS entry)

Asplund, M., Grevesse, N., Sauval, A. J., & Scott, P. 2009, ARA&A, 47, 481 (ADS entry)

Astier, P., Guy, J., Pain, R., & Balland, C. 2011, A&A, 525, A7+ (ADS entry)

Baade, W. 1938, ApJ, 88, 285 (ADS entry)

Baade, W., & Zwicky, F. 1934, Proceedings of the National Academy of Science, 20, 254 (ADS entry)

Badenes, C., Borkowski, K. J., & Bravo, E. 2005, ApJ, 624, 198 (ADS entry)

Badenes, C., Borkowski, K. J., Hughes, J. P., Hwang, U., & Bravo, E. 2006, ApJ, 645, 1373 (ADS entry)

Badenes, C., Bravo, E., Borkowski, K. J., & Domínguez, I. 2003, ApJ, 593, 358 (ADS entry)

Barbary, K., et al. 2010, ArXiv e-prints (ADS entry)

Barber, C. B., Dobkin, D. P., & Huhdanpaa, H. 1996, ACM TRANSACTIONS ON MATHEMATICAL SOFTWARE, 22, 469

Barbon, R., Ciatti, F., & Rosino, L. 1979, A&A, 72, 287 (ADS entry)

Beals, C. S., & Blanchet, G. H. 1937, PASP, 49, 224 (ADS entry)

Belokurov, V. A., & Evans, N. W. 2003, MNRAS, 341, 569 (ADS entry)

Benetti, S., et al. 2004, MNRAS, 348, 261 (ADS entry)

—. 2005, ApJ, 623, 1011 (ADS entry)

Bensby, T., Feltzing, S., & Lundström, I. 2003, A&A, 410, 527 (ADS entry)

Bertin, E., & Arnouts, S. 1996, A&AS, 117, 393 (ADS entry)

Bessell, M. S. 2007, PASP, 119, 605 (ADS entry)

Bessell, M. S., Castelli, F., & Plez, B. 1998, A&A, 333, 231 (ADS entry)

Bianco, F. B., et al. 2011, ArXiv e-prints (ADS entry)

Bildsten, L., Shen, K. J., Weinberg, N. N., & Nelemans, G. 2007, ApJ, 662, L95 (ADS entry)

Bionta, R. M., Blewitt, G., Bratton, C. B., Casper, D., & Ciocio, A. 1987, Physical Review Letters, 58, 1494 (ADS entry)

Blair, W. P., Long, K. S., & Vancura, O. 1991, ApJ, 366, 484 (ADS entry)

Blake, C., et al. 2011, MNRAS, 951 (ADS entry)

Blondin, J. M., & Mezzacappa, A. 2006, ApJ, 642, 401 (ADS entry)

Blondin, S., & Tonry, J. L. 2007, ApJ, 666, 1024 (ADS entry)

Brahe, T., & Kepler, J. 1602, Tychonis Brahe Astronomiae instauratae progymnasmata : quorum haec prima pars de restitutione motuum SOLIS et lunae stellarumque inerrantium tractat, et praeterea de admiranda nova stella anno 1572 exorta luculenter agit., ed. Brahe, T. & Kepler, J. (ADS entry)

Branch, D., Fisher, A., & Nugent, P. 1993, AJ, 106, 2383 (ADS entry)

Branch, D., & Tammann, G. A. 1992, ARA&A, 30, 359 (ADS entry)

Burrows, A., Livne, E., Dessart, L., Ott, C. D., & Murphy, J. 2007, ApJ, 655, 416 (ADS entry)

Caccin, B., Cavallini, F., Ceppatelli, G., Righini, A., & Sambuco, A. M. 1985, A&A, 149, 357 (ADS entry)

Canal, R., Méndez, J., & Ruiz-Lapuente, P. 2001, ApJ, 550, L53 (ADS entry)

Cannon, R., Hambly, N., & Zacharias, N. 2001, in Astronomical Society of the Pacific Conference Series, Vol. 232, The New Era of Wide Field Astronomy, ed. R. Clowes, A. Adamson, & G. Bromage, 311–+ (ADS entry)

Cardelli, J. A., Clayton, G. C., & Mathis, J. S. 1989, ApJ, 345, 245 (ADS entry)

Casagrande, L., Ramírez, I., Meléndez, J., Bessell, M., & Asplund, M. 2010, A&A, 512, A54+ (ADS entry)

Cassam-Chenaï, G., Hughes, J. P., Ballet, J., & Decourchelle, A. 2007, ApJ, 665, 315 (ADS entry)

Castelli, F., & Kurucz, R. L. 2003, in IAU Symposium, Vol. 210, Modelling of Stellar Atmospheres, ed. N. Piskunov, W. W. Weiss, & D. F. Gray, 20P–+ (ADS entry)

Castelli, F., & Kurucz, R. L. 2004, ArXiv Astrophysics e-prints (ADS entry)

Chakraborty, U. K., & Janikow, C. Z. 2003, Information Sciences, 156, 253 , evolutionary Computation (Link)

Chandrasekhar, S. 1931, ApJ, 74, 81 (ADS entry)

Chin, Y.-N., & Huang, Y.-L. 1994, Nature, 371, 398 (ADS entry)

Chiotellis, A., Schure, K. M., & Vink, J. 2011, ArXiv e-prints (ADS entry)

Clark, D. H., & Stephenson, F. R. 1977, The historical supernovae, ed. Clark, D. H. & Stephenson, F. R. (ADS entry)

Colgate, S. A. 1974, ApJ, 187, 333 (ADS entry)

Colgate, S. A., Moore, E. P., & Carlson, R. 1975, PASP, 87, 565 (ADS entry)

Dan, M., Rosswog, S., Guillochon, J., & Ramirez-Ruiz, E. 2011, ArXiv e-prints (ADS entry)

Di Stefano, R. 2010, ApJ, 719, 474 (ADS entry)

Di Stefano, R., Kong, A., & Primini, F. A. 2006, ArXiv Astrophysics e-prints (ADS entry)

Di Stefano, R., Voss, R., & Claeys, J. S. W. 2011, ArXiv e-prints (ADS entry)

Dotani, T., Hayashida, K., Inoue, H., Itoh, M., & Koyama, K. 1987, Nature, 330, 230 (ADS entry)

Eggleton, P. P. 1983, ApJ, 268, 368 (ADS entry)

Einstein, A. 1918, Sitzungsberichte der Königlich Preußischen Akademie der Wissenschaften (Berlin), Seite 154-167., 154 (ADS entry)

Ensman, L., & Burrows, A. 1992, ApJ, 393, 742 (ADS entry)

Filippenko, A. V., Li, W. D., Treffers, R. R., & Modjaz, M. 2001, in Astronomical Society of the Pacific Conference Series, Vol. 246, IAU Colloq. 183: Small Telescope Astronomy on Global Scales, ed. B. Paczynski, W.-P. Chen, & C. Lemme, 121–+ (ADS entry)

Filippenko, A. V., et al. 1992, AJ, 104, 1543 (ADS entry)

Fink, M., Röpke, F. K., Hillebrandt, W., Seitenzahl, I. R., Sim, S. A., & Kromer, M. 2010, A&A, 514, A53+ (ADS entry)

Fisher, A. K. 2000, PhD thesis, THE UNIVERSITY OF OKLAHOMA (ADS entry)

Foley, R. J., et al. 2003, PASP, 115, 1220 (ADS entry)

Gal-Yam, A., et al. 2009, Nature, 462, 624 (ADS entry)

Galama, T. J., et al. 1998, Nature, 395, 670 (ADS entry)

Ganeshalingam, M., Li, W., & Filippenko, A. V. 2011, ArXiv e-prints (ADS entry)

Garavini, G., et al. 2007, A&A, 471, 527 (ADS entry)

Garnavich, P. M., et al. 2002, in Bulletin of the American Astronomical Society, Vol. 34, American Astronomical Society Meeting Abstracts, 1233–+ (ADS entry)

Gaskell, C. M., Cappellaro, E., Dinerstein, H. L., Garnett, D. R., Harkness, R. P., & Wheeler, J. C. 1986, ApJ, 306, L77 (ADS entry)

Genet, R. M., Boyd, L. J., & Hall, D. S. 1986, in IAU Symposium, Vol. 118, Instrumentation and Research Programmes for Small Telescopes, ed. J. B. Hearnshaw & P. L. Cottrell, 47–54 (ADS entry)

Gerardy, C. L., et al. 2004, ApJ, 607, 391 (ADS entry)

Ghavamian, P., Raymond, J., Hartigan, P., & Blair, W. P. 2000, ApJ, 535, 266 (ADS entry)

Gilfanov, M., & Bogdán, Á. 2010, Nature, 463, 924 (ADS entry)

Goldberg, D. E. 1989, Genetic Algorithms in Search, Optimization, and Machine Learning, 1st edn. (Addison-Wesley Professional) (Link)

—. 1990, Complex Systems, 5, 139

Goldberg, D. E., & Deb, K. 1991, in Foundations of Genetic Algorithms (Morgan Kaufmann), 69–93

Goldstein, B. R. 1965, AJ, 70, 105 (ADS entry)

Goldstein, B. R., & Peng Yoke, H. 1965, AJ, 70, 748 (ADS entry)

González Hernández, J. I., Ruiz-Lapuente, P., Filippenko, A. V., Foley, R. J., Gal-Yam, A., & Simon, J. D. 2009, ApJ, 691, 1 (ADS entry)

Gooch, R. 1996, in Astronomical Society of the Pacific Conference Series, Vol. 101, Astronomical Data Analysis Software and Systems V, ed. G. H. Jacoby & J. Barnes, 80–+ (ADS entry)

Gray, D. F. 1977, ApJ, 211, 198 (ADS entry)

Green, D. A., & Gull, S. F. 1984, Nature, 312, 527 (ADS entry)

Green, D. A., & Stephenson, F. R. 2003, in Lecture Notes in Physics, Berlin Springer Verlag, Vol. 598, Supernovae and Gamma-Ray Bursters, ed. K. Weiler, 7–19 (ADS entry)

Gustafsson, B., Edvardsson, B., Eriksson, K., Jørgensen, U. G., Nordlund, Å., & Plez, B. 2008, A&A, 486, 951 (ADS entry)

Gutiérrez, J., Canal, R., & García-Berro, E. 2005, A&A, 435, 231 (ADS entry)

Guy, J., et al. 2007, A&A, 466, 11 (ADS entry)

Hachinger, S. 2007, Master's thesis, TU München

—. 2011, PhD thesis, TU München

Hachinger, S., Mazzali, P. A., Tanaka, M., Hillebrandt, W., & Benetti, S. 2008, MNRAS, 389, 1087 (ADS entry)

Hachinger, S., Mazzali, P. A., Taubenberger, S., Pakmor, R., & Hillebrandt, W. 2009, MNRAS, 399, 1238 (ADS entry)

Hachisu, I., Kato, M., & Nomoto, K. 1996, ApJ, 470, L97 (Link)

Hachisu, I., Kato, M., & Nomoto, K. 1999b, ApJ, 522, 487 (ADS entry)

—. 2008, ApJ, 683, L127 (ADS entry)

Hachisu, I., Kato, M., Nomoto, K., & Umeda, H. 1999a, ApJ, 519, 314 (Link)

Hamilton, A. J. S., & Fesen, R. A. 1988, ApJ, 327, 178 (Link)

Hamilton, A. J. S., Fesen, R. A., Wu, C.-C., Crenshaw, D. M., & Sarazin, C. L. 1997, ApJ, 481, 838 (ADS entry)

Hamuy, M., Phillips, M. M., Maza, J., Suntzeff, N. B., Schommer, R. A., & Aviles, R. 1995, AJ, 109, 1 (ADS entry)

Hamuy, M., & Pinto, P. A. 2002, ApJ, 566, L63 (ADS entry)

Hamuy, M., et al. 1993, AJ, 106, 2392 (ADS entry)

Han, Z. 2008, ApJ, 677, L109 (ADS entry)

Han, Z. 2008, accepted for publication in ApJL (Link)

Han, Z., & Podsiadlowski, P. 2004, MNRAS, 350, 1301 (Link)

Hanbury Brown, R., & Hazard, C. 1952, Nature, 170, 364 (ADS entry)

Hancock, P., Gaensler, B. M., & Murphy, T. 2011, ArXiv e-prints (ADS entry)

Harkness, R. P., et al. 1987, ApJ, 317, 355 (ADS entry)

Hartwig, E. 1885, Astronomische Nachrichten, 112, 360 (ADS entry)

Hatano, K., Branch, D., Fisher, A., Baron, E., & Filippenko, A. V. 1999, ApJ, 525, 881 (ADS entry)

Hauschildt, P. H., & Baron, E. 1999, Journal of Computational and Applied Mathematics, 109, 41 (ADS entry)

Hayden, B. T., et al. 2010, ApJ, 722, 1691 (ADS entry)

Heiter, U., et al. 2002, A&A, 392, 619 (ADS entry)

Herant, M., Benz, W., Hix, W. R., Fryer, C. L., & Colgate, S. A. 1994, ApJ, 435, 339 (ADS entry)

Herbig, G. H. 1966, ZAp, 64, 512 (ADS entry)

Herbig, G. H. 1967, in IAU Symposium, Vol. 31, Radio Astronomy and the Galactic System, ed. H. van Woerden, 85–+ (ADS entry)

—. 1975, ApJ, 196, 129 (ADS entry)

—. 1995, ARA&A, 33, 19 (ADS entry)

Hernandez, J. I. G., Ruiz-Lapuente, P., Filippenko, A. V., Foley, R. J., Gal-Yam, A., & Simon, J. D. 2009, ApJ, 691, 1 (ADS entry)

Hibbins, R. E., Miles, J. R., Sarre, P. J., & Herbig, G. H. 1994, in The Diffuse Interstellar Bands, ed. A. G. G. M. Tielens, 31–+ (ADS entry)

Hicken, M., Garnavich, P. M., Prieto, J. L., Blondin, S., DePoy, D. L., Kirshner, R. P., & Parrent, J. 2007, ApJ, 669, L17 (ADS entry)

Hillebrandt, W., & Niemeyer, J. C. 2000, ARA&A, 38, 191 (ADS entry)

Hinkle, K., Wallace, L., Valenti, J., & Harmer, D. 2000, Visible and Near Infrared Atlas of the Arcturus Spectrum 3727-9300 A, ed. Hinkle, K., Wallace, L., Valenti, J., & Harmer, D. (ADS entry)

Hirashita, H., Buat, V., & Inoue, A. K. 2003, A&A, 410, 83 (ADS entry)

Hirata, K., Kajita, T., Koshiba, M., Nakahata, M., & Oyama, Y. 1987, Physical Review Letters, 58, 1490 (ADS entry)

Holland, J. H. 1962, J. ACM, 9, 297 (Link)

—. 1975, Adaptation in Natural and Artificial Systems (Ann Arbor, MI, USA: University of Michigan Press)

Horne, K. 1986, PASP, 98, 609 (ADS entry)

Howell, D. A., et al. 2006, Nature, 443, 308 (ADS entry)

Hubble, E. 1929, Proceedings of the National Academy of Science, 15, 168 (ADS entry)

Hubble, E. P. 1926, ApJ, 64, 321 (ADS entry)

Hughes, J. P. 2000, ApJ, 545, L53 (ADS entry)

Hughes, J. P., et al. 1995, ApJ, 444, L81 (ADS entry)

Iben, Jr., I., & Tutukov, A. V. 1984, ApJS, 54, 335 (ADS entry)

Iben, I. J. 1997, in NATO ASIC Proc. 486: Thermonuclear Supernovae, ed. P. Ruiz-Lapuente, R. Canal, & J. Isern (Dordrecht: Kluwer), 111 (ADS entry)

Ihara, Y., Ozaki, J., Doi, M., Shigeyama, T., Kashikawa, N., Komiyama, K., & Hattori, T. 2007, PASJ, 59, 811 (ADS entry)

Iliadis, C. 2007, Nuclear Physics of Stars, ed. Iliadis, C. (Wiley-VCH Verlag) (ADS entry)

Ilkov, M., & Soker, N. 2011, ArXiv e-prints (ADS entry)

Iwamoto, K., Brachwitz, F., Nomoto, K., Kishimoto, N., Umeda, H., Hix, W. R., & Thielemann, F.-K. 1999, ApJS, 125, 439 (ADS entry)

Jafry, Y. R., Cornelisse, J., & Reinhard, R. 1994, ESA Journal, 18, 219 (ADS entry)

James, F., & Roos, M. 1975, Comput. Phys. Commun., 10, 343

Janikow, C. Z., & Michalewicz, Z. 1991, in Proc. of the 4th International Conference on Genetic Algorithms, ed. R. K. Belew & L. B. Booker (Morgan Kaufmann), 151–157

Jeffery, C. S., Woolf, V. M., & Pollacco, D. L. 2001, A&A, 376, 497 (ADS entry)

Jeffery, D. J., Ketchum, W., Branch, D., Baron, E., Elmhamdi, A., & Danziger, I. J. 2007, ApJS, 171, 493 (ADS entry)

Jenniskens, P., & Desert, F. 1994, A&AS, 106, 39 (ADS entry)

Jha, S., Riess, A. G., & Kirshner, R. P. 2007, ApJ, 659, 122 (ADS entry)

Jones, E., Oliphant, T., Peterson, P., et al. 2001, SciPy: Open source scientific tools for Python (Link)

Justham, S. 2011, ApJ, 730, L34+ (ADS entry)

Justham, S., Wolf, C., Podsiadlowski, P., & Han, Z. 2008, submitted

—. 2009, A&A, 493, 1081 (ADS entry)

Kaiser, N. 2004, in Presented at the Society of Photo-Optical Instrumentation Engineers (SPIE) Conference, Vol. 5489, Society of Photo-Optical Instrumentation Engineers (SPIE) Conference Series, ed. J. M. Oschmann Jr., 11–22 (ADS entry)

Karle, A. 2008, in International Cosmic Ray Conference, Vol. 4, International Cosmic Ray Conference, 835–838 (ADS entry)

Kasen, D. 2006, ApJ, 649, 939 (ADS entry)

—. 2010, ApJ, 708, 1025 (ADS entry)

Kasen, D., Röpke, F. K., & Woosley, S. E. 2009, Nature, 460, 869 (ADS entry)

Kasen, D., Thomas, R. C., & Nugent, P. 2006, ApJ, 651, 366 (ADS entry)

Keller, S. C., et al. 2007, PASA, 24, 1 (ADS entry)

Kepler, J. 1606, De Stella nova in pede Serpentarii

Kepler, S. O., Kleinman, S. J., Nitta, A., Koester, D., Castanheira, B. G., Giovannini, O., Costa, A. F. M., & Althaus, L. 2007, MNRAS, 375, 1315 (ADS entry)

Kerzendorf, W. E., Schmidt, B. P., Asplund, M., Nomoto, K., Podsiadlowski, P., Frebel, A., Fesen, R. A., & Yong, D. 2009, ApJ, 701, 1665 (ADS entry)

Kirshner, R. P., & Kwan, J. 1974, ApJ, 193, 27 (ADS entry)

Klebesadel, R. W., Strong, I. B., & Olson, R. A. 1973, ApJ, 182, L85+ (ADS entry)

Klein, R. I., & Chevalier, R. A. 1978, ApJ, 223, L109 (ADS entry)

Kobayashi, C., Umeda, H., Nomoto, K., Tominaga, N., & Ohkubo, T. 2006, ApJ, 653, 1145 (ADS entry)

Komatsu, E., et al. 2011, ApJS, 192, 18 (ADS entry)

Kowal, C. T. 1968, AJ, 73, 1021 (ADS entry)

Kozma, C., Fransson, C., Hillebrandt, W., Travaglio, C., Sollerman, J., Reinecke, M., Röpke, F. K., & Spyromilio, J. 2005, A&A, 437, 983 (ADS entry)

Krause, O., Tanaka, M., Usuda, T., Hattori, T., Goto, M., Birkmann, S., & Nomoto, K. 2008, Nature, 456, 617 (ADS entry)

Kreinovich, V., Quintana, C., & Fuentes, O. 1993, Cybernetics and Systems: an International Journal, 24, 9

Kromer, M., & Sim, S. A. 2009, MNRAS, 398, 1809 (ADS entry)

Kupka, F. G., Ryabchikova, T. A., Piskunov, N. E., Stempels, H. C., & Weiss, W. W. 2000, Baltic Astronomy, 9, 590 (ADS entry)

Kurucz, R., & Bell, B. 1995, Atomic Line Data (R.L. Kurucz and B. Bell) Kurucz CD-ROM No. 23. Cambridge, Mass.: Smithsonian Astrophysical Observatory, 1995., 23 (ADS entry)

Kurucz, R. L., Furenlid, I., Brault, J., & Testerman, L. 1984, Solar flux atlas from 296 to 1300 nm, ed. Kurucz, R. L., Furenlid, I., Brault, J., & Testerman, L. (ADS entry)

Leibundgut, B., & Tammann, G. A. 1990, A&A, 230, 81 (ADS entry)

Leloudas, G., et al. 2009, A&A, 505, 265 (ADS entry)

Leonard, D. C. 2007, ApJ, 670, 1275 (ADS entry)

Lesaffre, P., Podsiadlowski, P., & Tout, C. A. 2005, Nuclear Physics A, 758, 463 (ADS entry)

Li, W., et al. 2003, PASP, 115, 453 (ADS entry)

—. 2011, MNRAS, 412, 1441 (ADS entry)

Li, W. D., et al. 2000, in American Institute of Physics Conference Series, Vol. 522, American Institute of Physics Conference Series, ed. S. S. Holt & W. W. Zhang, 103–106 (ADS entry)

Li, X.-D., & van den Heuvel, E. P. J. 1997, A&A, 322, L9 (Link)

Livne, E. 1990, ApJ, 354, L53 (ADS entry)

Livne, E., & Arnett, D. 1995, ApJ, 452, 62 (ADS entry)

Maeda, K., Taubenberger, S., Sollerman, J., Mazzali, P. A., Leloudas, G., Nomoto, K., & Motohara, K. 2010, ApJ, 708, 1703 (ADS entry)

Mandel, K. S., Narayan, G., & Kirshner, R. P. 2011, ApJ, 731, 120 (ADS entry)

Mannucci, F., Della Valle, M., & Panagia, N. 2006, MNRAS, 370, 773 (ADS entry)

Mannucci, F., Della Valle, M., Panagia, N., Cappellaro, E., Cresci, G., Maiolino, R., Petrosian, A., & Turatto, M. 2005, A&A, 433, 807 (ADS entry)

Maoz, D., & Badenes, C. 2010, MNRAS, 407, 1314 (ADS entry)

Maoz, D., Sharon, K., & Gal-Yam, A. 2010, ApJ, 722, 1879 (ADS entry)

Marietta, E., Burrows, A., & Fryxell, B. 2000, ApJS, 128, 615 (ADS entry)

Matheson, T., Filippenko, A. V., Ho, L. C., Barth, A. J., & Leonard, D. C. 2000, AJ, 120, 1499 (ADS entry)

Mazzali, P. A. 2000, A&A, 363, 705 (ADS entry)

Mazzali, P. A., & Lucy, L. B. 1993, A&A, 279, 447 (ADS entry)

Mazzali, P. A., Röpke, F. K., Benetti, S., & Hillebrandt, W. 2007, Science, 315, 825 (ADS entry)

Mazzali, P. A., Sauer, D. N., Pastorello, A., Benetti, S., & Hillebrandt, W. 2008, MNRAS, 386, 1897 (ADS entry)

Mazzali, P. A., et al. 2005, ApJ, 623, L37 (ADS entry)

Meegan, C. A., Fishman, G. J., Wilson, R. B., Horack, J. M., Brock, M. N., Paciesas, W. S., Pendleton, G. N., & Kouveliotou, C. 1992, Nature, 355, 143 (ADS entry)

Meikle, W. P. S. 2000, MNRAS, 314, 782 (ADS entry)

Mennekens, N., Vanbeveren, D., De Greve, J. P., & De Donder, E. 2010, A&A, 515, A89+ (ADS entry)

Michalewicz, Z. 1994, Genetic algorithms + data structures = evolution programs (2nd, extended ed.) (New York, NY, USA: Springer-Verlag New York, Inc.)

Mihalas, D. 1978, Stellar atmospheres /2nd edition/, ed. Hevelius, J. (ADS entry)

Miller, D. L., & Branch, D. 1990, AJ, 100, 530 (ADS entry)

Minkowski, R. 1941, PASP, 53, 224 (ADS entry)

Miyaji, S., Nomoto, K., Yokoi, K., & Sugimoto, D. 1980, PASJ, 32, 303 (ADS entry)

Munari, U., Sordo, R., Castelli, F., & Zwitter, T. 2005, A&A, 442, 1127 (ADS entry)

Nelemans, G. 2005, in Astronomical Society of the Pacific Conference Series, Vol. 330, The Astrophysics of Cataclysmic Variables and Related Objects, ed. J.-M. Hameury & J.-P. Lasota, 27–+ (ADS entry)

Nelemans, G. 2010, http://www.lorentzcenter.nl/lc/web/2010/391/presentations/Nelemans.pdf

Noguchi, K., Ando, H., Izumiura, H., Kawanomoto, S., Tanaka, W., & Aoki, W. 1998, in Proc. SPIE, Optical Astronomical Instrumentation, ed. S. D'Odorico, Vol. 3355, 354 (ADS entry)

Nomoto, K. 1982, ApJ, 253, 798 (Link)

Nomoto, K., & Kondo, Y. 1991, ApJ, 367, L19 (ADS entry)

Nomoto, K., Saio, H., Kato, M., & Hachisu, I. 2007, ApJ, 663, 1269 (Link)

Nomoto, K., Thielemann, F.-K., & Yokoi, K. 1984, ApJ, 286, 644 (ADS entry)

Norgaard-Nielsen, H. U., Hansen, L., Jorgensen, H. E., Aragon Salamanca, A., & Ellis, R. S. 1989, Nature, 339, 523 (ADS entry)

Nugent, P., Phillips, M., Baron, E., Branch, D., & Hauschildt, P. 1995, ApJ, 455, L147+ (ADS entry)

Nugent, P., et al. 2006, ApJ, 645, 841 (ADS entry)

Oke, J. B., Cohen, J. G., Carr, M., et al. 1995, PASP, 107, 375 (ADS entry)

Ozaki, J., & Shigeyama, T. 2006, ApJ, 644, 954 (Link)

Paczyński, B. 1971, ARA&A, 9, 183 (ADS entry)

Pain, R., & SNLS Collaboration. 2003, in Bulletin of the American Astronomical Society, Vol. 35, American Astronomical Society Meeting Abstracts, 1335–+ (ADS entry)

Pakmor, R., Kromer, M., Röpke, F. K., Sim, S. A., Ruiter, A. J., & Hillebrandt, W. 2010, Nature, 463, 61 (ADS entry)

Pakmor, R., Röpke, F. K., Weiss, A., & Hillebrandt, W. 2008, A&A, 489, 943 (ADS entry)

Patat, F., Chugai, N. N., Podsiadlowski, P., Mason, E., Melo, C., & Pasquini, L. 2011, A&A, 530, A63+ (ADS entry)

Patat, F., et al. 2007, Science, 317, 924 (ADS entry)

Perlmutter, S., et al. 1995, NASA STI/Recon Technical Report N, 96, 29501 (ADS entry)

—. 1999, ApJ, 517, 565 (ADS entry)

Perryman, M. A. C., et al. 2001, A&A, 369, 339 (ADS entry)

Phillips, M. M. 1993, ApJ, 413, L105 (ADS entry)

Phillips, M. M., Wells, L. A., Suntzeff, N. B., Hamuy, M., Leibundgut, B., Kirshner, R. P., & Foltz, C. B. 1992, AJ, 103, 1632 (ADS entry)

Pietrinferni, A., Cassisi, S., Salaris, M., & Castelli, F. 2004, ApJ, 612, 168 (ADS entry)

Pinto, P. A., & Eastman, R. G. 2000, ApJ, 530, 757 (ADS entry)

Pinto, P. A., et al. 2006, in Bulletin of the American Astronomical Society, Vol. 38, American Astronomical Society Meeting Abstracts, 1017–+ (ADS entry)

Podsiadlowski, P. 2003 (ADS entry)

Podsiadlowski, P., Joss, P. C., & Hsu, J. J. L. 1992, ApJ, 391, 246 (ADS entry)

Quimby, R., Höflich, P., Kannappan, S. J., Rykoff, E., Rujopakarn, W., Akerlof, C. W., Gerardy, C. L., & Wheeler, J. C. 2006, ApJ, 636, 400 (ADS entry)

Ramírez, S. V., & Cohen, J. G. 2002, AJ, 123, 3277 (ADS entry)

Rau, A., et al. 2009, PASP, 121, 1334 (ADS entry)

Rechenberg, I. 1973, Evolutionsstrategie : Optimierung technischer Systeme nach Prinzipien der biologischen Evolution, Problemata No. 15 (Stuttgart-Bad Cannstatt: Frommann-Holzboog)

Reddy, B. E., Tomkin, J., Lambert, D. L., & Allende Prieto, C. 2003, MNRAS, 340, 304 (ADS entry)

Rest, A., et al. 2005, Nature, 438, 1132 (ADS entry)

—. 2008a, ApJ, 681, L81 (ADS entry)

—. 2008b, ApJ, 680, 1137 (ADS entry)

—. 2011, ApJ, 732, 3 (ADS entry)

Reynolds, S. P., Borkowski, K. J., Green, D. A., Hwang, U., Harrus, I., & Petre, R. 2008, ApJ, 680, L41 (ADS entry)

Reynolds, S. P., Borkowski, K. J., Hwang, U., Hughes, J. P., Badenes, C., Laming, J. M., & Blondin, J. M. 2007, ApJ, 668, L135 (ADS entry)

Reynoso, E. M., Moffett, D. A., Goss, W. M., Dubner, G. M., Dickel, J. R., Reynolds, S. P., & Giacani, E. B. 1997, ApJ, 491, 816 (ADS entry)

Richmond, M., Treffers, R. R., & Filippenko, A. V. 1993, PASP, 105, 1164 (ADS entry)

Riess, A. G., Press, W. H., & Kirshner, R. P. 1996, ApJ, 473, 88 (ADS entry)

Riess, A. G., et al. 1998, AJ, 116, 1009 (ADS entry)

—. 1999, AJ, 118, 2675 (ADS entry)

Ritossa, C., Garcia-Berro, E., & Iben, Jr., I. 1996, ApJ, 460, 489 (ADS entry)

Robin, A. C., Reylé, C., Derrière, S., & Picaud, S. 2003, A&A, 409, 523 (ADS entry)

Roelofs, G., Bassa, C., Voss, R., & Nelemans, G. 2008, MNRAS, 391, 290 (ADS entry)

Roeser, S., Demleitner, M., & Schilbach, E. 2010, AJ, 139, 2440 (ADS entry)

Röpke, F. K., & Bruckschen, R. 2008, New Journal of Physics, 10, 125009 (ADS entry)

Röpke, F. K., & Hillebrandt, W. 2005, A&A, 431, 635 (ADS entry)

Rudolph, G. 1994, Neural Networks, IEEE Transactions on, 5, 96 (Link)

Ruiter, A. J., Belczynski, K., & Fryer, C. 2009, ApJ, 699, 2026 (ADS entry)

Ruiz-Lapuente, P. 2004, ApJ, 612, 357 (ADS entry)

Ruiz-Lapuente, P., et al. 2004, Nature, 431, 1069 (ADS entry)

Saio, H., & Nomoto, K. 1985, A&A, 150, L21 (ADS entry)

Scalzo, R. A., et al. 2010, ApJ, 713, 1073 (ADS entry)

Schlegel, E. M. 1990, MNRAS, 244, 269 (ADS entry)

Schmidt, B. P., Kirshner, R. P., Eastman, R. G., Phillips, M. M., Suntzeff, N. B., Hamuy, M., Maza, J., & Aviles, R. 1994a, ApJ, 432, 42 (ADS entry)

Schmidt, B. P., Kirshner, R. P., Leibundgut, B., Wells, L. A., Porter, A. C., Ruiz-Lapuente, P., Challis, P., & Filippenko, A. V. 1994b, ApJ, 434, L19 (ADS entry)

Schmidt, W., Ciaraldi-Schoolmann, F., Niemeyer, J. C., Röpke, F. K., & Hillebrandt, W. 2010, ApJ, 710, 1683 (ADS entry)

Schweizer, F., & Middleditch, J. 1980, ApJ, 241, 1039 (ADS entry)

Shigeyama, T., Nomoto, K., Yamaoka, H., & Thielemann, F.-K. 1992, ApJ, 386, L13 (ADS entry)

Silverman, J. M., Ganeshalingam, M., Li, W., Filippenko, A. V., Miller, A. A., & Poznanski, D. 2011, MNRAS, 410, 585 (ADS entry)

Sim, S. A., Röpke, F. K., Hillebrandt, W., Kromer, M., Pakmor, R., Fink, M., Ruiter, A. J., & Seitenzahl, I. R. 2010, ApJ, 714, L52 (ADS entry)

Skrutskie, M. F., et al. 2006, ApJ, 131, 1163 (ADS entry)

Smartt, S. J. 2009, ARA&A, 47, 63 (ADS entry)

Sneden, C. 1973, ApJ, 184, 839 (ADS entry)

Sobolev, V. V. 1960, Moving envelopes of stars, ed. Sobolev, V. V. (ADS entry)

Soderberg, A. M., Nakar, E., Berger, E., & Kulkarni, S. R. 2006, ApJ, 638, 930 (ADS entry)

Soderberg, A. M., et al. 2008, Nature, 453, 469 (ADS entry)

—. 2010, Nature, 463, 513 (ADS entry)

Sollerman, J., Ghavamian, P., Lundqvist, P., & Smith, R. C. 2003, A&A, 407, 249 (ADS entry)

Sorokina, E. I., Blinnikov, S. I., Kosenko, D. I., & Lundqvist, P. 2004, Astronomy Letters, 30, 737 (ADS entry)

Staelin, D. H., & Reifenstein, III, E. C. 1968, Science, 162, 1481 (ADS entry)

Stehle, M., Mazzali, P. A., Benetti, S., & Hillebrandt, W. 2005, MNRAS, 360, 1231 (ADS entry)

Sternberg, A., et al. 2011, ArXiv e-prints (ADS entry)

Strolger, L.-G., et al. 2004, ApJ, 613, 200 (ADS entry)

Sullivan, M., et al. 2011, ArXiv e-prints (ADS entry)

Sunyaev, R., et al. 1987, Nature, 330, 230 (ADS entry)

Tammann, G. A., Loeffler, W., & Schroeder, A. 1994, ApJS, 92, 487 (ADS entry)

Tanaka, M., Mazzali, P. A., Maeda, K., & Nomoto, K. 2006, ApJ, 645, 470 (ADS entry)

Tanaka, M., Mazzali, P. A., Stanishev, V., Maurer, I., Kerzendorf, W. E., & Nomoto, K. 2011, MNRAS, 410, 1725 (ADS entry)

Tanaka, M., et al. 2010, ApJ, 714, 1209 (ADS entry)

Taubenberger, S., et al. 2011, MNRAS, 412, 2735 (ADS entry)

Thomas, R. C., Branch, D., Baron, E., Nomoto, K., Li, W., & Filippenko, A. V. 2004, ApJ, 601, 1019 (ADS entry)

Tonry, J., & Davis, M. 1979, AJ, 84, 1511 (ADS entry)

Totani, T., Morokuma, T., Oda, T., Doi, M., & Yasuda, N. 2008, PASJ, 60, 1327 (ADS entry)

Tucker, B. E. 2011, Ap&SS, 40 (ADS entry)

Turatto, M. 2003, in Lecture Notes in Physics, Berlin Springer Verlag, Vol. 598, Supernovae and Gamma-Ray Bursters, ed. K. Weiler, 21–36 (ADS entry)

Turatto, M., Benetti, S., & Pastorello, A. 2007, in American Institute of Physics Conference Series, Vol. 937, Supernova 1987A: 20 Years After: Supernovae and Gamma-Ray Bursters, ed. S. Immler, K. Weiler, & R. McCray, 187–197 (ADS entry)

Umeda, H., & Yoshida, T. 2010, in American Institute of Physics Conference Series, Vol. 1279, American Institute of Physics Conference Series, ed. N. Kawai & S. Nagataki, 171–178 (ADS entry)

van den Bergh, S. 1960, ZAp, 49, 201 (ADS entry) van den Bergh, S., & Tammann, G. A. 1991, ARA&A, 29, 363 (ADS entry)

van den Heuvel, E. P. J., Bhattacharya, D., Nomoto, K., & Rappaport, S. A. 1992, A&A, 262, 97 (ADS entry)

van Dokkum, P. G. 2001, PASP, 113, 1420 (ADS entry)

van Dyk, S. D., Treffers, R. R., Richmond, M. W., Filippenko, A. V., & Paik, Y. 1994, in Bulletin of the American Astronomical Society, Vol. 26, American Astronomical Society Meeting Abstracts, 1444–+ (ADS entry)

van Kerkwijk, M. H., Chang, P., & Justham, S. 2010, ApJ, 722, L157 (ADS entry)

Vink, J. 2008, ApJ, 689, 231 (ADS entry)

Vogt, F., & Wagner, A. 2011, Astrophysics and Space Science, submitted.

Vogt, S. S., et al. 1994, in Presented at the Society of Photo-Optical Instrumentation Engineers (SPIE) Conference, Vol. 2198, Society of Photo-Optical Instrumentation Engineers (SPIE) Conference Series, ed. D. L. Crawford & E. R. Craine, 362–+ (ADS entry)

Voss, R., & Nelemans, G. 2008, Nature, 451, 802 (ADS entry)

Walborn, N. R., Prevot, M. L., Prevot, L., Wamsteker, W., Gonzalez, R., Gilmozzi, R., & Fitzpatrick, E. L. 1989, A&A, 219, 229 (ADS entry)

Warren, J. S., et al. 2005, ApJ, 634, 376 (ADS entry)

Webbink, R. F. 1984, ApJ, 277, 355 (ADS entry)

Wehrse, R. 1974, A list of all Fraunhofer lines of the Rowland tables arranged by elements (Heidelberg: Universität) (ADS entry)

Whelan, J., & Iben, Jr., I. 1973, ApJ, 186, 1007 (ADS entry)

Whitley, D. 1994, Statistics and Computing, 4, 65

Williams, B. J., et al. 2011, ArXiv e-prints (ADS entry)

Wilson, R. 1958, ApJ, 128, 57 (ADS entry)

Winkler, P. F., Gupta, G., & Long, K. S. 2003, ApJ, 585, 324 (ADS entry)

Winkler, P. F., Long, K. S., Hamilton, A. J. S., & Fesen, R. A. 2005, ApJ, 624, 189 (ADS entry)

Wolpert, D., & Macready, W. G. 1997, IEEE Trans. Evolutionary Computation, 1, 67

Wood-Vasey, W. M., et al. 2008, ApJ, 689, 377 (ADS entry)

Woosley, S. E., Heger, A., & Weaver, T. A. 2002, Reviews of Modern Physics, 74, 1015 (ADS entry)

Woosley, S. E., Kasen, D., Blinnikov, S., & Sorokina, E. 2007, ApJ, 662, 487 (ADS entry)

Wright, A. H. 1991, in Foundations of Genetic Algorithms (Morgan Kaufmann), 205–218

Wu, C.-C., Crenshaw, D. M., Fesen, R. A., Hamilton, A. J. S., & Sarazin, C. L. 1993, ApJ, 416, 247 (ADS entry)

Wu, C.-C., Crenshaw, D. M., Hamilton, A. J. S., Fesen, R. A., Leventhal, M., & Sarazin, C. L. 1997, ApJ, 477, L53+ (ADS entry)

Wu, C.-C., Leventhal, M., Sarazin, C. L., & Gull, T. R. 1983, ApJ, 269, L5 (ADS entry)

Xu, D., et al. 2009, ApJ, 696, 971 (ADS entry)

Yamanaka, M., et al. 2009, ApJ, 707, L118 (ADS entry)

Yong, D., Lambert, D. L., Paulson, D. B., & Carney, B. W. 2008, ApJ, 673, 854 (ADS entry)

Yoon, S.-C., & Langer, N. 2004, A&A, 419, 623 (ADS entry)

—. 2005, A&A, 435, 967 (ADS entry)

Yu, S., & Jeffery, C. S. 2010, A&A, 521, A85+ (ADS entry)

Zhang, B., Dai, X., Lloyd-Ronning, N. M., & Mészáros, P. 2004, ApJ, 601, L119 (ADS entry)

Zhao, F., Strom, R. G., & Jiang, S. 2006, Chinese J. Astron. Astrophys., 6, 635 (ADS entry)

Zwicky, F. 1938, ApJ, 88, 529 (ADS entry)

—. 1940, Reviews of Modern Physics, 12, 66 (ADS entry)

APPENDIX A

Linear interpolation in N Dimensions

Interpolation is one of the most common operations in astronomy. Resampling spectra to a different wavelength grid, projecting images or interpolating physical quantities in n-dimensional fluid dynamics simulation are all examples of interpolation. Interpolation can be described as a special case of curve fitting which requires the function to go through all points.

In one dimension interpolation is relatively easy and there exist multiple methods. The simplest method is nearest-neighbour interpolation in which the algorithm picks the closest neighbour point to the point to be interpolated.

Linear interpolation is one of the most common methods of interpolation. The two neighbouring points of the point to be interpolated are found and their slope and offset is used to obtain the interpolated point.

A more sophisticated approach is the spline-method of interpolation. Splines are piecewise polynomials of n-th degree whose first and second derivation are the same at the data points.

In one dimensional space there exists an abundance of interpolation methods. This multitude of options decreases rapidly with increasing number of dimensions. We will focus on the implementation of linear interpolation in N-dimensions, although there are a few other options like nearest neighbour interpolation and radial basis function.

For our linear interpolation we have opted to use Delauney Triangulation as a interpolation method. The interpolation involves multiple steps to arrive at an interpolation solution: At first a Delauney Triangulation is performed on the existing points. As a next step we need to find the simplex(geometric structure; a triangle in two dimensions) that contains the point to be interpolated. Finally we will use the barycentric coordinate system of the simplex to perform the actual interpolation.

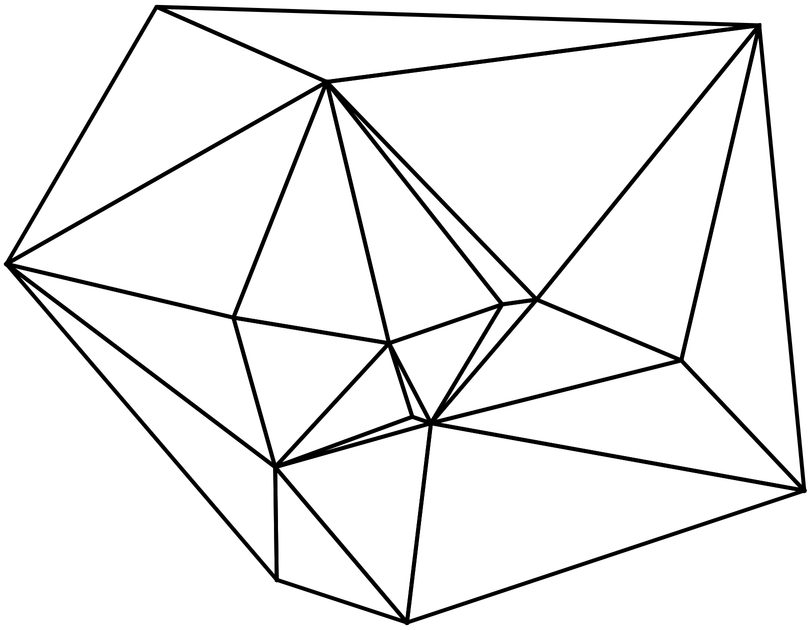

Figure A.1 Delauney Triangulation of 20 points in two dimensions.

A.1. Delauney triangulation

A triangulation is the process of connecting all points in a set with straight lines without any two lines crossing (see Figure A.1). It is obvious that there many ways for a set to be triangulated. All triangulations however have the same outer boundary called the convex hull. One special kind of triangulation is the Delauney Triangulation. The Delauney Triangulation can be defined a various abstract ways and has intriguing properties.

For a description of the process we will limit ourselves to two dimensions. This process is expandable to n dimensions in which the triangles become geometric structures called n-simplices. One such defintion is that the circum-circle (circle going through all three points of the triangle) of each triangle must only contain three points. Figure A.2, a simple example, shows one *legal* triangulation and one *illegal* triangulation. One can see in the *illegal* triangulation that the circum-circles of both triangles contain more than tree points. By doing a simple "*edge-flip*" one arrives at the Delauney Triangulation. In addition this ensures that the triangulation gives the largest minimum angle for both triangles.

Delauney Triangulation and convex hulls have a very interesting relation. It is possible construct the Delauney Triangulation in n dimensions from a convex hull of the points projected on a paraboloid in n+1 dimensions. Figure A.3 shows an example of a Delauney Triangulation in two dimensions constructed from the convex hull in three dimensions. To project the points onto the paraboloid one just square sums the coordinates n dimensions

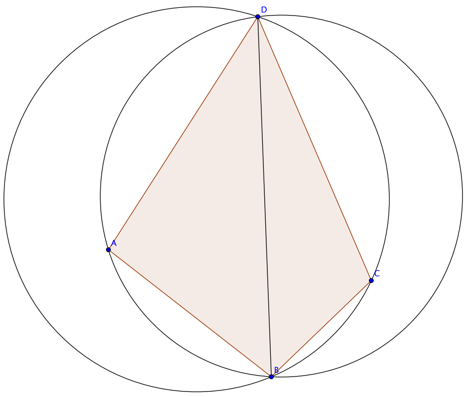

Figure A.2 The left figure shows an '*illegal*' triangulation of the 4 points. Both circles include all the points. With a so called edge flip one can arrive at a '*legal*' triangulation.

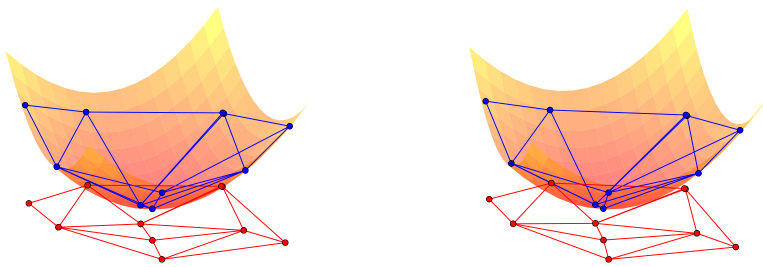

Figure A.3 Stereogram (produced using a method described in Vogt & Wagner, 2011) of the projection of the convex hull in three dimensions to form the Delauney Triangulation in two dimensions.

and uses this as the coordinate for the point in n+1 dimensions.

A.2. Convex Hull

In section A.1 we have described the relation between the convex hull and the Delauney Triangulation. There are multiple ways to construct the convex hull for N points, we will limit ourselves to the description of the Quickhull algorithm (Barber et al., 1996). Similar to the Quicksort algorithm it follows the divide and conquer strategy.

As an initial input we have N data points. Although this method works in n-dimensions, we will show an example in two dimensions. The first operation is finding the two extreme

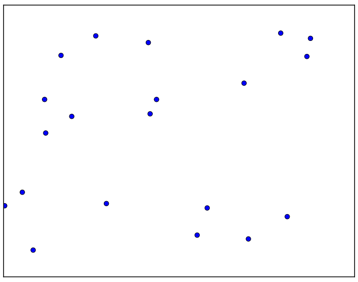

(a) Twenty points for which we are trying to find the convex hull.

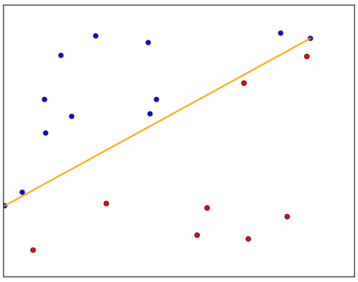

(b) We find the points with the lowest and highest x-value and connect them with a line.

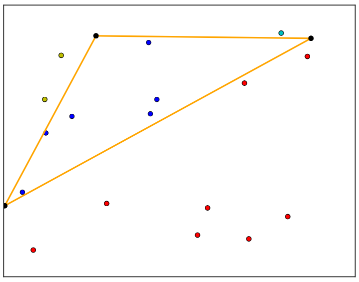

(c) Continuing with the points on the left (same process happens recursively on the right) we find the point furthest away from the line. We then draw two more lines and build a triangle. The points inside of the triangle are not part of the convex hull and are discarded. We will repeat the current step with the two new lines of the triangle.

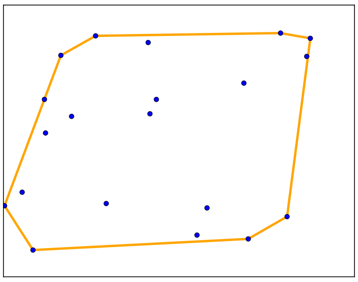

(d) We have found points of the convex hull once we can't build a new triangle anymore.

Figure A.4 Determination of a convex hull in two dimensions.

points in the horizontal axis, which are guaranteed to be part of the convex hull. We connect these two extreme points thus creating a division between a "left" and a "right" set of point. Now the divide and conquer method begins. We will only describe what happens to the left side, but imply that the same steps are taken on the right side. We find the point furthest away from the dividing line and add it. A triangle is formed out of the two points of the initial dividing line and the additional point. All points inside the triangle do not belong to the convex hull and thus we exclude them. The triangle again divides the remaining points into two sets, one left of the triangle and one right which are again iterated over recursively.

The method is repeated until each subset only contains the start and end point of the dividing line. We have created the convex hull, which if projected to a $d-1$-dimensional space provides the Delauney Triangulation of the projected points. For this projection to work we need to construct a convex hull in more than two dimensions which uses the same technique as described.

A.3. Barycentric coordinates system

The actual interpolation transforms the interpolant's coordinate into the barycentric coordinates of the containing triangle.

One can construct the barycenter of a triangle by drawing lines from each point to the midpoint of the opposing side (see Figure A.5).

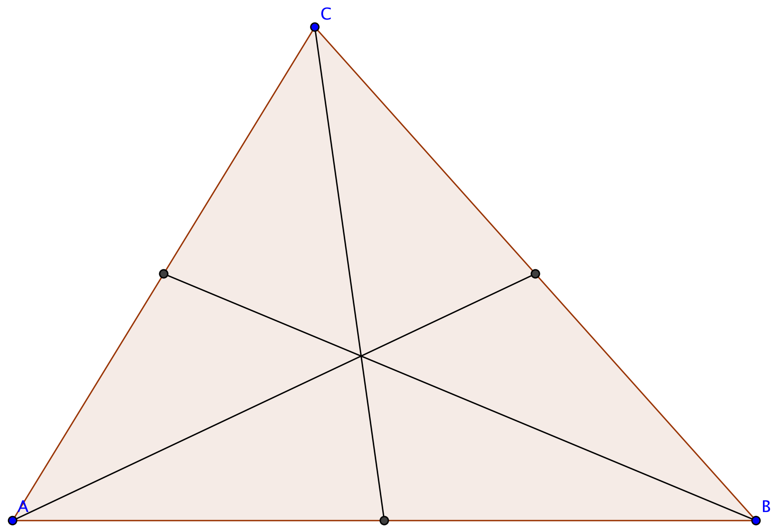

Figure A.5 The triangle and its barycenter marked by the intersection of lines.

The coordinates of the barycenter M can simply be expressed by,

$$\vec{M} = \frac{1}{3}(\vec{A} + \vec{B} + \vec{C}).$$

Not only the barycenter can be expressed by the vectors of $\vec{A}$, $\vec{B}$ and $\vec{C}$ but every point p inside the triangle can be expressed by,

$$\vec{p} = \alpha\vec{A} + \beta\vec{B} + \gamma\vec{C},$$

where

$$\alpha + \beta + \gamma = 1.$$

α, β and γ are called the barycentric coordinates. If the point p lies within the triangle all barycentric coordinates are positive.

A.4. Triangle Finding and Interpolation

To calculate the interpolation using barycentric coordinates we need to find the n-simplex that contains the interpolant. We use a method called directed walk (priv. comm. Pauli Virtanen). We choose a random starting n-simplex. In order to interpolate to a given point (interpolant) we calculate the barycentric coordinates for the interpolant and test if all of them are larger than 0. In that case we have found the n-simplex that contains the point. If the n-th barycentric coordinate is negative we jump to the neighbouring n-simplex which is opposite the n-th point. This is iterated until the containing n-simplex is found or the next jump would lead outside the convex hull of the Delauney Triangulation. For the latter case the point is outside of the grid and can not be interpolated.

If this algorithm converges and the right n-simplex is found the interpolation can be easily performed using the barycentric coordinates:

$$f(\vec{p}) = \alpha f(\vec{A}) + \beta f(\vec{B}) + \gamma f(\vec{C})$$

where $\vec{A}$, $\vec{B}$ and $\vec{C}$ are the points of the triangle.

A.5. Conclusion

We have described the method of linear interpolation using Delauney Triangulation mainly in two dimensions. As mentioned this method is easily extensible to n dimensions. The triangles (3-simplices) become n-simplices in n dimensions (e.g. Tetrahedrons in three dimensions). The method itself however stays very similar for higher dimensions.

In this work we have made extensive use of n-dimensional linear interpolation using the implementation present in the Scipy package, called LinearNDInterpolator. In this case creation of the convex-hull is performed by the QHULL implementation described in Barber et al. (1996).

We have tested the performance of the algorithm by creating a three dimensional grid with $20 \times 10 \times 10$ gridpoints and an array of 10, 000 double values at each gridpoint. On a standard 2011 MacBook Pro (Intel Core i7, 2.6 GHz, running only on a single processor) we have measured the initial building of the Delauney Triangulationand storing it in an appropriate data structure to 256 ms. The interpolation for random points took on average $\approx 600\,\mu$ s. This technique lends itself very well to explore large datasets even on moderately equipped machines.

We have used this technique extensively to interpolate a spectral grid in three dimension (effective temperature, surface gravity and metallicity). When trying to extract stellar parameters from an input spectrum we calculated the χ^2 for the observed spectrum with interpolated synthetic spectra from the grid. The interpolated spectra resulting from the interpolation are continuous, but not differentiable at the ridges of the grid structure (ridges are the borders of the simplices that make the grid). This non-differentiability at the ridges can be seen even in the χ^2 space. Optimisers that employ gradient methods (such as MIGRAD James & Roos, 1975) show some difficulties in some regions of the search space. We have tried to alleviate this problem by beginning the optimisation from different starting points. In almost all cases this lead to the same minimum.

In summary, the presented linear n-dimensional interpolator is a very robust and quick way to explore large parameter spaces without having to compute each single point.

Future work will be directed to exploring other n-dimensional interpolators in the astrophysical context.

APPENDIX B

Genetic Algorithms

B.1. Introduction

Numerical mathematics has been developing steadily over the last century and especially over the last 50 years when computers became readily available. Like many other sciences numerical mathematics has been getting much inspiration from nature. Advancements in our understanding of the brain inspired numerical mathematicians to recreate some of the structures of this biological computer. These attempts resulted in Neural Networks which today have wide applications in many areas of science and engineering. Optimisation algorithms, which are a sizeable subfield of numerical mathematics, have also borrowed heavily from nature. Some examples are Ant Colony Optimisation and Particle Swarm Optimisation. The time line in Figure B.1 shows some of the milestones in optimisation.

Biological evolution can be seen as an optimisation algorithm that adjusts organisms to adapt well to their environment. The idea of an algorithm which imitates the principal of natural evolution was first introduced by Holland (1962). Shortly after other groups independently started using similar approaches (e.g. Rechenberg, 1973). The entire field of

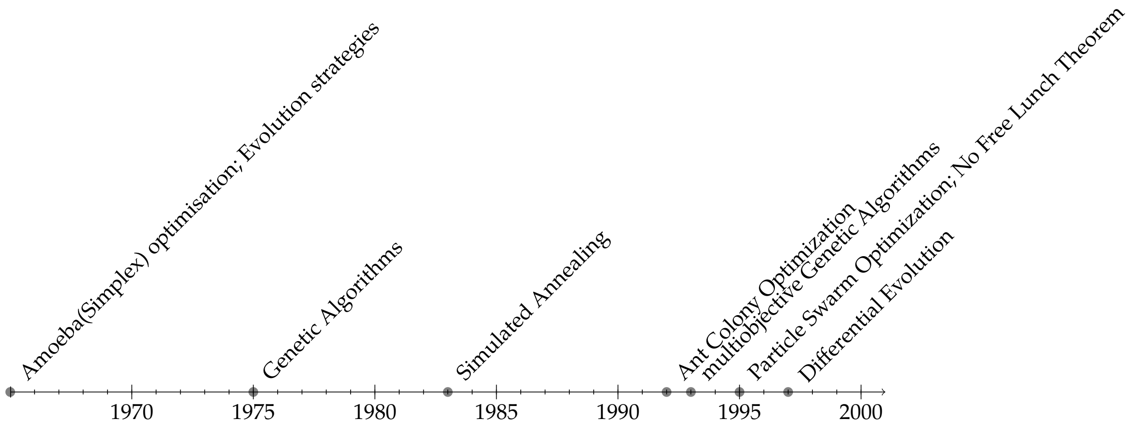

Figure B.1 Time line of milestones in numerical optimisation evolutionary algorithms has since split up into many subfields (e.g. genetic programming, evolutionary programming, evolution strategy, evolutionary algorithms, etc.). Out of these subfields, the GAs are the most widely known and have been applied to many different problems.

In general, optimisation algorithms have two seemingly conflicting goals: exploiting good leads (optimum seeking) while still exploring the parameter space sufficiently. Simple algorithms like Hillclimbing (randomly selecting a point in the neighbourhood of the current point and then picking the better point as the new basis) will exploit good leads but will neglect to explore the search space often leading to the convergence on local optima. Random searches, on the other hand, are excellent at exploring the search space but will fail to quickly converge on an optimal solution (and are not guaranteed to converge at all). Which algorithm to use naturally depends on the type of parameter space. Spaces with independent variables can be solved relatively simply by employing optimum seeking methods. Random search algorithms are suited to parameter spaces with highly correlated variables. One should note that the better an algorithm is optimised for a specific search space the more poorly it performs on other problems. This constitutes the so called 'No Free Lunch' theorem (Wolpert & Macready, 1997) , which also states that across the space of all problems, all algorithms perform equally well. GAs seem to strike a balance between exploration and exploiting the current best solution. Consequently they can be applied to a wide range of different parameter spaces. In addition, they have many options and fine tuning parameters so that one can adjust them to individual problems.

B.2. Genetic Algorithms

GAs are a stochastic search technique that tries to find solutions in n-dimensional search spaces. In most optimisation algorithm we have a function $f(\vec{x}) = s$, where $\vec{x}$ is are the input parameters and s is a solution scalar (sometimes referred to as figure-of-merit). The goal is to find the input parameters that optimise s (finding a maximum or minimal value of s). In some optimisation algorithms, however, this function $f(\vec{x})$ does not immediately produce a scalar solution s but instead produces a solution vector $\vec{y}$ (e.g. curve fitting where input coefficients produce a number of output points). This gives two options, first we can find a function $g(\vec{y}) = s$ that maps the solution to an optimisable scalar and proceed as above, or we can try to optimise the individual components of $\vec{y}$ simultaneously. The latter option is called multi-objective optimisation and is a vast field of research, but outside the scope of this work. From now on we will consider that we have a function $f(\vec{x}) = \vec{y}$ and a function $g(\vec{y}) = s$.

GAs have terms for the described functions and parameters that borrow heavily from evolutionary science. The individual input parameters of $\vec{x}$ are often referred to as genes. The input vector $\vec{x}$ is called individual or sometimes genome. We refer to representation in parameter space as genotype ($\vec{x}$) and the representation in solution space as phenotype ($\vec{y}$) of a solution. This is similar to biology where the input $\vec{x}$ can be thought of as the DNA sequence. The phenotype in biology however does not resemble a vector (strictly speaking). Mathematically speaking it is possible to have multiple genotypes map to one phenotype, however each genotype only maps to one phenotype. One should also note that in many, if not most, optimisation problems there exists no phenotype as the function $f(\vec{x})$ maps directly to the optimisable scalar s. Finally, the function that results in the figure-of-merit ($f(\vec{x}) = s$ or $g(\vec{y}) = s$) is called the fitness function which results in the fitness s.

In general, GAs maintain a pool of individuals called a population or generation. The general idea is that each new generation is created out the old generation. Owing to the special processes of the GA each new generation will consist of individuals that are on average closer to the optimal solution than the last generation. Following the notation of Michalewicz (1994) we introduce the population $P(t)$ with the individuals $\{p_1^t, \ldots, p_n^t\}$, where t denotes the iteration (or generation number). Each individual (p_i^t) is a data structure consisting of a vector $\vec{x_i}$ and its corresponding fitness scalar s_i. When we speak of evaluating p_i^t we mean that we use $g(f(\vec{x_i})) = s_i$ to determine the fitness. A new population (or generation) $P(t+1)$ is formed by choosing, in the *select step*, the more fit individuals. Some or all of the new population undergo transformations in the *recombine step*. These transformations are called genetic operators. We define unary transformations, which create new individuals by small changes in single individuals called mutations. Higher order transformations called crossovers combine the traits of multiple individuals to form a next generation individual. After the new population has been created in the *recombine step*, it is evaluated (perform the computation $g(f(\vec{x_i})) = s_i$) and the *select step* begins anew.

This procedure is repeated until some termination condition is reached (see Algorithm B.2.1). One way is to wait until best individual in a generation or the whole generation has reached a certain threshold fitness. Another way is to set a limit on the number of generations.

Algorithm B.2.1: Genetic Algorithm()

procedure Genetic Algorithm()
$t \leftarrow 0$
Initialize($P(t)$)
Evaluate($P(t)$)
while (**not** termination condition)
do $\begin{cases} t \leftarrow t+1 \\ P(t) \leftarrow \text{Select}(P(t-1)) \\ \text{Recombine}(P(t)) \\ \text{Evaluate}(P(t)) \end{cases}$

In order to apply a GA to an optimisation problem, the following are needed:

- a genetic representation of the search space (e.g. a vector)
- a function (or a chain of functions) that can calculate a fitness for a genetic representation
- transformations that create a new population/generation out of selected members of the old population/generation
- a method of creating an initial population

All of these points need to be considered before developing a GA for any given problem. This involves multiple steps the first of which is choosing a suitable genetic representation for each solution in the parameter space.

There are two main ways to represent a genome, binary encoding and value encoding (sometimes called gray encoding). Binary encoding was the form of encoding used in early genetic algorithms, the advantage being that the same GA can be easily adapted for many problems. In one-dimensional problems, for example, value encoding only offers one gene, whereas binary encoding, depending on the requested precision of the value, offers multiple genes. This becomes obvious in the one-dimensional minimization example: $f(\vec{x}) = (x_0 - 3.141)^2$. The solution vector that minimises the problem in value encoding is $\vec{x} = (3.141)$ using IEEE 754 floating point encoding the optimal vector is $\vec{x} = (0,1,0,0,0,0,0,0,0,1,0,0,1,0,0,1,0,0,0,0,0,1,1,0,0,0,1,0,0,1,0,1)$. There are however many problems with binary encoding. The so called *hamming cliff* describes the problem that a simple bit-flip at one high encoding bit (occurring in the *recombination step* using mutation or crossover) can dramatically change the encoded value (e.g. Chakraborty & Janikow, 2003). This can improve covering of search space but also can hinder the code from converging. In addition, when using binary encoding for many input variables the genomes can get incredibly long and GAs have been shown to perform poorly for very long genomes. Value encoding often is a natural way to encode the parameters of a problem. In contrast to binary encoding the genetic operators are often much more problem specific. It seems that for the moment value encoding is the preferred method in many cases (e.g. Janikow & Michalewicz, 1991; Wright, 1991; Goldberg, 1990). The 'No Free Lunch' theorem proves that there is no one optimal encoding, but the optimal encoding is different for each problem.

The fitness function maps the phenotype ($\vec{y}$) to a scalar and is one of the requirements for optimisation. It is often hard to define one number that describes how good a solution is for any given problem. For example it is not possible to map desirable traits of a car to one number and one might have prioritize which traits to optimise at the cost of others. A sensible fitness function that maps from the multi-dimensional phenotype to a scalar is sometimes impossible to construct. As described above these cases need to be treated under multi-objective optimisation schemes. Multi-objective optimisation is a vast field of research and outside the scope of this work.

Many GAs employ a so called fitness scaling operation in every generation to the fitness function. This scaling often helps the GA to follow promising leads but also explore the parameter space. For example, it sometimes happens, especially in early generations, that a fitness function values a small fraction of individuals extremely highly when compared to the rest of the solutions. These individuals with a near optimal value in very few genes might have a much higher fitness than an individual with a subpar value for these few genes, but which has near optimal values for all other genes. The subsequent populations will then be reigned by the genes of these few individuals which prohibits the GA from exploring the search space. In GA terms individuals with extremely high fitness based on very few near optimal genes are called *superindividual*s. They can drastically reduce the genetic breadth and often cause the GA to fail. One way to overcome this problem is scaling the fitness of all individuals after they have been computed. There are other steps which can be undertaken in the *select step* described later. The scaling is often a simple algebraic transformation, like linear or exponential scaling. A specific example can be found in Section 5.5. In addition to fitness scaling, there exists the possibility to just use the rank of the individuals as a fitness measure. In the case of ranking, we order the individuals according to their fitness value and assign them monotonically incrementing values (see Figure B.3). In summary, fitness functions and scaling are a very crucial part of a successful algorithm. For a description of different scaling methods please refer to Kreinovich et al. (1993).

*Superindividual*s can not only be avoided with fitness scaling but also by initial population choice. The most basic quantity to consider when choosing the initial population is that of population size. Generally the population size remains the same over the course of a GA. The population size should be chosen in relation to the size and complexity of the parameter space. For example, a small population size and a large search space can lead the GA to find local optima rather than the global optimum. In this work, we have chosen a population which is roughly 15 times bigger than the number of input parameters. After having chosen the population size the most basic method of selecting the initial population is to draw individuals uniformly and randomly from the entire search space. One might however know a probability distribution for the parameter space and can draw randomly weighted by the distribution (e.g. when trying to find parameters for a random star, we can rule out a 20 $M_\odot$white dwarfs with some likelihood). An initial population that is closer to predicted optimal values will converge faster, but won't explore the parameter space that well.

Once we have evaluated the fitness for each member of the individual population the next step is the *selection step*. There are many different approaches for selecting individuals from the current generation to create the next generation. Before selecting individuals we can a make coarse selection on the entire population. One selection that is often performed is elitism in which a fraction of the fittest individuals is selected to advance unaltered to the next generation. Another possibility is to discard a fraction of the least fit individuals. The gene combinations of these individuals then won't be used in the upcoming *recombination step*. After this first coarse selection on the population the remaining members form the so-called mating population.

We then start with the recombination step acting only on the current mating population. The first action in the recombination step is the selection of two or more individuals from the mating population and subsequent addition to a mating pool. A mating pool is a collection of individuals whose genes will be combined to form one or more individuals of the next generation. In all our next examples we will assume a mating-pool with only two slots (similar to two parents in biological reproduction). There is a multitude of options for selecting members from the mating population and adding them to a mating pool (for an overview see Goldberg & Deb, 1991). The most widely used of the selection algorithms is the roulette wheel selection. In Figure B.2 we see that individuals are assigned a wedge of the wheel. The area of the wedge is according to the individual's fitness. The wheel is then spun and slows down until the wheel comes to a halt. The selection chevron on the left points then to the chosen individual. In roulette wheel selection fitter individuals are more likely to be chosen than individuals with poorer fitness. In Figure B.3 we show how rank scaling of the fitnesses can alleviate the problem of early *superindividual*s. In addition to roulette wheel selection there is *tournament selection* where we randomly select

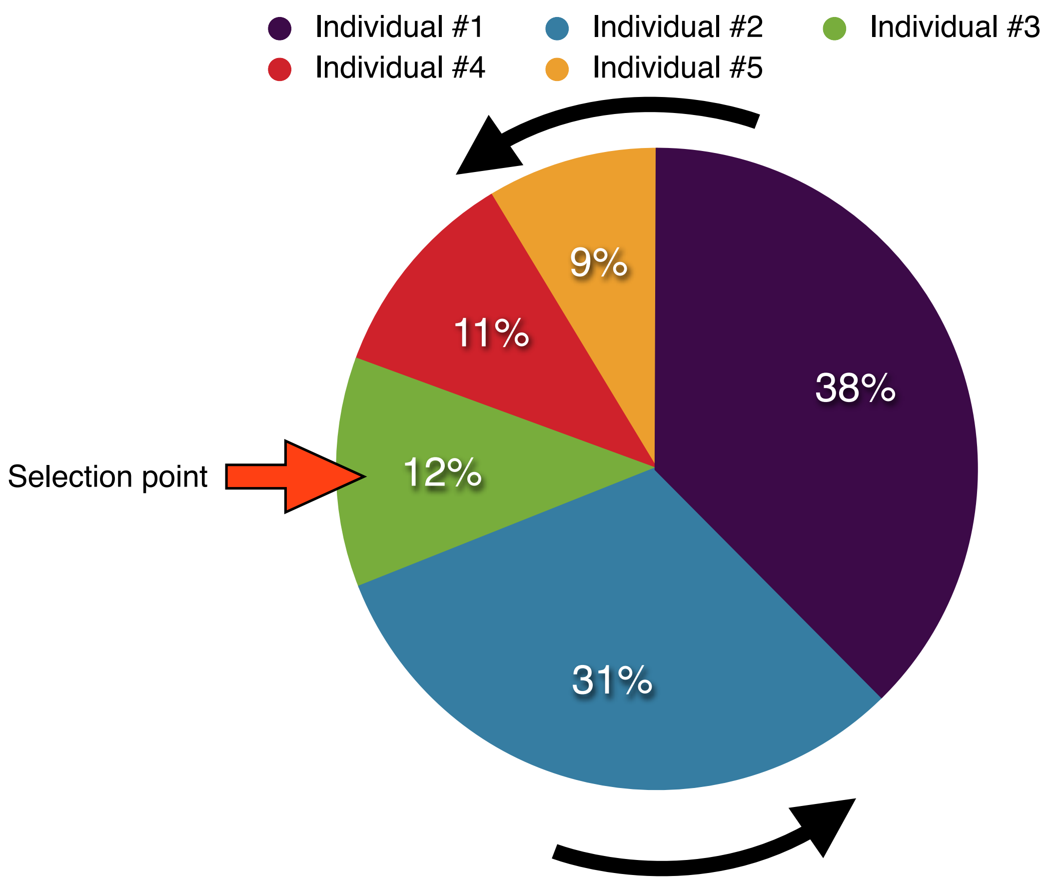

Figure B.2 The individual fitnesses are assigned proportional fractions on the roulette wheel. The wheel is then spun and will slowly decelerate and stop at some point. Individuals with a higher fitness have a higher chance of being chosen with this method.

two individuals and compare those. The fitter of those two individuals is selected.

There are multiple steps for creating a new population from the current mating population. In the previous paragraph we described how to select individuals and place them in a mating pool. The individuals in the mating pool are also often referred to as parents. Similar to the term parent we refer to the newly created individuals as children. The reader should notice that the same individual can be in the mating pool twice (unlike with biological parents)! We create one or multiple children from this mating pool and place them in the next generation. The current mating pool is disbanded and a new one is formed. These steps are repeated until the new population has the same number as the old population (minus the number of individuals that advanced to the new population through elitism). There are two main processes to create a new individual from a mating pool: crossover and mutation. The simplest form of a crossover is the single-point crossover (see Figure B.4). A random integer $r \in [1, N-1]$, where N describes the number of genes in a genome, is selected. The new individual is created out of the first r genes from the first parent and the last $N-r$ genes from the second parent (see Figure B.4). Now it is trivial to create a second child (using the same random number r) from the mating pool by just switching first and second parent. Two-point crossover is very similar to single-point

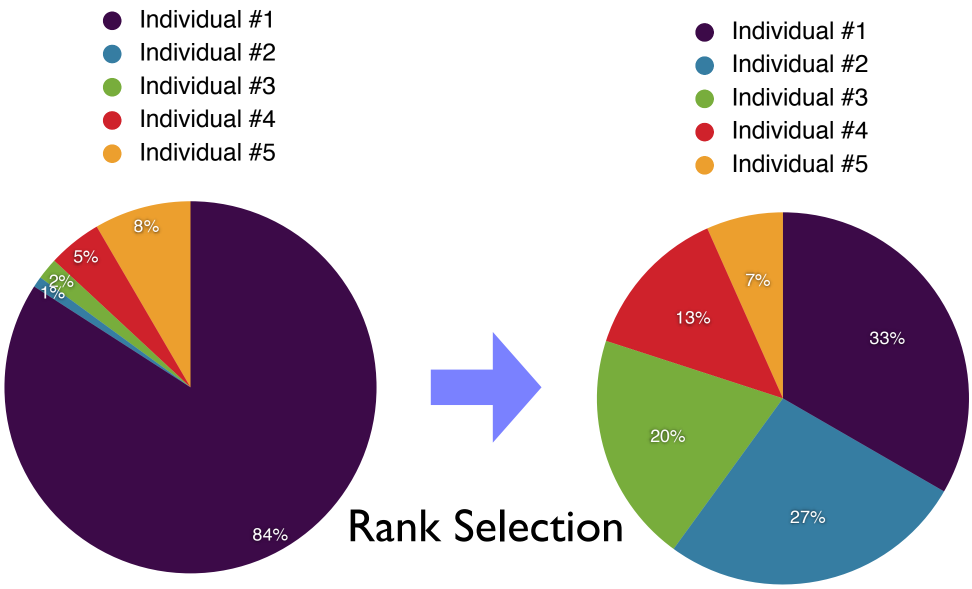

Figure B.3 We assign new fitness values to individuals before assigning them probabilities on the roulette wheel. The fitnesses are assigned by location in an ordered list. The least fit individual gets assigned the value 1 the fittest individual the number n, where n is the population size. This is can be viewed as a special case of fitness scaling. After the new fitnesses have been chosen we use normal roulette wheel selection to select for the mating pool in the population.

crossover. In two-point crossover Two random numbers are selected and the crossover occurs at these places. Multi-point crossover (see Figure B.4) is essentially just an extension of two-point crossover. In addition, there is uniform crossover in the case that each gene is selected randomly with equal chance from either parent. Finally, arithmetic crossovers use a function to calculate the new gene from each of the parent genes. For a value encoding this function could be the *mean* function. For a binary encoding the function could be the *and* operator. One can mix arithmetic and Multi-point crossovers. For example we select the r genes from the first parent and create the last $N - r$ genes by taking the mean of first and second parent's genes. After the new child or children have been created through crossovers they are subjected to the mutation operator. There is a chance for each individual gene (often chosen to be less than 5%) that it is altered. For bit encoding this altering is a simple bit inversion. There are many options for value encoding. For example, one can add or multiply with a random number. Once this step is complete the children are added to the new population.

Once the new generation is created by crossovers and mutations we start the iterative process anew. First we calculate the fitness of all individuals, then scale the resulting fitness, create a mating population and select individuals with, for example, roulette wheel selec-

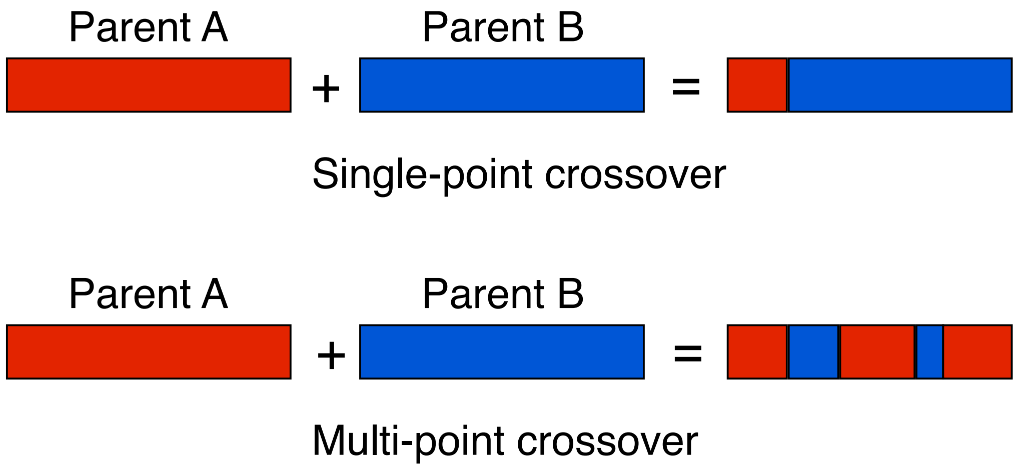

Figure B.4 In the single-point crossover a random point in the individual is chosen. Before this point the genes are taken from the first parent and after that the we use the genes from the second parent. Using the same random number it easily allows for the creation of two children by reversing the roles of first and second parent. The multi-point crossover employs multiple places in the genome where the crossover happens.

tion to create children which forms the next generation. This iterative process is run until we have reached a certain number of generations or some individuals have reached some fitness threshold.

B.3. Convergence in Genetic Algorithms

A key problem with many GA-implementations is the premature convergence on a local optimum. The more complex the search space and the more interlinked the parameters are, the more likely it is that traditional search routines will fail. GAs are inherently better at bypassing local optima but are in no way immune to this problem. A feature that separates GAs from traditional optimisation algorithms is that they will never fully converge. The algorithm will get close to the optimum but due to continued mutation of the individuals the GA will in most cases not reach an optimal value. To alleviate this problem some authors suggest switching to a different algorithm when close to the optimal solution, whereas others suggest changing the mutation rate over time (see Rudolph, 1994, and references therein).

One of the unsolved problems is determining a mathematical description for the GAs convergence. The next section is dedicated to the predominate schemata theory, which however only explains a subset of the intrinsic complexity of GAs.

B.4. Genetic Algorithm Theory

The schemata theory first described by Holland (1975) is one of the accepted theoretical interpretations of GAs. There is some criticism and it is known that this theory only explains part of the complexity that are inherent to GAs (see Whitley, 1994, and references therein). We will describe the basic concepts of schemata using an example in binary encoding (notation adapted from Goldberg, 1989). A schemata or similarity template is formed by adding an extra letter to the binary alphabet denoted by $*$. Using the ternary alphabet $0, 1, *$ we can now describe a pattern matching schemata were the $*$ symbol can be thought of as *don't care*-symbol. The schemata $0, 1, 0, *$ for example, matches both the string $0, 1, 0, 0$ and $0, 1, 0, 1$. The order of a schemata is defined as how many places are not filled by the $*$-symbol. For example, the given example is a third order schemata. Schematas provide a powerful way to describe similarities in a set of individuals. A whole population with many individuals therefore samples a range of different schematas . Essentially low-order and above-average schemata receive exponentially increasing trials in subsequent generations of a GA. Michalewicz (1994) describe the workings of a GA in the following way: "A genetic algorithm seeks near optimal performance through the juxtaposition of low-order, high-performance schemata, called building blocks". This schemata theory is the standard explanation for GAs, there are however some examples that violate the implications that stem from this schemata theory (see Chapter 3 of Michalewicz, 1994, for some examples).

B.5. A Simple Example

As a last explanation we will offer a simple example, to give a more 'hands-on' description of GAs.We will illustrate the use of a GA on a simple astrophysical problem. The task at hand is to fit an observed spectrum with a synthetic spectrum. The input parameters for this synthetic spectrum are effective temperature, surface gravity, metallicity, α-enhancement, $v_{\rm rad}$ and $v_{\rm rot}$. The simplest genetic representation of this is the vector $\vec{x} = (T_{\rm eff}, \log g, [{\rm Fe/H}], \alpha, v_{\rm rad}, v_{\rm rot})$. $\vec{x}$ is the *genotype* of the individual. The resulting synthetic spectrum is the *phenotype*.

For this relatively small number of genes a population size of 75 should suffice. The first step is drawing an initial population. We will draw uniformly randomly from the search space: $T_{\rm eff} \in [2000, 9000]$, $\log g \in [0, 5]$, $[{\rm Fe/H}] \in [-5, 1]$, $\alpha \in [0, 0.4]$, $v_{\rm rad} \in [-100, 100]$ and $v_{\rm rot} \in [0, 200]$. We compute the synthetic spectrum for each individual. The fitness of each individual is the inverse of the root-mean-square of the residuals between the observed and the synthetic spectrum. In the select step we will first advance 10 % of the fittest individuals to the next population unaltered (elitism). For the next population to be complete we need $75 - 8 = 67$ individuals which are created through mating. We select two individuals through roulette wheel selection and place them in the mating pool. A single crossover point is randomly selected and the child is created. Before being placed in the new population the mutation operator is applied but has a very small chance to mutate any of the child's genes (in this case we choose 2%). This mating step is repeated 67 times. The new population now consists of the 8 fittest individuals of the old population and 67 new individuals created by mating. We will then start again to compute the synthetic spectrum and the resulting fitness for each individual of the new population. This loop is continued until one individual or a whole population has reached a predefined convergence criterium.

B.6. Conclusion

GAs with their inherently parallel nature are very useful in the increasingly parallel computing. They are relatively easy to implement and can be used for a variety of problems. In many applications GA quickly deliver impressive results, but require a lot of time for fine-tuning to be able to sufficiently handle the problem. GAs also offer a plethora for each of the individual steps (encoding type, selection type, etc.), which can confuse users that are not very familiar with the consequence for each choice. To alleviate this problem in our work we have sought the help of experts in GAs and hope to find the best set of options for our GA. In summary, although there are some drawbacks (no guaranteed convergence, many choices for implementation, etc.) we find that we progressed much quicker with GAs than with other algorithms.

APPENDIX C

SN 1006 Data

Table C.1 SN 1006 optical photometry (Candidates with V < 17.5 marked with gray)

Star	RA	Dec	U	σ_U	B	σ_B	V	σ_V	I	σ_I
	hh:mm:ss.ss	dd:mm:ss.ss	mag	mag	mag	mag	mag	mag	mag	mag
01	15:02:58.27	-41:55:20.9	16.03	0.02	14.76	0.00	13.50	0.08	12.30	0.18
02	15:02:59.95	-41:56:25.2	18.84	0.08	16.96	0.01	15.37	0.01	13.95	0.05
03	15:02:51.80	-41:56:39.9	16.16	0.02	15.86	0.01	15.04	0.01	14.23	0.09
04	15:02:53.35	-41:54:18.0	16.67	0.02	16.33	0.00	15.47	0.00	14.62	0.00
05	15:02:49.97	-41:56:23.9	16.90	0.03	16.41	0.00	15.50	0.01	14.65	0.00
06	15:02:45.68	-41:54:35.2	16.21	0.01	16.17	0.01	15.50	0.00	14.78	0.01
07	15:02:51.19	-41:55:58.5	17.62	0.05	16.91	0.02	15.90	0.01	14.92	0.02
08	15:02:47.00	-41:55:28.3	16.57	0.03	16.53	0.01	15.86	0.01	15.16	0.00
09	15:02:55.07	-41:57:14.4	18.46	0.20	17.73	0.01	16.58	0.01	15.53	0.02
10	15:03:01.87	-41:54:59.2	17.18	0.04	17.06	0.00	16.30	0.00	15.51	0.00
11	15:02:56.05	-41:54:53.5	17.02	0.03	17.12	0.00	16.33	0.05	15.61	0.01
12	15:02:58.83	-41:56:35.5	17.60	0.03	17.22	0.00	16.39	0.02	15.50	0.02
13	15:02:49.22	-41:57:31.1	17.93	0.09	17.41	0.01	16.49	0.00	15.74	0.06
14	15:02:59.24	-41:54:51.6	17.93	0.04	17.44	0.00	16.56	0.00	15.75	0.01
15	15:03:00.33	-41:56:29.8	17.81	0.01	17.42	0.01	16.63	0.01	15.87	0.04
16	15:02:58.09	-41:54:47.9	19.60	0.47	18.37	0.01	17.26	0.00	16.11	0.03
17	15:03:02.49	-41:55:46.7	17.45	0.02	17.40	0.00	16.66	0.04	16.02	0.13
18	15:02:50.99	-41:56:39.4	18.00	0.03	17.61	0.00	16.77	0.03	15.87	0.04
19	15:02:50.12	-41:57:05.5	20.28	0.00	18.75	0.01	17.39	0.01	16.01	0.00
20	15:02:48.03	-41:56:19.4	-	-	19.59	0.03	18.04	0.01	15.97	0.17
21	15:02:58.44	-41:54:50.1	20.60	0.00	18.47	0.01	17.36	0.01	16.30	0.03
22	15:02:59.95	-41:55:41.9	17.26	0.04	17.25	0.00	16.71	0.06	16.18	0.04
23	15:02:43.94	-41:56:15.4	19.62	0.32	18.50	0.01	17.39	0.00	16.24	0.01
24	15:02:56.14	-41:54:49.2	-	-	18.28	0.00	17.59	0.13	16.49	0.11
25	15:02:59.79	-41:56:43.2	17.75	0.01	17.64	0.06	17.03	0.02	16.35	0.03
26	15:02:54.92	-41:55:27.7	18.10	0.10	17.95	0.01	17.23	0.02	16.43	0.00
27	15:02:52.72	-41:55:58.9	18.61	0.08	18.26	0.02	17.47	0.03	16.64	0.05

Table C.1 – continued from previous page

Star	RA hh:mm:ss.ss	Dec dd:mm:ss.ss	U mag	σ_U mag	B mag	σ_B mag	V mag	σ_V mag	I mag	σ_I mag
28	15:02:54.86	-41:56:36.4	18.52	0.13	18.24	0.00	17.43	0.02	16.70	0.02
29	15:02:51.84	-41:54:47.9	-	-	19.23	0.00	18.00	0.02	16.72	0.04
30	15:02:44.71	-41:55:15.4	18.05	0.03	18.24	0.03	17.54	0.02	16.75	0.01
32	15:02:53.61	-41:55:13.7	18.72	0.18	18.42	0.02	17.64	0.03	16.78	0.03
33	15:02:43.38	-41:55:51.5	19.07	0.23	18.56	0.04	17.66	0.04	16.69	0.05
34	15:02:56.13	-41:56:05.1	18.64	0.11	18.52	0.02	17.76	0.01	16.94	0.01
35	15:02:44.66	-41:55:10.0	19.06	0.17	18.74	0.00	17.84	0.02	16.88	0.05
36	15:02:58.70	-41:55:02.9	19.46	0.40	18.65	0.01	17.79	0.01	16.86	0.02
38	15:02:50.29	-41:55:45.6	18.58	0.08	18.48	0.03	17.80	0.03	17.00	0.01
39	15:02:43.76	-41:55:25.6	18.86	0.06	18.44	0.02	17.69	0.01	16.97	0.01
40	15:02:52.23	-41:56:37.9	-	-	-	-	-	-	16.28	0.06
41	15:02:52.06	-41:55:05.2	17.97	0.01	18.02	0.00	17.61	0.01	17.11	0.02
42	15:02:57.08	-41:54:34.3	19.22	0.27	18.78	0.03	17.99	0.01	17.16	0.03
43	15:02:48.27	-41:56:15.9	-	-	20.14	0.04	18.76	0.08	17.25	0.06
44	15:02:51.96	-41:54:31.4	-	-	19.79	0.01	18.54	0.02	17.06	0.01
45	15:02:47.43	-41:56:05.3	18.45	0.11	18.43	0.02	17.71	0.03	17.00	0.05
46	15:02:49.93	-41:57:35.3	20.09	0.17	19.04	0.03	18.05	0.04	17.19	0.20
47	15:02:52.86	-41:54:25.7	18.89	0.24	18.63	0.01	17.96	0.03	17.14	0.03
48	15:02:54.52	-41:55:29.9	-	-	19.29	0.03	18.38	0.01	17.38	0.06
49	15:02:52.83	-41:56:06.1	18.90	0.33	18.84	0.00	18.17	0.01	17.37	0.05
50	15:02:53.93	-41:56:22.6	19.68	0.11	18.99	0.03	18.07	0.03	17.19	0.02
51	15:02:54.58	-41:53:58.4	19.47	0.00	18.90	0.26	17.99	0.19	16.93	0.17
52	15:03:00.97	-41:54:58.6	19.41	0.17	18.89	0.00	18.08	0.03	17.24	0.02
53	15:02:57.45	-41:56:14.7	19.32	0.43	18.90	0.03	18.13	0.01	17.24	0.05
54	15:02:48.09	-41:57:07.7	20.33	0.58	19.40	0.02	18.45	0.01	17.48	0.03
55	15:02:44.67	-41:55:35.9	-	-	19.90	0.01	18.68	0.03	17.36	0.04
56	15:02:50.38	-41:54:34.5	-	-	20.15	0.16	18.83	0.06	17.46	0.08
57	15:02:54.15	-41:56:40.9	19.59	0.57	18.91	0.02	18.26	0.04	17.63	0.07
58	15:02:49.42	-41:55:33.5	18.90	0.09	18.92	0.02	18.21	0.02	17.41	0.02
59	15:02:51.38	-41:57:34.9	19.59	0.37	19.21	0.01	18.54	0.02	17.78	0.02
60	15:02:59.64	-41:57:03.8	20.05	0.18	19.22	0.01	18.48	0.13	18.62	0.43
61	15:02:53.45	-41:57:09.2	-	-	20.49	0.05	19.24	0.02	17.82	0.07
62	15:02:44.94	-41:55:48.3	-	-	19.38	0.02	18.53	0.01	17.54	0.01
63	15:02:50.89	-41:55:17.4	20.19	0.15	19.41	0.00	18.55	0.02	17.62	0.05
64	15:02:55.53	-41:57:28.3	19.45	0.28	18.87	0.02	18.51	0.03	17.87	0.08
65	15:02:44.57	-41:55:28.2	18.79	0.04	18.93	0.03	18.38	0.04	17.63	0.05
66	15:02:57.28	-41:54:19.6	-	-	20.02	0.03	19.09	0.02	18.00	0.03
67	15:02:48.88	-41:55:03.4	19.69	0.38	19.11	0.03	18.37	0.01	17.57	0.01
68	15:02:43.51	-41:56:23.9	20.65	0.00	19.60	0.04	18.75	0.04	17.94	0.01
69	15:03:01.11	-41:56:40.2	20.07	0.00	19.59	0.03	18.59	0.17	17.91	0.09
70	15:02:58.01	-41:56:45.0	20.38	0.57	19.49	0.01	18.73	0.03	18.00	0.06
71	15:03:00.93	-41:55:35.3	-	-	19.95	0.02	18.84	0.02	17.92	0.25
72	15:02:58.39	-41:57:20.6	19.34	0.00	19.90	0.11	18.85	0.11	18.01	0.14

Table C.1 – continued from previous page

Star	RA	Dec	U	σ_U	B	σ_B	V	σ_V	I	σ_I
	hh:mm:ss.ss	dd:mm:ss.ss	mag	mag	mag	mag	mag	mag	mag	mag
73	15:02:50.64	-41:54:49.5	-	-	20.00	0.04	19.04	0.06	17.92	0.12
74	15:03:02.32	-41:56:05.2	-	-	19.88	0.08	18.76	0.16	18.21	0.02
75	15:02:53.19	-41:54:05.5	19.23	0.11	19.07	0.03	18.34	0.03	17.50	0.03
76	15:02:44.17	-41:55:45.8	19.56	0.09	19.40	0.02	18.70	0.03	17.91	0.08
77	15:02:55.98	-41:55:47.4	19.58	0.20	19.22	0.02	18.56	0.05	17.69	0.02
78	15:02:48.76	-41:56:59.9	-	-	20.87	0.10	19.53	0.01	18.06	0.05
79	15:02:53.45	-41:56:41.7	-	-	21.53	0.06	19.90	0.02	18.04	0.05

Table C.2 SN 1006 infrared photometry (Candidates with V < 17.5 marked in gray)

Star	J	σ_J	H	σ_H	K	σ_K	QFlag	T_{eff}(B-V)	T_{eff}(V-K)
	mag	mag	mag	mag	mag	mag		K	K
01	11.05	0.02	10.32	0.02	10.21	0.02	AAA	4531	4376
02	12.67	0.03	11.87	0.03	11.71	0.02	AAA	3990	4150
03	13.63	0.04	13.26	0.04	13.19	0.05	AAA	5559	5780
04	13.92	0.03	13.56	0.03	13.43	0.03	AAA	5467	5518
05	13.93	0.02	13.50	0.03	13.33	0.04	AAA	5299	5367
06	14.15	0.02	13.82	0.03	13.77	0.04	AAA	6051	5947
07	14.11	0.03	13.68	0.03	13.57	0.04	AAA	5080	5178
08	14.51	0.03	14.32	0.04	14.18	0.07	AAA	6067	6026
09	14.45	0.03	13.85	0.04	13.72	0.05	AAA	4754	4687
10	14.79	0.03	14.37	0.03	14.34	0.06	AAA	5751	5619
11	14.93	0.05	14.69	0.07	14.55	0.09	AAA	5669	5876
12	14.81	0.04	14.39	0.05	14.28	0.06	AAA	5523	5437
13	14.86	0.04	14.52	0.05	14.49	0.09	AAA	5277	5576
14	15.01	0.04	14.67	0.04	14.56	0.08	AAA	5420	5566
15	15.23	0.04	14.96	0.06	14.86	0.11	AAA	5660	5890
16	15.17	0.07	14.63	0.07	14.47	0.08	AAA	4843	4742
17	15.48	0.06	15.06	0.07	15.08	0.13	AAB	5800	-
18	15.37	0.06	14.99	0.06	14.91	0.13	AAB	5533	-
19	15.00	0.04	14.34	0.05	14.13	0.06	AAA	4356	4393
20	14.92	0.04	14.29	0.05	14.04	0.07	AAA	4044	3978
21	15.41	0.05	14.96	0.06	14.90	0.11	AAB	4849	-
22	15.70	0.07	15.43	0.08	15.06	0.12	AAB	6537	-
23	15.35	0.05	14.76	0.05	14.51	0.08	AAA	4833	4673
24	15.90	0.08	15.22	0.09	15.08	0.13	AAB	5969	-
25	15.56	0.05	15.27	0.06	15.05	0.13	AAB	6278	-
26	16.05	0.09	15.66	0.13	15.92	0.24	ABD	5872	-
27	16.08	0.08	15.59	0.11	15.56	0.21	ABC	5636	-
28	16.08	0.08	15.38	0.09	15.53	0.20	AAC	5600	-
29	15.75	0.06	15.18	0.08	15.09	0.13	AAB	4587	-
30	15.98	0.09	15.72	0.11	15.92	0.27	AAD	5932	-
32	16.17	0.11	15.69	0.12	15.57	0.19	ABC	5680	-
33	16.00	0.08	15.41	0.09	15.23	0.19	AAC	5338	-
34	16.25	0.09	15.54	0.10	15.62	0.20	AAC	5750	-
35	16.08	0.12	15.72	0.12	15.53	0.20	BBC	5346	-
36	16.56	0.13	16.60	0.24	15.85	-	BDU	5461	-
37	-	-	-	-	-	-	-	-	-
38	16.24	0.08	16.03	0.13	15.73	0.23	ABD	5999	-
39	16.28	0.12	16.16	0.15	16.39	-	BCU	5759	-
40	14.96	0.04	14.28	0.04	14.06	0.05	AAA	-	-
41	16.43	0.11	16.02	0.14	15.67	0.23	ABD	7102	-
42	16.30	0.08	15.98	0.14	16.12	-	ABU	5667	-
43	16.39	0.12	15.49	0.08	14.74	-	BAU	4330	-

Table C.2 – continued from previous page

Star	J	σ_J	H	σ_H	K	σ_K	QFlag	T_{eff}(B-V)	T_{eff}(V-K)
	mag	mag	mag	mag	mag	mag		K	K
44	16.19	0.09	15.39	0.09	15.39	0.16	AAC	4565	-
45	16.59	0.13	15.92	0.12	15.53	-	BBU	5868	-
46	16.52	0.12	15.76	0.12	15.46	0.18	BBC	5125	-
47	16.43	0.11	16.08	0.14	16.00	0.28	ABD	6044	-
48	16.76	0.13	16.04	0.15	15.62	0.21	BBC	5319	-
49	16.72	0.13	16.37	0.18	16.96	-	BCU	6019	-
50	16.59	0.12	15.89	0.14	15.86	-	BBU	5297	-
51	16.72	0.13	16.08	0.15	15.18	0.14	BBB	5331	-
52	16.66	0.12	16.15	0.17	16.49	-	BCU	5598	-
53	16.69	0.13	16.15	0.17	16.08	-	BCU	5736	-
54	16.64	0.13	16.02	-	16.09	-	BUU	5220	-
55	16.50	0.15	15.99	0.14	15.61	-	BBU	4613	-
56	16.54	0.13	15.72	0.13	15.33	0.15	BBC	4425	-
57	-	-	-	-	-	-	-	6120	-
58	16.82	0.15	16.78	0.28	16.01	-	BDU	5897	-
59	-	-	-	-	-	-	-	6017	-
60	-	-	-	-	-	-	-	5816	-
61	16.50	0.12	15.93	0.13	15.67	0.23	BBD	4570	-
62	17.15	0.23	16.10	0.14	15.98	0.28	DBD	5485	-
63	16.95	0.17	16.15	0.15	15.44	-	CCU	5461	-
64	-	-	-	-	-	-	-	7316	-
65	17.20	0.20	16.51	0.22	15.95	0.28	CDD	6495	-
66	-	-	-	-	-	-	-	5274	-
67	16.91	0.18	16.53	0.21	15.65	0.22	CDD	5786	-
68	-	-	-	-	-	-	-	5495	-
69	16.94	0.14	17.68	-	15.42	-	CUU	5109	-
70	-	-	-	-	-	-	-	5774	-
71	16.71	0.14	16.42	0.21	15.81	0.27	CCD	4840	-
72	-	-	-	-	-	-	-	4974	-
73	16.85	0.16	16.11	0.16	17.09	-	CCU	5193	-
74	17.17	0.23	16.00	0.15	16.12	-	DBU	4824	-
75	16.84	0.14	16.73	-	17.03	-	BUU	5862	-
76	-	-	-	-	-	-	-	5947	-
77	-	-	-	-	-	-	-	6074	-
78	17.02	0.19	16.11	0.17	15.54	-	CCU	4381	-
79	16.68	0.13	15.87	0.13	15.68	0.21	BBC	3924	-

Table C.3 SN 1006 candidate kinematics with statistical errors and number of measurements (candidates with $V < 17.5$ marked in gray)

Name	v_{rad} km s^{-1}	σ_{rad} km s^{-1}	N_{rad}	v_{rot} km s^{-1}	σ_{rot} km s^{-1}	N_{rot}
01	-109.1	0.0	5	< 10	0.7	5
02	56.2	0.4	3	< 10	0.2	3
03	5.9	1.0	3	< 10	0.0	3
04	-14.3	0.0	5	< 10	0.7	5
05	-1.1	0.0	5	< 10	1.0	5
06	-103.9	0.2	5	< 10	0.7	5
07	-76.3	2.1	5	10	0.2	5
08	-0.6	0.2	5	< 10	0.6	5
09	-47.0	0.8	5	< 10	0.4	5
10	-20.2	0.5	5	< 10	0.9	5
11	-5.9	0.3	5	< 10	1.6	5
12	-59.8	0.4	5	16	0.4	5
13	12.3	0.1	5	< 10	1.6	5
14	-17.0	0.4	5	< 10	0.6	5
15	-72.0	0.2	5	< 10	0.7	5
16	9.4	0.1	5	14	2.3	5
17	-102.1	0.3	5	< 10	1.9	5
18	11.6	0.7	5	12	0.6	5
19	-47.8	0.3	5	17	6.7	4
20	-22.4	0.5	4	-	0.0	2
21	-18.5	0.0	5	13	4.0	4
22	-22.9	0.7	2	13	0.1	2
23	-63.3	1.3	5	14	0.4	4
24	-67.2	0.8	5	10	-	1
25	40.7	0.3	5	< 10	4.1	5
26	-7.0	0.1	5	< 10	0.8	5
27	-52.0	2.1	5	< 10	0.5	5
28	-43.5	0.3	3	< 10	0.5	3
29	-13.3	0.2	4	14	2.3	5
30	-28.2	1.3	3	< 10	0.5	3
32	-104.0	0.3	5	11	3.2	3
33	-120.9	0.2	5	< 10	1.3	4
34	-47.1	0.5	5	< 10	3.0	4
35	-24.6	1.5	5	12	0.9	4
36	-96.7	1.2	3	< 10	-	1
37	-22.7	16.1	4	-	-	-
38	-12.4	2.2	5	< 10	0.8	5
39	22.4	1.3	3	< 10	0.8	2
40	-13.8	8.6	4	-	-	-
41	-4.4	4.3	5	16	1.2	4
42	-64.9	0.3	5	< 10	0.5	3
43	-7.6	1.7	5	-	-	-

Table C.3 – continued from previous page

Name	v_{rad} km s^{-1}	σ_{rad} km s^{-1}	$\mathrm{N_{rad}}$	v_{rot} km s^{-1}	σ_{rot} km s^{-1}	$\mathrm{N_{rot}}$
44	-28.2	0.2	4	-	-	-
45	-135.4	0.3	5	< 10	3.9	4
46	-13.0	0.3	5	11	0.6	2
47	-0.3	0.1	5	< 10	2.7	4
48	3.6	0.6	3	11	1.9	3
49	-90.4	64.7	3	< 10	1.0	3
50	-82.7	1.5	5	< 10	1.0	5
51	-59.8	0.5	5	14	1.2	2
52	-8.8	1.1	4	-	-	-
53	-63.2	1.3	5	< 10	-	1
54	-51.8	0.0	5	10	1.4	2
55	-24.7	1.5	5	-	-	-
56	-0.0	1.9	4	-	-	-
57	-40.7	2.0	4	-	-	-
58	2.0	0.2	5	< 10	1.5	4
59	-17.5	0.4	5	< 10	-	1
60	-73.0	2.2	3	< 10	-	1
61	-34.6	24.7	5	-	0.0	5
62	21.2	1.1	3	12	-	1
63	-45.8	42.1	5	14	2.4	2
64	-24.1	0.4	2	< 10	-	1
65	38.3	55.3	3	< 10	-	-
66	-15.4	13.7	2	-	-	-
67	-146.2	1.1	4	< 10	-	1
68	-71.3	0.5	5	10	-	1
69	-47.6	0.4	5	12	0.1	2
70	-23.9	1.0	5	19	1.8	5
71	0.7	0.1	5	14	2.0	5
72	-4.5	5.9	2	-	-	-
73	-8.0	1.0	4	< 10	2.0	2
74	-27.2	23.0	5	-	-	-
75	-147.9	0.4	5	< 10	0.5	3
76	23.3	24.1	5	-	-	-
77	-3.3	3.8	4	-	-	-
78	-7.5	0.3	5	-	-	-
79	-0.6	4.5	4	-	-	-

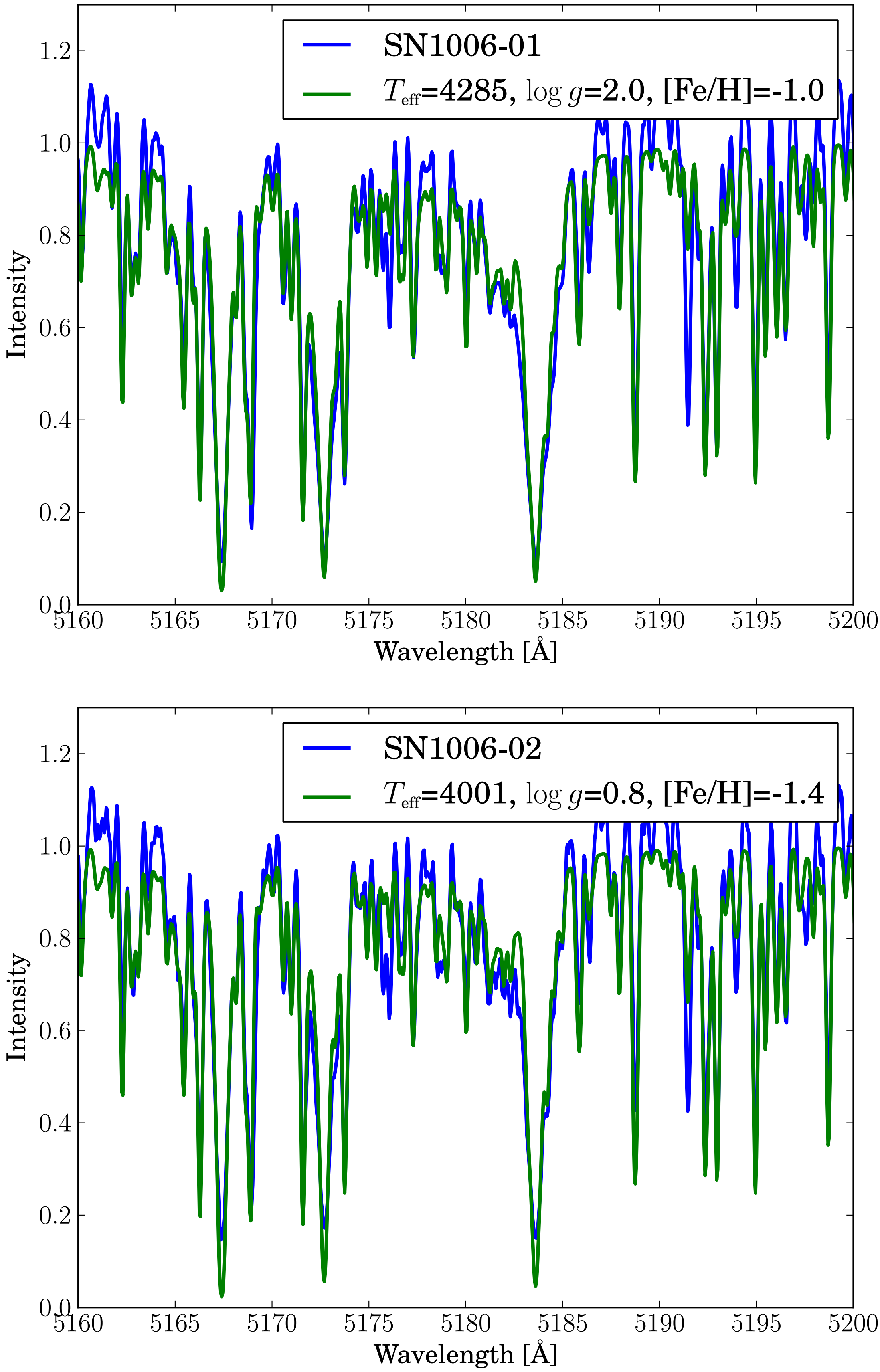

Figure C.1 Fit of SN 1006 candidate spectra

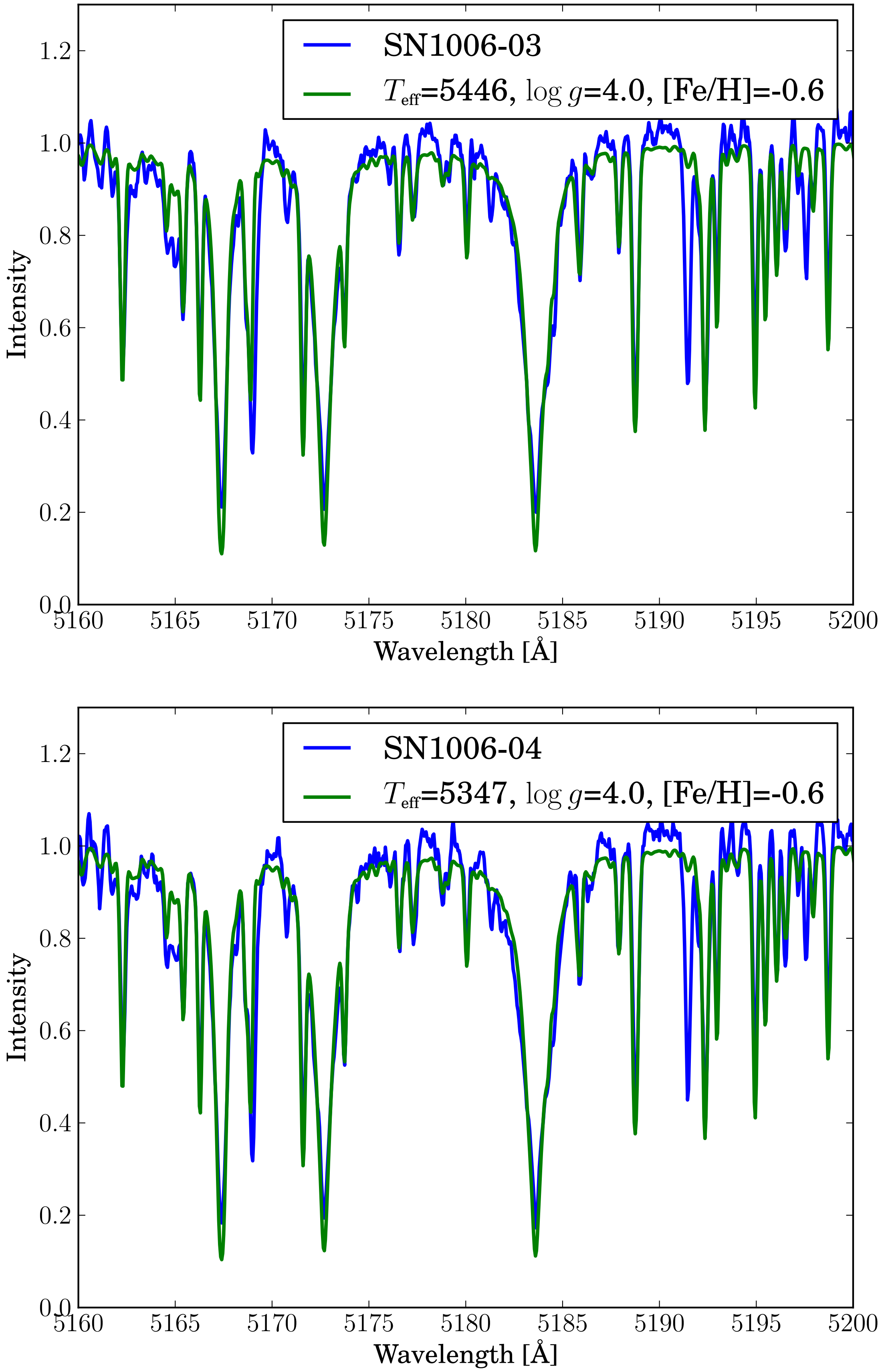

Figure C.1 Fit of SN 1006 candidate spectra

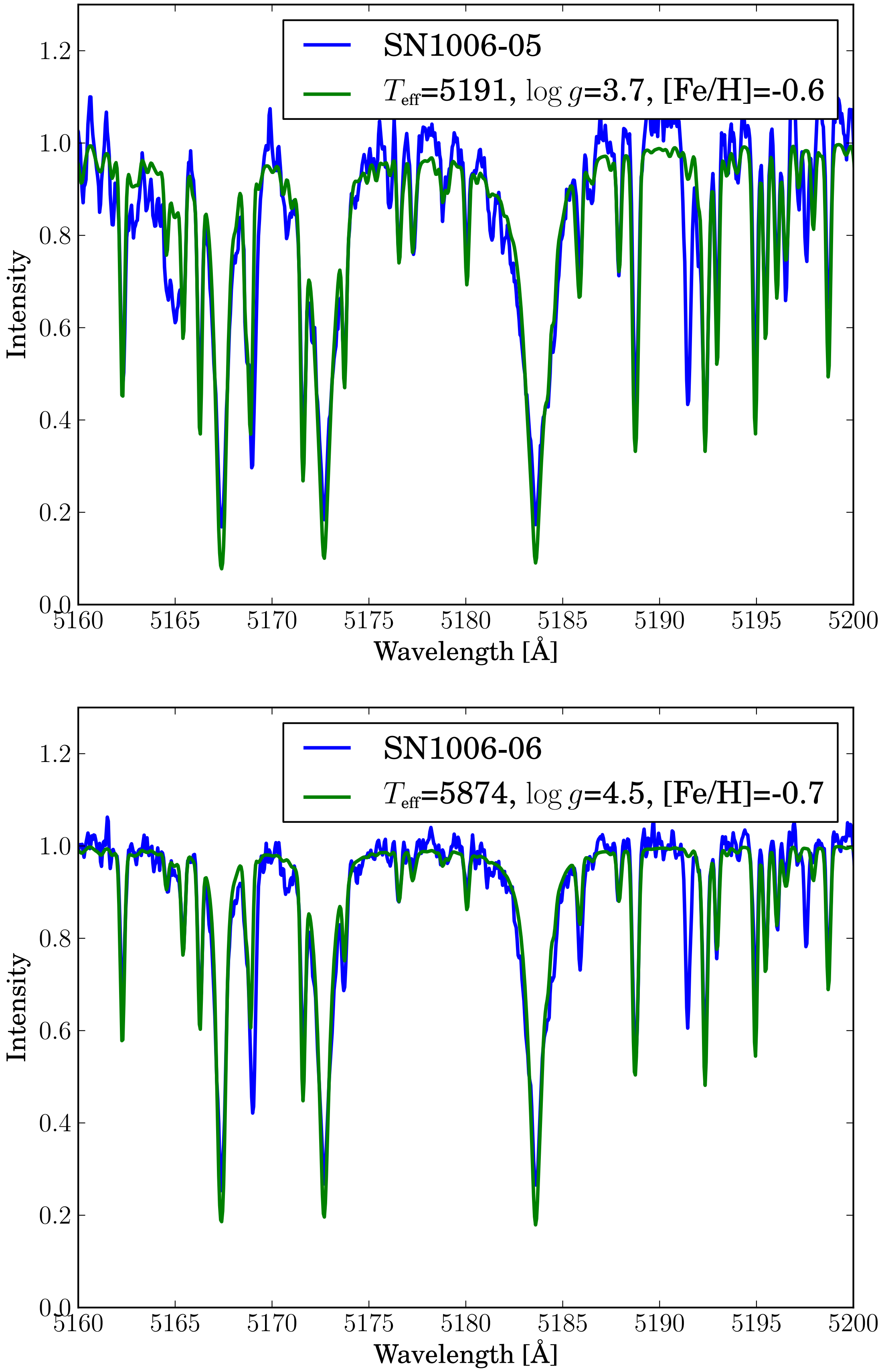

Figure C.1 Fit of SN 1006 candidate spectra

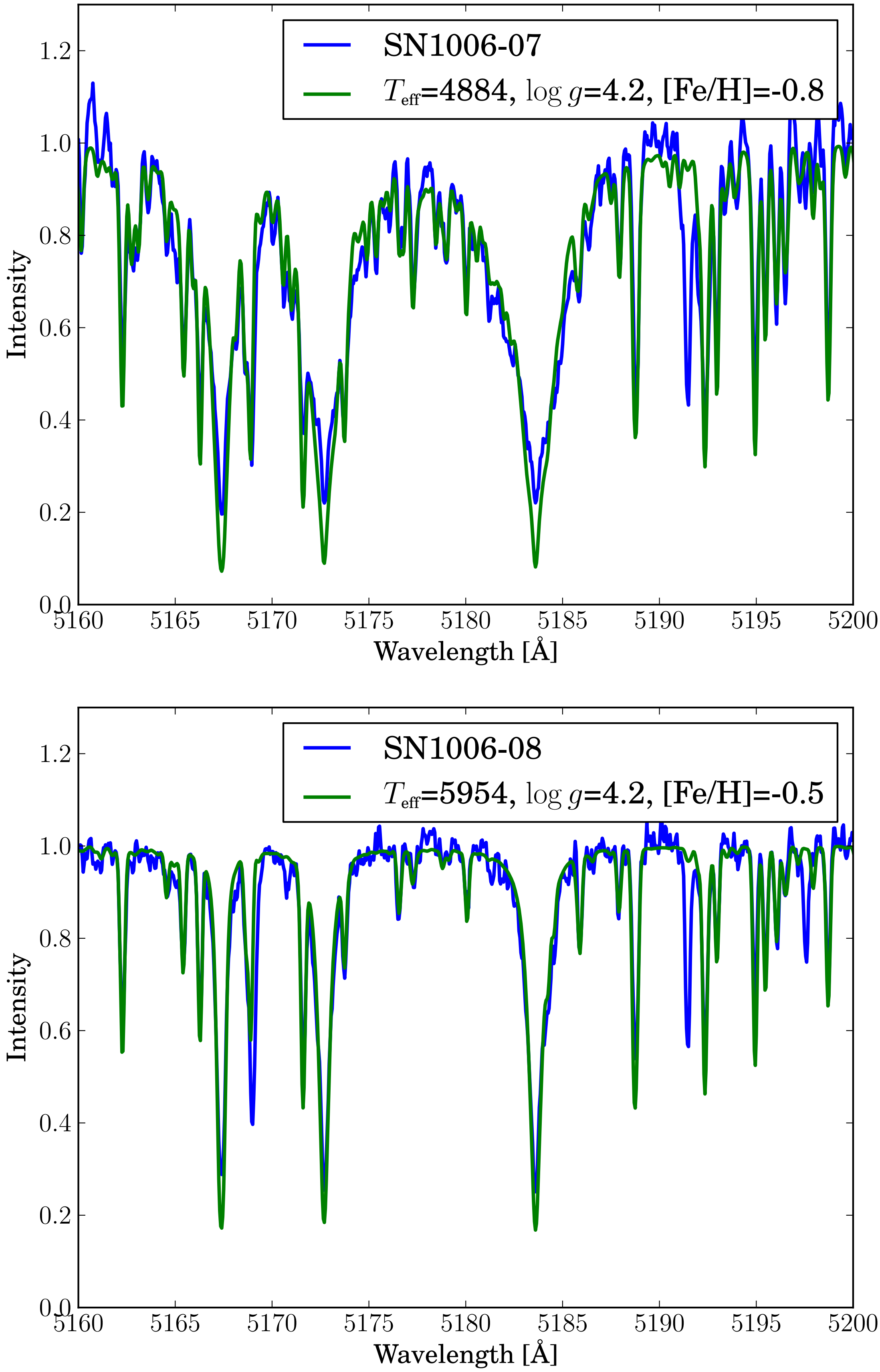

Figure C.1 Fit of SN 1006 candidate spectra

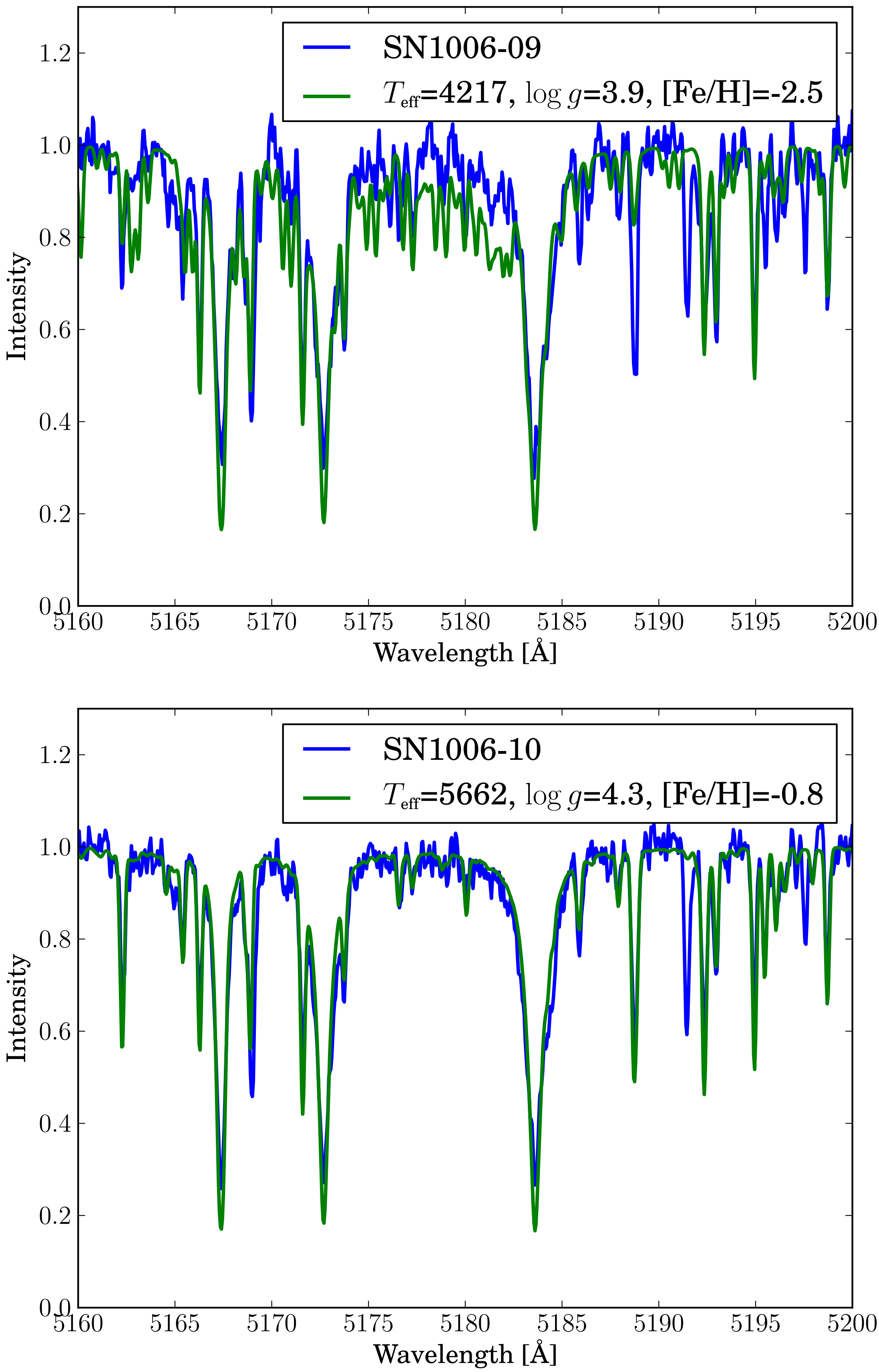

Figure C.1 Fit of SN 1006 candidate spectra

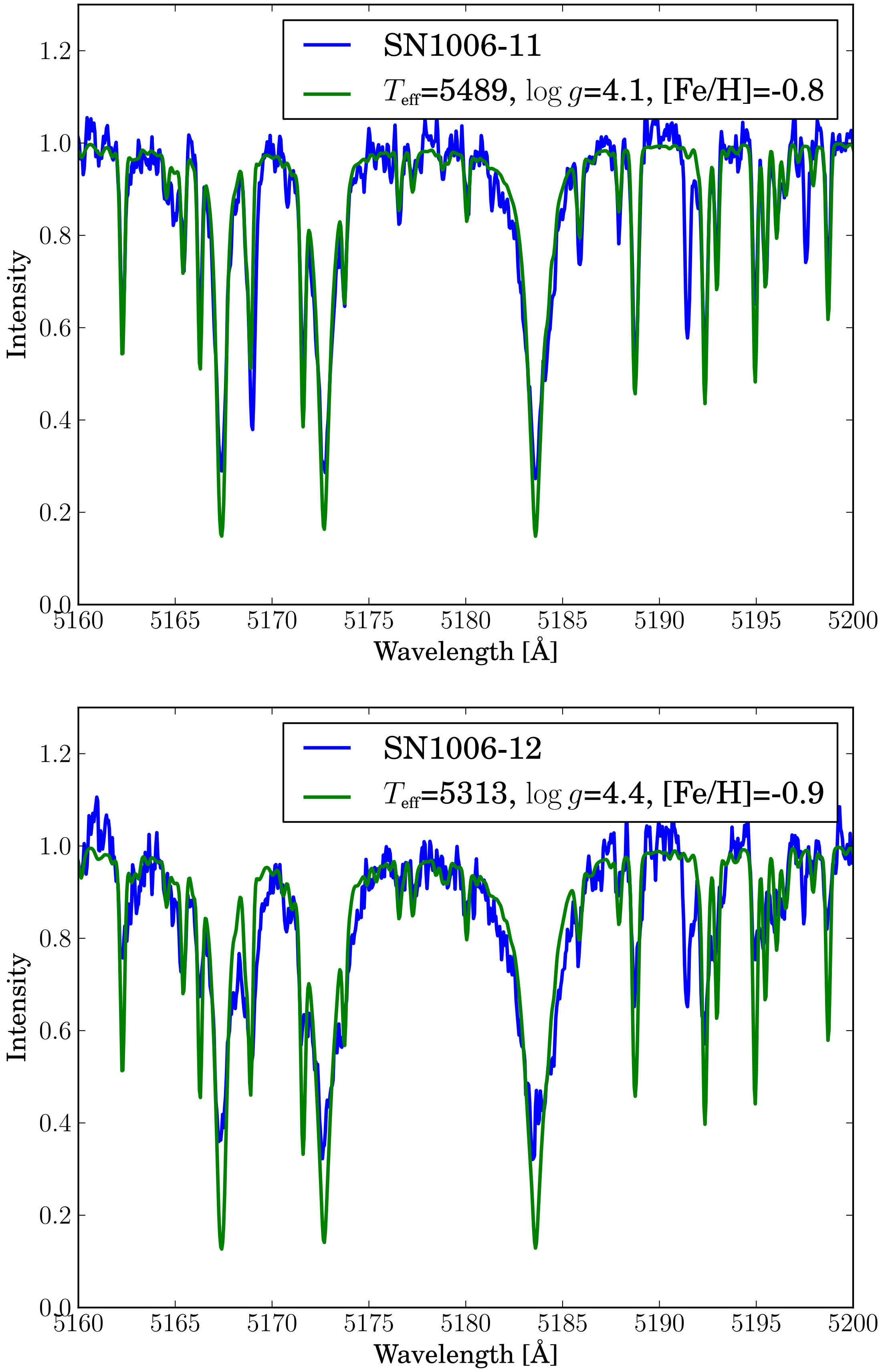

Figure C.1 Fit of SN 1006 candidate spectra

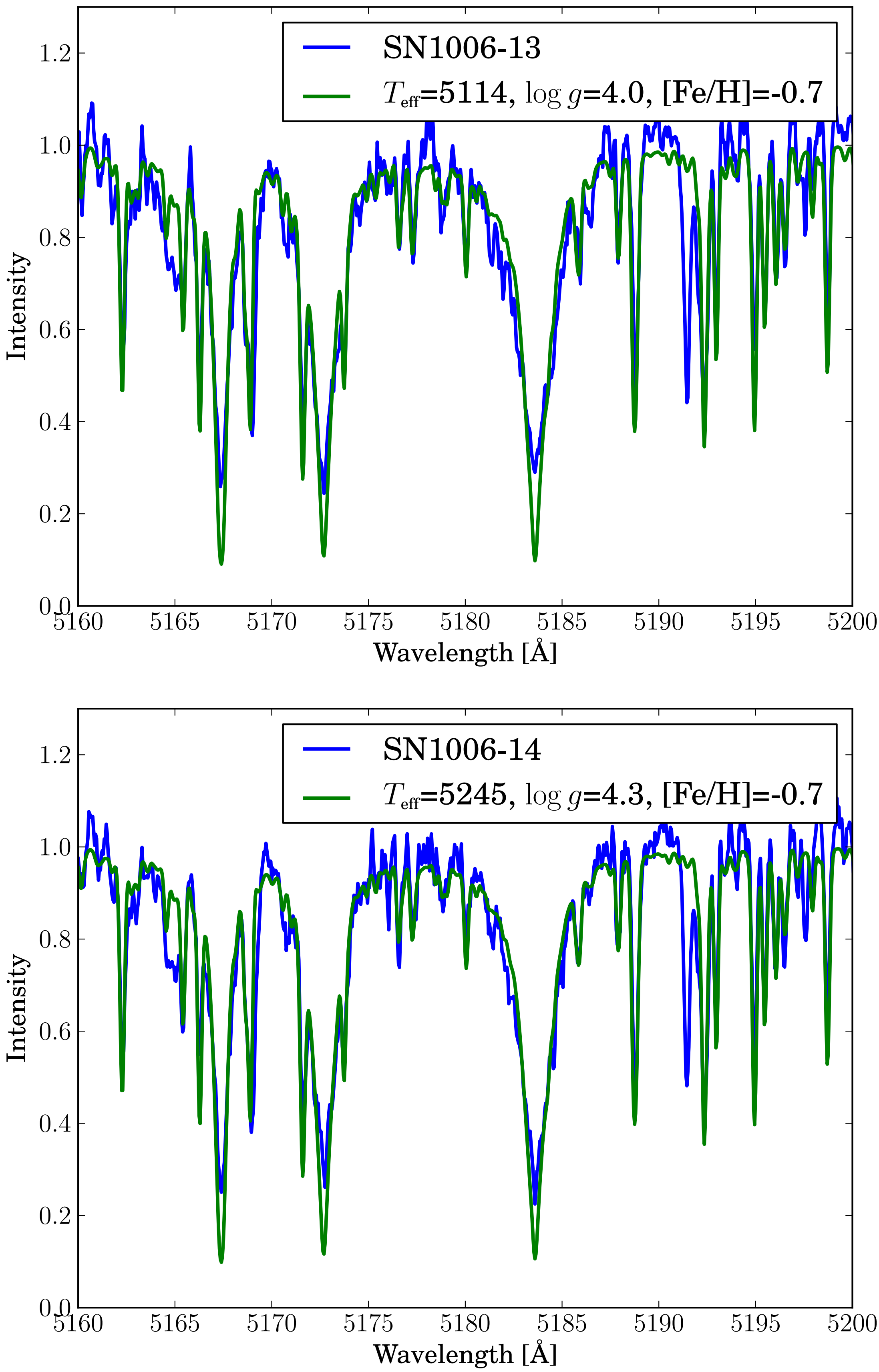

Figure C.1 Fit of SN 1006 candidate spectra

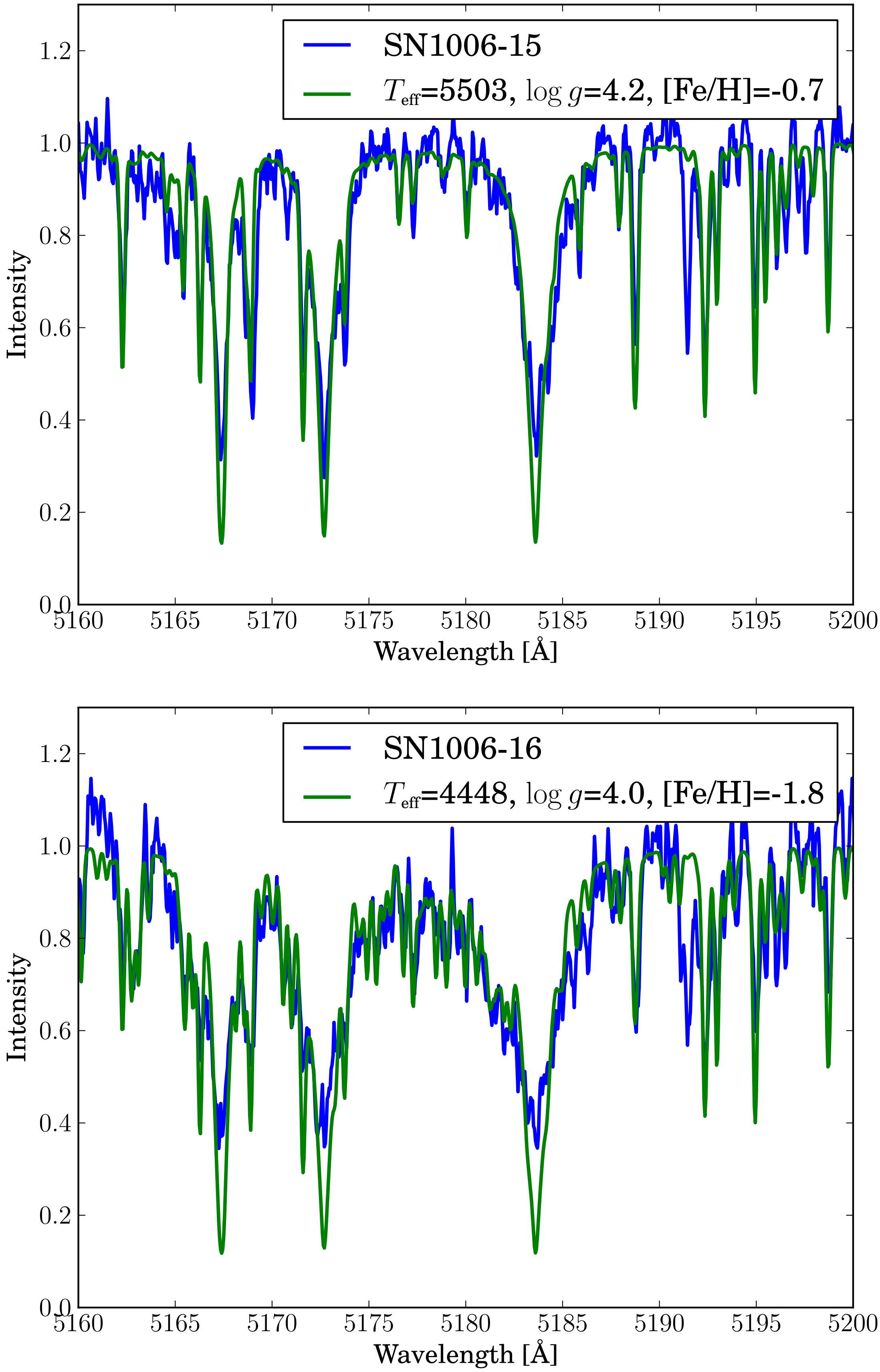

Figure C.1 Fit of SN 1006 candidate spectra

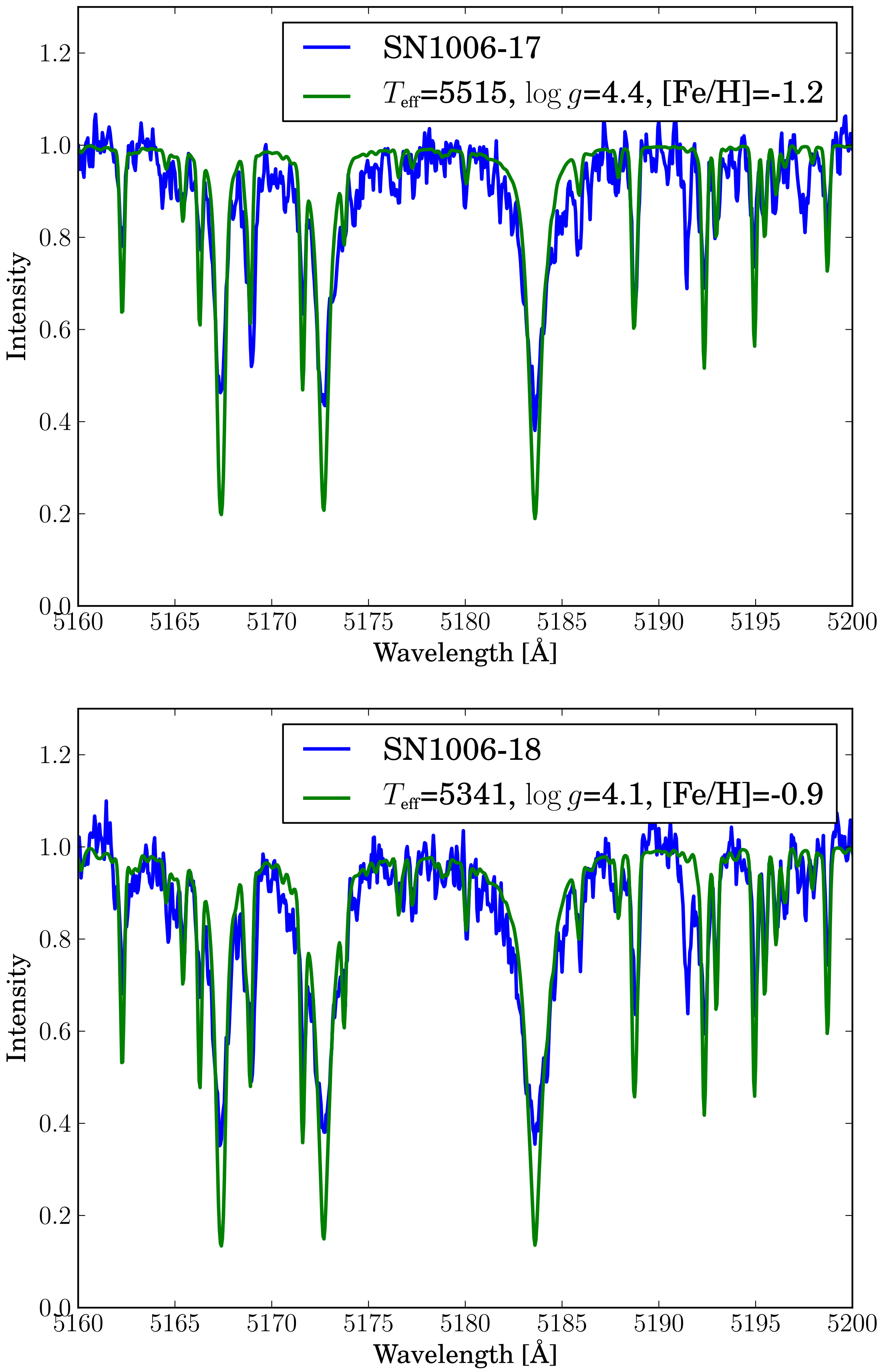

Figure C.1 Fit of SN 1006 candidate spectra

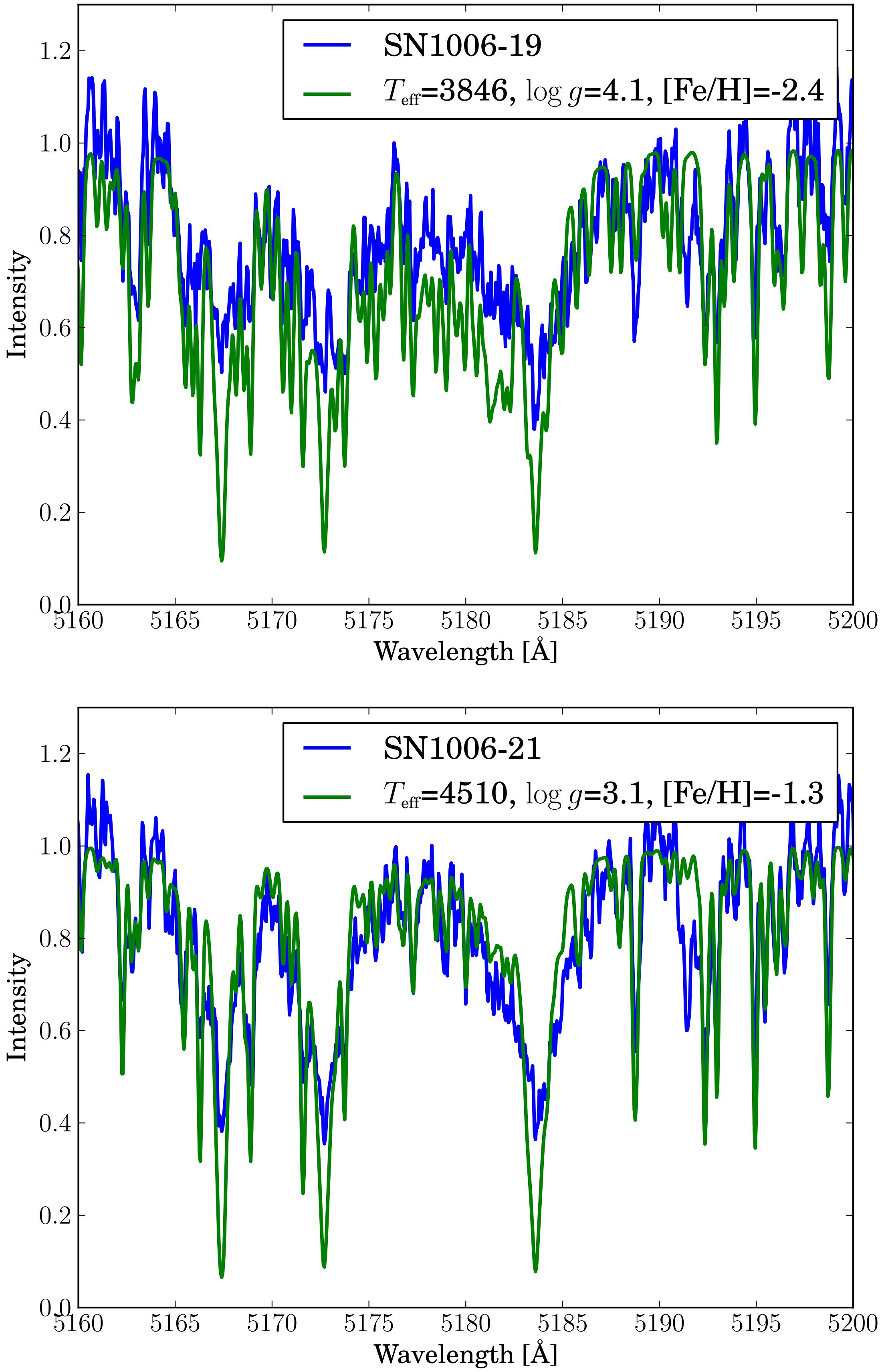

Figure C.1 Fit of SN 1006 candidate spectra

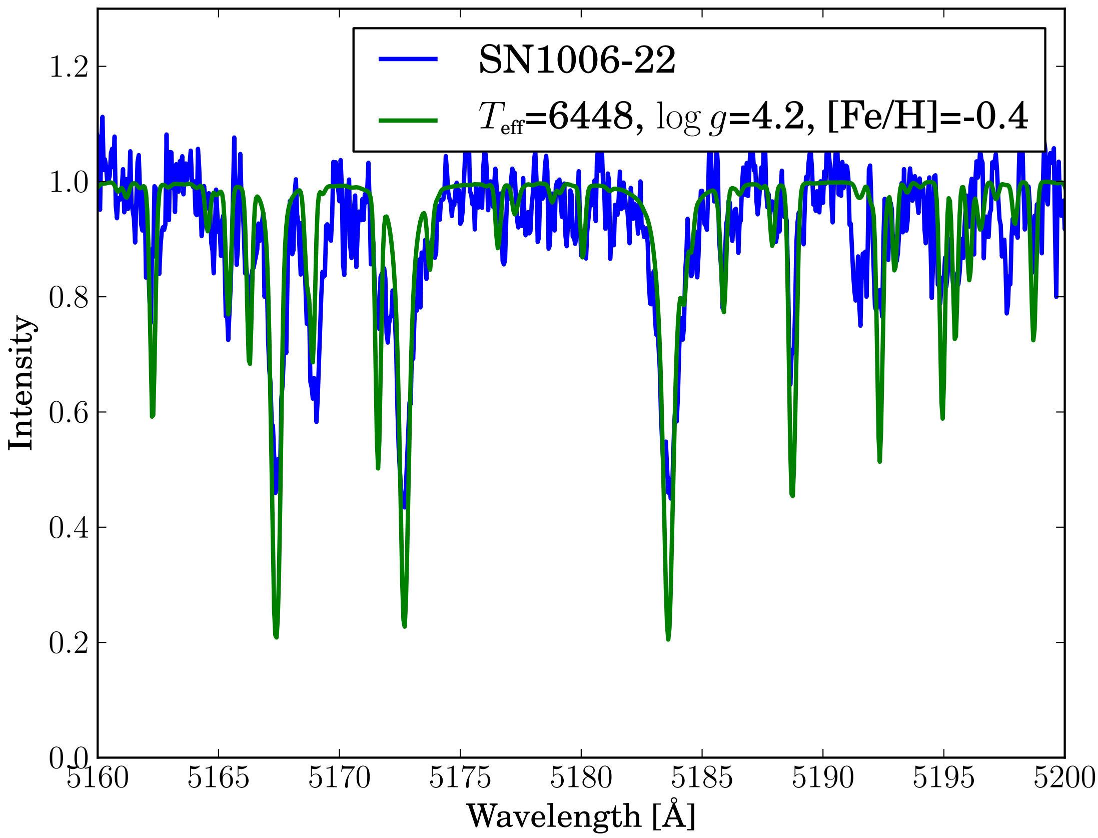

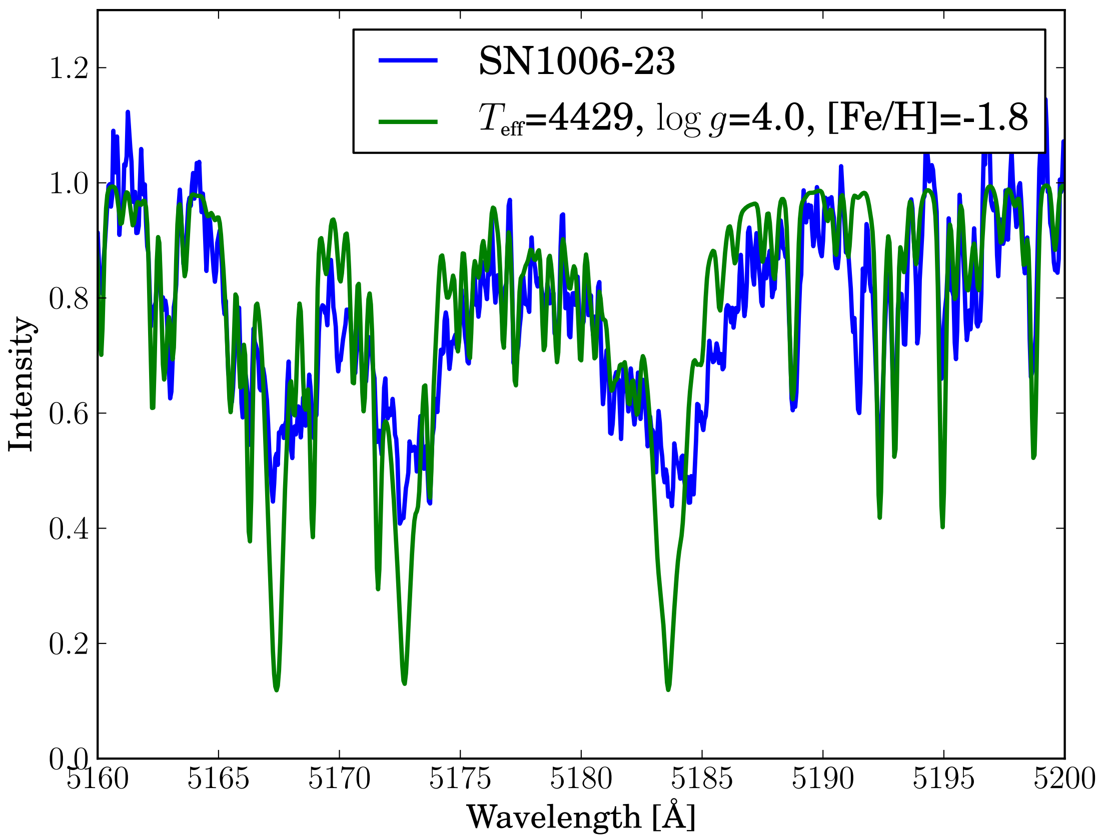

Figure C.1 Fit of SN 1006 candidate spectra

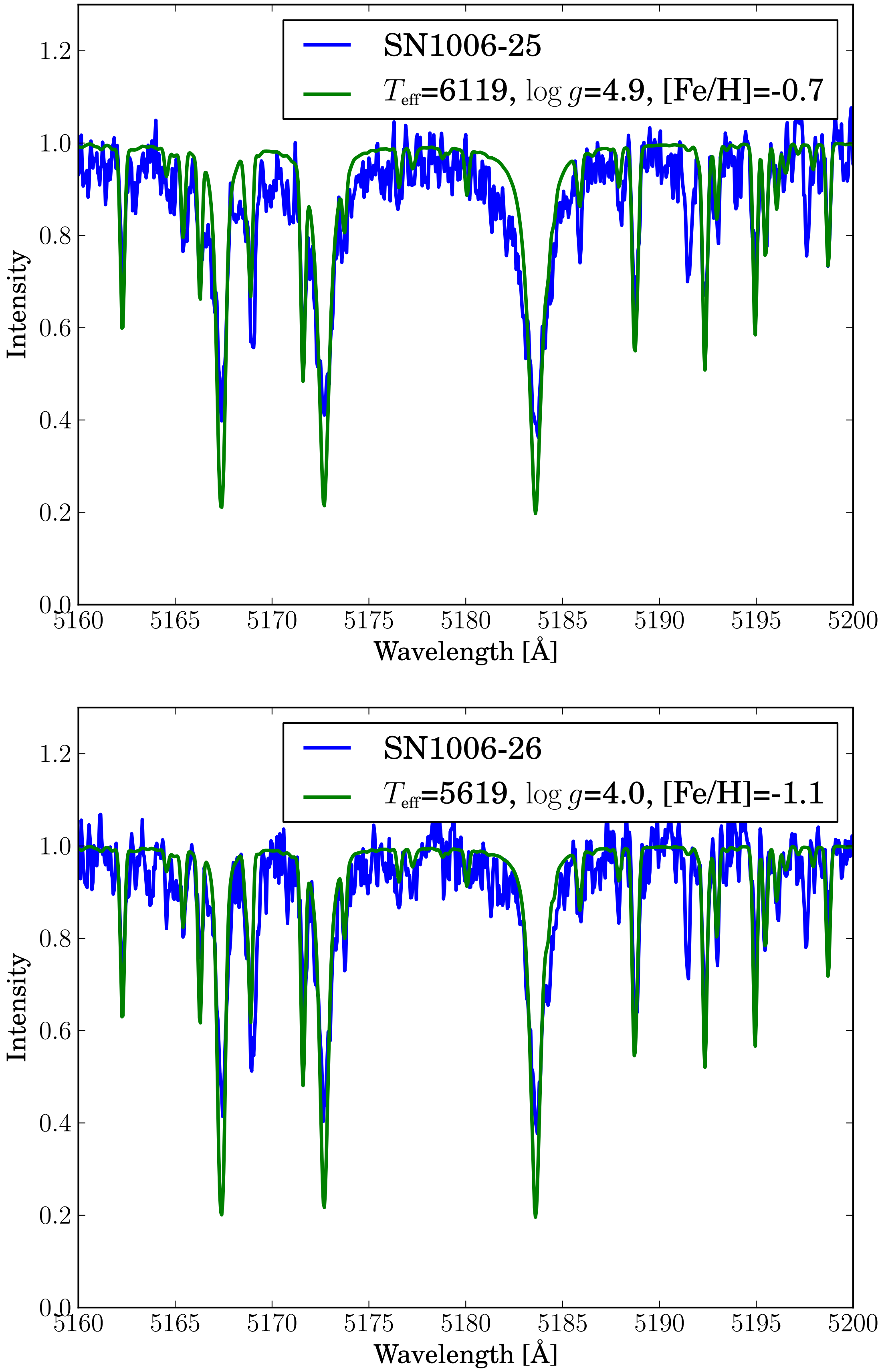

Figure C.1 Fit of SN 1006 candidate spectra

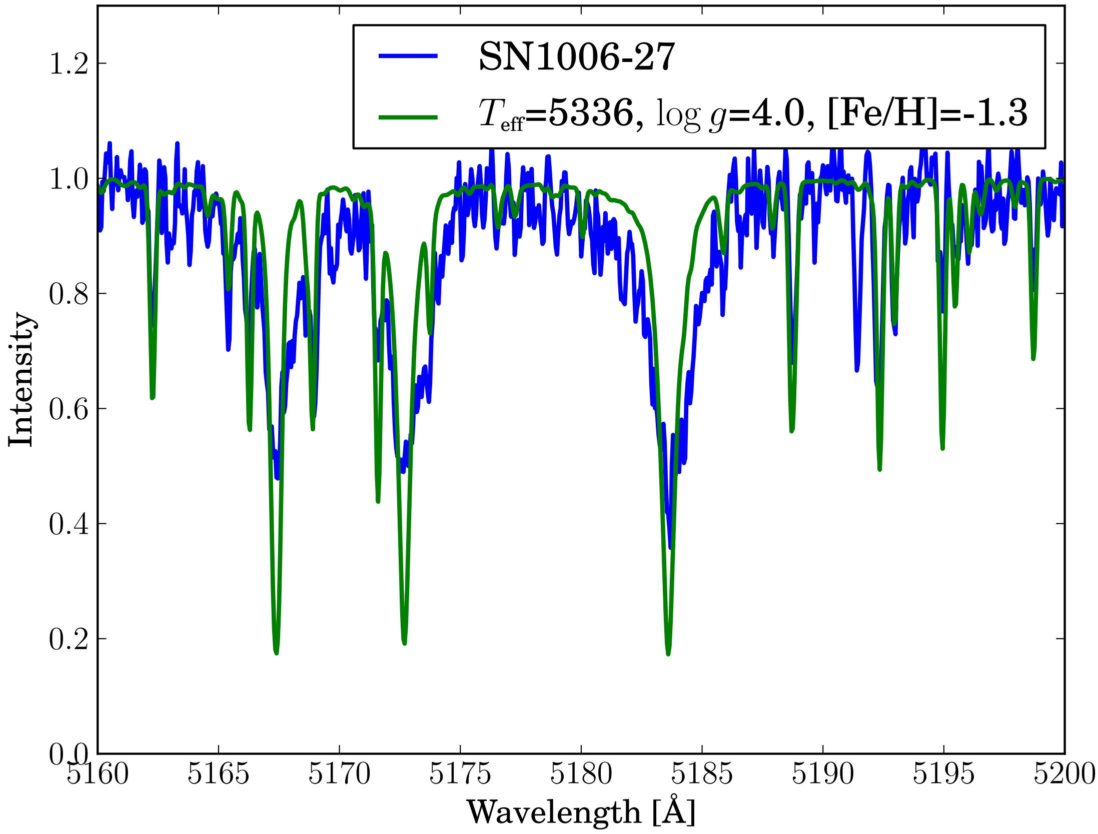

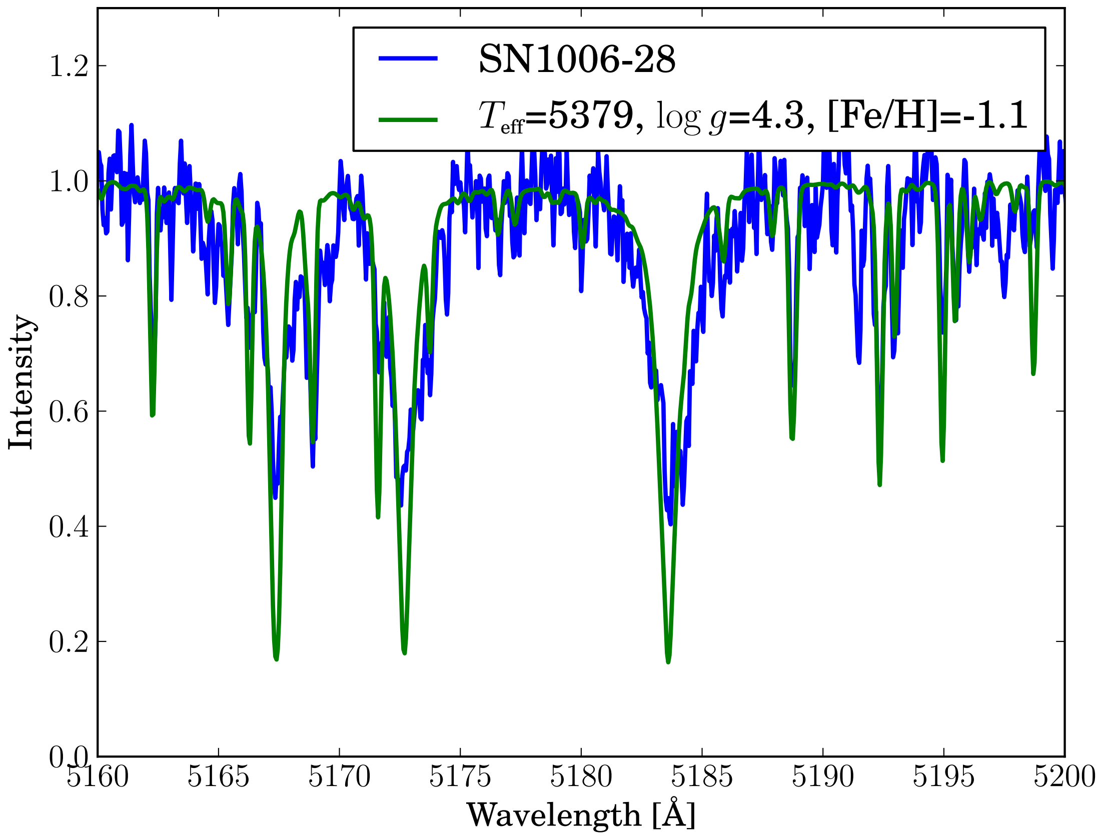

Figure C.1 Fit of SN 1006 candidate spectra